

Advances

in Clinical and Experimental Medicine

MONTHLY ISSN 1899-5276 (PRINT) ISSN 2451-2680 (ONLINE)

advances.umw.edu.pl

2024, Vol. 33, No. 5 (May)

Impact Factor (IF) – 2.1
Ministry of Science and Higher Education – 70 pts
Index Copernicus (ICV) – 161.11 pts



WROCLAW
MEDICAL UNIVERSITY

Advances
in Clinical and Experimental
Medicine



Advances in Clinical and Experimental Medicine

ISSN 1899-5276 (PRINT)

ISSN 2451-2680 (ONLINE)

advances.umw.edu.pl

MONTHLY 2024
Vol. 33, No. 5
(May)

Advances in Clinical and Experimental Medicine (*Adv Clin Exp Med*) publishes high-quality original articles, research-in-progress, research letters and systematic reviews and meta-analyses of recognized scientists that deal with all clinical and experimental medicine.

Editorial Office

ul. Marcinkowskiego 2–6
50-368 Wrocław, Poland
Tel.: +48 71 784 12 05
E-mail: redakcja@umw.edu.pl

Editor-in-Chief

Prof. Donata Kurpas

Deputy Editor

Prof. Wojciech Kosmala

Managing Editor

Marek Misiak, MA

Statistical Editors

Wojciech Bombała, MSc

Łucja Janek, MSc

Anna Kopszak, MSc

Dr. Krzysztof Kujawa

Jakub Wronowicz, MSc

Manuscript editing

Marek Misiak, MA

Paulina Piątkowska, MA

Publisher

Wrocław Medical University
Wybrzeże L. Pasteura 1
50-367 Wrocław, Poland

Online edition is the original version
of the journal

Scientific Committee

Prof. Sandra Maria Barbalho

Prof. Antonio Cano

Prof. Chong Chen

Prof. Breno Diniz

Prof. Erwan Donal

Prof. Chris Fox

Prof. Yuko Hakamata

Prof. Carol Holland

Prof. Sabine Bährer-Kohler

Prof. Markku Kurkinen

Prof. Christos Lionis

Prof. Raimundo Mateos

Prof. Zbigniew W. Raś

Prof. Jerzy W. Rozenblit

Prof. Silvina Santana

Prof. Sajee Sattayut

Prof. James Sharman

Prof. Jamil Shibli

Prof. Michał J. Toborek

Prof. László Vécsei

Prof. Cristiana Vitale

Prof. Hao Zhang

Section Editors

Basic Sciences

Prof. Iwona Bil-Lula

Prof. Bartosz Kempisty

Dr. Wiesława Kranc

Dr. Anna Lebedeva

Clinical Anatomy, Legal Medicine, Innovative Technologies

Prof. Rafael Boscolo-Berto

Dentistry

Prof. Marzena Dominiak

Prof. Tomasz Gedrange

Prof. Jamil Shibli

Laser Dentistry

Assoc. Prof. Kinga Grzech-Leśniak

Dermatology

Prof. Jacek Szepietowski

Emergency Medicine, Innovative Technologies

Prof. Jacek Smereka

Gynecology and Obstetrics

Prof. Olimpia Sipak-Szmigiel

Histology and Embryology

Dr. Mateusz Olbromski

Internal Medicine

Angiology

Dr. Angelika Chachaj

Cardiology

Prof. Wojciech Kosmala

Dr. Daniel Morris

Endocrinology

Prof. Marek Bolanowski

Gastroenterology

Assoc. Prof. Katarzyna Neubauer

Hematology

Prof. Andrzej Deptała
Prof. Dariusz Wołowicz

Nephrology and Transplantology

Assoc. Prof. Dorota Kamińska
Prof. Krzysztof Letachowicz

Pulmonology

Prof. Anna Brzecka

Microbiology

Prof. Marzenna Bartoszewicz
Assoc. Prof. Adam Junka

Molecular Biology

Dr. Monika Bielecka

Prof. Jolanta Sączko

Neurology

Assoc. Prof. Magdalena Koszewicz
Assoc. Prof. Anna Pokryszko-Dragan
Dr. Masaru Tanaka

Neuroscience

Dr. Simone Battaglia
Dr. Francesco Di Gregorio

Oncology

Prof. Andrzej Deptała
Prof. Adam Maciejczyk

Gynecological Oncology

Dr. Marcin Jędryka

Ophthalmology

Dr. Małgorzata Gajdzis

Orthopedics

Prof. Paweł Reichert

Otolaryngology

Assoc. Prof. Tomasz Zatoński

Pediatrics

Pediatrics, Metabolic Pediatrics, Clinical Genetics, Neonatology, Rare Disorders

Prof. Robert Śmigiel

Pediatric Nephrology

Prof. Katarzyna Kiliś-Pstrusińska

Pediatric Oncology and Hematology

Assoc. Prof. Marek Ussowicz

Pharmaceutical Sciences

Assoc. Prof. Marta Kepińska
Prof. Adam Matkowski

Pharmacoeconomics, Rheumatology

Dr. Sylwia Szafraniec-Buryło

Psychiatry

Dr. Melike Küçükkarapınar
Prof. Jerzy Leszek
Assoc. Prof. Bartłomiej Stańczykiewicz

Public Health

Prof. Monika Sawhney
Prof. Izabella Uchmanowicz

Qualitative Studies, Quality of Care

Prof. Ludmiła Marcinowicz

Radiology

Prof. Marek Szaśiadek

Rehabilitation

Dr. Elżbieta Rajkowska-Labon

Surgery

Assoc. Prof. Mariusz Chabowski
Assoc. Prof. Mirosław Kozłowski
Prof. Renata Taboła

Telemedicine, Geriatrics, Multimorbidity

Assoc. Prof. Maria Magdalena
Bujnowska-Fedak

Editorial Policy

Advances in Clinical and Experimental Medicine (Adv Clin Exp Med) is an independent multidisciplinary forum for exchange of scientific and clinical information, publishing original research and news encompassing all aspects of medicine, including molecular biology, biochemistry, genetics, biotechnology and other areas. During the review process, the Editorial Board conforms to the "Uniform Requirements for Manuscripts Submitted to Biomedical Journals: Writing and Editing for Biomedical Publication" approved by the International Committee of Medical Journal Editors (www.ICMJE.org). The journal publishes (in English only) original papers and reviews. Short works considered original, novel and significant are given priority. Experimental studies must include a statement that the experimental protocol and informed consent procedure were in compliance with the Helsinki Convention and were approved by an ethics committee.

For all subscription-related queries please contact our Editorial Office: redakcja@umw.edu.pl

For more information visit the journal's website: advances.umw.edu.pl

Pursuant to the ordinance of the Rector of Wrocław Medical University No. 37/XVI R/2024, from March 1, 2024, authors are required to pay a fee for each manuscript accepted for publication in the journal Advances in Clinical and Experimental Medicine. The fee amounts to 1600 EUR for all types of papers.

Advances in Clinical and Experimental Medicine has received financial support from the resources of Ministry of Science and Higher Education within the "Social Responsibility of Science – Support for Academic Publishing" project based on agreement No. RCN/SP/0584/2021.



Ministry of Education and Science
Republic of Poland

Czasopismo Advances in Clinical and Experimental Medicine korzysta ze wsparcia finansowego ze środków Ministerstwa Edukacji i Nauki w ramach programu „Społeczna Odpowiedzialność Nauki – Rozwój Czasopism Naukowych” na podstawie umowy nr RCN/SP/0584/2021.



Ministerstwo
Edukacji i Nauki

Indexed in: MEDLINE, Science Citation Index Expanded, Journal Citation Reports/Science Edition, Scopus, EMBASE/Excerpta Medica, Ulrich's™ International Periodicals Directory, Index Copernicus

Typographic design: Piotr Gil, Monika Kołęda

DTP: Wydawnictwo UMW

Cover: Monika Kołęda

Printing and binding: PRINT PROFIT Sp. z o.o., Koźmin 27, 59-900 Zgorzelec

Contents

Editorial

- 423 Rafael Boscolo-Berto
Challenges and future trends of forensic toxicology to keep a cut above the rest
- 427 Donato Liloia, Tommaso Costa, Franco Cauda, Jordi Manuella
Building diagnostic neuroimaging biomarkers for psychiatric disorders using reverse inference approaches: A viable route?

Meta-analysis

- 435 Qingli Chen, Na Li, Yue Wu
Neostigmine for postoperative surgical urine retention: A systematic review and meta-analysis
- 445 Zhen Li, Xiang Ma, Ziquan Wang, Suwei Dong, Baoqing Wang
A meta-analysis of the efficacy and safety of first-line chemotherapeutic agents for osteosarcoma

Original papers

- 455 Hüseyin Aydın, Hasan Aydın, Adnan Karaibrahimoğlu, Baris Afsar
Evaluation of the parenchymal distribution of renal steatosis in chronic kidney disease using chemical shift magnetic resonance imaging
- 463 Kun Li, Wen-Wen Cao, Shao-Hua Chen, Bin-Fei Zhang, Yu-Min Zhang
Association between total cholesterol and all-cause mortality in geriatric patients with hip fractures: A prospective cohort study with 339 patients
- 473 Zhihe Zeng, Xiao Tian, Lin Li, Yugang Diao, Tiezheng Zhang
An interpretable machine learning model to predict off-pump coronary artery bypass grafting-associated acute kidney injury
- 483 Baris Baser, Mehmet Birol Ozel
Comparison of primary stability of used and unused self-tapping and self-drilling orthodontic mini-implants
- 491 Mehmet Erinmez, Yasemin Zer
In vitro effects of deferoxamine on antibiotic susceptibility in Gram-negative bacteria
- 499 Luyao Liu, Wang Xiao, Zhulin Yang, Qunwei Wang, Jianing Yi
Human umbilical cord mesenchymal stem cell-derived exosomal miR-214-3p regulates the progression of gallbladder cancer by regulating ACLY/GLUT1
- 511 Shuling Zhang, Annamalai Vijayalakshmi, Lingjun Meng
Oridonin attenuated human PC-3 cell activity by modulating the Wnt/ β -catenin signaling

Reviews

- 519 Piotr Kocełak, Monika Puzianowska-Kuźnicka, Magdalena Olszanecka-Glinianowicz, Jerzy Chudek
Wnt signaling pathway and sclerostin in the development of atherosclerosis and vascular calcification

Research letters

- 533 Xiumin Li, Qiaoling Su, Yutian Pan
Transcriptome analysis of immune-inflammatory regulation in *Tremella fuciformis*-derived polysaccharide reeducated B16 cells: A subcutaneous model
- 543 Dariusz Grzelecki, Dariusz Marczak, Piotr Dudek, Tomasz Okoń, Bartłomiej Kordasiewicz, Jacek Kowalczewski
Is there a role of calprotectin testing in the diagnosis of surgical site infections after total hip and knee arthroplasty? A preliminary study

Challenges and future trends of forensic toxicology to keep a cut above the rest

Rafael Boscolo-Berto^{A–F}

Department of Neurosciences, Institute of Human Anatomy, University of Padova, Italy

A – research concept and design; B – collection and/or assembly of data; C – data analysis and interpretation; D – writing the article; E – critical revision of the article; F – final approval of the article

Advances in Clinical and Experimental Medicine, ISSN 1899–5276 (print), ISSN 2451–2680 (online)

Adv Clin Exp Med. 2024;33(5):423–425

Address for correspondence

Rafael Boscolo-Berto
E-mail: rafael.boscoloberto@unipd.it

Funding sources

None declared

Conflict of interest

None declared

Received on January 31, 2024

Reviewed on March 3, 2024

Accepted on March 6, 2024

Published online on March 21, 2024

Abstract

Forensic toxicology faces several challenges in research and daily practice, including new drugs and futuristic technologies requiring innovative testing methods and continuous education and training of professionals. One of the most pressing issues in recent years is the emergence of novel psychoactive substances, often created by modifying the chemical structure of existing drugs to produce compounds with similar effects that are not yet regulated and lack standardized references. To overcome this challenge, forensic toxicologists have employed a range of analytical methods, including qualitative and quantitative analysis using highly sensitive technologies such as liquid chromatography-mass spectrometry (LC-MS) and gas chromatography-mass spectrometry (GC-MS), which are the most reliable and accurate methods for detecting drugs in biological samples. Liquid chromatography coupled with tandem mass spectrometry (LC-MS-MS) is becoming the gold standard for detecting controlled substances, their derivatives and metabolites. Despite advancements in testing methods, challenges persist in forensic toxicology. As such, the field must invest in research and development to improve testing methods, utilize cutting-edge technologies, increase funding for training programs, and promote multidisciplinary interactions.

Key words: forensic toxicology, forensic medicine, mass spectrometry, chromatography, immunoassay

Cite as

Boscolo-Berto R. Challenges and future trends of forensic toxicology to keep a cut above the rest. *Adv Clin Exp Med.* 2024;33(5):423–425. doi:10.17219/acem/185730

DOI

10.17219/acem/185730

Copyright

Copyright by Author(s)

This is an article distributed under the terms of the Creative Commons Attribution 3.0 Unported (CC BY 3.0) (<https://creativecommons.org/licenses/by/3.0/>)

Introduction

Forensic toxicology is an essential field that plays a pivotal role in solving crimes, ensuring public safety and monitoring social phenomena of substance abuse, even in young people.^{1,2} However, the field encounters several challenges and innovations in research and daily forensic practice, including the emergence of new drugs that activate specific interconnected metabolic systems in the human brain, cutting-edge technologies requiring new testing methods, and the need for continuous education and training of professionals to keep up with these developments.³

Techniques in use

In recent years, forensic toxicology has faced the increasing prevalence of novel psychoactive substances (NPS). A lack of standardized references and the emergence of new substances pose a challenge for forensic toxicologists in identifying and quantifying NPS in bodily fluids. To overcome this issue, the systematic application of mass spectrometry (MS)-based technologies is required, and forensic toxicology laboratories must maintain the highest scientific integrity in their analytical processes. Immunoassay (IA) was the traditional standard for screening purposes, followed by MS for confirmation analysis. However, gas and liquid chromatography coupled with mass spectrometry (GC-MS and LC-MS) have grown in popularity over time. These methods can analyze many molecules at low concentrations in one run, making them useful for clinical applications, including therapeutic drug and psychoactive substance abuse monitoring, forensic investigations and anti-doping controls.⁴

Liquid chromatography-mass spectrometry, in particular, has become crucial to the field, replacing immuno-enzymatic methods for screening and confirmation.^{5,6} The method has higher analytical specificity and sensitivity than IA, which may suffer from calibration bias, diminished sensitivity and specificity, and potential vulnerability to various interferences. The accuracy of IA can also be compromised by cross-reactivity with endogenous and exogenous compounds linked to the analyte of interest, leading to incorrect positive or negative results. Moreover, inconsistency across platforms is a pressing concern, as the impact of cross-reactivity relies heavily on the antibodies used. Experts recommend using hyphenated MS techniques to overcome the limitations of immunoassay-based screening methods, especially in systematic toxicological analysis and drug abuse testing.⁷ However, challenges such as high instrument costs, personnel qualification requirements and longer processing times hinder the implementation of MS techniques. More user-friendly and fully automated MS instruments should be used to address these issues. Nonetheless, due to fast sample preparation and analysis, IA is still widely used in routine laboratory practices.

In toxicology workflows, a confirmation technique is only used after a positive result from a screening technique, particularly for forensic applications. As a consequence, negative outcome of a screening technique must be reliable to a near-certainty. On these bases, forensic toxicology laboratories need to optimize screening cutoffs for specific case scenarios rather than relying solely on manufacturer's recommendations, as recently published.⁸

Recent developments

Forensic toxicology has been prioritizing the development and validation of techniques for detecting an ever-growing number of "classic drugs" and NPS in biological samples taken from living and deceased individuals.^{9,10} A range of analytical methods have been implemented to identify and characterize NPS. Among these, qualitative and quantitative methods, such as LC-MS and GC-MS, are considered the most reliable and accurate. However, these techniques are not universally accessible in all forensic toxicology laboratories and require trained operators and continuous updates from national and international networks. Additionally, more cost-effective techniques such as LC-photodiode array and GC-flame ionization detection are employed.

Liquid chromatography coupled with tandem MS has emerged as the gold standard analytical tool for detecting controlled substances, their derivatives and metabolites.^{11,12} The combination of chromatographic retention time and high-resolution (tandem) MS helps identify a drug molecule by determining the precise mass of a precursor ion and its fragmentation pattern. During the identification process, similarity search algorithms compare the tandem mass spectra of targeted compounds with those in a database. An extensive MS-MS database is crucial for LC-MS-MS-based drug analysis and monitoring, though it is not as comprehensive as required to meet the increasing number of newly synthesized drugs.

Identifying novel synthetic drugs has been one of the most challenging analytical issues in the drug regulatory community. To address this, recent approaches have used artificial intelligence (AI) to study illicit drug analogs, specifically, the hybrid similarity search (HSS).¹³ Furthermore, NPS analysis requires labor-intensive and expensive reference standards, which might not be accessible for recently emerged NPS on the illicit market. Deep learning methods have been developed to predict known and hypothesized NPS MS/MS spectra from their chemical structures alone.¹⁴ However, implementing AI-based technologies in forensic toxicology encounters significant problems, including limited or poor-quality training data that can limit accuracy. Furthermore, biological samples can vary significantly in composition between individuals, making interpreting the results difficult, and if the training data contain biases, AI can inherit and amplify these biases. Data from forensic toxicology laboratories should be collected and integrated

to achieve larger and homogeneous datasets, which is particularly relevant if the training data are representative of specific demographic groups or if there are inequalities in the samples. The interpretation of results requires specialized expertise, which means that forensic toxicology often requires the experience of a multidisciplinary team.

Conclusions

The field of forensic toxicology is experiencing a dual challenge. On the one hand, there is a need for highly reliable techniques that can deliver scientifically sound evidence with the utmost precision and accuracy, which are an integral prerequisite in criminal justice proceedings. On the other hand, the illicit market is increasing, bringing a surge of unfamiliar molecules, meaning we must invest in research and development to improve testing methods and the use of cutting-edge technologies. Future research should focus on developing methods for detecting many substances in progressively smaller sample volumes while ensuring the high accuracy and precision levels necessary for forensic analysis.

Sharing data among laboratories by creating national and international networks is crucial to meeting the aims outlined and will require increased funding for training programs and promoting multidisciplinary interactions.¹⁵ By doing so, we can support forensic toxicology to achieve and maintain excellence at the highest analytical level. A cut above the rest.

ORCID iDs

Rafael Boscolo-Berto  <https://orcid.org/0000-0001-7556-1943>

References

- Bertol E, Vaiano F, Boscolo-Berto R, et al. Alcohol, caffeine, and nicotine consumption in adolescents: Hair analysis versus self-report. *Am J Drug Alcohol Abuse*. 2017;43(3):341–349. doi:10.1080/00952990.2016.1216556
- Favretto D, Stocchero G, Nalesso A, et al. Monitoring haloperidol exposure in body fluids and hair of children by liquid chromatography–high-resolution mass spectrometry. *Ther Drug Monit*. 2013;35(4):493–501. doi:10.1097/FTD.0b013e3182892d11
- Boscolo-Berto R, Viel G, Cecchi R, et al. Journals publishing biomedicolegal research in Europe. *Int J Legal Med*. 2012;126(1):129–137. doi:10.1007/s00414-011-0620-3
- Bertol E, Mari F, Boscolo-Berto R, Mannaioni G, Vaiano F, Favretto D. A mixed MDPV and benzodiazepine intoxication in a chronic drug abuser: Determination of MDPV metabolites by LC–HRMS and discussion of the case. *Forensic Sci Int*. 2014;243:149–155. doi:10.1016/j.forsciint.2014.08.002
- Antonelli G, Marinova M, Artusi C, Plebani M. Mass spectrometry or immunoassay: Est modus in rebus. *Clin Chem Lab Med*. 2017;55(9):1243–1245. doi:10.1515/cclm-2017-0197
- Barone R, Giorgetti A, Cardella R, et al. Development and validation of a fast UPLC-MS/MS screening method for the detection of 68 psychoactive drugs and metabolites in whole blood and application to post-mortem cases. *J Pharm Biomed Anal*. 2023;228:115315. doi:10.1016/j.jpba.2023.115315
- Peters FT, Wissenbach D. Current state-of-the-art approaches for mass spectrometry in clinical toxicology: An overview. *Exp Opin Drug Metab Toxicol*. 2023;19(8):487–500. doi:10.1080/17425255.2023.2252324
- Giorgetti A, Pascali JP, Pelletti G, et al. Optimizing screening cutoffs for drugs of abuse in hair using immunoassay for forensic applications [published online as ahead of print on February 27, 2024]. *Adv Clin Exp Med*. 2024. doi:10.17219/acem/183124
- Pelletti G, Rossi F, Garagnani M, et al. Optimization of cloned enzyme donor immunoassay cut-offs for drugs of abuse in post-mortem whole blood. *Forensic Sci Int*. 2020;312:110291. doi:10.1016/j.forsciint.2020.110291
- Pelletti G, Garagnani M, Rossi F, Roffi R, Barone R, Pelotti S. Optimization of cloned enzyme donor immunoassay cut-offs for drugs of abuse in whole blood of drivers involved in road accidents. *Forensic Sci Int*. 2019;294:27–33. doi:10.1016/j.forsciint.2018.10.023
- Ji JJ, Xu D, Yan H, Xiang P, Shen M. LC–MS–MS determination of 88 psychotropic drugs in 1,865 hair samples from addicts in drug abstinence. *J Anal Toxicol*. 2023;47(1):52–58. doi:10.1093/jat/bkac024
- Rubicondo J, Scuffi L, Pietrosevoli L, et al. A new multi-analyte LC–MS–MS screening method for the detection of 120 NPSs and 49 drugs in hair. *J Anal Toxicol*. 2023;46(9):e262–e273. doi:10.1093/jat/bkac093
- Lee SY, Lee ST, Suh S, Ko BJ, Oh HB. Revealing unknown controlled substances and new psychoactive substances using high-resolution LC–MS–MS machine learning models and the hybrid similarity search algorithm. *J Anal Toxicol*. 2022;46(7):732–742. doi:10.1093/jat/bkab098
- Wang F, Pasin D, Skinnider MA, et al. Deep learning-enabled MS/MS spectrum prediction facilitates automated identification of novel psychoactive substances. *Anal Chem*. 2023;95(50):18326–18334. doi:10.1021/acs.analchem.3c02413
- Viel G, Boscolo-Berto R, Cecchi R, Bajanowski T, Vieira ND, Ferrara SD. Bio-medicolegal scientific research in Europe: A country-based analysis. *Int J Legal Med*. 2011;125(5):717–725. doi:10.1007/s00414-011-0576-3

Building diagnostic neuroimaging biomarkers for psychiatric disorders using reverse inference approaches: A viable route?

Donato Liloia^{A–F}, Tommaso Costa^{E,F}, Franco Cauda^{E,F}, Jordi Manuella^{C–F}

Department of Psychology, University of Turin, Italy

A – research concept and design; B – collection and/or assembly of data; C – data analysis and interpretation; D – writing the article; E – critical revision of the article; F – final approval of the article

Advances in Clinical and Experimental Medicine, ISSN 1899–5276 (print), ISSN 2451–2680 (online)

Adv Clin Exp Med. 2024;33(5):427–433

Address for correspondence

Donato Liloia

E-mail: donato.liloia@unito.it

Funding sources

None declared

Conflict of interest

None declared

Received on February 12, 2024

Reviewed on March 17, 2024

Accepted on April 4, 2024

Published online on May 13, 2024

Abstract

The advent of structural magnetic resonance imaging (sMRI) at the end of the 20th century opened the way toward a deeper understanding of the neurophysiology of psychiatric disorders, substantiating regional structural abnormalities underlying this group of clinical conditions. However, despite abundant and flourishing scientific research, sMRI methodologies are not currently integrated into daily diagnostic practice. One reason behind this failed translation may be the prevailing approach to logical reasoning in neuroimaging: The forward inference via frequentist-based statistics. This reasoning prevents clinicians from obtaining information about the selectivity of results, which are therefore of limited use regarding the definition of biomarkers and refinement of diagnostic processes. Recently, another type of inferential approach has started to emerge in the neuroimaging field: The reverse inference via Bayesian statistics. Here, we introduce the key concepts of this approach, with a particular emphasis on the clinical sMRI environment. We survey recent findings showing significant potential for clinical translation. Clinical opportunities and challenges for developing reverse inference-based neural markers for psychiatry are also discussed. We propose that a systematic sharing of imaging data across the human brain mapping community is an essential first step toward a paradigmatic clinical shift. We conclude that a defined synergy between forward-based and reverse-based sMRI research can illuminate current discussions on diagnostic brain markers, offering clarity on key issues and fostering new tailored diagnostic avenues.

Key words: magnetic resonance imaging, psychiatry, gray matter, biological markers, neurophysiology

Cite as

Liloia D, Costa T, Cauda F, Manuella J. Building diagnostic neuroimaging biomarkers for psychiatric disorders using reverse inference approaches: A viable route?

Adv Clin Exp Med. 2024;33(5):427–433.

doi:10.17219/acem/186816

DOI

10.17219/acem/186816

Copyright

Copyright by Author(s)

This is an article distributed under the terms of the Creative Commons Attribution 3.0 Unported (CC BY 3.0) (<https://creativecommons.org/licenses/by/3.0/>)

Neuronal markers in psychiatry: (Still) an open issue

In the context of clinical research, the term “diagnostic biomarker” denotes a diverse spectrum of medically relevant signals or objective indices of clinical status with the potential to detect and/or confirm the presence of a condition of interest.¹ The advent of structural magnetic resonance imaging (sMRI) nearly 3 decades ago generated fervent enthusiasm about its potential to revolutionize our comprehension of the neuroanatomical basis of psychiatric disorders and to identify clinically valuable brain-based markers. Although the development of several sMRI-based techniques and the associated exponential proliferation of studies have facilitated substantial progress in elucidating the former goal (graphical overview in Fig. 1), it is crucial to emphasize that no discernible metrics or models stemming from these advanced techniques have been integrated into daily clinical diagnostic practice thus far.^{2–11} As a result, contemporary psychiatric diagnoses rely on descriptive data collected through clinical observation,¹² leaving the development of neuroimaging biomarkers for predicting diagnostic categories or disease progression an open challenge.

What underlies this translational gap in psychiatric neuroimaging? While some researchers advocate for the need to reform the current standards concerning group-level sample size,^{13,14} others posit that the further development of single-subject methods is essential to capture inter-individual features of this group of conditions characterized by aberrations in mood, cognition and behavior.^{15–17} Choices pertaining population stratification, phenotypic profile selection, MRI data transformation, imaging modalities, multimodal measures, and algorithms are also a matter of ongoing debate.^{18–24} No less important, the clinical and biological heterogeneity of patients in terms of type of symptomatology, medication status, neurodevelopmental stage, and medical comorbidities makes it challenging to detect a sound neurophysiological signature for the clinical population of interest.^{25–30}

Here, we add further complexity to the issue by stating that clinical inferences drawn from canonical group-level sMRI techniques with case-control designs fall short of translational goals. The main claim of this editorial is to elucidate the inferential drawbacks evident in current sMRI psychiatric research and provide suggestions for overcoming these drawbacks within an existing knowledge framework. We propose that reverse inference reasoning via Bayesian statistics provides an ideal stepping stone to suit specific clinically relevant questions across the spectrum of translational neuroimaging.

Inferential reasoning in clinical neuroimaging

In the field of clinical neuroscience, sMRI techniques such as voxel-based morphometry (VBM), cortical thickness

(CT), diffusion-weighted imaging (DWI), and diffusion tensor imaging (DTI) play a pivotal role. As well as their specific biological significance, these advanced computational techniques allow researchers to identify regional neuroanatomical variations associated with a clinical population of interest by means of a whole-brain data-driven voxel-wise intergroup comparison with a neurotypical control group.^{31,32} Frequentist-based parametric statistics like the two-sample t-test are generally employed to this end, which reveals clusters of voxels where the null hypothesis (i.e., no difference in neuronal morphometry between the groups in question) is rejected using a certain user-selected p-value.³³ In this scenario, a precise type of reasoning can be delineated: A “disorder-to-alteration estimation” or forward inference.³⁴ In formal terms, the forward inference represents the probability $p(\text{alteration}|\text{disorder})$ of detecting alteration of some brain territories based on the hypothesis of the presence of a given disorder (Fig. 1). For example, it answers

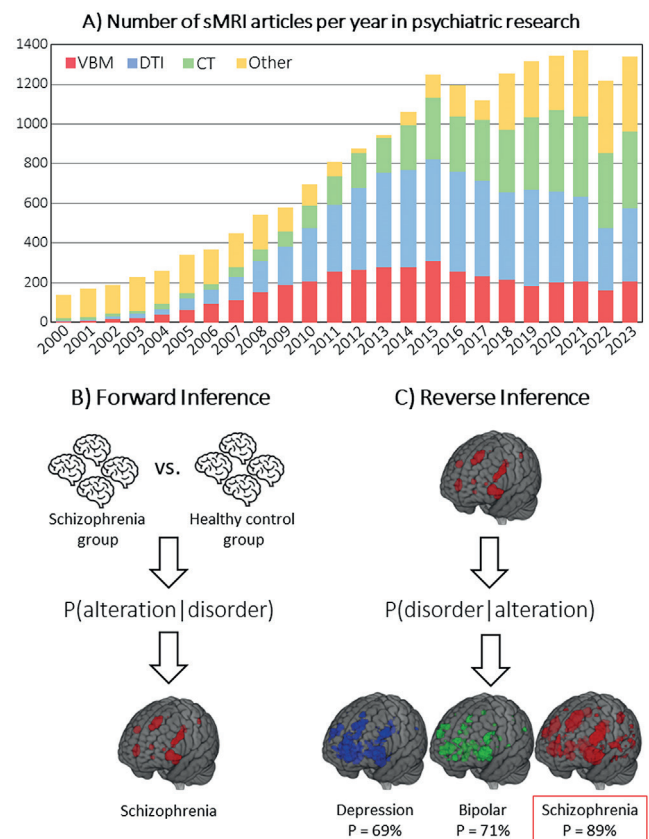


Fig. 1. A. Annual publication count in PubMed search engine for psychiatric research using structural magnetic resonance imaging (sMRI). Search, conducted on January 15, 2024, reveals trends in voxel-based morphometry (VBM), diffusion tensor imaging (DTI), cortical thickness (CT), and other sMRI-based techniques (Other); B. Forward inference in brain imaging. Given a known psychiatric disorder (e.g., schizophrenia), one can identify the corresponding changes in brain anatomy and generate a forward inference; C. Reverse inference in brain imaging. Given posterior probability maps for multiple disorders (e.g., depression, bipolar, and schizophrenia), one can classify a new alteration map by identifying the disorder with the highest probability (P) given the new data (in this example, schizophrenia). The maps shown here were obtained from the NeuroSynth database [<https://www.neurosynth.org/>], serving a sole purpose for visualization

the question “How probable is it to observe this pattern of neuroanatomical variation since I hypothesize that my patient is affected by this given disorder?”

Forward inference-based reasoning is used extensively in quantitative clinical sMRI research due to its role in uncovering the neural substrates co-occurring with a mental illness.^{35,36} Nevertheless, it is important to note that such reasoning was not designed with translational goals in mind and has a number of fundamental limitations, most importantly its inability to establish differential diagnosis and estimate the selectivity of the effect under investigation.^{24,37,38} In other words, researchers can only infer the presence of a neuroanatomical pattern of variation in the disorder under study, but not “whether” and “to what extent” this pattern is pathognomonic for the disorder of interest or observable in other clear-cut clinical conditions. In recent years, this issue has been repeatedly accentuated in MRI-derived meta-analyses, which have demonstrated a shared neuroanatomical/functional abnormal substrate for major psychiatric disorders.^{39–45} For example, recent studies^{46,47} taking into account forward-inference based VBM data from 82 different brain disorders and over 19,000 study participants found that a broad array of cortical and subcortical regions exhibit alterations in the context of numerous, if not all, of the considered disorders (Fig. 2). Hence, this substantial convergence hinders the utility of sMRI methods for diagnostic purposes in pinpointing a specific clinical condition, given the noticeable absence of selectivity in the alteration patterns within these regions.

Building on the seminal contributions of Poldrack,^{48,49} a different reasoning pattern in the human brain mapping community has recently been introduced: The reverse inference via Bayesian statistics. In formal terms, the reverse inference represents the probability $p(\text{disorder}|\text{alteration})$ of the presence of a given disorder based on the observed alteration (Fig. 1). Moreover, in practice, it can answer the question “How probable is that my patient is indeed affected with the disorder I hypothesize since I observe this pattern of neuroanatomical variation?” Of note, this type of experimental evidence can be quantified using Bayes’ rule⁵⁰ (for methodological details and explanations specific to the MRI environment, refer to Poldrack⁴⁹ and Liloia et al.⁵¹). This perspective underscores that the degree of belief of a reverse inference hinges on the selectivity of neuroanatomical alterations in the disorder under scrutiny (i.e., the ratio of disorder-specific variation in the brain to the overall likelihood of variation across all other brain disorders), along with the prior belief of observing neuroanatomical variations associated with the disorder of interest. Consequently, we can obtain an estimate of how likely the disorder is given the observed pattern of neuroanatomical variation. It is crucial to acknowledge that this reasoning offers numerous advantages over canonical forward-inference methods.⁵² Primarily, it overcomes the binary decision of rejecting or not

rejecting null hypotheses, instead providing a quantitative assessment of the evidence supporting the hypothesis under scrutiny.³⁷

Neuronal markers and reverse inference: State of the field

While the reverse inference reasoning has provided important new information about the functional architecture of the human brain in normative populations using task-based fMRI data,^{48,53–55} its application in the field of clinical sMRI has been systematically neglected. Recently, a new trend has started to emerge to address this issue. Specifically, in Cauda et al.,⁵² the authors delved into the 2 distinct selective volumetric alteration patterns observed in Alzheimer’s disease and schizophrenia. This was achieved by analyzing published data derived from the entire VBM BrainMap database⁵⁶ utilizing the Bayes factor (BF),⁵⁷ a statistical measure that quantifies the strength of evidence for one hypothesis over another. Taking the research a step further, the same group developed a meta-analytic reverse inference toolbox called Bayes fACTor mOdeliNg (BACON).⁵⁸ This user-friendly and open access resource facilitates the generation of whole-brain maps, which display the selective alteration landscape at the voxel-level for a given disorder. In doing so, it compares the pattern of alteration that can be observed based on VBM results about a given disorder of interest (e.g., schizophrenia) against the pattern of alteration that can be observed based on VBM results about all the possible disorders excluding that of interest (e.g., everything but schizophrenia). Then, the BF is computed to quantify the strength of evidence for selective alterations associated with the disorder of interest (in our example, the pattern of alteration that can be observed in schizophrenia is much more likely than in any other disorder) (Fig. 2).

Recently, BACON was used to explore the presence of selective brain abnormalities in autism spectrum disorder across an extensive dataset of 849 VBM experiments, accounting for over 22,000 clinical study participants diagnosed with 132 different brain disorders.⁵¹ Intriguingly, findings highlighted the existence of significant abnormalities in both cortical and cerebellar regions, with a selectivity value $\geq 90\%$ (i.e., $p < 0.05$) (Fig. 2). Significantly, this study not only introduced a new perspective on understanding the autistic brain, but also presented a reverse inference framework with wide-reaching potential. In fact, the BACON approach is applicable to any other clinical condition that exhibits regional variations in brain structure, as detected through VBM, CT, DWI, DTI, or other group-level sMRI techniques with case-control designs. Furthermore, this toolbox is also potentially applicable to the study of disorder-selective functional brain aberrations as revealed using several whole-brain voxel-wise nuclear medicine and fMRI techniques, such as positron emission tomography

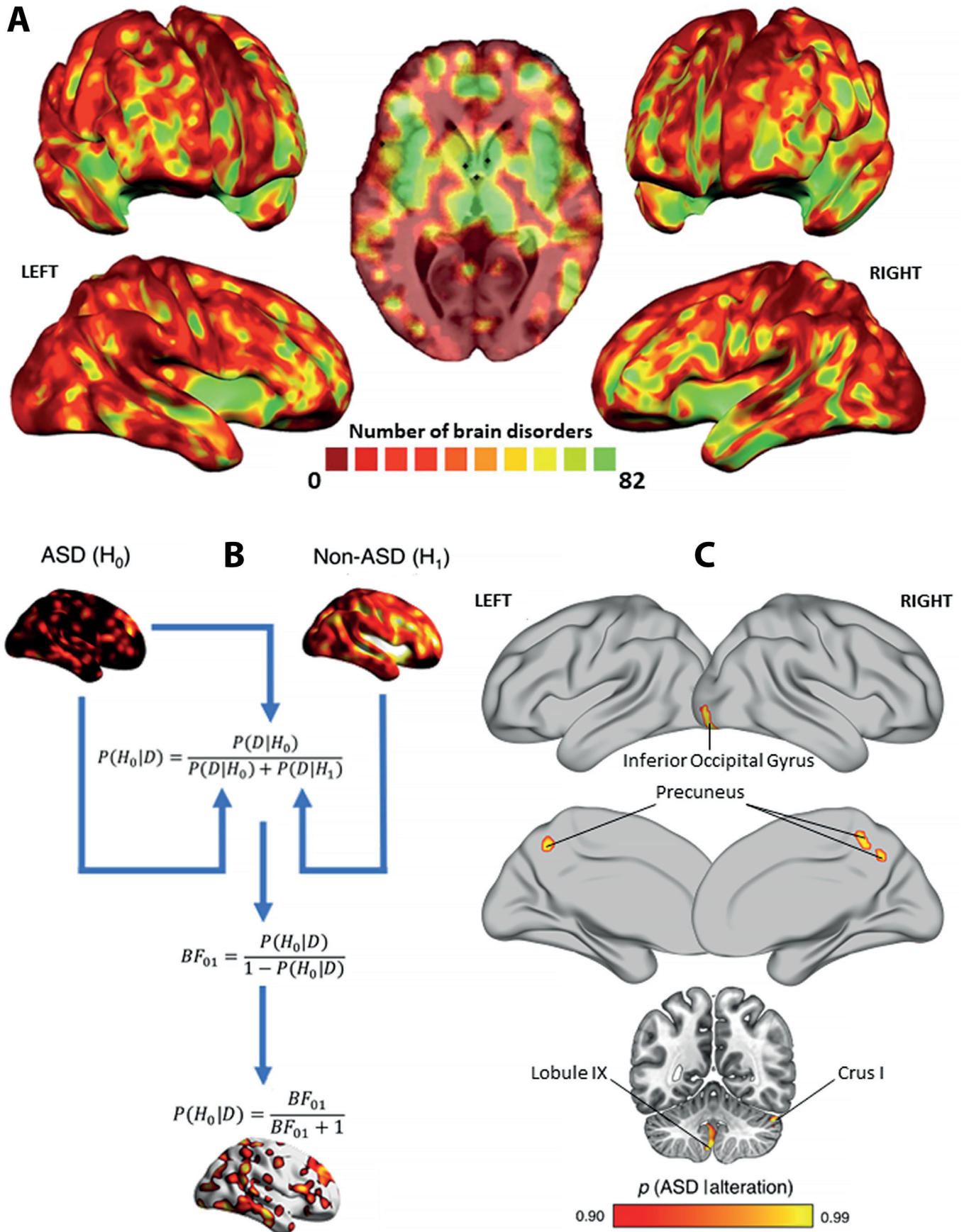


Fig. 2. A. The voxel-wise extent of spatial overlap in neuroanatomical alterations among the complete range of neurological and psychiatric disorders stored in the BrainMap database [adapted with permission from Cauda et al.⁴⁰]; B. Graphical representation of the data analytic pipeline of the Bayes fActor mOdeliNg (BACON) toolbox (adapted with permission from Costa et al.⁴³); C. Selective clusters of neuroanatomical variation in autism spectrum disorder (ASD) derived from Bayes fActor mOdeliNg (BACON) analysis and thresholded at p (ASD |alteration) ≥ 0.9 (i.e., 90%) (adapted with permission from Liloia et al.⁴⁴)

(PET), arterial spin labeling (ASL), regional homogeneity (ReHo), or amplitude of low-frequency fluctuations (ALFF), broadening its utility in the field of clinical neuroimaging. Nonetheless, it is crucial to note the current lack of studies in this specific area of research, which underscores the necessity for future multimodal imaging endeavors.

Methodological considerations and future (clinical) directions

The studies surveyed above offer hope for understanding the neuropathological basis of psychiatric disorders and yielding valuable diagnostic applications. Nevertheless, there are essential initial ways in which modeling efforts may undergo to start a paradigm shift.

Current reverse inference literature is based on meta-analytic data that, by definition, are characterized by more spatial uncertainty than native statistical parametric mapping data, thereby diminishing the ability to identify smaller but potentially highly selective brain areas.^{59,60} As a matter of fact, so far, the use of meta-analytic and coordinate-based repositories (i.e., BrainMap⁵⁶ or NeuroSynth⁵³) is the prime approach to create posterior probability maps capable of giving an overarching picture of the disorder-specific brain variations utilizing VBM and fMRI data exclusively.^{48,51,61} While the trend toward sharing is gaining traction,^{62–65} the establishment of publicly accessible, automated repositories for storing, sharing and querying voxel-wise whole-brain multimodal data from published neuroimaging studies is still in its infancy. In this context, we expect that the systematic and widespread use of fine-grained maps derived from a plethora of advanced imaging techniques will enhance the relevance of reverse inference research. The culture of sharing is also crucial to improve the generalizability of brain reverse inference models. For translational utility, these models must generalize to new individual cases, and their key signatures should be globally distributed across laboratories. This can enable testing in diverse settings with reduced complexity and error potential.

Can these methodological enhancements initiate the development of imaging biomarkers for psychiatry, or even modify current diagnostic criteria, in the absence of a definitive biological gold standard? We anticipate an iterative process in the near future, where prior neuroimaging-based prediction findings inform new hypotheses and serve as foundational knowledge for future diagnostic-oriented studies. In this context, we claim that the Bayesian reverse inference approach offers a significant advantage over traditional frequentist methods, as it allows for continuous updating of data supporting the hypotheses of interest (i.e., Bayesian updating).^{58,66} Furthermore, if this process proves capable of identifying highly selective regions of interest among studies, future clinical efforts will be able to adopt tailored measurements on these specific areas,

e.g., utilizing targeted strategies based on biological approaches at the micro- and meso-levels.

Another concrete goal of clinical neuroimaging based on reverse inference can be seen in its potential ability to integrate information from daily clinical practice. We expect that selective brain maps can assist in convincing clinicians of the robustness of their behavioral-based predictions, especially when the highlighted areas have been independently linked to the outcome by other reports, or to resolve uncertainties regarding complex scenarios.

In summary, this editorial discusses the latest developments in the role of reverse inference reasoning in structural MRI in psychiatry. The essence of this work is programmatic, aiming to delineate the interplay and potential synergies between forward-based and reverse-based research approaches. We posit that this distinction can illuminate current discussions on diagnostic brain markers, offering clarity on key issues, and fostering new avenues for methodological and clinical consideration in this domain.

ORCID iDs

Donato Liloia  <https://orcid.org/0000-0002-9481-8510>

Tommaso Costa  <https://orcid.org/0000-0002-0822-862X>

Franco Cauda  <https://orcid.org/0000-0003-1526-8475>

Jordi Manuella  <https://orcid.org/0000-0002-9928-0924>

References

1. Califf RM. Biomarker definitions and their applications. *Exp Biol Med (Maywood)*. 2018;243(3):213–221. doi:10.1177/1535370217750088
2. Abi-Dargham A, Moeller SJ, Ali F, et al. Candidate biomarkers in psychiatric disorders: State of the field. *World Psychiatry*. 2023;22(2):236–262. doi:10.1002/wps.21078
3. Caroli A. Diffusion-weighted magnetic resonance imaging: Clinical potential and applications. *J Clin Med*. 2022;11(12):3339. doi:10.3390/jcm11123339
4. Fu CHY, Costafreda SG. Neuroimaging-based biomarkers in psychiatry: Clinical opportunities of a paradigm shift. *Can J Psychiatry*. 2013;58(9):499–508. doi:10.1177/070674371305800904
5. Kraguljac NV, McDonald WM, Widge AS, Rodriguez CI, Tohen M, Nemeroff CB. Neuroimaging biomarkers in schizophrenia. *Am J Psychiatry*. 2021;178(6):509–521. doi:10.1176/appi.ajp.2020.20030340
6. Krystal JH, State MW. Psychiatric disorders: Diagnosis to therapy. *Cell*. 2014;157(1):201–214. doi:10.1016/j.cell.2014.02.042
7. Podwalski P, Szczygieł K, Tyburski E, Sagan L, Misiak B, Samochowiec J. Magnetic resonance diffusion tensor imaging in psychiatry: A narrative review of its potential role in diagnosis. *Pharmacol Rep*. 2021;73(1):43–56. doi:10.1007/s43440-020-00177-0
8. Shizukuishi T, Abe O, Aoki S. Diffusion tensor imaging analysis for psychiatric disorders. *Magn Reson Med Sci*. 2013;12(3):153–159. doi:10.2463/mrms.2012-0082
9. Tanabe J, Thaker A. Microstructure and diffusion-weighted imaging in neuropsychiatry: A neuroradiology perspective. *Biol Psychiatry Cogn Neurosci Neuroimaging*. 2020;5(11):1009–1010. doi:10.1016/j.bpsc.2020.09.005
10. Tanaka M, Chen C. Editorial: Towards a mechanistic understanding of depression, anxiety, and their comorbidity: Perspectives from cognitive neuroscience. *Front Behav Neurosci*. 2023;17:1268156. doi:10.3389/fnbeh.2023.1268156
11. Uddin LQ, Dajani DR, Voorhies W, Bednarz H, Kana RK. Progress and roadblocks in the search for brain-based biomarkers of autism and attention-deficit/hyperactivity disorder. *Transl Psychiatry*. 2017;7(8):e1218. doi:10.1038/tp.2017.164
12. Stein DJ, Shoptaw SJ, Vigo DV, et al. Psychiatric diagnosis and treatment in the 21st century: Paradigm shifts versus incremental integration. *World Psychiatry*. 2022;21(3):393–414. doi:10.1002/wps.20998

13. Marek S, Tervo-Clemmens B, Calabro FJ, et al. Reproducible brain-wide association studies require thousands of individuals. *Nature*. 2022;603(7902):654–660. doi:10.1038/s41586-022-04492-9
14. Schnack HG, Kahn RS. Detecting neuroimaging biomarkers for psychiatric disorders: Sample size matters. *Front Psychiatry*. 2016;7:50. doi:10.3389/fpsy.2016.00050
15. Arbabshirani MR, Plis S, Sui J, Calhoun VD. Single subject prediction of brain disorders in neuroimaging: Promises and pitfalls. *NeuroImage*. 2017;145:137–165. doi:10.1016/j.neuroimage.2016.02.079
16. Bzdok D, Karrer TM. Single-subject prediction: A statistical paradigm for precision psychiatry. In: Diwadkar VA, B. Eickhoff S, eds. *Brain Network Dysfunction in Neuropsychiatric Illness*. Cham, Switzerland: Springer International Publishing; 2021:397–411. doi:10.1007/978-3-030-59797-9_19
17. Elad D, Cetin-Karayumak S, Zhang F, et al. Improving the predictive potential of diffusion MRI in schizophrenia using normative models: Towards subject-level classification. *Human Brain Mapp*. 2021;42(14):4658–4670. doi:10.1002/hbm.25574
18. Dhamala E, Yeo BTT, Holmes AJ. One size does not fit all: Methodological considerations for brain-based predictive modeling in psychiatry. *Biol Psychiatry*. 2023;93(8):717–728. doi:10.1016/j.biopsych.2022.09.024
19. Kopal J, Bzdok D. Endorsing complexity through diversity: Computational psychiatry meets big data analytics. *Biol Psychiatry*. 2023;93(8):655–657. doi:10.1016/j.biopsych.2022.07.023
20. Liloia D, Brasso C, Cauda F, et al. Updating and characterizing neuroanatomical markers in high-risk subjects, recently diagnosed and chronic patients with schizophrenia: A revised coordinate-based meta-analysis. *Neurosci Biobehav Rev*. 2021;123:83–103. doi:10.1016/j.neubiorev.2021.01.010
21. Liloia D, Mancuso L, Uddin LQ, et al. Gray matter abnormalities follow non-random patterns of co-alteration in autism: Meta-connectomic evidence. *NeuroImage Clin*. 2021;30:102583. doi:10.1016/j.nicl.2021.102583
22. Tanaka M, Vécsei L. From lab to life: Exploring cutting-edge models for neurological and psychiatric disorders. *Biomedicine*. 2024;12(3):613. doi:10.3390/biomedicine12030613
23. Rashid B, Calhoun V. Towards a brain-based predictome of mental illness. *Human Brain Mapp*. 2020;41(12):3468–3535. doi:10.1002/hbm.25013
24. Woo CW, Chang LJ, Lindquist MA, Wager TD. Building better biomarkers: Brain models in translational neuroimaging. *Nat Neurosci*. 2017;20(3):365–377. doi:10.1038/nn.4478
25. Segal A, Parkes L, Aquino K, et al. Regional, circuit and network heterogeneity of brain abnormalities in psychiatric disorders. *Nat Neurosci*. 2023;26(9):1613–1629. doi:10.1038/s41593-023-01404-6
26. Tahmasian M, Sepehry AA, Samea F, et al. Practical recommendations to conduct a neuroimaging meta-analysis for neuropsychiatric disorders. *Human Brain Mapp*. 2019;40(17):5142–5154. doi:10.1002/hbm.24746
27. Tanaka M, ed. *Crosstalk Between Depression, Anxiety, and Dementia: Comorbidity in Behavioral Neurology and Neuropsychiatry*. Basel, Switzerland: MDPI; 2022. doi:10.3390/books978-3-0365-4002-3
28. Tanaka M, Spekker E, Szabó Á, Polyák H, Vécsei L. Modelling the neurodevelopmental pathogenesis in neuropsychiatric disorders: Bioactive kynurenines and their analogues as neuroprotective agents. In celebration of 80th birthday of Professor Peter Riederer. *J Neural Transm*. 2022;129(5–6):627–642. doi:10.1007/s00702-022-02513-5
29. Tanaka M, Szabó Á, Vécsei L, Giménez-Llort L. Emerging translational research in neurological and psychiatric diseases: From in vitro to in vivo models. *Int J Mol Sci*. 2023;24(21):15739. doi:10.3390/ijms242115739
30. Liloia D, Crocetta A, Cauda F, Duca S, Costa T, Manuella J. Seeking overlapping neuroanatomical alterations between dyslexia and attention-deficit/hyperactivity disorder: A meta-analytic replication study. *Brain Sci*. 2022;12(10):1367. doi:10.3390/brainsci12101367
31. Backhausen LL, Herting MM, Tamnes CK, Vetter NC. Best practices in structural neuroimaging of neurodevelopmental disorders. *Neuropsychol Rev*. 2022;32(2):400–418. doi:10.1007/s11065-021-09496-2
32. Mechelli A, Price C, Friston K, Ashburner J. Voxel-based morphometry of the human brain: Methods and applications. *Curr Med Imaging Rev*. 2005;1(2):105–113. doi:10.2174/1573405054038726
33. Whitwell JL. Voxel-based morphometry: An automated technique for assessing structural changes in the brain. *J Neurosci*. 2009;29(31):9661–9664. doi:10.1523/JNEUROSCI.2160-09.2009
34. Henson R. Forward inference using functional neuroimaging: Dissociations versus associations. *Trends Cogn Sci*. 2006;10(2):64–69. doi:10.1016/j.tics.2005.12.005
35. Mulert C, Shenton ME, eds. *MRI in Psychiatry*. Berlin–Heidelberg, Germany: Springer Berlin Heidelberg; 2014. doi:10.1007/978-3-642-54542-9
36. Scarpazza C, De Simone M. Voxel-based morphometry: Current perspectives. *Neurosci Neuroecon*. 2016;5:19–35. doi:10.2147/NAN.S66439
37. Costa T, Liloia D, Ferraro M, Manuella J. Plausible reasoning in neuroscience. In: Magnani L, ed. *Handbook of Abductive Cognition*. Cham, Switzerland: Springer International Publishing; 2023:1581–1618. doi:10.1007/978-3-031-10135-9_74
38. Friston KJ, Penny W, Phillips C, Kiebel S, Hinton G, Ashburner J. Classical and Bayesian inference in neuroimaging: Theory. *NeuroImage*. 2002;16(2):465–483. doi:10.1006/nimg.2002.1090
39. Cauda F, Costa T, Nani A, et al. Are schizophrenia, autistic, and obsessive spectrum disorders dissociable on the basis of neuroimaging morphological findings? A voxel-based meta-analysis. *Autism Res*. 2017;10(6):1079–1095. doi:10.1002/aur.1759
40. Crossley NA, Mechelli A, Scott J, et al. The hubs of the human connectome are generally implicated in the anatomy of brain disorders. *Brain*. 2014;137(8):2382–2395. doi:10.1093/brain/awu132
41. Goodkind M, Eickhoff SB, Oathes DJ, et al. Identification of a common neurobiological substrate for mental illness. *JAMA Psychiatry*. 2015;72(4):305. doi:10.1001/jamapsychiatry.2014.2206
42. McTeague LM, Rosenberg BM, Lopez JW, et al. Identification of common neural circuit disruptions in emotional processing across psychiatric disorders. *Am J Psychiatry*. 2020;177(5):411–421. doi:10.1176/appi.ajp.2019.18111271
43. Opel N, Goltermann J, Hermesdorf M, Berger K, Baune BT, Dannowski U. Cross-disorder analysis of brain structural abnormalities in six major psychiatric disorders: A secondary analysis of mega- and meta-analytical findings from the ENIGMA Consortium. *Biol Psychiatry*. 2020;88(9):678–686. doi:10.1016/j.biopsych.2020.04.027
44. Sagarwala R, Nasrallah HA. White matter pathology is shared across multiple psychiatric brain disorders: Is abnormal diffusivity a transdiagnostic biomarker for psychopathology? *Biomark Neuropsychiatry*. 2020;2:100010. doi:10.1016/j.bionps.2019.100010
45. Van Den Heuvel MP, Sporns O. A cross-disorder connectome landscape of brain dysconnectivity. *Nat Rev Neurosci*. 2019;20(7):435–446. doi:10.1038/s41583-019-0177-6
46. Cauda F, Nani A, Manuella J, et al. The alteration landscape of the cerebral cortex. *NeuroImage*. 2019;184:359–371. doi:10.1016/j.neuroimage.2018.09.036
47. Liloia D, Cauda F, Nani A, et al. Low entropy maps as patterns of the pathological alteration specificity of brain regions: A meta-analysis dataset. *Data in Brief*. 2018;21:1483–1495. doi:10.1016/j.dib.2018.10.142
48. Poldrack R. Can cognitive processes be inferred from neuroimaging data? *Trends Cogn Sci*. 2006;10(2):59–63. doi:10.1016/j.tics.2005.12.004
49. Poldrack RA. Inferring mental states from neuroimaging data: From reverse inference to large-scale decoding. *Neuron*. 2011;72(5):692–697. doi:10.1016/j.neuron.2011.11.001
50. Bayes T. LII. An essay towards solving a problem in the doctrine of chances. By the late Rev. Mr. Bayes, F.R. S. communicated by Mr. Price, in a letter to John Canton, A.M. F.R. S. *Phil Trans R Soc*. 1763;53:370–418. doi:10.1098/rstl.1763.0053
51. Liloia D, Cauda F, Uddin LQ, et al. Revealing the selectivity of neuroanatomical alteration in autism spectrum disorder via reverse inference. *Biol Psychiatry Cogn Neurosci Neuroimaging*. 2023;8(11):1075–1083. doi:10.1016/j.bpsc.2022.01.007
52. Cauda F, Nani A, Liloia D, et al. Finding specificity in structural brain alterations through Bayesian reverse inference. *Human Brain Mapp*. 2020;41(15):4155–4172. doi:10.1002/hbm.25105
53. Yarkoni T, Poldrack RA, Nichols TE, Van Essen DC, Wager TD. Large-scale automated synthesis of human functional neuroimaging data. *Nat Methods*. 2011;8(8):665–670. doi:10.1038/nmeth.1635
54. Lieberman MD, Eisenberger NI. The dorsal anterior cingulate cortex is selective for pain: Results from large-scale reverse inference. *Proc Natl Acad Sci U S A*. 2015;112(49):15250–15255. doi:10.1073/pnas.1515083112

55. Wager TD, Kang J, Johnson TD, Nichols TE, Satpute AB, Barrett LF. A Bayesian model of category-specific emotional brain responses. *PLoS Comput Biol*. 2015;11(4):e1004066. doi:10.1371/journal.pcbi.1004066
56. Vanasse TJ, Fox PM, Barron DS, et al. BrainMap VBM: An environment for structural meta-analysis. *Human Brain Mapp*. 2018;39(8):3308–3325. doi:10.1002/hbm.24078
57. Jeffreys H. *Theory of Probability*. 3rd ed. Oxford, UK–New York, USA: Clarendon Press & Oxford University Press; 1998. ISBN:978-0-19-850368-2.
58. Costa T, Manuella J, Ferraro M, et al. BACON: A tool for reverse inference in brain activation and alteration. *Human Brain Mapp*. 2021;42(11):3343–3351. doi:10.1002/hbm.25452
59. Manuella J, Costa T, Cauda F, Liloia D. Six actions to improve detection of critical features for neuroimaging coordinate-based meta-analysis preparation. *Neurosci Biobehav Rev*. 2022;137:104659. doi:10.1016/j.neubiorev.2022.104659
60. Müller VI, Cieslik EC, Laird AR, et al. Ten simple rules for neuroimaging meta-analysis. *Neurosci Biobehav Rev*. 2018;84:151–161. doi:10.1016/j.neubiorev.2017.11.012
61. Calzavarini F, Cevolani G. Abductive reasoning in cognitive neuroscience: weak and strong reverse inference. *Synthese*. 2022;200(2):70. doi:10.1007/s11229-022-03585-2
62. Eickhoff S, Nichols TE, Van Horn JD, Turner JA. Sharing the wealth: Neuroimaging data repositories. *NeuroImage*. 2016;124:1065–1068. doi:10.1016/j.neuroimage.2015.10.079
63. Markiewicz CJ, Gorgolewski KJ, Feingold F, et al. The OpenNeuro resource for sharing of neuroscience data. *eLife*. 2021;10:e71774. doi:10.7554/eLife.71774
64. Norgaard M, Matheson GJ, Hansen HD, et al. PET-BIDS, an extension to the brain imaging data structure for positron emission tomography. *Sci Data*. 2022;9(1):65. doi:10.1038/s41597-022-01164-1
65. Tian Q, Fan Q, Witzel T, et al. Comprehensive diffusion MRI dataset for in vivo human brain microstructure mapping using 300 mT/m gradients. *Sci Data*. 2022;9(1):7. doi:10.1038/s41597-021-01092-6
66. Moerbeek M. Bayesian updating: Increasing sample size during the course of a study. *BMC Med Res Methodol*. 2021;21(1):137. doi:10.1186/s12874-021-01334-6

Neostigmine for postoperative surgical urine retention: A systematic review and meta-analysis

Qingli Chen^{E,F}, Na Li^{A,B}, Yue Wu^{C,D}

Department of Urinary Surgery, Jiangsu Province Hospital, Nanjing, China

A – research concept and design; B – collection and/or assembly of data; C – data analysis and interpretation; D – writing the article; E – critical revision of the article; F – final approval of the article

Advances in Clinical and Experimental Medicine, ISSN 1899–5276 (print), ISSN 2451–2680 (online)

Adv Clin Exp Med. 2024;33(5):435–444

Address for correspondence

Qingli Chen

E-mail: Qinglichen6688@outlook.com

Funding sources

None declared

Conflict of interest

None declared

Received on May 1, 2023

Reviewed on June 22, 2023

Accepted on July 14, 2023

Published online on September 4, 2023

Abstract

Postoperative urinary retention (POUR) is a common surgical complication that can result in bladder overdistension, urinary tract infection and an extended hospital stay. Although neostigmine is an effective therapy for POUR, its usage remains controversial. The purpose of this study was to investigate the effectiveness of neostigmine in improving POUR after surgery. PubMed, Embase, Web of Science, and the Cochrane Library databases were reviewed. A methodical search approach was used for data extraction, while meta-analysis and bias analysis employed Review Manager 5.2 and MedCalc.

Fourteen studies involving 4196 postoperative patients were included. With an odds ratio (OR) of 1.70, 95% confidence interval (95% CI) of 1.11–2.60 and an overall effect with $p < 0.05$, our analysis indicated that the patients receiving neostigmine had a greater effective urine retention rate than after other standard therapies. The subgroup analysis showed that neostigmine recipients had reduced residual urine volume (mean difference (MD) = -1.16 , 95% CI: -2.05 – -0.27 , overall $p < 0.05$, and $I^2 = 90\%$) and POUR (standardized MD (SMD) = 3.76 , 95% CI: 2.19 – 5.34 , overall $p < 0.001$, and $I^2 = 99\%$ using a random effects model) as compared to controls. A random-effects model was utilized due to the substantial heterogeneity between trials. The studies were consistent and had no publication bias. Based on the findings of this meta-analysis, neostigmine can be considered an effective POUR treatment.

Key words: meta-analysis, urinary retention, neostigmine, postoperative urinary retention (POUR), volume of urine excreted

Cite as

Chen Q, Li N, Wu Y. Neostigmine for postoperative surgical urine retention: A systematic review and meta-analysis.

Adv Clin Exp Med. 2024;33(5):435–444.

doi:10.17219/acem/169608

DOI

10.17219/acem/169608

Copyright

Copyright by Author(s)

This is an article distributed under the terms of the Creative Commons Attribution 3.0 Unported (CC BY 3.0)

(https://creativecommons.org/licenses/by/3.0/)

Introduction

Postoperative urinary retention, commonly referred to as POUR, is a condition characterized by the inability of patients to effectively void their bladders after surgical interventions despite having a full bladder. The condition results in an elevated postvoid residual volume. Untreated POUR can cause adverse outcomes, such as acute renal injury, detrusor injury and excessive bladder dilatation. These events may lead to extended hospital stay and necessitate supplementary care after discharge.¹

After a surgical procedure or anesthesia, POUR can present in various forms, including tenderness or uneasiness in the suprapubic region, bladder contractions, urinary incontinence, and an inability to void.² Urinary retention is a prevalent medical condition impacting a significant proportion of the population, with a reported incidence rate of 5–70%.³ Several factors can contribute to increased urinary retention susceptibility after a surgical procedure, including anesthesia administration, the type of operation performed, the presence of postoperative inflammation, and limited mobility.⁴ If left untreated, POUR may result in significant bladder distension, acute renal dysfunction and detrusor muscle damage. Consequently, a patient's discharge from the hospital and their subsequent treatment may be delayed.^{5,6}

Catheterization is a frequently recommended therapeutic intervention for POUR due to its potential to facilitate the management of the condition. Notwithstanding its benefits, this method is associated with an increased likelihood of urinary tract infection and other potential complications.⁷ However, it is possible to reduce the incidence of complications and postoperative morbidity by employing diverse methods that improve patients' physical and emotional well-being while also avoiding POUR, as suggested by previous research.⁸ Hence, plausible preventive measures encompass implementing anesthetic and analgesic interventions in conjunction with acupuncture, heated compresses and massage therapy.⁹ Pharmacological intervention for POUR management can involve drugs that impede β -adrenergic and cholinergic activity.¹⁰

Neostigmine is classified as a parasympathomimetic drug due to its ability to mimic the effects of the parasympathetic nervous system. It functions as a reversible acetylcholinesterase inhibitor via indirect activation of nicotinic and muscarinic receptors by inhibiting acetylcholine breakdown, specifically targeting step 5 of the process.¹¹ Neostigmine has demonstrated effectiveness, safety and success in various POUR patient management trials.^{12,13} Nonetheless, certain studies have reported unsatisfactory outcomes due to the development of tension in the smooth muscle of the bladder.^{14,15} The data suggest that further research is required to explore the utilization of neostigmine for POUR. Consequently, pertinent publications^{16–29} were procured and reviewed to conduct a thorough investigation into the efficacy of neostigmine in POUR.

Objectives

This investigation aimed to assess the efficacy of neostigmine in ameliorating POUR.

Materials and methods

Eligibility criteria

All possibly relevant papers were examined in their entirety to assess whether or not they fulfilled the inclusion criteria listed below: 1) studies that compared patients receiving neostigmine to conventional therapy; 2) studies including patients diagnosed with POUR; 3) studies that contained indicators assessing efficacy or additional pertinent variables comparing neostigmine treatment to standard treatment; and 4) studies that were readily available in their entirety. The exclusion criteria were as follows: 1) studies regarding other disorders; 2) studies including comparisons with other therapies; 3) studies with insufficient data; and 4) reviews, abstracts or duplicate publications.

Information sources and literature search strategy

We conducted a search for randomized controlled trials (RCTs) published between January 1, 2000, and January 1, 2023, in the PubMed, Web of Science, Embase, and Cochrane Library databases using the following search terms: 1) neostigmine; 2) postoperative urinary retention OR POUR; 3) clinical effects; 4) volume of urine excreted; and 5) urinary retention. Within the context of the search strategy, the Boolean operator "AND" was used to combine the Medical Subject Headings (MeSH) with the text keywords. We carried out a comprehensive search across various databases and did not impose any limitations on the language used or the publication status of the studies. Two researchers, NL and YW, independently searched the literature and analyzed the bibliographies to find additional publications related to the topic.

Study selection and data collection process

The parameters for this review were based on the most recent edition of the *Cochrane Handbook for Systematic Reviews of Interventions*.³⁰ A predesigned data collection form was used to extract data from the main research. Two investigators (NL and YW) independently screened titles, abstracts and full texts of potentially eligible studies and used the 27-item Preferred Reporting Items for Systematic Reviews and Meta-Analyses (PRISMA) checklist criteria to grade each study as "yes" (1 point), "partially" (0.5 points) or "no" (0 points). The points assigned to each study comply with PRISMA guidelines. Both investigators extracted

the data independently, and the 3rd investigator (QC) was involved if the data extracted from the same study differed between the 2 investigators. Information, including the name of the first author, publication year, journal, country, patient population, number of participants, age, sex (male/female), intervention dosage (neostigmine), and primary outcome measures, was extracted for each arm. The primary endpoints were the amount of urine excreted and the extent of POUR decrease. The likelihood of bias across studies was assessed using a visual examination of a funnel plot³¹ and Egger's test.³²

Risk of bias evaluation

The “risk of bias” table prepared in the Review Manager (RevMan) software (v. 5.3; The Nordic Cochrane Centre, Copenhagen, Denmark) was used to assess study quality.³³ The table documented random sequence generation, allocation concealment, blinding of participants and personnel, blinding of outcome assessments, insufficient outcome data, selective reporting, and other forms of bias. Based on the retrieved data, we assigned a score of “low”, “high”, or “some concerns” to each parameter for each study. The inquiry was independently conducted by 2 investigators (NL and YW). Any disagreements were addressed by the 3rd investigator (QC).

Statistical analyses

Statistical analysis of the findings from the selected studies was performed using RevMan software (v. 5.3; The Nordic Cochrane Center). Pairwise meta-analyses were performed with a DerSimonian and Laird random-effects model³⁴ to calculate the pooled estimates of odds ratio (OR) and mean difference (MD), with 95% confidence intervals (95% CIs) of direct comparisons between the experimental and control groups. A random-effects model was used due to the substantial heterogeneity among the studies. The purpose of these analyses was to determine the degree to which the effect size (OR and MD) remained consistent. It was determined that heterogeneity ranging from 0% to 40% “might not be important”, heterogeneity ranging from 30% to 60% was considered “moderate heterogeneity”, heterogeneity ranging from 50% to 90% was treated as “substantial heterogeneity”, and heterogeneity ranging from 75% to 100% was “considerable heterogeneity”. The random-effects model was implemented due to the high heterogeneity in the data.³⁵

Results

Literature search results

The preliminary search yielded 657 articles in the PubMed, Embase, Web of Science, and Cochrane Library databases. Following the initial screening, 316 records remained, and

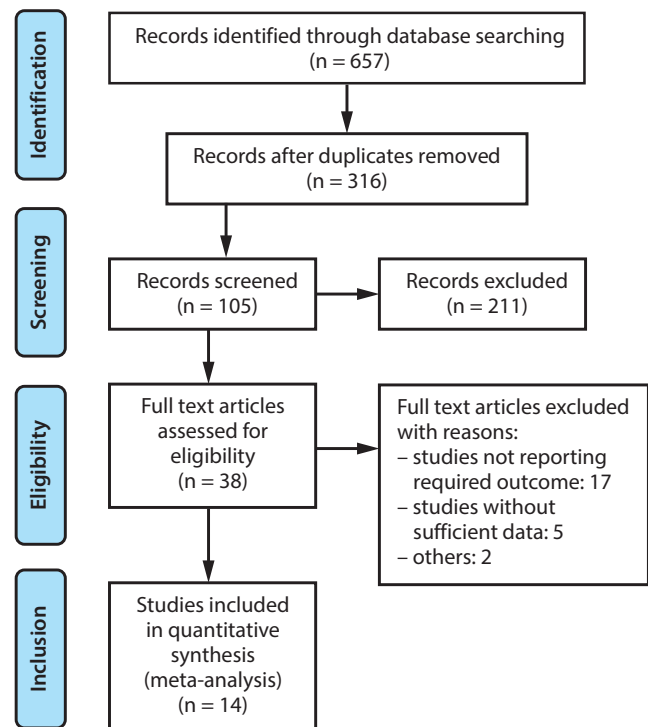


Fig. 1. Study flow diagram as per Preferred Reporting Items for Systematic Reviews and Meta-Analyses (PRISMA) guidelines

after screening titles and abstracts, additional 211 studies were removed due to their type (review articles, letters, case reports, comments, or editorials). Then, 105 studies were evaluated, of which 38 were selected for final screening. Out of these, 24 publications were deemed ineligible for further consideration for various reasons, such as not reporting the required outcome or having insufficient data. Ultimately, 14 studies involving 4196 patients fulfilled the inclusion criteria and were eligible for meta-analysis. Figure 1 depicts the selection procedure, which followed PRISMA guidelines,³⁶ and includes an explanation of the factors that led to the exclusion of certain studies.

Study characteristics

The primary features of the 14 clinical studies^{16–29} are outlined in Table 1. The publication dates ranged from 2000 to 2023. During the interventions, experimental groups received neostigmine, and control groups were given different types of medicine. A total of 4196 patients participated in these investigations, with 2342 patients in the intervention groups and 1854 in the control groups. The number of people in the study samples ranged from 13 to 1000.

Risk of bias and publication bias assessment

A predesigned questionnaire was used to conduct a risk of bias assessment for each of the 14 studies, and the findings are presented in Table 2. There was a low risk of bias in 10 studies and a moderate risk in 3 studies

Table 1. Characteristics of the included studies

Study	Publication journal	Year	Country	Neostigmine dosage [mg]	Sex (male/female)	Age [years]	Total number of participants
Borneo et al. ¹⁶	<i>International Journal of Innovative Science and Research Technology</i>	2019	Indonesia	1	59/15	21–60	13
Cha et al. ¹⁷	<i>Anesthesia and Pain Medicine</i>	2018	South Korea	0.2	52/519	60–77	671
Chae et al. ¹⁸	<i>Journal of Clinical Medicine</i>	2019	South Korea	0.5	310/275	50–75	585
Chang et al. ¹⁹	<i>Journal of the Formosan Medical Association</i>	2022	Taiwan	0.5	460/540	44–66	1000
El Dahab et al. ²⁰	<i>Egyptian Journal of Anaesthesia</i>	2011	Egypt	0.5	45/55	23–47	100
Daquioag et al. ²¹	<i>Journal of Cardiothoracic and Vascular Anaesthesia</i>	2022	China	4	140/136	55–75	276
Ziemba-Davis et al. ²²	<i>Journal of Arthroplasty</i>	2019	USA	0.5	274/359	50–70	679
Fiorda Diaz et al. ²³	<i>Frontiers in Medicine</i>	2022	Thailand	0.5	29/27	44–65	37
Han et al. ²⁴	<i>Journal of Clinical Medicine</i>	2021	South Korea	0.2	40/37	40–60	77
Bowman et al. ²⁵	<i>Clinical Spine Surgery</i>	2021	USA	0.5	40/160	50–70	200
Koh et al. ²⁶	Research Square (preprint)	2020	South Korea	0.4	48/88	56–70	136
Mayo et al. ²⁷	<i>Spine</i>	2016	USA	5	102/103	45–60	205
Valencia Morales et al. ²⁸	<i>Surgical Laparoscopy, Endoscopy & Percutaneous Techniques</i>	2021	USA	5	120/61	18–80	181
Senapathi et al. ²⁹	<i>Therapeutics and Clinical Risk Management</i>	2018	Indonesia	0.5	16/20	25–50	36

Table 2. Risk assessment of the included studies

Study	Did the study avoid inappropriate exclusions?	Did all patients receive the same reference standard?	Were all patients included in the analysis?	Was the sample frame appropriate to address the target population?	Were study participants sampled in an appropriate way?	Were the study subjects and the setting described in detail?	Were valid methods used for the identification of the condition?	Was the condition measured in a standard, reliable way for all participants?
Borneo et al. ¹⁶	Y	Y	N	Y	Y	Y	Y	Y
Cha et al. ¹⁷	Y	Y	N	Y	Y	Y	Y	Y
Chae et al. ¹⁸	Y	Y	N	Y	Y	Y	Y	Y
Chang et al. ¹⁹	Y	Y	N	Y	Y	Y	Y	Y
El Dahab et al. ²⁰	Y	Y	N	Y	Y	Y	Y	Y
Daquioag et al. ²¹	Y	Y	N	Y	Y	Y	Y	Y
Ziemba-Davis et al. ²²	Y	Y	N	Y	Y	Y	Y	Y
Fiorda Diaz et al. ²³	Y	Y	N	Y	Y	Y	Y	Y
Han et al. ²⁴	Y	Y	N	Y	Y	Y	Y	Y
Bowman et al. ²⁵	Y	Y	N	Y	Y	Y	Y	Y
Koh et al. ²⁶	Y	Y	N	Y	Y	Y	Y	Y
Mayo et al. ²⁷	Y	Y	N	Y	Y	Y	Y	Y
Valencia Morales et al. ²⁸	Y	Y	N	Y	Y	Y	Y	Y
Senapathi et al. ²⁹	Y	Y	N	Y	Y	Y	Y	Y

due to the randomization procedure and bias in selecting the data reported. As can be seen in the risk of bias summary (Fig. 2) and risk of bias graph (Fig. 3), only 1 publication had a significantly high risk due to bias in selecting the results reported. The funnel plot for publication bias is presented in Fig. 4. The symmetrically shaped funnel plot for the overall effect size, specifically the OR of neostigmine compared to the control group, is shown in Fig. 4A. The results indicate a low probability

of publication bias, as evidenced by a significant p-value of 0.463 for Egger's test.³⁷ The symmetrically shaped funnel plot for the percentage reduction in POUR in neostigmine groups (NG) compared to control groups (Cg) is depicted in Fig. 4B. The plot indicates a low probability of publication bias, with a significant p-value of 0.385 for Egger's test. The results in Fig. 4C indicate the volume of urine excreted, with a statistically significant p-value of 0.241.³⁷

Study	Risk of bias domains					Overall
	D1	D2	D3	D4	D5	
Borneo et al [16]	+	+	+	+	+	+
Cha et al [17]	-	+	+	+	+	-
Chae et al [18]	+	+	+	+	+	+
Chang et al [19]	+	+	+	+	+	+
Dahab et al [20]	+	+	+	+	-	-
Daquiaoag et al [21]	+	+	+	+	X	X
Davis et al [22]	+	+	+	+	+	+
Diaz et al [23]	+	+	+	+	+	+
Han et al [24]	+	+	+	+	+	+
John et al [25]	+	+	+	+	+	+
Koh et al [26]	-	+	+	+	+	-
Mayo et al [27]	+	+	+	+	+	+
Morales et al [28]	+	+	+	+	+	+
Senapathi et al [29]	+	+	+	+	+	+

Domains:
 D1: Bias arising from the randomization process.
 D2: Bias due to deviations from intended intervention.
 D3: Bias due to missing outcome data.
 D4: Bias in measurement of the outcome.
 D5: Bias in selection of the reported result.

Judgement
 X High
 - Some concerns
 + Low

Fig. 2. Risk of bias summary

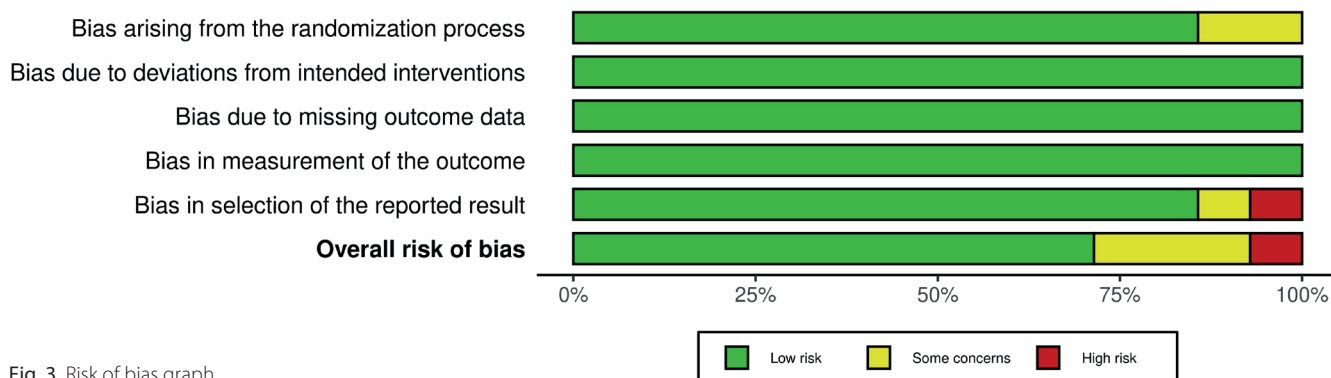


Fig. 3. Risk of bias graph

Primary study outcomes

Table 3 displays the findings of the primary outcomes, including the volume of urine expelled [mL], reported in 3 studies,^{16,17,29} and the reduction in POUR, reported in 11 studies.^{18–28}

Heterogeneity analysis of the experimental and control groups

This meta-analysis compared differences in urine retention efficiency rates between experimental and control

groups using heterogeneity analysis. The overall result demonstrated that the NG had a greater effective rate than the CG (OR = 1.70, 95% CI: 1.11–2.60, $\tau^2 = 0.58$, $\chi^2 = 257$, degrees of freedom (df) = 13, overall effect $p < 0.05$, $I^2 = 95%$, in the random effects model), as shown in Fig. 5. The findings of the subgroup analysis revealed that neostigmine performed noticeably better than the conventional treatments typically used for urinary retention. Figure 6 highlights that the neostigmine group had a lower residual urine volume (MD = -1.16, 95% CI: -2.05--0.27, overall $p < 0.05$, $I^2 = 90%$) and a more substantial POUR reduction than controls (standardized MD (SMD) = 3.76,

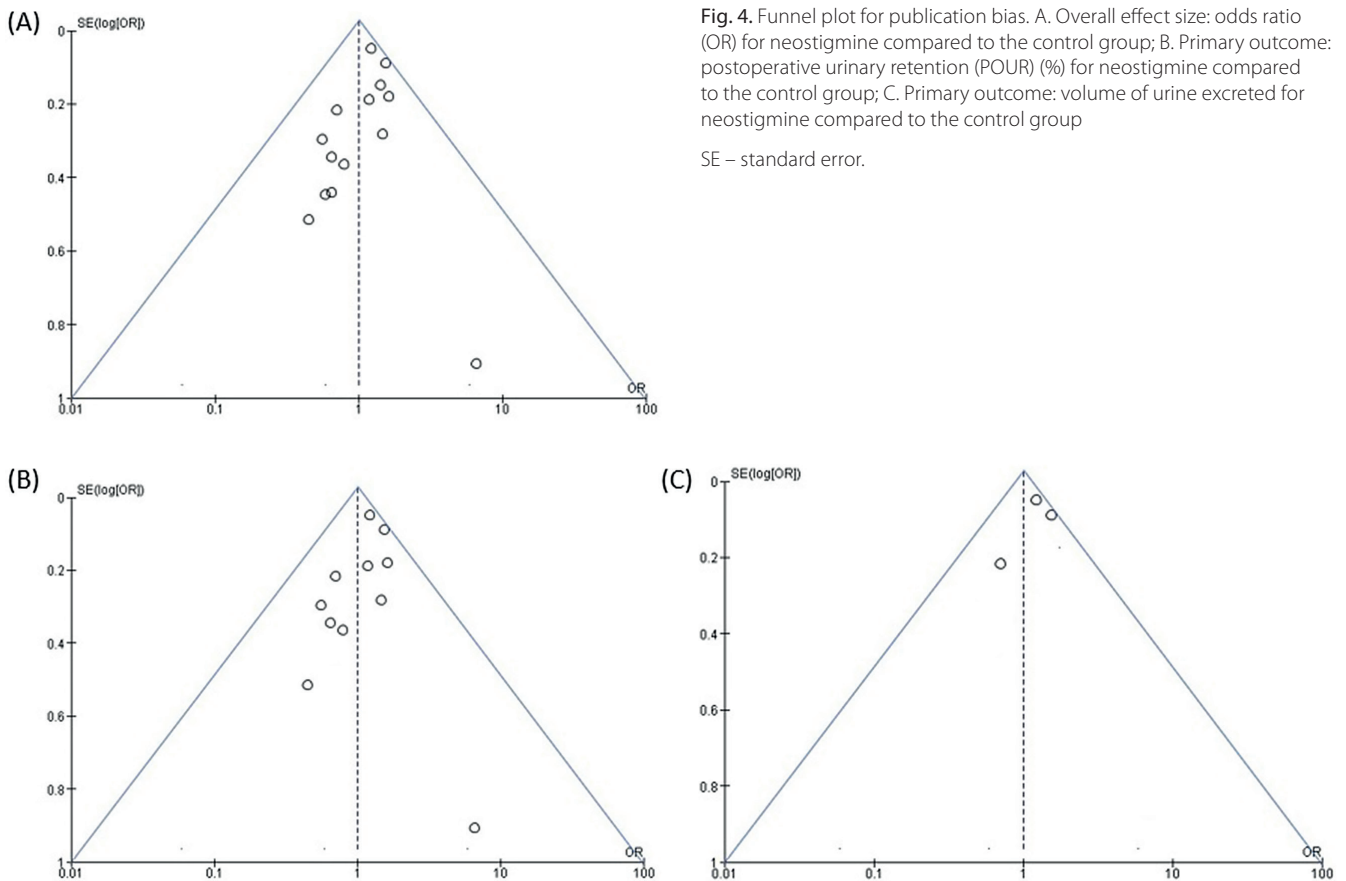


Fig. 4. Funnel plot for publication bias. A. Overall effect size: odds ratio (OR) for neostigmine compared to the control group; B. Primary outcome: postoperative urinary retention (POUR) (%) for neostigmine compared to the control group; C. Primary outcome: volume of urine excreted for neostigmine compared to the control group
SE – standard error.

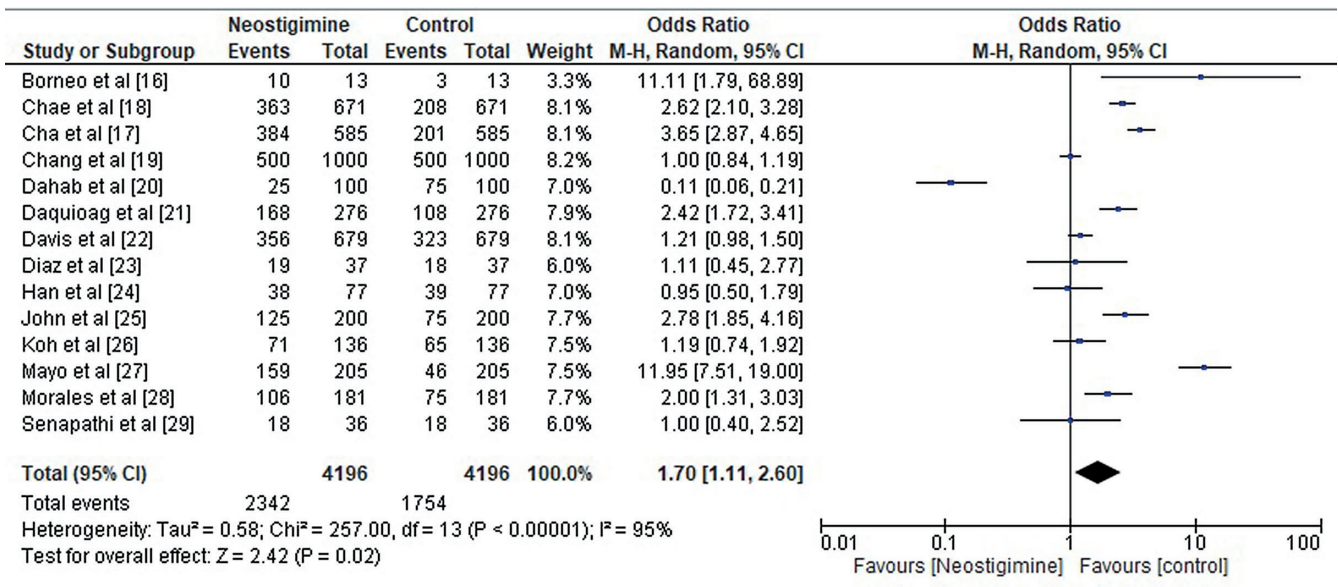


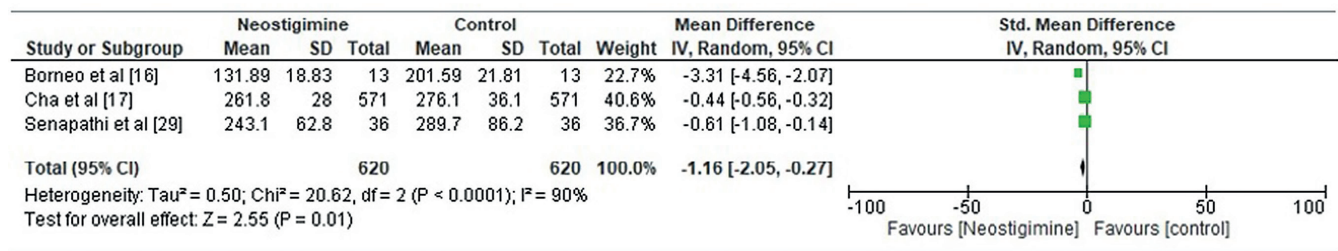
Fig. 5. Forest plot odds ratio (OR) for the effective rate of urinary retention in the neostigmine and control groups

95% CI – 95% confidence interval; df – degrees of freedom.

95% CI: 2.19–5.34, overall $p < 0.001$ $I^2 = 99\%$). Figure 7 displays comparative scatter plots indicating that the NG had a higher percentage of participants with POUR improvements and a lower volume of urine retention than the CG.

Similarly, the correlation plot depicted in Fig. 8 demonstrates a noteworthy higher POUR and residual urine volume decrease in the NG than in the CG. All of these results were statistically significant, with $p < 0.05$.

Primary outcome: Volume of Urine excreted (ml)



Primary outcome: Reduction in Post Operative Urinary retention (POUR %)

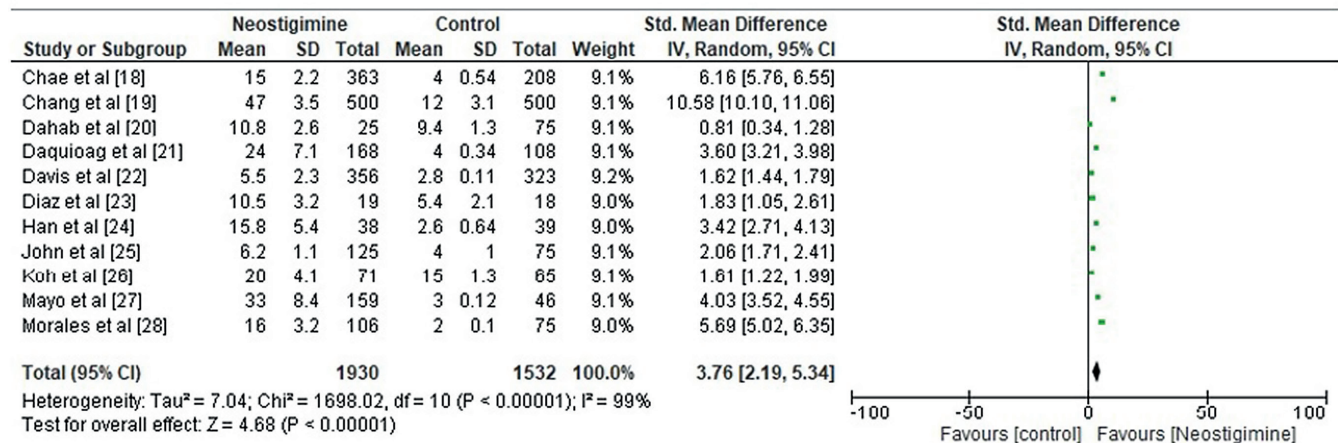


Fig. 6. Forest plot of primary outcomes: urine volume excreted [mL] and postoperative urinary retention (POUR) reduction

95% CI – 95% confidence interval; df – degrees of freedom; SD – standard deviation.

Discussion

This meta-analysis investigated the effectiveness of neostigmine as a POUR treatment method. A total of 14 studies, comprising 4196 participants, were included in the analysis. The primary indicators considered were the effective urinary retention rate, voided urine volume and POUR reduction. The results indicate that neostigmine is a viable therapeutic option for addressing POUR.

The regulation of bladder function is thought to be significantly influenced by the parasympathetic nervous system. The system is responsible for urination through detrusor muscle contraction and sphincter muscle relaxation, though it remains inactive during bladder filling.^{38,39} Neostigmine is a potent acetylcholinesterase inhibitor that exhibits dual functionality by reducing cholinesterase activity and enhancing acetylcholine efficacy. The drug achieves this through dose-dependent stimulation of the detrusor muscle of the bladder, resulting in direct contractions that ultimately lead to an augmentation in micturition frequency and urine volume output.^{40,41}

Several preventative strategies targeting POUR have been published recently. Due to a limited understanding of the efficacy of different treatments and concerns surrounding their potential side effects, there is currently no established protocol for preventing this particular ailment.⁴² However, reports suggest that neostigmine could be a potential medication for POUR. The plasma half-life

of neostigmine following intravenous administration is variable, ranging from 47 min to 60 min, with a mean value of 53 min. Clinical manifestations of neostigmine are typically observed within 20–30 min of intramuscular administration, with a duration of action ranging from 2.5 h to 4 h.⁴³ According to Zhong et al., epidural neostigmine administration (at doses of 1 g/kg, 2 g/kg or 4 g/kg) in combination with lidocaine produced a dose-independent analgesic effect that persisted for 8 h after knee surgery, in contrast to the patients who received only lidocaine and did not display concomitant escalation in adverse reactions.⁴⁴ Similarly, Hassanin et al. conducted a blinded RCT to investigate the impact of neostigmine supplementation with bupivacaine on ultrasound-guided supraclavicular brachial plexus block in forearm surgeries.⁴⁵ The study findings revealed that the neostigmine group exhibited statistically significant reductions in visual analogue scale (VAS) scores compared to the control group at 1 h, 2 h, 4 h, and 6 h. Nevertheless, it is advisable to only employ this approach in cases where surgical procedures extend beyond 4 h. Thus, neostigmine exhibits promising prospects as a viable pharmaceutical agent for surgical procedures of diverse durations.

Prior meta-analyses carried out by Sirisreetreerux et al.⁴⁶ and Jackson et al.⁴⁷ demonstrated neostigmine efficacy, a medication classified as either a parasympathomimetic or a reversible cholinesterase inhibitor, in the management and prevention of POUR. Nonetheless, it is imperative

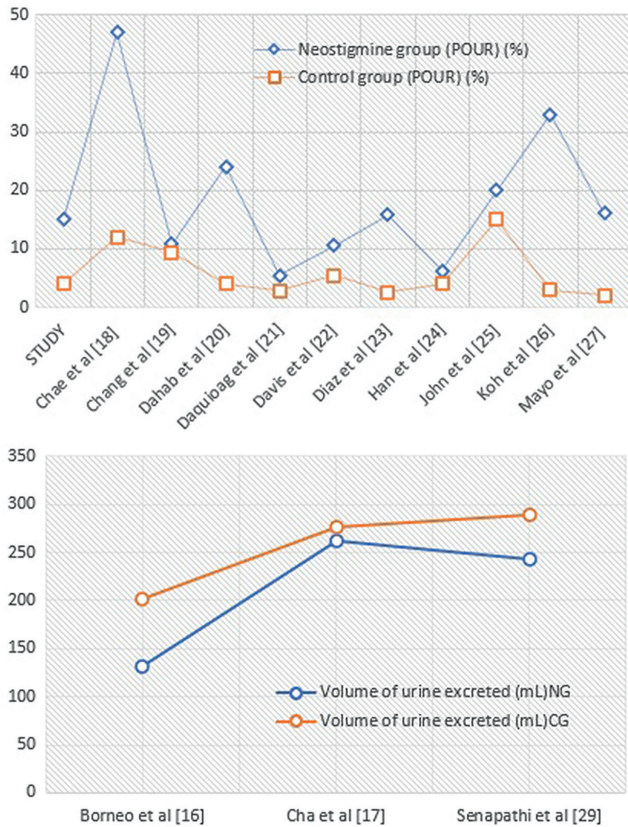


Fig. 7. Comparative scatter plots of primary outcomes for NG compared to CG

POUR – postoperative urinary retention; NG – neostigmine group; CG – control group.

Table 3. Primary outcome of the included studies

Study	Groups	Number of participants	Primary outcome
			volume of urine excreted [mL]
Borneo et al. ¹⁶	NG CG	10 3	131.89 ±18.83 201.59 ±21.81
Cha et al. ¹⁷	NG CG	363 208	261.8 ±280.0 276.1 ±361.1
Senapathi et al. ²⁹	NG CG	18 18	243.1 ±62.8 289.7 ±86.2
Patients with postoperative urine retention (POUR) (%)			
Chae et al. ¹⁸	NG CG	384 201	15 4
Chang et al. ¹⁹	NG CG	500 500	47 12
El Dahab et al. ²⁰	NG CG	25 75	10.8 9.4
Daquioag et al. ²¹	NG CG	168 108	24 4.0
Ziemba-Davis et al. ²²	NG CG	356 323	5.5 2.8
Fiorda Diaz et al. ²³	NG CG	19 18	10.5 5.4
Han et al. ²⁴	NG CG	38 39	15.8 2.6
Bowman et al. ²⁵	NG CG	50 50	6.2 4.0
Koh et al. ²⁶	NG CG	71 65	20 15
Mayo et al. ²⁷	NG CG	159 46	33 3
Valencia Morales et al. ²⁸	NG CG	106 75	16 2

NG – neostigmine group; CG – control group.

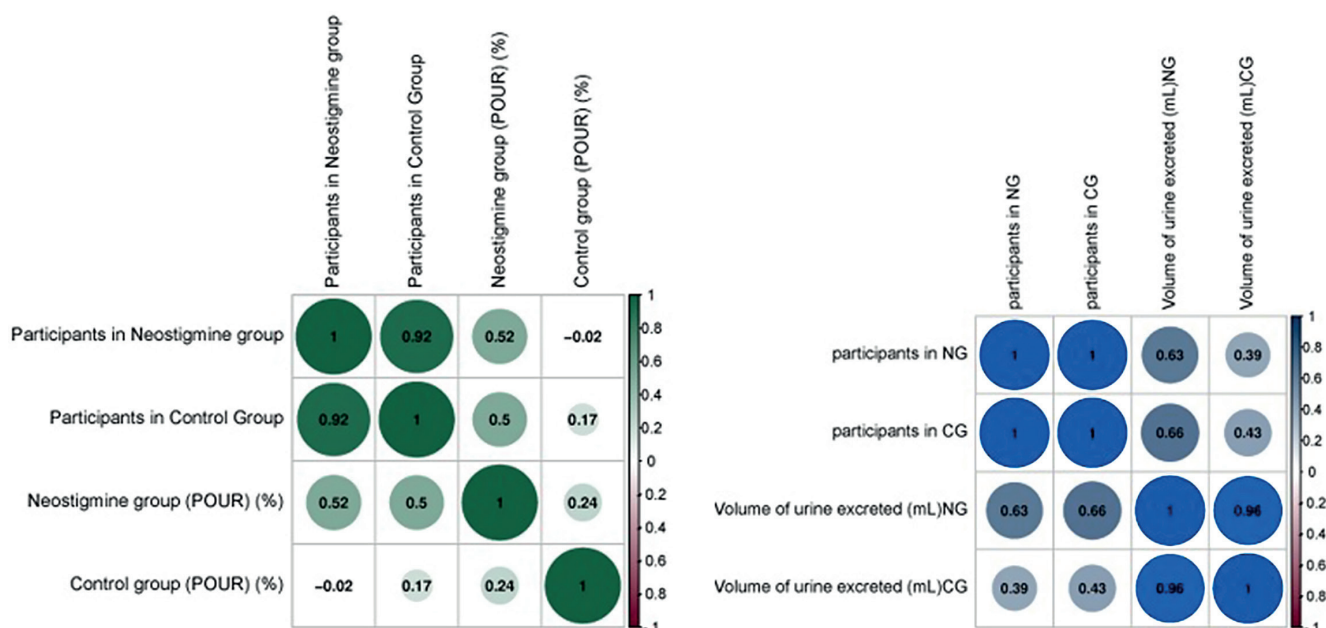


Fig. 8. Correlation plots of primary outcomes for NG compared to the CG

POUR – postoperative urinary retention; NG – neostigmine group; CG – control group.

to subject these medications to RCTs with substantial sample sizes to determine their clinical efficacy and patient acceptability.

In a recent systematic review and meta-analysis conducted by Cao et al., the neostigmine group exhibited a higher rate of effectiveness in treating urine retention compared to traditional Chinese treatments and physical therapy.⁴⁸ The authors derived an OR of 7.47 (95% CI: 4.10–13.59, $p < 0.001$) to support their findings. Neostigmine has been found to effectively mitigate POUR symptoms. The results of our study align with previous meta-analyses and support the utilization of neostigmine as a viable intervention for addressing POUR.

Limitations

This study had several limitations. Indeed, it is probable that the “small study effect”, which occurs when most studies have extremely small sample sizes, skewed the results. The problem stems from the paucity of available reports. As such, more research is required on a larger sample size to reach robust scientific conclusions. Any future evaluations must account for new data, especially on adverse incidents or issues. Due to the low number of studies published on this subject up to this point, any future study and analysis must incorporate a greater number of articles that feature research from many countries.

Conclusions

According to the findings of this meta-analysis, neostigmine may be related to decreased POUR incidence and could effectively manage POUR symptoms with enhanced therapeutic effects. However, validating the impact of the interventions evaluated in this meta-analysis and designing an effective treatment and prevention plan for surgical patients at risk of developing POUR requires further analysis of large, robust and properly designed RCTs.

Data availability statement

All data generated or analyzed during this study are included in this article. Further inquiries should be directed to the corresponding author.

ORCID iDs

Na Li  <https://orcid.org/0000-0001-6756-1548>

Yue Wu  <https://orcid.org/0000-0002-8065-9440>

Qingli Chen  <https://orcid.org/0000-0003-1038-7571>

References

- Balderi T, Mistraletti G, D'Angelo E, Carli F. Incidence of postoperative urinary retention (POUR) after joint arthroplasty and management using ultrasound-guided bladder catheterization. *Minerva Anestesiol.* 2011;77(11):1050–1057. PMID:21597444.
- Golubovsky JL, Ilyas H, Chen J, Tanenbaum JE, Mroz TE, Steinmetz MP. Risk factors and associated complications for postoperative urinary retention after lumbar surgery for lumbar spinal stenosis. *Spine J.* 2018;18(9):1533–1539. doi:10.1016/j.spinee.2018.01.022
- Dreijer B, Møller MH, Bartholdy J. Post-operative urinary retention in a general surgical population: *Eur J Anaesthesiol.* 2011;28(3):190–194. doi:10.1097/EJA.0b013e328341ac3b
- Scott AJ, Mason SE, Langdon AJ, et al. Prospective risk factor analysis for the development of post-operative urinary retention following ambulatory general surgery. *World J Surg.* 2018;42(12):3874–3879. doi:10.1007/s00268-018-4697-4
- Yuruktumen A, Karcioğlu O, Topacoglu H, Arslan ED. Acute renal failure associated with dysfunctioning detrusor muscle in multiple sclerosis. *Adv Ther.* 2004;21(6):343–347. doi:10.1007/BF02850098
- Mevcha A, Drake MJ. Etiology and management of urinary retention in women. *Indian J Urol.* 2010;26(2):230–235. doi:10.4103/0970-1591.65396
- Møller T, Engedal MS, Plum LM, Aasvang EK. Reduced need for urinary bladder catheterization in the postanesthesia care unit after implementation of an evidence-based protocol: A prospective cohort comparison study. *Eur Urol Open Sci.* 2021;26:27–34. doi:10.1016/j.euros.2021.01.013
- Geller EJ. Prevention and management of postoperative urinary retention after urogynecologic surgery. *Int J Womens Health.* 2014; 6:829–838. doi:10.2147/IJWH.S55383
- Hu J, Sun Y, Cao L, Shen S, Hu X. Different moxibustion therapies for urinary retention after anorectal surgery: A protocol for systematic review and network meta-analysis. *Medicine (Baltimore).* 2021;100(2): e24132. doi:10.1097/MD.00000000000024132
- Buckley BS, Lapitan MCM. Drugs for treatment of urinary retention after surgery in adults. *Cochrane Database Syst Rev.* 2010;(10):CD008023. doi:10.1002/14651858.CD008023.pub2
- Luo J, Chen S, Min S, Peng L. Reevaluation and update on efficacy and safety of neostigmine for reversal of neuromuscular blockade. *Ther Clin Risk Manag.* 2018;14:2397–2406. doi:10.2147/TCRM.S179420
- Low J, Escobar M, Baquero S, Goldman HS, Rosen G. Glycopyrrolate and post-operative urinary retention: A narrative review. *Cureus.* 2020;12(11):e11379. doi:10.7759/cureus.11379
- Abrishamkar S, Attari M, Saket A. Comparing the effectiveness of intrathecal injection of marcaine with magnesium sulfate, neostigmine or phentanyl on post-operative pain, urinary retention, nausea or vomiting in patients undergoing spinal anesthesia for lumbar disk herniation surgery. *J Isfahan Med Sch.* 2016;34(374):221–228. https://jims.mui.ac.ir/article_14898.html?lang=en. Accessed February 28, 2023.
- Hristovska AM, Duch P, Allingstrup M, Afshari A. The comparative efficacy and safety of sugammadex and neostigmine in reversing neuromuscular blockade in adults: A Cochrane systematic review with meta-analysis and trial sequential analysis. *Anaesthesia.* 2018; 73(5):631–641. doi:10.1111/anae.14160
- Tomaszewski D, Bałkota M. Intramuscular administration of drotaverine hydrochloride decreases both incidence of urinary retention and time to micturition in orthopedic patients under spinal anesthesia: A single blinded randomized study. *Biomed Res Int.* 2015;2015:926953. doi:10.1155/2015/926953
- Borneo F, Nasution A, Harto S. Comparison of the effectiveness of intramuscular 0.5 mg neostigmine and intramuscular 1 mg neostigmine for bladder emptying after spinal anesthesia. *Int J Innov Sci Res Technol.* 2019;4(4):154–162. <https://ijisrt.com/wp-content/uploads/2019/04/IJISRT19AP405.pdf>. Accessed February 28, 2023.
- Cha JE, Park SW, Choi YI, et al. Sugammadex use can decrease the incidence of post-operative urinary retention by avoiding anticholinergics: A retrospective study. *Anesth Pain Med.* 2018;13(1):40–46. doi:10.17085/apm.2018.13.1.40
- Chae YJ, Joe HB, Oh J, Lee E, Yi IK. Thirty-day postoperative outcomes following sugammadex use in colorectal surgery patients: Retrospective study. *J Clin Med.* 2019;8(1):97. doi:10.3390/jcm8010097
- Chang HC, Liu SY, Lee MJ, Lee SO, Wong CS. Sugammadex reversal of muscle relaxant blockade provided less post-anesthesia care unit adverse effects than neostigmine/glycopyrrolate. *J Formos Med Assoc.* 2022;121(12):2639–2643. doi:10.1016/j.jfma.2022.04.017

20. El Dahab HA, Samir R, Menesy T, Adel G, Habib E. Adding neostigmine to morphine epidurally lessens the incidence of postoperative urine retention: A comparative study. *Egypt J Anaesth*. 2011;27(2): 89–94. doi:10.1016/j.egja.2011.03.002
21. Daquioag TK, Mele NJ, Peterson DR, et al. Urinary retention after video-assisted thoracoscopic surgery: Role of neuromuscular blockade reversal. *J Cardiothorac Vasc Anesth*. 2022;36(1):350–351. doi:10.1053/j.jvca.2021.05.048
22. Ziemba-Davis M, Nielson M, Kraus K, Duncan N, Nayyar N, Meneghini RM. Identifiable risk factors to minimize postoperative urinary retention in modern outpatient rapid recovery total joint arthroplasty. *J Arthroplasty*. 2019;34(7S):S343–S347. doi:10.1016/j.arth.2019.03.015
23. Fiorda Diaz J, Echeverria-Villalobos M, Esparza Gutierrez A, et al. Sugammadex versus neostigmine for neuromuscular blockade reversal in outpatient surgeries: A randomized controlled trial to evaluate efficacy and associated healthcare cost in an academic center. *Front Med (Lausanne)*. 2022;9:1072711. doi:10.3389/fmed.2022.1072711
24. Han J, Oh AY, Jeon YT, et al. Quality of recovery after laparoscopic cholecystectomy following neuromuscular blockade reversal with neostigmine or sugammadex: A prospective, randomized, controlled trial. *J Clin Med*. 2021;10(5):938. doi:10.3390/jcm10050938
25. Bowman JJ, Edwards CC, Dean C, Park J, Edwards CC. Incidence and risk factors for postoperative urinary retention following lumbar spine fusion. *Clin Spine Surg*. 2021;34(7):E397–E402. doi:10.1097/BSD.0000000000001202
26. Koh GH, Park JY, Yu J, et al. Effect of sugammadex versus glycopyrrolate-neostigmine mixture on catheter-related bladder discomfort after retrograde intrarenal surgery: A retrospective observational analysis [preprint]. Published January 21, 2020. <https://assets.researchsquare.com/files/rs-12051/v1/d6c310ff-3e62-4bb2-a765-5f69a9c3aead.pdf?c=1631829915>. doi:10.21203/rs.2.21459/v1
27. Mayo BC, Louie PK, Bohl DD, et al. Effects of intraoperative anesthetic medications on postoperative urinary retention after single-level lumbar fusion. *Spine (Phila Pa 1976)*. 2016;41(18):1441–1446. doi:10.1097/BRS.00000000000001554
28. Valencia Morales DJ, Stewart BR, Heller SF, et al. Urinary retention following inguinal herniorrhaphy: Role of neuromuscular blockade reversal. *Surg Laparosc Endosc Percutan Tech*. 2021;31(5):613–617. doi:10.1097/SLE.0000000000000962
29. Senapathi TGA, Wiryana M, Subagiarta IM, et al. Effectiveness of intramuscular neostigmine to accelerate bladder emptying after spinal anesthesia. *Ther Clin Risk Manag*. 2018;14:1685–1689. doi:10.2147/TCRM.S176281
30. Higgins J, Green S, eds. *Cochrane Handbook for Systematic Reviews of Interventions Version 5.1.0 [Updated March 2011]*. London, UK: The Cochrane Collaboration; 2011. <https://handbook-5-1.cochrane.org/>. Accessed February 28, 2023.
31. Simmonds M. Quantifying the risk of error when interpreting funnel plots. *Syst Rev*. 2015;4:24. doi:10.1186/s13643-015-0004-8
32. Lin L, Chu H. Quantifying publication bias in meta-analysis. *Biometrics*. 2018;74(3):785–794. doi:10.1111/biom.12817
33. Schmidt L, Shokraneh F, Steinhausen K, Adams CE. Introducing RAPTOR: RevMan parsing tool for reviewers. *Syst Rev*. 2019;8(1):151. doi:10.1186/s13643-019-1070-0
34. Jackson D, Bowden J, Baker R. How does the DerSimonian and Laird procedure for random effects meta-analysis compare with its more efficient but harder to compute counterparts? *J Stat Plan*. 2010;140(4): 961–970. doi:10.1016/j.jspi.2009.09.017
35. Huedo-Medina TB, Sánchez-Meca J, Marín-Martínez F, Botella J. Assessing heterogeneity in meta-analysis: Q statistic or I² index? *Psychol Methods*. 2006;11(2):193–206. doi:10.1037/1082-989X.11.2.193
36. Page MJ, McKenzie JE, Bossuyt PM, et al. The PRISMA 2020 statement: An updated guideline for reporting systematic reviews. *Syst Rev*. 2021;10(1):89. doi:10.1186/s13643-021-01626-4
37. Van Enst WA, Ochodo E, Scholten RJ, Hoof L, Leeflang MM. Investigation of publication bias in meta-analyses of diagnostic test accuracy: A meta-epidemiological study. *BMC Med Res Methodol*. 2014;14:70. doi:10.1186/1471-2288-14-70
38. Fowler CJ, Griffiths D, De Groat WC. The neural control of micturition. *Nat Rev Neurosci*. 2008;9(6):453–466. doi:10.1038/nrn2401
39. Yoshimura N, Chancellor MB. Neurophysiology of lower urinary tract function and dysfunction. *Rev Urol*. 2003;5(Suppl 8):S3–S10. PMID:16985987.
40. de Groat WC, Griffiths D, Yoshimura N. Neural control of the lower urinary tract. *Compr Physiol*. 2015;5(1):327–396. doi:10.1002/cphy.c130056
41. Chai TC, Kudze T. New therapeutic directions to treat underactive bladder. *Investig Clin Urol*. 2017;58(Suppl 2):S99–S106. doi:10.4111/icu.2017.58.S2.S99
42. El-Tamalawy MM, Soliman MM, Omara AF, Rashad A, Ibrahim OM, El-Shishtawy MM. Efficacy and safety of neostigmine adjunctive therapy in patients with sepsis or septic shock: A randomized controlled trial. *Front Pharmacol*. 2022;13:855764. doi:10.3389/fphar.2022.855764
43. Ji W, Zhang X, Liu J, et al. Efficacy and safety of neostigmine for neuromuscular blockade reversal in patients under general anesthesia: A systematic review and meta-analysis. *Ann Transl Med*. 2021;9(22): 1691. doi:10.21037/atm-21-5667
44. Zhong QS, Ge SJ, Wang B, Xue ZG. Optimal single-dose epidural neostigmine for postoperative analgesia after partial hepatectomy. *Indian J Pharmacol*. 2014;46(6):613–616. doi:10.4103/0253-7613.144918
45. Hassanin AAM, Youssef IA, Mohamed HAA, Hanna GA. Effect of adding neostigmine to bupivacaine for ultrasound-guided supraclavicular brachial plexus block in forearm surgeries: A randomized, blinded, controlled study. *Egypt J Anaesth*. 2023;39(1):32–39. doi:10.1080/11101849.2023.2165890
46. Sirisreetreerux P, Wattanayingcharoenchai R, Rattanasiri S, Pattanaprateep O, Numthavaj P, Thakkinstian A. Medical and non-medical interventions for post-operative urinary retention prevention: Network meta-analysis and risk–benefit analysis. *Ther Adv Urol*. 2021;13:175628722110222. doi:10.1177/17562872211022296
47. Jackson J, Davies P, Leggett N, et al. Systematic review of interventions for the prevention and treatment of postoperative urinary retention. *BJS Open*. 2018;3(1):11–23. doi:10.1002/bjs5.50114
48. Cao M, Wu X, Xu J. A systematic review and meta-analysis of neostigmine for urinary retention after surgeries. *Transl Androl Urol*. 2022; 11(2):190–201. doi:10.21037/tau-22-16

A meta-analysis of the efficacy and safety of first-line chemotherapeutic agents for osteosarcoma

*Zhen Li^{1,A,B,E,F}, *Xiang Ma^{2,B-D}, Ziquan Wang^{1,B-D}, Suwei Dong^{3,A,B,E,F}, Baoqing Wang^{1,A,C,E,F}

¹ Department of Medical Oncology, The Second Affiliated Hospital of Xuzhou Medical University, China

² Department of Orthopaedics, The Third Affiliated Hospital of Kunming Medical University, China

³ Department of Orthopaedics, The Second Affiliated Hospital of Xuzhou Medical University, China

A – research concept and design; B – collection and/or assembly of data; C – data analysis and interpretation; D – writing the article; E – critical revision of the article; F – final approval of the article

Advances in Clinical and Experimental Medicine, ISSN 1899–5276 (print), ISSN 2451–2680 (online)

Adv Clin Exp Med. 2024;33(5):445–454

Address for correspondence

Suwei Dong

E-mail: dongsuweidsw@163.com

Funding sources

National Natural Science Foundation of China (82203396), the Natural Science Foundation of Jiangsu Province (BK20220235), Basic Research Program of Xuzhou Health Commission (KC21060, KC21049), and Development Foundation of Affiliated Hospital of Xuzhou Medical University (XYFY2020001, XYFY2020002), Applied Basic Research of Yunnan Science & Technology Agency-Joint Funds of Yunnan Science & Technology Agency and Kunming Medical University (202201AY070001-152).

Conflict of interest

None declared

*Zhen Li and Xiang Ma contributed equally to this work.

Received on April 23, 2023

Reviewed on July 12, 2023

Accepted on July 27, 2023

Published online on September 25, 2023

Cite as

Li Z, Ma X, Wang Z, Dong S, Wang B. A meta-analysis of the efficacy and safety of first-line chemotherapeutic agents for osteosarcoma.

Adv Clin Exp Med. 2024;33(5):445–454.

doi:10.17219/acem/170098

DOI

10.17219/acem/170098

Copyright

Copyright by Author(s)

This is an article distributed under the terms of the Creative Commons Attribution 3.0 Unported (CC BY 3.0) (<https://creativecommons.org/licenses/by/3.0/>)

Abstract

Background. Osteosarcoma is a pleomorphic cancer that frequently affects children and teenagers. Although several chemotherapy regimens have been utilized for many years, the best therapeutic option for the treatment of osteosarcoma has not yet been determined.

Objectives. This meta-analysis was designed to assess the clinical efficacy of a high-dose methotrexate, doxorubicin and cisplatin (MAP) regimen and compare its survival outcomes with those of other chemotherapy strategies in patients diagnosed with osteosarcoma.

Materials and methods. We systematically searched databases, namely Embase, the Cochrane Library and PubMed, up to August 2022, for relevant studies investigating the impact of the MAP chemotherapy protocol on survival among patients with osteosarcoma. The odds ratio (OR) pooled estimates and their 95% confidence intervals (95% CIs) were calculated.

Results. Twelve studies including 4102 patients were eligible for analysis in this study. The estimated pooled ORs of the 3-year overall survival (OS) and event-free survival (EFS) were OR = 1.08 (95% CI: 0.72–1.62, $p = 0.70$) and OR = 1.04 (95% CI: 0.81–1.32, $p = 0.78$, respectively). The 5-year OS and EFS were OR = 0.87 (95% CI: 0.62–1.23, $p = 0.42$) and OR = 1.13 (95% CI: 0.76–1.68, $p = 0.54$), respectively, with no statistical differences. The subgroup analysis of MAP compared to a 2-drug regimen (doxorubicin and cisplatin) revealed a significant difference between the 2 chemotherapy strategy groups in 3-year OS rates (OR = 0.72 (95% CI: 0.56–0.92, $p = 0.009$)) and 5-year EFS rates (OR = 0.57 (95% CI: 0.43–0.76, $p < 0.001$)).

Conclusions. The MAP chemotherapy strategy for osteosarcoma showed superiority over other regimens, especially over the 2-drug regimen (doxorubicin/cisplatin), in terms of better prognosis and safety.

Key words: doxorubicin, overall survival, cisplatin, osteosarcoma, ifosfamide

Introduction

Osteosarcoma is a pleomorphic malignancy that commonly occurs in children and adolescents. It is defined as a primary malignancy of the mesenchymal tissues in bones and accounts for 20–40% of all diagnosed bone cancers.¹ The etiology of osteosarcoma remains unknown; however, exposure to radiotherapy, alkylating agent-based chemotherapy, Li–Fraumeni syndrome, and Paget’s disease of bone are considered risk factors and account for a proportion of the cases.² The main treatment approach for this type of bone cancer was amputation, which had limited clinical efficacy. Chemotherapy and surgical strategies were introduced in the 1970s and improved the overall 5-year survival rate to about 70%.³ During that time, chemotherapy was used postoperatively to eliminate unresectable lesions. Later, preoperative chemotherapeutic regimens were clinically applied and known as neoadjuvant chemotherapy. This approach was widely adopted in clinical practice since it helped in the elimination of potential micro-metastases, reduced tumor edema, increased limb salvage rates, reduced recurrence rates, and improved the overall survival (OS) rates.⁴

In the past decades, a number of trials have been conducted to evaluate the efficacy of different postoperative chemotherapeutic agents. Initially, methotrexate was reported, followed by other agents with some degree of survival improvement.^{5,6} The studied drugs included ifosfamide, dacarbazine, and their combination with doxorubicin, with a response rate reaching up to 40%. Single-agent chemotherapy has been shown to be inadequate for osteosarcoma treatment. A trial conducted in 2014 comparing doxorubicin alone with its combination with ifosfamide revealed a significant improvement in the rates of progression-free survival (PFS) and the overall response for the combined chemotherapeutic regimen. However, the OS between the 2 regimens did not significantly differ ($p = 0.076$).⁷ Recently, as approved by the National Comprehensive Cancer Network (NCCN) guidelines,^{8,9} the most commonly used chemotherapeutic agents for osteosarcoma include doxorubicin, high-dose methotrexate, cisplatin, and ifosfamide.

Nowadays, novel approaches are applied for osteosarcoma management, including targeted drug therapy, experimental therapy, immunotherapy, and radiotherapy. The combination of up to 4 drugs, namely doxorubicin, methotrexate, cisplatin, and ifosfamide, is the main osteosarcoma treatment in today’s protocols.^{6,9,10} The recommended regimens, according to the NCCN guidelines, include a doxorubicin and cisplatin combination; high-dose methotrexate, doxorubicin and cisplatin (MAP) combination; methotrexate, doxorubicin, cisplatin, and ifosfamide (MAPI) combination; and ifosfamide, cisplatin and epirubicin combination.⁹ Most healthcare settings worldwide conduct a number of preoperative chemotherapy courses, ranging from 2 to 6 courses for up

to 18 weeks.¹¹ The toxicity of chemotherapeutic regimens should also be considered, which includes bone marrow suppression, neurological toxicity, liver and kidney damage, and gastrointestinal disorders. Although these regimens have been used for many years, the optimal therapeutic choice for osteosarcoma treatment has not been established.

Objectives

Therefore, studies that compared the above regimens were eligible for the present meta-analysis to establish a detailed comparison between the available regimens and assess the clinical efficacy and toxicity of first-line chemotherapeutic agents for patients diagnosed with osteosarcoma.

Materials and methods

Search strategy and identification

This meta-analysis was designed and conducted according to the Preferred Reporting Items for Systematic Review and Meta-Analyses (PRISMA) guidelines. The ethical approval was waived due to the type of the study. The protocol of this meta-analysis has been registered in PROSPERO as CRD42022385111. Original research studies written in English and published up to August 2022 were verified by the PubMed, Embase and Cochrane Library databases. The keywords or medical subject headings (MeSH) terms related to osteosarcoma, chemotherapy, methotrexate, doxorubicin, cisplatin, ifosfamide, and survival rate were combined during the database search, as presented in Table 1. The retrieved studies were carefully investigated for eligibility. Only human research studies were included. Irrelevant publications, assessed on the basis of the title, abstract or full article, were excluded. Also, commentaries, review articles, editorials, and irrelevant studies were all excluded. All chosen publications were collected using EndNote software (Clarivate, London, UK), and duplications were excluded.

Inclusion criteria

The current meta-analysis inclusion criteria were:

1. Well-designed randomized controlled or comparative studies, either prospective or retrospective;
2. Studies in which the intended target patients were those with a confirmed diagnosis of osteosarcoma using typical imaging or pathological biopsy;
3. Studies in which the procedure of intervention included a comparison of the first-line chemotherapeutic regimens, according to the NCCN recommendations for the treatment of osteosarcoma;

Table 1. Search strategy for each electronic database

Database	Search strategy
PubMed	(#1) "Osteosarcoma" [MeSH terms] OR "Chemotherapy" [all fields] OR "Osteosarcomas" [all fields] (#2) "Methotrexate" [MeSH terms] OR "Cisplatin" [all fields] OR "Doxorubicin" [all fields] OR "Ifosamide" [all fields] (#3) "overall survival" [all fields] OR "progressive-free survival" (#4) #1 AND #2 AND #3
Embase	(#1) '(Osteosarcoma)/exp OR '(Chemotherapy)/exp OR 'Osteosarcomas'/exp (#2) '(Methotrexate)/exp OR '(Cisplatin)/exp OR '(Doxorubicin)/exp OR '(Ifosamide)/exp (#3) '(overall survival)/exp OR '(progressive-free survival)/exp (#4) #1 AND #2 AND #3
Cochrane Library	(#1) (Osteosarcoma): ti,ab,kw OR (Chemotherapy): ti,ab,kw OR (osteosarcomas): ti,ab,kw (#2) (Methotrexate): ti,ab,kw OR (Cisplatin): ti,ab,kw OR (Doxorubicin): ti,ab,kw OR (Ifosamide): ti,ab,kw (#3) (overall survival): ti,ab,kw OR (progressive-free survival) (#4) #1 AND #2 AND #3

MeSH – medical subject headings; ti,ab,kw – terms in either title or abstract or keyword fields; exp – exploded indexing term.

4. Studies in which data were adequately described to estimate the overall pooled effect size of the intervention and 95% confidence interval (95% CI).

The exclusion criteria

The exclusion criteria were:

1. Reports, editorials, abstracts, reviews, animal experiments, and studies in languages other than English;
2. Publications with missing or incomplete outcomes;
3. Research articles with aims other than the examination of the recommended first-line chemotherapeutic regimens such as target receptor-based therapy, immunotherapy, radiotherapy, and vaccine-based therapy.

Data extraction

The methodological quality was evaluated and data extraction was performed by 2 independent authors, according to the Cochrane Collaboration guidelines.¹² We used a pre-designed form to summarize the study- and participant-related variables under the following headings: the name of the first author, study period, region, target patients, study protocol, number of subjects, demographical characteristics, applied chemotherapeutic protocol, and survival status. The main outcome measures included the OS rate, which is the time elapsed from the inclusion in the study to death or the last follow-up; event-free survival (EFS), which is the time from the inclusion in the study to metastatic disease appearance or death; and the total number of adverse effects (grade ≥ 3) after the implementation of different chemotherapeutic regimens. The targeted adverse effects included neutropenia, thrombocytopenia, cardiac and renal dysfunction, mucositis, and anemia.

Risk of bias

Following data extraction, the authors assessed the quality of the chosen studies according to the Cochrane

Collaboration guidelines. The risk of bias was graded as low, medium or high, and was assessed based on the employed randomization method, the outcome assessment blinding, and any missing data or selective reporting. We reviewed the original article to clarify any discrepancies or misunderstandings.

Statistical analyses

The odds ratios (ORs) and 95% CIs were computed using fixed- or random-effect models. The pooled estimates of the interventions' effect sizes and graphs were performed using the Reviewer Manager (RevMan) software v. 5.3 (The Nordic Cochrane Centre, The Cochrane Collaboration, Copenhagen, Denmark). The χ^2 tests were utilized to test for heterogeneity. The estimated I^2 index ranged between 0% and 100% and was used to evaluate heterogeneity.¹³ When the value of the I^2 index was 0%, it was interpreted as an absence of heterogeneity, an I^2 index of 25% was identified as a low level of heterogeneity, and the values of 50% and 75% were identified to represent moderate and high heterogeneity levels, respectively. If the I^2 index was higher than 50%, we applied a random-effect model, and if it was less than 50%, we applied a fixed-effect model. The sensitivity analysis was conducted to identify the source of significant incoherence for the main outcomes. The value of $p < 0.05$ indicated statistical significance. The assessment of bias was quantitatively performed using the Egger's regression test ($p \leq 0.05$ denoted bias between studies), and qualitatively, by visual inspection of the funnel plots.

Results

A total of 1258 potential publications were retrieved through a database search. After full-text assessment, 12 studies met the inclusion criteria and were evaluated in this meta-analysis.^{14–25} The process of literature search and screening is depicted in Fig. 1. The selected studies

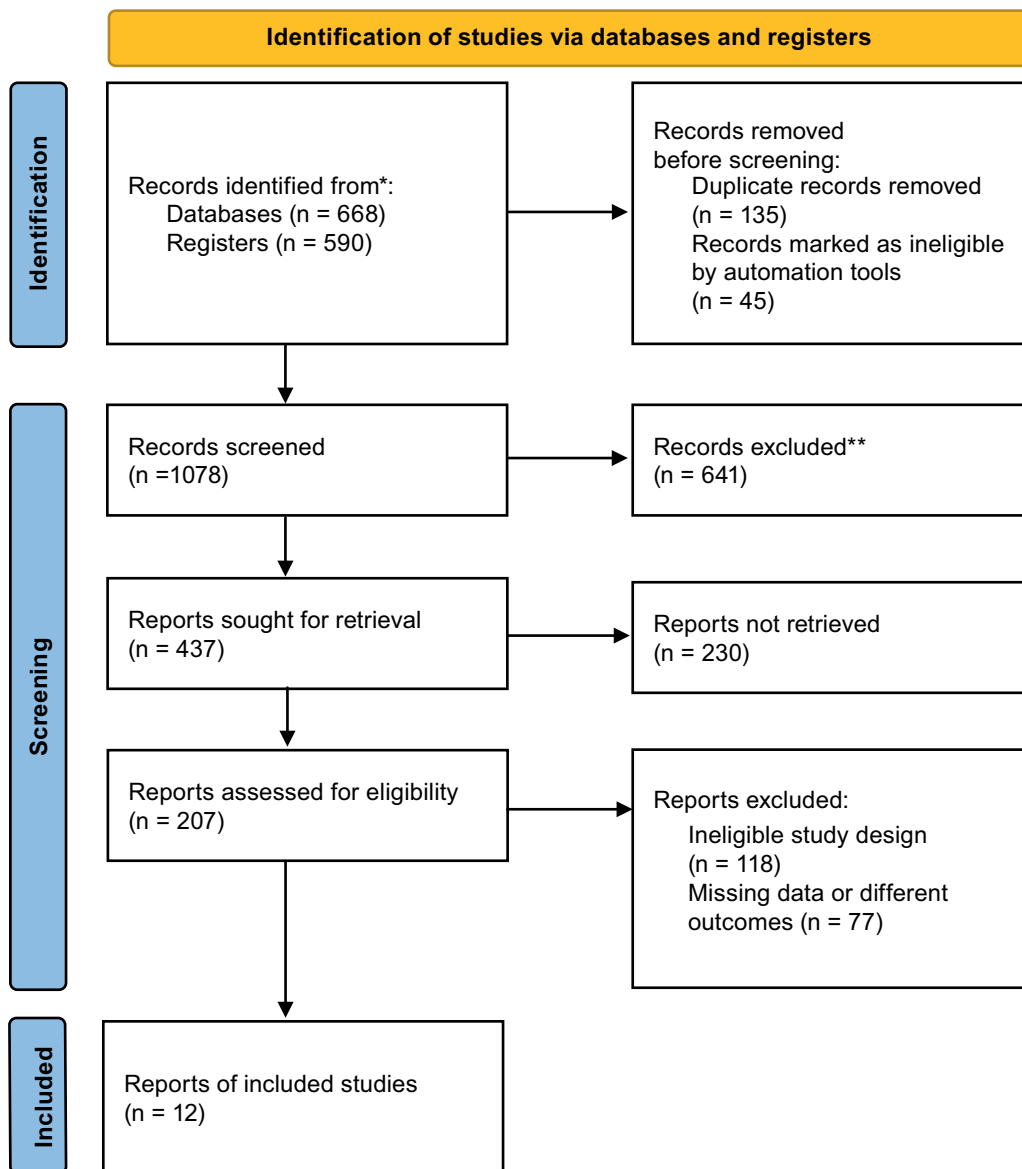


Fig. 1. Flowchart of the search and selection strategy

involved a total of 4102 patients. All included studies were randomized controlled trials (RCTs). The sample size of the integrated studies ranged from 36 to 716 osteosarcoma patients at the beginning of the trial. The main features of the selected studies are summarized in Table 2.

The risk of bias in the eligible studies was evaluated according to the Cochrane Collaboration tool (Risk of Bias 2 (RoB2)). All included trials adequately described the randomization procedures, while blinding and allocation concealment were variable. The evaluation of the risk of bias is summarized in Fig. 2.

Overall survival rates

Four studies ($n = 1886$) reported data related to the 3-year OS rates. The comparison of MAP with different therapeutic regimens, including doxorubicin and cisplatin regimens or MAP chemotherapy regimens plus adjuvant drugs, showed no differences between groups (OR = 1.08

(95% CI: 0.72–1.62), Z-test = 0.38, $p = 0.700$), with high heterogeneity ($I^2 = 69\%$), as shown in Fig. 3A. The subgroup analysis of the pooled OR of the survival rate with MAP chemotherapy compared to doxorubicin and cisplatin combination chemotherapy revealed a significant difference between the 2 groups regarding 3-year OS rates (OR = 0.72 (95% CI: 0.56–0.92), Z-test = 2.59, $p = 0.009$) (Fig. 3B).

The 5-year OS rate was assessed in 4 studies ($n = 1657$). The forest plot, presented in Fig. 4A, summarizes the overall ORs with non-statistically significant differences between the arms of comparison (OR = 0.87 (95% CI: 0.62–1.23), Z-test = 0.80, $p = 0.420$). Moderate heterogeneity was observed ($I^2 = 57\%$). The subgroup analysis of the 5-year OS rate after MAP chemotherapy compared to doxorubicin and cisplatin combination chemotherapy revealed a non-statistically significant difference (OR = 0.82 (95% CI: 0.58–1.17), Z-test = 1.09, $p = 0.270$), with moderate heterogeneity between the studies ($I^2 = 73\%$, $\chi^2 = 7.43$, $p = 0.020$) (Fig. 4B).

Table 2. Characteristics of the included studies

Study ID and publication year	Country	Study design	Patients, n	Chemotherapeutic regimen/number of patients	Comparative group regimen/number of patients	Outcome measures
Link et al., 1991 ¹⁴	USA	RCT	36	MAP/18	MAPI/18	OS, EFS, side effects
Bramwell et al., 1992 ¹⁵	Canada	RCT	307	MAP/152	doxorubicin, cisplatin/155	OS, EFS, side effects
Bramwell et al., 1997 ¹⁶	Canada	RCT	37	MAP/13	doxorubicin, cisplatin/24	OS, EFS, side effects
Meyers et al., 2005 ¹⁷	USA	RCT	399	MAP/232	MAPI/167	OS, EFS, side effects
Craft, 2009 ¹⁸	UK	RCT	388	MAP/191	doxorubicin, cisplatin/197	OS, EFS, side effects
Ferrari et al., 2012 ¹⁹	Italy	RCT	246	MAP/123	MAPI/123	OS, EFS, side effects
Whelan et al., 2012 ²⁰	UK	RCT	179	MAP/90	doxorubicin, cisplatin/89	OS, EFS, side effects
Bielack et al., 2015 ²¹	international study (17 countries)	RCT	716	MAP/359	methotrexate, doxorubicin, cisplatin plus alpha-2b/357	OS, EFS, side effects
Marina et al., 2016 ²²	international study (17 countries)	RCT	618	MAP/310	methotrexate, doxorubicin, cisplatin plus etoposide-ifosfamide/308	OS, EFS, side effects
Piperno-Neumann et al., 2016 ²³	France	RCT	315	MAP/156	methotrexate, doxorubicin, cisplatin plus zoledronate/159	OS, EFS, side effects
Senerchia et al., 2017 ²⁴	USA	RCT	296	MAP/157	methotrexate, doxorubicin, cisplatin plus MC/139	OS, EFS, side effects
Gaspar et al., 2018 ²⁵	France	RCT	565	MAP/156	methotrexate, doxorubicin, cisplatin plus etoposide-ifosfamide/409	OS, EFS, side effects

MAP – methotrexate, doxorubicin and cisplatin; MAPI – MAP with ifosfamide; EFS – event-free survival; OS – overall survival; RCT – randomized controlled trial; MC – metronomic chemotherapy.

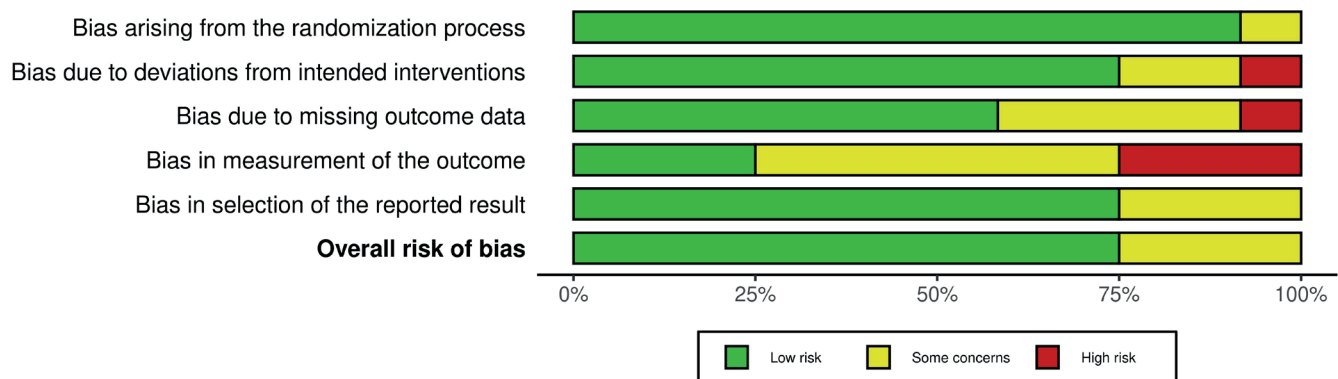


Fig. 2. Summary plot of the risk of bias (RoB 2 tool) of the analyzed studies presented as percentages

Event-free survival rates

Six studies (n = 3001) reported data related to the 3-year EFS. The comparison of MAP chemotherapy regimens with other regimens revealed no significant differences, with an overall OR of 1.04 (95% CI: 0.81–1.32, Z-test = 0.28, p = 0.780). The estimated heterogeneity between studies was moderate (I² = 54%) (Fig. 5).

The 5-year EFS rate was reported in 6 studies (n = 1902). The estimated 5-year EFS rate was 61.2% (1164/1902) with the use of MAP regimens compared to the other

chemotherapeutic regimens. The forest plot, as shown in Fig. 6A, revealed non-significant differences between the comparison groups (OR = 1.13 (95% CI: 0.76–1.68), Z-test = 0.61, p = 0.540) with moderate heterogeneity (I² = 74%). The subgroup analysis of the pooled OR of the 5-year EFS rate with MAP chemotherapy compared to 2-drug combinations, doxorubicin and cisplatin chemotherapy, revealed a significant difference between the 2 groups in 5-year EFS rates (OR = 0.57 (95% CI: 0.43–0.76), Z-test = 3.89, p < 0.001) (Fig. 6B). The comparison of MAP regimen with MAPI revealed preferable 5-year EFS rates with the addition

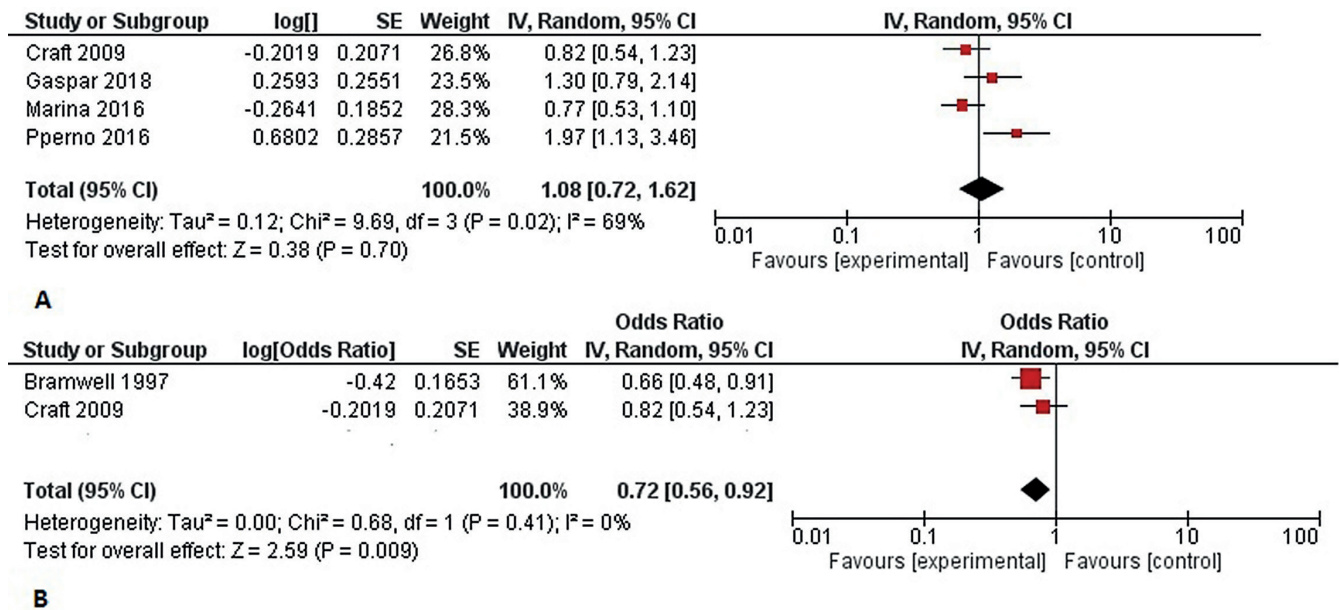


Fig. 3. Forest plot of 3-year overall survival (OS) between methotrexate, doxorubicin and cisplatin (MAP) and other regimens of chemotherapy. A. Forest plot of 3-year OS rates between MAP and other regimens of chemotherapy; B. Forest plot of MAP 3-year OS rates compared to the 2-drug chemotherapy regimen, doxorubicin and cisplatin

SE – standard error; 95% CI – 95% confidence interval; df – degrees of freedom.

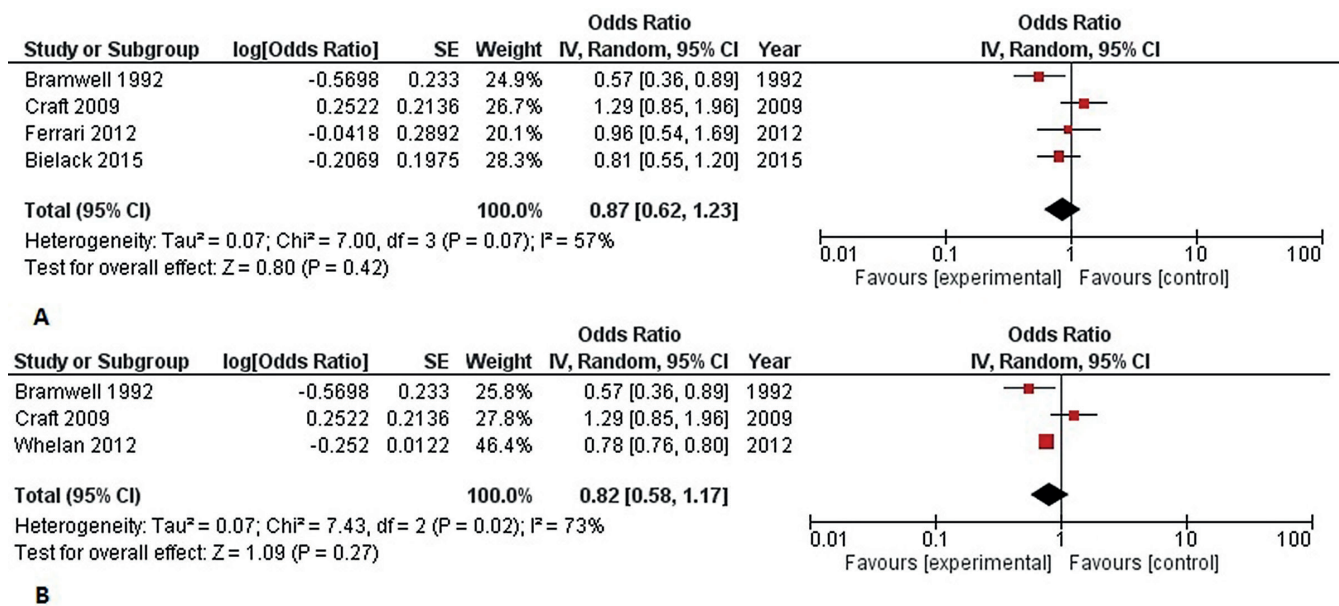


Fig. 4. Forest plot of 5-year overall survival (OS) between methotrexate, doxorubicin and cisplatin (MAP) and other regimens of chemotherapy. A. Forest plot of 5-year OS rates between MAP and other regimens of chemotherapy; B. Forest plot of MAP 5-year OS rates compared to the 2-drug chemotherapy regimen, doxorubicin and cisplatin

SE – standard error; 95% CI – 95% confidence interval; df – degrees of freedom.

of ifosfamide, as shown in Fig. 6C. However, the overall OR was statistically non-significant (OR = 1.73 (95% CI: 0.96–3.11), Z-test = 1.82, p = 0.070), with moderate heterogeneity ($\chi^2 = 4.65$, p = 0.100, I² = 57%). The adjustment for factors such as gender, race, and age, as well as subgroup analysis were not conducted because of the limited data on the influence of these variables in the included studies. We assessed the impact of each study on the overall results using sensitivity analysis. The symmetrical shape of the funnel plots and

the results of Eggers's test, as illustrated in Table 3, did not show any evidence of publication bias.

Overall severe adverse effects and systemic toxicities

The chemotherapy-related toxicities are summarized in Table 4. Seven common adverse effects of chemotherapy were observed in the eligible studies. These included

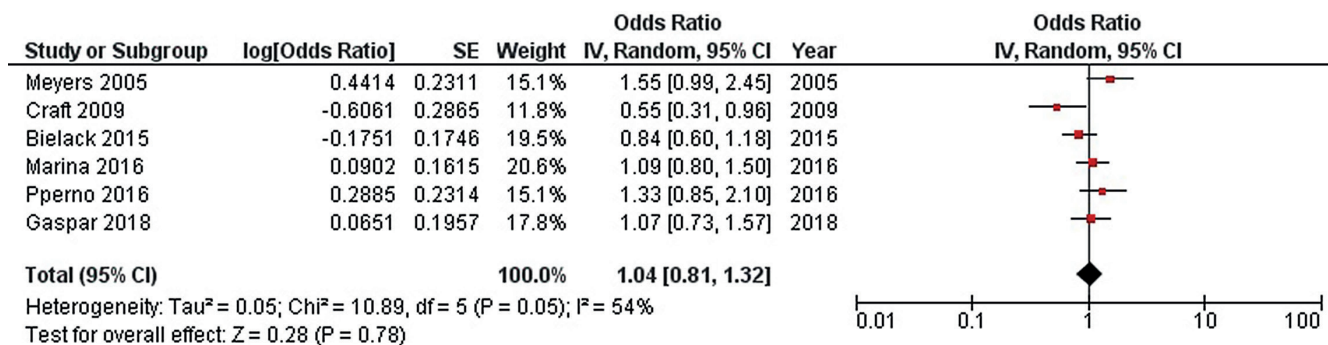
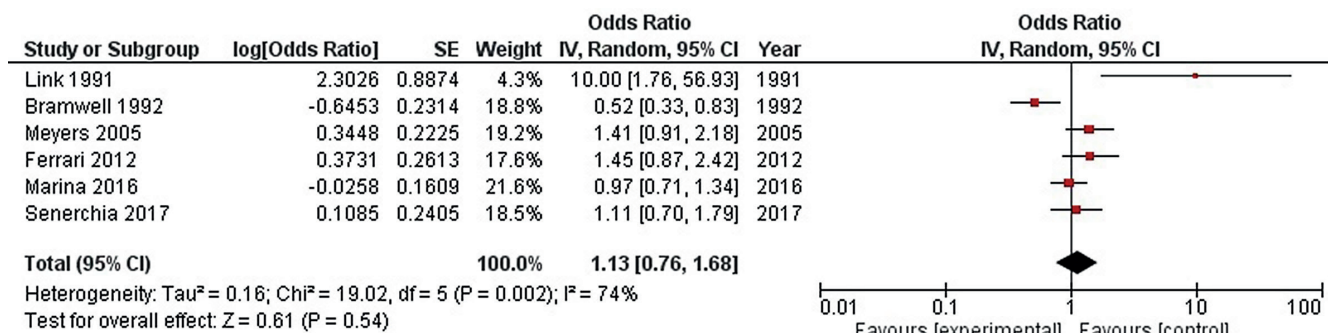
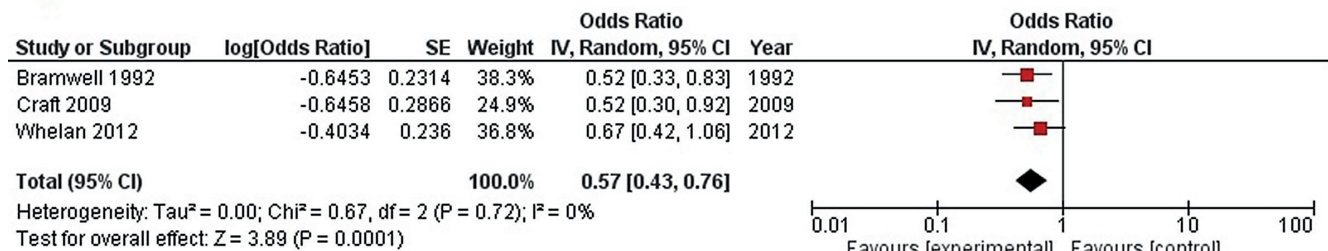


Fig. 5. Forest plot of 3-year event-free survival (EFS) between methotrexate, doxorubicin and cisplatin (MAP) and other regimens of chemotherapy

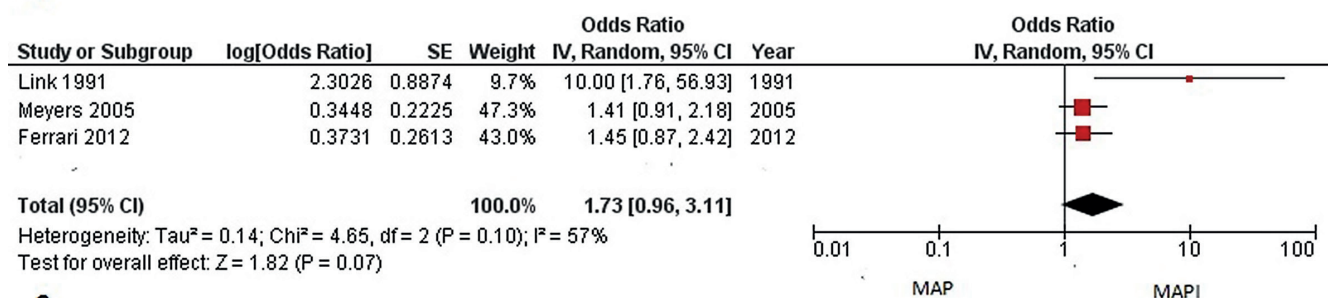
SE – standard error; 95% CI – 95% confidence interval; df – degrees of freedom.



A



B



C

Fig. 6. Forest plot of 5-year event-free survival (EFS) between methotrexate, doxorubicin and cisplatin (MAP) and other regimens of chemotherapy. A. Forest plot of 5-year EFS rates between MAP and other regimens of chemotherapy; B. Forest plot of MAP 5-year EFS rates compared to 2-drug chemotherapy regimen, doxorubicin and cisplatin; C. Forest plot of MAP 5-year EFS compared to the MAP with ifosfamide (MAPI) regimen

SE – standard error; 95% CI – 95% confidence interval; df – degrees of freedom.

neutropenia, febrile neutropenia, thrombocytopenia, hypophosphatemia, cardiac toxicity, mucositis, and anemia. Neutropenia events were the most common, with an incidence rate of 87.4% (615/703) for MAP or MAPI regimens and 92.9% (416/448) for other chemotherapy regimens. The thrombocytopenia incidence rate was lower for

the MAP or MAPI regimen (69.1% (484/700)), compared to other combinations of chemotherapy (78.9% (355/450)). The incidence rates for febrile neutropenia and anemia were lower for MAP or MAPI regimens compared to other chemotherapy combination regimens: 62.8% compared to 79.5% and 70.2% compared to 81.6%, respectively.

Table 3. Egger's test results for publication bias

Outcome			Egger's test	
			t	p-value
OS	3-year OS	MAP vs. other	1.02	0.356
		MAP vs. 2-drug regimen	1.08	0.841
	5-year OS	MAP vs. other	-0.66	0.752
		MAP vs. 2-drug regimen	0.53	0.923
EFS	3-year EFS	MAP vs. other	0.33	0.633
		MAP vs. other	0.87	0.325
	5-year EFS	MAP vs. 2-drug regimen	0.42	0.561
		MAP vs. MAPI	0.21	0.582

MAP – methotrexate, doxorubicin and cisplatin; MAPI – MAP with ifosfamide; EFS – event-free survival; OS – overall survival.

Table 4. Complications and adverse effects

Adverse effects*	Events, n	Patients, n	MAP or MAPI chemotherapy		Other chemotherapy regimens	
			events/patients, n	rate	events/patients, n	rate
Neutropenia	1031	1151	615/703	0.874	416/448	0.929
Thrombocytopenia	839	1150	484/700	0.691	355/450	0.789
Febrile neutropenia	1221	1716	538/857	0.628	683/859	0.795
Hypophosphatemia	202	885	69/442	0.156	133/443	0.30
Cardiac toxicity	27	1283	11/639	0.017	16/644	0.025
Mucositis	256	838	127/423	0.30	129/415	0.311
Anemia	689	908	321/457	0.702	368/451	0.816

* severe adverse effects with grade ≥ 3 ; MAP – methotrexate, doxorubicin and cisplatin; MAPI – MAP with ifosfamide.

Discussion

Osteosarcoma is the most prevalent bone tumor in the young age group, with a high mortality rate and the risk of metastasis to other organs, commonly the lymph nodes and lungs, in about 30% of patients.²⁶ Multi-drug combination chemotherapy and surgery have been associated with improved survival rates of up to 80%.^{9,27} The frontline chemotherapy combination for osteosarcoma treatment includes high-dose methotrexate, cisplatin and doxorubicin with or without ifosfamide. However, the overall efficacy of this regimen is still controversial in many RCTs. To the best of our knowledge, this study is the latest meta-analysis on the effectiveness and tolerability of first-line chemotherapy combination drugs for osteosarcoma.

This meta-analysis included 12 RCTs with a total of 4102 patients. The outcomes for the 3- and 5-year OS and EFS were used for efficacy assessment. The total number of severe adverse events was evaluated as a measure of the safety and tolerability of different chemotherapeutic regimens. Based on the conducted analysis, no significant difference was observed in the survival rate between MAP and other regimens. These results are consistent with a recently published meta-analysis by Yu et al.²⁸ However, the subgroup analysis showed that the MAP regimen significantly improved 3-year OS and 5-year PFS when compared to the doxorubicin and cisplatin combination.

Consistent with our results, Bacci et al. reported significant survival benefits with a methotrexate-based regimen among patients with osteosarcoma.²⁹ High-dose methotrexate seems to play a pivotal role in the efficacy of the multi-drug combination regimen; however, its exact mechanism has not yet been clarified.³⁰ Ifosfamide, a cyclophosphamide analog, is a highly effective therapeutic agent in osteosarcoma treatment. In our results, the comparison of MAP with MAPI revealed a favorable 5-year event-free prognosis with the addition of ifosfamide to the regimen, but the difference was not significant ($p = 0.070$). The relatively small number of the included studies could have prevented the detection of significance. A meta-analysis conducted by Fan et al. reported a reduced mortality rate of about 17% and remarkable responses with a chemotherapeutic regimen based on ifosfamide.³¹

According to our results, the MAPI regimen could significantly improve the survival rates of patients with osteosarcoma compared to the 2-drug chemotherapeutic regimen (doxorubicin and cisplatin). Furthermore, MAPI showed better outcomes compared to the MAP regimen; however, the difference was non-significant.

Although the MAP regimen, with or without ifosfamide, showed better responses and prognoses in patients with osteosarcoma, its adverse effects are also a matter of concern. The safety assessment of MAP and MAPI chemotherapy-based regimens showed lower rates of toxicities,

including neutropenia, thrombocytopenia, febrile neutropenia, hypophosphatemia, cardiac toxicity, mucositis, and anemia. These results are consistent with the meta-analysis by Yu et al., which reported lower rates of adverse effects with MAP-based regimens, especially with regards to febrile neutropenia, thrombocytopenia, anemia, and hypophosphatemia.²⁸ The combination of both neoadjuvant and adjuvant chemotherapeutic regimens with surgery has become the major strategy for osteosarcoma treatment.³² The addition of neoadjuvant chemotherapy before resection has many advantages, including better control of the primary tumor, reduced metastasis incidence, and early assessment of the prognosis. Several studies have confirmed a similar efficacy with MAPI as neoadjuvant and adjuvant chemotherapy regimen.^{32,33}

This meta-analysis had numerous strong points. First, this is the latest meta-analysis on the efficacy and safety of the first-line regimens of chemotherapy for osteosarcoma treatment. Second, we explored the efficacy of the ifosfamide addition to the MAP regimen, and we compared the 2-drug regimen, cisplatin/doxorubicin, with the methotrexate-based multi-chemotherapy regimens. Third, the absence of publication bias was evident qualitatively, after visual inspection of the funnel plot, and quantitatively, after conducting the statistical test for publication bias. Besides, our findings provide clear and concise evidence for the efficacy and safety of osteosarcoma chemotherapy.

Limitations

Nonetheless, the present meta-analysis had some limitations. The main limitation of the study was the use of evidence with potential bias. Some of the included RCTs did not adequately describe the allocation and blinding techniques, which might affect the validity of the findings. Second, the lack of adjustment to the confounding factors could affect the overall outcomes. Besides, some comparisons included a small number of studies; therefore, further studies are warranted to develop the optimum strategy for osteosarcoma treatment and prognosis.

Conclusions

The MAP chemotherapy regimen for osteosarcoma showed superiority over other regimens, especially over the 2-drug regimen (doxorubicin/cisplatin) for osteosarcoma treatment in terms of better prognosis and safety.

ORCID iDs

Suwei Dong  <https://orcid.org/0000-0001-8059-5865>

References

- Belayneh R, Fourman MS, Bhogal S, Weiss KR. Update on osteosarcoma. *Curr Oncol Rep*. 2021;23(6):71. doi:10.1007/s11912-021-01053-7
- Lee JA, Lim J, Jin HY, et al. Osteosarcoma in adolescents and young adults. *Cells*. 2021;10(10):2684. doi:10.3390/cells10102684
- Longhi A, Errani C, De Paolis M, Mercuri M, Bacci G. Primary bone osteosarcoma in the pediatric age: State of the art. *Cancer Treat Rev*. 2006;32(6):423–436. doi:10.1016/j.ctrv.2006.05.005
- Zhao X, Wu Q, Gong X, Liu J, Ma Y. Osteosarcoma: A review of current and future therapeutic approaches. *BioMed Eng Online*. 2021;20(1):24. doi:10.1186/s12938-021-00860-0
- Anderson ME. Update on survival in osteosarcoma. *Orthop Clin North Am*. 2016;47(1):283–292. doi:10.1016/j.jocl.2015.08.022
- Jaffe N. Adjuvant chemotherapy in osteosarcoma. In: Jaffe N, Bruland OS, Bielack S, eds. *Pediatric and Adolescent Osteosarcoma*. Cancer Treatment and Research. Vol. 152. Boston, USA: Springer US; 2009:219–237. doi:10.1007/978-1-4419-0284-9_11
- Judson I, Verweij J, Gelderblom H, et al. Doxorubicin alone versus intensified doxorubicin plus ifosfamide for first-line treatment of advanced or metastatic soft-tissue sarcoma: A randomised controlled phase 3 trial. *Lancet Oncol*. 2014;15(4):415–423. doi:10.1016/S1470-2045(14)70063-4
- Bajpai J, Chandrasekharan A, Talreja V, et al. Outcomes in non-metastatic treatment naive extremity osteosarcoma patients treated with a novel non-high dose methotrexate-based, dose-dense combination chemotherapy regimen 'OGS-12.' *Eur J Cancer*. 2017;85:49–58. doi:10.1016/j.ejca.2017.08.013
- Wagner MJ, Livingston JA, Patel SR, Benjamin RS. Chemotherapy for bone sarcoma in adults. *J Oncol Pract*. 2016;12(3):208–216. doi:10.1200/JOP.2015.009944
- Brookes MJ, Chan CD, Baljer B, et al. Surgical advances in osteosarcoma. *Cancers (Basel)*. 2021;13(3):388. doi:10.3390/cancers13030388
- Eaton BR, Schwarz R, Vatner R, et al. Osteosarcoma. *Pediatr Blood Cancer*. 2021;68(Suppl 2):e28352. doi:10.1002/pbc.28352
- Higgins JPT, Thomas J, Chandler J, Cumpston M, Li T, Page MJ, Welch VA, eds. *Cochrane Handbook for Systematic Reviews of Interventions*. 2022. London, UK: Cochrane Collaboration. www.training.cochrane.org/handbook.
- Higgins JPT, Thompson S, Deeks J, Altman D. Measuring inconsistency in meta-analyses. *BMJ*. 2003;327(7414):557–560. doi:10.1136/bmj.327.7414.557
- Link MP, Goorin AM, Horowitz M, et al. Adjuvant chemotherapy of high-grade osteosarcoma of the extremity. Updated results of the Multi-Institutional Osteosarcoma Study. *Clin Orthop Relat Res*. 1991;(270):8–14. PMID:1884563.
- Bramwell VH, Burgers M, Sneath R, et al. A comparison of two short intensive adjuvant chemotherapy regimens in operable osteosarcoma of limbs in children and young adults: The first study of the European Osteosarcoma Intergroup. *J Clin Oncol*. 1992;10(10):1579–1591. doi:10.1200/JCO.1992.10.1579
- Bramwell VHC, Burgers MV, Souhami RL, et al. A randomized comparison of two short intensive chemotherapy regimens in children and young adults with osteosarcoma: Results in patients with metastases: A study of the European Osteosarcoma Intergroup. *Sarcoma*. 1997;1(3–4):155–160. doi:10.1080/13577149778245
- Meyers PA, Schwartz CL, Krailo M, et al. Osteosarcoma: A randomized, prospective trial of the addition of ifosfamide and/or muramyl tripeptide to cisplatin, doxorubicin, and high-dose methotrexate. *J Clin Oncol*. 2005;23(9):2004–2011. doi:10.1200/JCO.2005.06.031
- Craft AW. Osteosarcoma: The European Osteosarcoma Intergroup (EOI) perspective. In: Jaffe N, Bruland OS, Bielack S, eds. *Pediatric and Adolescent Osteosarcoma*. Cancer Treatment and Research. Vol. 152. Boston, USA: Springer US; 2009:263–274. doi:10.1007/978-1-4419-0284-9_13
- Ferrari S, Ruggieri P, Cefalo G, et al. Neoadjuvant chemotherapy with methotrexate, cisplatin, and doxorubicin with or without ifosfamide in nonmetastatic osteosarcoma of the extremity: An Italian sarcoma group trial ISG/OS-1. *J Clin Oncol*. 2012;30(17):2112–2118. doi:10.1200/JCO.2011.38.4420
- Whelan JS, Jinks RC, McTiernan A, et al. Survival from high-grade localized extremity osteosarcoma: Combined results and prognostic factors from three European Osteosarcoma Intergroup randomised controlled trials. *Ann Oncol*. 2012;23(6):1607–1616. doi:10.1093/annonc/mdr491
- Bielack SS, Smeland S, Whelan JS, et al. Methotrexate, doxorubicin, and cisplatin (MAP) plus maintenance pegylated interferon alfa-2b versus MAP alone in patients with resectable high-grade osteosarcoma and good histologic response to preoperative MAP: First results of the EUR-AMOS-1 Good Response randomized controlled trial. *J Clin Oncol*. 2015;33(20):2279–2287. doi:10.1200/JCO.2014.60.0734

22. Marina NM, Smeland S, Bielack SS, et al. Comparison of MAPIE versus MAP in patients with a poor response to preoperative chemotherapy for newly diagnosed high-grade osteosarcoma (EURAMOS-1): An open-label, international, randomised controlled trial. *Lancet Oncol*. 2016;17(10):1396–1408. doi:10.1016/S1470-2045(16)30214-5
23. Piperno-Neumann S, Le Deley MC, Rédini F, et al. Zoledronate in combination with chemotherapy and surgery to treat osteosarcoma (OS2006): A randomised, multicentre, open-label, phase 3 trial. *Lancet Oncol*. 2016;17(8):1070–1080. doi:10.1016/S1470-2045(16)30096-1
24. Senerchia AA, Macedo CR, Ferman S, et al. Results of a randomized, prospective clinical trial evaluating metronomic chemotherapy in nonmetastatic patients with high-grade, operable osteosarcomas of the extremities: A report from the Latin American Group of Osteosarcoma Treatment. *Cancer*. 2017;123(6):1003–1010. doi:10.1002/cncr.30411
25. Gaspar N, Occean BV, Pacquement H, et al. Results of methotrexate-etoposide-ifosfamide based regimen (M-EI) in osteosarcoma patients included in the French OS2006/sarcome-09 study. *Eur J Cancer*. 2018;88:57–66. doi:10.1016/j.ejca.2017.09.036
26. Meazza C, Scanagatta P. Metastatic osteosarcoma: A challenging multidisciplinary treatment. *Expert Rev Anticancer Ther*. 2016;16(5):543–556. doi:10.1586/14737140.2016.1168697
27. Zhang Y, Yang J, Zhao N, et al. Progress in the chemotherapeutic treatment of osteosarcoma. *Oncol Lett*. 2018;16(5):6228–6237. doi:10.3892/ol.2018.9434
28. Yu D, Zhang S, Feng A, et al. Methotrexate, doxorubicin, and cisplatin regimen is still the preferred option for osteosarcoma chemotherapy: A meta-analysis and clinical observation. *Medicine (Baltimore)*. 2019;98(19):e15582. doi:10.1097/MD.00000000000015582
29. Bacci G, Picci P, Ruggieri P, et al. Primary chemotherapy and delayed surgery (neoadjuvant chemotherapy) for osteosarcoma of the extremities. The Istituto Rizzoli Experience in 127 patients treated preoperatively with intravenous methotrexate (high versus moderate doses) and intraarterial cisplatin. *Cancer*. 1990;65(11):2539–2553. doi:10.1002/1097-0142(19900601)65:11<2539::AID-CNCR2820651125>3.0.CO;2-M
30. Comandone A, Passera R, Boglione A, Tagini V, Ferrari S, Cattel L. High dose methotrexate in adult patients with osteosarcoma: Clinical and pharmacokinetic results. *Acta Oncol*. 2005;44(4):406–411. doi:10.1080/02841860510029770
31. Fan XL, Cai GP, Zhu LL, Ding GM. Efficacy and safety of ifosfamide-based chemotherapy for osteosarcoma: A meta-analysis. *Drug Des Devel Ther*. 2015;9:5925–5932. doi:10.2147/DDDT.S91217
32. Luetke A, Meyers PA, Lewis I, Juergens H. Osteosarcoma treatment: Where do we stand? A state of the art review. *Cancer Treat Rev*. 2014;40(4):523–532. doi:10.1016/j.ctrv.2013.11.006
33. Isakoff MS, Bielack SS, Meltzer P, Gorlick R. Osteosarcoma: Current treatment and a collaborative pathway to success. *J Clin Oncol*. 2015;33(27):3029–3035. doi:10.1200/JCO.2014.59.4895

Evaluation of the parenchymal distribution of renal steatosis in chronic kidney disease using chemical shift magnetic resonance imaging

Hüseyin Aydın^{1,A–F}, Hasan Aydın^{2,A,C,E,F}, Adnan Karabrahimoğlu^{3,A,C,E,F}, Baris Afsar^{4,C,E,F}

¹ Department of Radiology, Faculty of Medicine, Suleyman Demirel University, Isparta, Turkey

² Department of Radiology, Ankara Oncology Training and Research Hospital, University of Health Sciences, Turkey

³ Department of Biostatistics, Faculty of Medicine, Suleyman Demirel University, Isparta, Turkey

⁴ Department of Nephrology, Faculty of Medicine, Suleyman Demirel University, Isparta, Turkey

A – research concept and design; B – collection and/or assembly of data; C – data analysis and interpretation;

D – writing the article; E – critical revision of the article; F – final approval of the article

Advances in Clinical and Experimental Medicine, ISSN 1899–5276 (print), ISSN 2451–2680 (online)

Adv Clin Exp Med. 2024;33(5):455–462

Address for correspondence

Hüseyin Aydın

E-mail: huseyinrad@yahoo.com

Funding sources

None declared

Conflict of interest

None declared

Acknowledgements

The authors would like to thank Ozgur Pirgon (Professor, Department of Pediatric Endocrinology and Diabetes, Faculty of Medicine, Suleyman Demirel University, Isparta, Turkey) and Uğur Toprak (Professor, Department of Radiology, Faculty of Medicine, Eskişehir Osmangazi University, Turkey) for careful reading of the manuscript and helpful comments and suggestions.

Received on December 14, 2022

Reviewed on February 7, 2023

Accepted on May 25, 2023

Published online on June 21, 2023

Cite as

Aydın H, Aydın H, Karabrahimoğlu A, Afsar B. Evaluation of the parenchymal distribution of renal steatosis in chronic kidney disease using chemical shift magnetic resonance imaging. *Adv Clin Exp Med.* 2024;33(5):455–462. doi:10.17219/acem/166512

DOI

10.17219/acem/166512

Copyright

Copyright by Author(s)

This is an article distributed under the terms of the Creative Commons Attribution 3.0 Unported (CC BY 3.0) (<https://creativecommons.org/licenses/by/3.0/>)

Abstract

Background. Renal steatosis is an abnormal accumulation of fat in the kidney and may cause chronic kidney disease (CKD) or CKD progression.

Objectives. This pilot study aimed to evaluate the quantitative measurability of the parenchymal distribution of lipid deposition in the renal cortex and medulla using chemical shift magnetic resonance imaging (MRI) and investigate its relationship with clinical stages in CKD patients.

Materials and methods. The study groups included CKD patients with diabetes (CKD-d) (n = 42), CKD patients without diabetes (CKD-nd) (n = 31) and control subjects (n = 15), all of whom underwent a 1.5T MRI of the abdomen using the Dixon two-point method. The fat fraction (FF) values in the renal cortex and medulla were calculated from measurements made on Dixon sequences, and then compared between the groups.

Results. The cortical FF value was higher than the medullary FF value in control (0.057 (0.053–0.064) compared to 0.045 (0.039–0.052)), CKD-nd (0.066 (0.059–0.071) compared to 0.063 (0.054–0.071)), and CKD-d (0.081 (0.071–0.091) compared to 0.069 (0.061–0.077)) groups (all p < 0.001). The CKD-d group cortical FF values were higher than those of the CKD-nd group (p < 0.001). The FF values began increasing at CKD stages 2 and 3, and reached statistical significance at stages 4 and 5 in CKD patients (p < 0.001).

Conclusions. Renal parenchymal lipid deposition can be quantified separately in the cortex and medulla using chemical shift MRI. Fat accumulation occurred in cortical and medullary parenchyma in CKD patients, though predominantly in the cortex. This accumulation increased proportionally with the disease stage.

Key words: magnetic resonance imaging, chemical shift imaging, chronic kidney disease, renal steatosis, fatty kidney disease

Background

Renal steatosis is an abnormal accumulation of intracellular triglycerides/lipids in the kidney, which may cause the development and/or progression of chronic kidney disease (CKD).^{1–3} Fatty acids accumulate as intracellular droplets and cause the release of toxic cytokines, resulting in interstitial fibrosis and loss of kidney function.^{4–6} Inspired by non-alcoholic fatty liver disease (NAFLD), the term “fatty kidney disease (FKD)” has been used recently in the literature.⁶ In this regard, the effects of intra-abdominal, perirenal and parenchymal fat deposits on the kidneys are evaluated, as well as the relationships between FKD and insulin resistance, type 2 diabetes, obesity, metabolic syndrome, hyperlipidemia, hypertension, NAFLD, and cardiovascular disorders.^{6–8}

To evaluate renal steatosis, parenchymal lipid accumulation must be quantitatively measured. The gold standard renal steatosis assessment method is a biopsy followed by quantitative enzymatic measurement of triglycerides and qualitative oil red O staining. However, these methods are invasive and can increase the risk of complications.⁹ Non-invasive lipid measurement is also possible using fatty tissue-sensitive chemical shift magnetic resonance imaging (MRI).^{10–12} Chemical shift imaging is an MRI technique for detecting small areas (voxels) that contain water and fat protons. In this technique, the difference in resonance between water and oil protons is used to obtain images, with images taken from the in-phase (IP) and out-of-phase (OP) times of water and fat protons. In voxels containing both water and fat, signal loss occurs in OP images, though voxels containing only fat or water protons have no signal difference between the OP and IP images.¹³ With the simple addition and subtraction of the 2 images, 1 image containing only water and 1 containing only fat can be obtained. The Dixon technique can be generally used for the suppression or quantification of fat in various types of pulse sequences and allows for the measurement of the fat–water fraction in a precise region of interest (ROI) with higher spatial resolution.^{14,15} A few molecular imaging studies have recently evaluated lipid accumulation in the kidneys.^{7,11,12,15–17} However, no study has separately evaluated lipid deposition in the cortical and medullary components of the parenchyma.

Objectives

This pilot study evaluated the quantitative measurability of cortical and medullary parenchymal lipid deposition in CKD patients using chemical shift MRI.

Materials and methods

The study was carried out as a retrospective archive search. It was conducted in accordance with the Declaration of Helsinki after obtaining approval from the Clinical

Research Local Ethics Committee of the Faculty of Medicine of Suleyman Demirel University (Isparta, Turkey; decision No. 14/210 issues on July 27, 2020).

Study setting and participants

Study subjects were selected randomly from patients registered in the picture archiving and communication system (PACS) of our hospital, who were treated and followed up with a diagnosis of CKD and/or diabetes between 2016 and 2020, and those who had an upper abdominal MRI examination for any reason. In total, 117 CKD patients followed up in the Department of Nephrology were considered eligible for the study. Patients younger than 18 years ($n = 2$) or with malignancy ($n = 2$), polycystic or multicystic kidney disease ($n = 5$), renal transplantation ($n = 2$), or chronic liver disease ($n = 9$) were excluded from the study. Patients were also excluded if they had insufficient data in PACS ($n = 13$) or artifacts on MRI that prevented measurement ($n = 11$). The remaining 73 CKD patients were divided into 2 subgroups based on the presence or absence of diabetes, including CKD patients with diabetes (CKD-d) ($n = 31$) and CKD patients without diabetes (CKD-nd) ($n = 42$). The presence of diabetes was determined using the patient’s history registered in the hospital PACS, the use of oral antidiabetic/insulin, or daily urine albumin level greater than 30 mg.¹⁸ The clinical staging of CKD was assigned according to the estimated glomerular filtration rate (eGFR),¹⁹ which was calculated using the CKD Epidemiology Collaboration (CKD-EPI) method.²⁰ The control group ($n = 15$) consisted of patients who underwent upper abdomen MRI for any reason other than kidney disease (such as liver hemangioma and gallbladder pathologies) and who, according to PACS data, did not have urinary disease, diabetes, malignancy, connective tissue disease, or chronic systemic disease. The final evaluation included 176 kidneys of 88 patients – 73 in the CKD group and 15 in the control group. All measurements required for fat fraction (FF) calculation from the renal cortical and medullary parenchyma were performed by a single radiologist (the corresponding author) with 10 years of abdominal MRI experience.

MRI examination parameters

Magnetic resonance imaging scans were obtained using a 1.5 Tesla unit (Magnetom Avanto; Siemens Medical Solutions, Erlangen, Germany) and a 16-channel body coil with the patient in supine position without sedation. Images were acquired as axial and coronal plane turbo spin-echo T2-weighted (TSE T2W) without fat saturation and breath-hold, and gradient-echo sequence fat saturated T1 volumetric interpolated breath-hold examination (VIBE), based on the Dixon two-point method and taken as IP and OP to detect intracellular lipid. The version of the VIBE-Dixon sequence applied in this study was a generic version

Table 1. Magnetic resonance examination parameters

Examination parameters	In-phase (IP)	Out-of-phase (OP)	Dixon Water (DW)	Dixon Fat (DF)
Voxel size [mm]	0.6 × 0.6 × 3	0.6 × 0.6 × 3	0.6 × 0.6 × 3	0.6 × 0.6 × 3
FOV [mm]	261 × 380	261 × 380	261 × 380	261 × 380
Matrix size [mm]	288 × 320	288 × 320	288 × 320	288 × 320
TR [ms]	7.08	7.08	7.1	7.1
TE [ms]	2.39	4.77	2.4	2.4
Flip angle [°]	10	10	10	10
Bandwidth [Hz/Px]	490	490	490	490
Slice thickness [mm]	3	3	3	3
NEX	1	1	1	1
Acquisition time [s]	16	16	16	16
Slice gap [mm]	20	20	20	20

FOV – field of view; TR – repetition time; TE – echo time; NEX – number of excitations.

rather than the modified quantitative Dixon sequence, so that IP, OP, water, fat, proton density fat fraction (PDFF), and T2* maps could be calculated. The chemical shift MRI examination parameters are presented in Table 1.

Evaluation of images and measurements

All images were evaluated using OsiriX MD v.10.0.2 software (General Public License (GPL) licensed free to access resource code and commercially licensed with US. Food and Drug Administration (FDA) approval; UCLA, Pixmeo, Bernex, Switzerland) on a MacOS-X radiology workstation (Apple Inc., Cupertino, USA). The measurements were performed by a single radiologist with 10 years of abdominal MRI experience. The intra-observer agreement values for measurements were found to be 0.918 (for cortical FF) and 0.956 (for medullary FF). Slices were evaluated on T2W images to exclude artifacts, space-occupying lesions or vascular pathologies. Measurements in the axial plane were made on Dixon Fat (DF) and Dixon Water (DW) sequences from the most appropriate single slice passing through the renal hilus level without any space-occupying lesions.

The ROI used for measurement in the DW sequence was placed using the copy–paste method in the same parenchymal location of the corresponding slice in the DF sequence so that the measurements were from the same location on both sequences, with the same ROI. Three measurements were taken using a 20-mm² circular ROI from the areas where the cortex and medulla meet, and then the average was calculated for analysis (Fig. 1). Renal FF values were calculated using the formula below¹³:

$$FF = [DF/(DF + DW)].$$

The sample size was found to be sufficient as a result of power analysis performed using the GPower 3.1.9.2 software (Kiel University, Kiel, Germany). The selected test family included F tests and fixed effects one-way analysis of variance (ANOVA). The effect size was calculated

as $d = 0.80$ using the measurements from the pilot study. The Type-I error rate and the power were considered 5% and 0.95, respectively. Therefore, the total sample size was determined as $n = 32$.

Statistical analyses

The statistical analyses employed IBM Statistical Package for Social Sciences (SPSS) v. 20.0 (IBM Corp., Armonk, USA) software. The continuous variables were expressed as mean with 95% confidence intervals (95% CIs), and the categorical variables as frequency (percentage (%)). The Shapiro–Wilk test assessed the normality of continuous variables. For comparisons between 2 independent groups, Student's t-test was applied with Welch robust correction test if the variances were not equal. One-way ANOVA with the Tamhane post hoc test was used for multiple groups since the variances were not homogenous, and the Brown–Forsythe robust correction test was applied to meet the assumptions of homogeneity. The receiver operating characteristic (ROC) analysis was performed, and the diagnostic ratios for sensitivity and specificity for cortical and medullary measurements were calculated. The intra-observer agreement was calculated using interclass correlation (ICC) with two-way mixed and average single-measure methods. There were no missing data in the dataset. A value of $p < 0.05$ was considered statistically significant.

Results

The evaluations included 176 kidneys of 88 adults (53.3% males, 46.7% females). The mean patient age was 59.28 ± 13.05 years in the CKD group and 55.41 ± 14.41 years in the control group ($p = 0.001$). Gender did not affect the FF values ($p > 0.05$).

The cortical FF values were significantly higher than the medullary FF in all groups ($p < 0.001$) (Table 2).

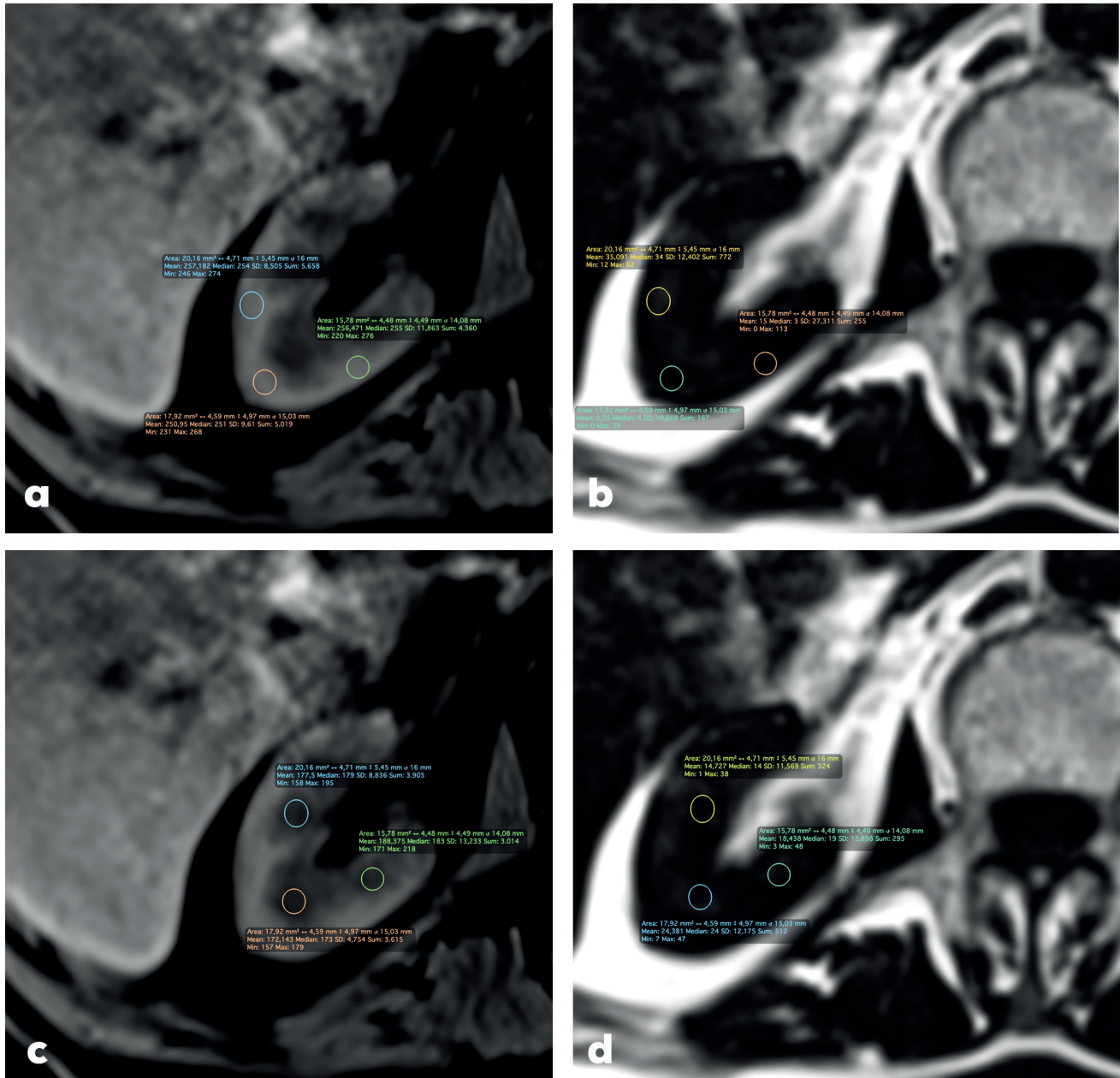


Fig. 1. Measurements recorded for Dixon Water (A) and Dixon Fat imaging (B) used to calculate cortical fat fraction (FF) values, and for Dixon Water (C) and Dixon Fat imaging (D) used to calculate medullary FF values

Table 2. Evaluation of the cortical and medullary distribution of renal lipid accumulation in the study groups

Study groups	n	Cortical FF	Medullary FF	Mean difference; t (Welch); df; p
		mean (95% CI)		
Control group	30	0.057 (0.053–0.064) ^a	0.045 (0.039–0.052) ^b	0.011; 5.022; 29; p < 0.001**
CKD patients	146	0.072 (0.064–0.078)	0.063 (0.054–0.071)	0.009; 4.103; 145; p < 0.001**
CKD without diabetic	84	0.066 (0.059–0.071)	0.058 (0.051–0.061)	0.007; 3.108; 83; p = 0.004**
CKD with diabetes	62	0.081 (0.071–0.091) ^a	0.069 (0.061–0.077) ^b	0.012; 3.172; 61; p = 0.002**
F_{contrast} ; df and p		5.081; df = 3 and p = 0.002*	6.753; df = 3 and p < 0.001*	–
Brown–Forsythe; df and p		10.444; df = 3 and p < 0.001*	78.435; df = 3 and p < 0.001*	–

* significant at p < 0.05 level according to one-way analysis of variance (ANOVA) with Brown–Forsythe robust correction test for heterogeneity of variances; H_0 – mean difference between the groups are the same; H_1 – at least 1 mean is different from other means; ** significant at p < 0.05 level according to t-test with Welch robust correction test for unequal variances; ^a the same superscript letters denote the significant pairwise comparison for the cortex fat fraction (FF) values between the study groups according to the Tamhane post hoc test; ^b the same symbols denote the significant pairwise comparison for the medullary FF values between the study groups according to the Tamhane post hoc test; CKD – chronic kidney disease; df – degrees of freedom; 95% CI – 95% confidence interval.

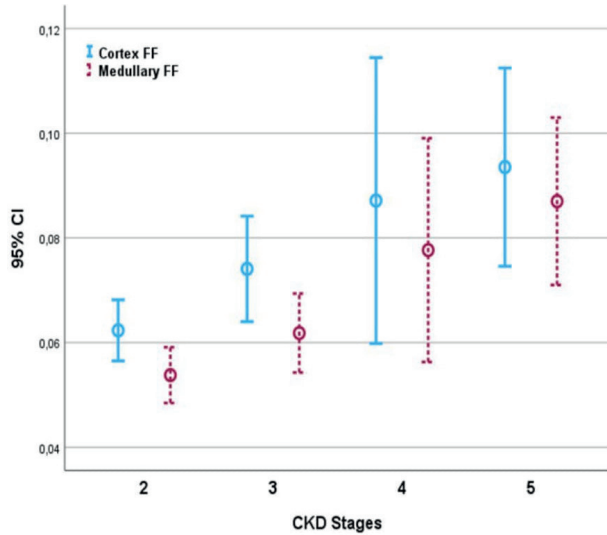


Fig. 2. Bar graph of the cortex and medulla fat fraction (FF) values with 95% confidence intervals (95% CIs) for chronic kidney disease (CKD) stages in all CKD patients (Brown–Forsythe = 3.817, degrees of freedom (df) = 3, 45.14; $p = 0.016$ for cortex FF with a significant Tamhane post hoc test result of comparison between stages 2 and 5 ($p = 0.021$); Brown–Forsythe = 6.318, $df = 3, 46.71$; $p = 0.001$ for medullary FF with a significant Tamhane post hoc test result of comparison between stages 2 and 5 ($p = 0.003$) and 3 and 5 ($p = 0.037$))

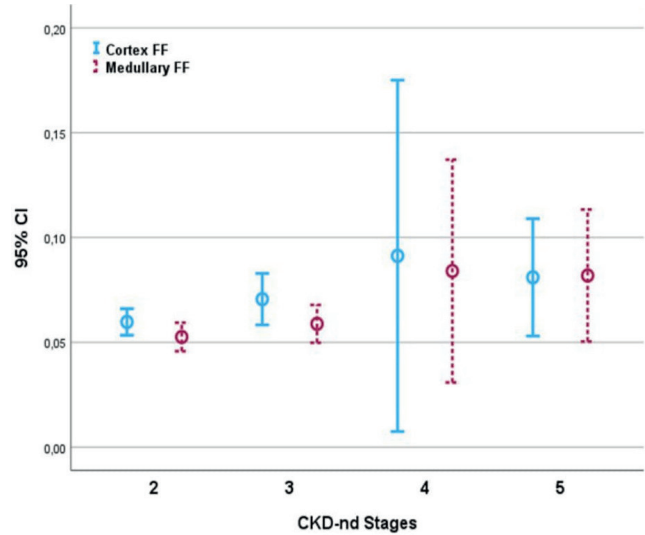


Fig. 4. Bar graph of the cortex and medulla fat fraction (FF) values with 95% confidence intervals (95% CIs) for chronic kidney disease (CKD) stages in non-diabetic chronic kidney disease (CKD-nd) patients (Brown–Forsythe = 2.954, degrees of freedom (df) = 3, 9.61; $p = 0.046$, for Cortex FF with significant a Tamhane post hoc test result of comparison between stages 2 and 5 ($p = 0.047$); Brown–Forsythe = 3.851, $df = 3, 12.83$; $p = 0.037$, for medullary FF with a significant Tamhane post hoc test result of comparison between stages 2 and 5 ($p = 0.040$))

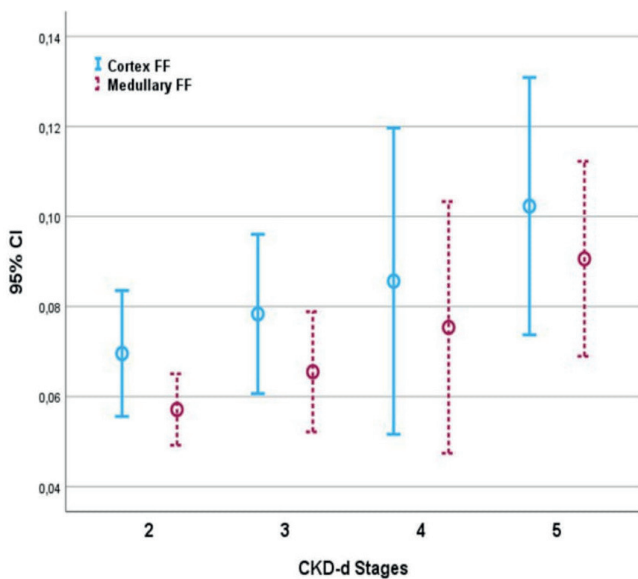


Fig. 3. Bar graph of the cortex and medulla fat fraction (FF) values with 95% confidence intervals (95% CIs) for chronic kidney disease (CKD) stages in diabetic chronic kidney disease (CKD-d) patients (Brown–Forsythe = 3.428, degrees of freedom (df) = 3, 34.73; $p = 0.038$, for Cortex FF with a significant Tamhane post hoc test result of comparison between stages 2 and 5 ($p = 0.037$); Brown–Forsythe = 4.634, $df = 3, 30.03$; $p = 0.043$, for medullary FF with a significant Tamhane post hoc test result of comparison between stages 2 and 5 ($p = 0.041$))

In the CKD-d patients, a significant increase was observed in the cortical FF values compared to the control subjects ($p < 0.001$). The medullary FF values in both CKD groups increased, but the values were significantly higher in the CKD-d group than in the control group ($p < 0.001$). However, in contrast to the CKD-d group, the elevated cortical and medullary FF values in the CKD-nd group

had no statistical significance compared to the control group ($p > 0.05$).

The cortical and medullary FF measurements in the CKD groups, based on the CKD stages, are presented in Fig. 2–4. There was no significant difference between the control group (healthy kidneys) and the CKD groups at stage 1 for cortical and medullary FF values ($p > 0.05$). When all CKD patients were considered as a single group, there was no significant difference between stage 1 and 2 cortical FF values. A statistically significant difference was determined in the cortical and medullary FF values at stage 2 compared to stage 5 values (cortex, $p = 0.021$; medulla, $p = 0.003$). In addition, there was a significant difference between stage 3 and stage 5 for medulla values ($p = 0.037$) (Fig. 2). In the CKD-d group, the cortical and medullary FF values increased with the clinical stage and reached statistical significance between stages 2 and 5 ($p = 0.037$ and $p = 0.041$, respectively) (Fig. 3). The cortical and medullary FF values in the CKD-nd group were similar to those of the CKD-d group, with statistical significance between stages 2 and 5 (cortex, $p = 0.047$; medulla, $p = 0.040$) (Fig. 4).

The ROC analysis showed a significant difference between the control and CKD-d patient groups with respect to the area under the curve (AUC) values for both cortical and medullary FF. The cutoff value of 0.076 for cortical FF had a sensitivity of 96.7%, while the cutoff value of 0.056 for medullary FF had better diagnostic ratios, as shown in Table 3.

The results of normality and homogeneity of variance assumptions with related tests are presented in Supplementary Table 1 (<https://doi.org/10.5281/zenodo.7961812>).

Table 3. Receiver operating characteristic (ROC) analysis results of cortical and medullary fat fraction (FF) values between the control group and diabetic chronic kidney disease (CKD-d) patients

FF measurements	Comparison group 1	Comparison group 2	AUC (95% CI)	p-value	Cutoff value	Sensitivity [%] (95% CI)	Specificity [%] (95% CI)
Cortical FF	control	CKD-d	0.699 (0.591–0.806)	0.002*	0.076	96.7 (91.05–99.24)	39.0 (29.40–49.27)
Medullary FF	control	CKD-d	0.768 (0.670–0.866)	<0.001*	0.056	83.3 (74.52–90.01)	61.7 (51.44–71.25)

* significant at 0.05 level according to ROC analysis; AUC – area under curve; 95% CI – 95% confidence interval.

Discussion

This study demonstrated for the first time the separate quantitative evaluation of parenchymal lipid deposition in the cortex and medulla and its relationship with the clinical stages of CKD using a radiological imaging method. We found that fat accumulation occurs in the cortex and medulla in CKD patients, predominantly in the cortex, and is positively correlated with the clinical stages of CKD. The importance of lipid accumulation in the cortex relative to the medulla in the early stages of diabetes demonstrated using MRI was consistent with the biopsy findings, suggesting that this technique is valid for measuring cortical and medullary lipid accumulation in the kidney. Previous histopathological studies have shown that parenchymal intracellular lipid deposition in CKD mainly occurs in the parts of the renal cortex containing the glomerulus and proximal tubules.^{21,22} Magnetic resonance imaging studies have demonstrated the presence of very little renal parenchymal lipid in healthy volunteers and an increase in the amount of lipid in the kidney parenchyma (without cortex/medulla distinction) in diabetic patients.^{11,17,23} However, as far as we know, an MRI study on the distribution of parenchymal lipid deposition in the cortex and medullary components in CKD patients, as well as on its relationship with clinical stages, has not yet been performed.

Cortical and medullary lipid depositions differed according to the CKD stage.^{24,25} At stage 1 CKD, there was no significant increase in the amount of parenchymal lipid, and the cortical and medullary lipid distributions were similar to those of the control group. In CKD patients, parenchymal lipids increased from stage 2 and reached a statistically significant level at stages 4 and 5. Although there was no statistical significance at stages 2 and 3, the FF increase was greater in the cortex than in the medulla. There was no significant difference between the cortex and medulla in lipid accumulation at stages 4 and 5, which suggests that parenchymal lipid accumulation is diffuse in advanced CKD. The detection of different amounts of lipid accumulation in parenchymal components in different clinical stages suggests that this novel technique presents a new area of research for experimental clinical and drug studies. If the technique proves useful, it can be applied free of charge to patients undergoing MRI for any reason, since chemical shift sequences are routinely obtained during abdominal MRI scans. In this regard, prospective multicenter studies can be conducted with larger patient groups to determine

cutoff values according to the clinical stages of CKD and test inter-observer and intra-observer reliability.

Renal lipid accumulation may develop independently of hyperglyceridemia.⁶ In the CKD-nd group, cortical and medullary FF values increased in parallel with the increase in the clinical stage, but no statistical significance was identified (Table 2). The possible reason for this discrepancy may be the lower number of stage 4 and 5 CKD patients in this group compared to those at stages 1 and 2.

The relationship between diabetes and renal parenchymal lipid accumulation is not clear. Some studies have reported that diabetes does not have a significant relationship with renal lipid accumulation.^{22,24} In contrast, other studies have reported a significant increase of renal lipid content in diabetes patients.^{11,17,23} Yokoo et al. conducted a study using 3T MRI, with measurements taken from an ROI through the whole parenchyma, and reported that the renal parenchyma FF rate (2.38%) was high in diabetes patients, independently of serum creatinine, body mass index (BMI) and Hb-A1c, and concluded that steatosis was an independent risk factor.¹¹ In the present study, the increase in FF values in CKD-d group was higher than in the CKD-nd group, and the cortical and medullary FF values increased in parallel with the increasing stage. This finding suggests that diabetes could have a triggering effect on lipid accumulation in patients with CKD. However, it would not be correct to make a conclusion regarding the impact of diabetes on renal steatosis based on the results of the current study. Indeed, this study only focused on measuring FF in the renal cortex and medulla in CKD, and there was no evaluation of other risk factors that may affect renal steatosis, such as diabetes severity and duration, concomitant hypertension, metabolic syndrome, or obesity.

Inspired by the concept of NAFLD, the term FKD has recently been proposed to express the local and systemic effects of ectopic fat accumulation. Within this concept, the renal effects of intra-abdominal, perirenal and parenchymal fat depositions are evaluated (albuminuria, CKD, and podocyte toxicity).⁷ Thus, as for NAFLD, it has been reported that renal steatosis can be treated as a separate disease or can be a part of a more extended metabolic disorder.^{6,7} Such a distinction is important for clinical purposes, and targeting metabolic disorders as a whole may also impact kidney structure and function. In this regard, it is crucial to evaluate if the medications for NAFLD can also decrease kidney lipid accumulation.⁸ Moreover, it is clinically important to investigate the relative impact of cortical

or medullary lipid accumulation. As this pilot study primarily aimed to measure fat accumulation quantitatively in the cortex and medulla but not to investigate the clinical significance of cortical and medullary fat accumulation, future studies are needed to highlight these issues. However, in contrast to NAFLD, in which fat accumulation is clearly evident, lipid accumulation in the kidney is scarce and sensitive techniques may be necessary to evaluate trace amounts of fat deposition, which may be clinically important.

Multiparametric renal MRI biomarkers have been developed and proposed for evaluating renal inflammation, oxidative stress, hypoxia, and fibrosis.^{26,27} However, a standard radiological approach that will contribute to the definition of FKD has not yet been developed.⁷ The present study showed that the addition of quantitative parenchymal FF measurements using chemical shift renal MRI could contribute to FKD understanding and development, though more studies are required to highlight the clinical importance of our findings.

Limitations

This study had several limitations. Selection bias is inherent to the retrospective design of the study. Although biopsy is the gold standard, it was not performed to measure the amount of fat in the renal parenchyma. However, the chemical shift MRI technique, which is accepted for assessing lipids in the liver, was used for the noninvasive measurement of the amount of renal parenchymal lipids. The diagnosis and staging of CKD were defined according to eGFR, though there is an increasing recognition that eGFR alone may not be specific to CKD, and the Kidney Disease: Improving Global Outcomes (KDIGO) recommendations suggest adding proteinuria to the classification.²⁶ Moreover, the study focused on quantifying fat accumulation in the renal cortex and medulla in patients with CKD and evaluating its relationship with the clinical stage. However, it may be interesting to investigate the relationship between renal parenchymal steatosis and parameters such as obesity, hypertension, metabolic syndrome, uric acid, insulin resistance, triglycerides, fasting blood glucose, and hemoglobin A1C (HbA1c) using this method. Also, the reliability of the measurements could not be evaluated, as they were made by a single observer. However, the measurements were reliable since the cortex and medulla are clearly distinguished in Dixon Water images, measurements are made from the same section and region with the cut–copy–paste technique, and the number and size of the measurements are standard.

Conclusions

Results of this study demonstrated that fat accumulation occurred in both the cortex and medulla, predominantly in the cortex of CKD patients, and correlated positively with the clinical stages of CKD. As such, FF measurements

using chemical shift MRI could be used as a radiological criterion for developing the FKD concept, since even very small cortical and medullary lipid deposits can be measured quantitatively. However, to validate these findings, there is a need for prospective multicenter trials with larger patient groups to determine cutoff values and test intra-observer and inter-observer reliabilities according to the clinical stages of CKD.

Supplementary data

The supplementary materials are available at <https://doi.org/10.5281/zenodo.7961812>. The package contains the following files:

Supplementary Table 1. The results of normality and variance homogeneity assumptions.

ORCID iDs

Hüseyin Aydın  <https://orcid.org/0000-0003-4704-4759>

Hasan Aydın  <https://orcid.org/0000-0002-8038-7035>

Adnan Karabrahimoğlu  <https://orcid.org/0000-0002-8277-0281>

Baris Afsar  <https://orcid.org/0000-0002-1369-3657>

References

- Escasany E, Izquierdo-Lahuerta A, Medina-Gomez G. Underlying mechanisms of renal lipotoxicity in obesity. *Nephron*. 2019;143(1):28–32. doi:10.1159/000494694
- Garofalo C, Borrelli S, Minutolo R, Chiodini P, De Nicola L, Conte G. A systematic review and meta-analysis suggests obesity predicts onset of chronic kidney disease in the general population. *Kidney Int*. 2017;91(5):1224–1235. doi:10.1016/j.kint.2016.12.013
- Foster MC, Hwang SJ, Porter SA, Massaro JM, Hoffmann U, Fox CS. Fatty kidney, hypertension, and chronic kidney disease: The Framingham Heart Study. *Hypertension*. 2011;58(5):784–790. doi:10.1161/HYPERTENSIONAHA.111.175315
- Restini CBA, Ismail A, Kumar RK, et al. Renal perivascular adipose tissue: Form and function. *Vasc Pharmacol*. 2018;106:37–45. doi:10.1016/j.vph.2018.02.004
- Simon N, Hertig A. Alteration of fatty acid oxidation in tubular epithelial cells: From acute kidney injury to renal fibrogenesis. *Front Med (Lausanne)*. 2015;2:52. doi:10.3389/fmed.2015.00052
- Mende CW, Einhorn D. Fatty kidney disease: A new renal and endocrine clinical entity? Describing the role of the kidney in obesity, metabolic syndrome, and type 2 diabetes. *Endocrine Pract*. 2019;25(8):854–858. doi:10.4158/EP-2018-0568
- Mende C, Einhorn D. Fatty kidney disease: The importance of ectopic fat deposition and the potential value of imaging. *J Diabetes*. 2022;14(1):73–78. doi:10.1111/1753-0407.13232
- Byrne CD, Targher G. NAFLD as a driver of chronic kidney disease. *J Hepatol*. 2020;72(4):785–801. doi:10.1016/j.jhep.2020.01.013
- Bobulescu IA. Renal lipid metabolism and lipotoxicity. *Curr Opin Nephrol Hypertens*. 2010;19(4):393–402. doi:10.1097/MNH.0b013e32833aa4ac
- Pacifico L, Nobili V, Anania C, Verdecchia P, Chiesa C. Pediatric nonalcoholic fatty liver disease, metabolic syndrome and cardiovascular risk. *World J Gastroenterol*. 2011;17(26):3082–3091. doi:10.3748/wjg.v17.i26.3082
- Yokoo T, Clark HR, Pedrosa I, et al. Quantification of renal steatosis in type II diabetes mellitus using dixon-based MRI. *J Magn Reson Imaging*. 2016;44(5):1312–1319. doi:10.1002/jmri.25252
- Klinkhammer BM, Lammers T, Mottaghy FM, Kiessling F, Floege J, Boor P. Non-invasive molecular imaging of kidney diseases. *Nat Rev Nephrol*. 2021;17(10):688–703. doi:10.1038/s41581-021-00440-4
- Dixon WT. Simple proton spectroscopic imaging. *Radiology*. 1984;153(1):189–194. doi:10.1148/radiology.153.1.6089263
- Lins CF, Salmon CEG, Nogueira-Barbosa MH. Applications of the Dixon technique in the evaluation of the musculoskeletal system. *Radiol Bras*. 2021;54(1):33–42. doi:10.1590/0100-3984.2019.0086

15. Jonker JT, De Heer P, Engelse MA, et al. Metabolic imaging of fatty kidney in diabetes: Validation and dietary intervention. *Nephrol Dial Transplant*. 2018;33(2):224–230. doi:10.1093/ndt/gfx243
16. Dekkers IA, De Heer P, Bizino MB, De Vries APJ, Lamb HJ. ¹H-MRS for the assessment of renal triglyceride content in humans at 3T: A primer and reproducibility study. *J Magn Reson Imaging*. 2018;48(2):507–513. doi:10.1002/jmri.26003
17. Sijens PE. MRI-determined fat content of human liver, pancreas and kidney. *World J Gastroenterol*. 2010;16(16):1993. doi:10.3748/wjg.v16.i16.1993
18. Kidney Disease: Improving Global Outcomes (KDIGO) CKD Work Group. Notice: KDIGO 2012 clinical practice guideline for the evaluation and management of chronic kidney disease. *Kidney Int Suppl*. 2013;3(1):1. doi:10.1038/kisup.2012.73
19. Kidney Disease: Improving Global Outcomes (KDIGO) CKD-MBD Work Group. KDIGO clinical practice guideline for the diagnosis, evaluation, prevention, and treatment of chronic kidney disease—mineral and bone disorder (CKD-MBD). *Kidney Int Suppl*. 2009;76(Suppl 113):S1–S2. doi:10.1038/ki.2009.188
20. Florkowski CM, Chew-Harris JS. Methods of estimating GFR: Different equations including CKD-EPI. *Clin Biochem Rev*. 2011;32(2):75–79. PMID:21611080.
21. Kim JJ, Wilbon SS, Fornoni A. Podocyte lipotoxicity in CKD. *Kidney360*. 2021;2(4):755–762. doi:10.34067/KID.0006152020
22. Bobulescu IA, Lotan Y, Zhang J, et al. Triglycerides in the human kidney cortex: Relationship with body size. *PLoS One*. 2014;9(8):e101285. doi:10.1371/journal.pone.0101285
23. Hammer S, De Vries APJ, De Heer P, et al. Metabolic imaging of human kidney triglyceride content: Reproducibility of proton magnetic resonance spectroscopy. *PLoS One*. 2013;8(4):e62209. doi:10.1371/journal.pone.0062209
24. Wang YC, Feng Y, Lu CQ, Ju S. Renal fat fraction and diffusion tensor imaging in patients with early-stage diabetic nephropathy. *Eur Radiol*. 2018;28(8):3326–3334. doi:10.1007/s00330-017-5298-6
25. Gai Z, Wang T, Visentin M, Kullak-Ublick G, Fu X, Wang Z. Lipid accumulation and chronic kidney disease. *Nutrients*. 2019;11(4):722. doi:10.3390/nu11040722
26. Selby NM, Blankestijn PJ, Boor P, et al. Magnetic resonance imaging biomarkers for chronic kidney disease: A position paper from the European Cooperation in Science and Technology Action PARENCHIMA. *Nephrol Dial Transplant*. 2018;33(Suppl 2):ii4–ii14. doi:10.1093/ndt/gfy152
27. Pruijm M, Mendichovszky IA, Liss P, et al. Renal blood oxygenation level-dependent magnetic resonance imaging to measure renal tissue oxygenation: A statement paper and systematic review. *Nephrol Dial Transplant*. 2018;33(Suppl 2):ii22–ii28. doi:10.1093/ndt/gfy243

Association between total cholesterol and all-cause mortality in geriatric patients with hip fractures: A prospective cohort study with 339 patients

Kun Li^D, Wen-Wen Cao^{C,E}, Shao-Hua Chen^{B,C}, Bin-Fei Zhang^{A-C,E,F}, Yu-Min Zhang^{A,E,F}

Department of Joint Surgery, Honghui Hospital, Xi'an Jiaotong University, China

A – research concept and design; B – collection and/or assembly of data; C – data analysis and interpretation; D – writing the article; E – critical revision of the article; F – final approval of the article

Advances in Clinical and Experimental Medicine, ISSN 1899–5276 (print), ISSN 2451–2680 (online)

Adv Clin Exp Med. 2024;33(5):463–471

Address for correspondence

Bin-Fei Zhang

E-mail: zhangbf07@gmail.com

Funding sources

This work was supported by the Foundation of Xi'an Municipal Health Commission (grant No. 2021ms10) and the Key Research and Development Program of Shaanxi Province (grants No. 2021SF-250 and No. 2022SF-377).

Conflict of interest

None declared

Acknowledgements

The authors thank Editage Academic Services (<http://www.editage.cn/>) for the English-language editing and review services.

Received on December 16, 2022

Reviewed on April 30, 2023

Accepted on July 19, 2023

Published online on August 18, 2023

Cite as

Li K, Cao WW, Chen SH, Zhang BF, Zhang YM. Association between total cholesterol and all-cause mortality in geriatric patients with hip fractures: A prospective cohort study with 339 patients. *Adv Clin Exp Med.* 2024;33(5):463–471. doi:10.17219/acem/169795

DOI

10.17219/acem/169795

Copyright

Copyright by Author(s)

This is an article distributed under the terms of the Creative Commons Attribution 3.0 Unported (CC BY 3.0) (<https://creativecommons.org/licenses/by/3.0/>)

Abstract

Background. Total cholesterol (TC) levels represent the comprehensive level of human cholesterol metabolism, which is closely related to the nutritional status, metabolic level, disease development, and aging of the human body. Total cholesterol plays an important role in the maintenance of bodily functions, regulation of sexual function, immune regulation, and in the development of organisms. Abnormal TC levels are an important risk factor for cardiovascular disease (CVD), and TC is closely related to the development of many diseases, and is used as an important indicator of human blood lipid levels and overall health status. However, the relationship between serum TC levels and the prognosis of patients with hip fractures remains unclear.

Objectives. To evaluate the association between TC levels and all-cause mortality in patients with geriatric hip fractures.

Materials and methods. Elderly patients with hip fractures were screened between January 2015 and September 2019. Patient demographic and clinical characteristics were recorded. Linear multivariate Cox regression models were used to identify the association between TC levels and all-cause mortality. Analyses were performed using Empower Stats and R software.

Results. Three hundred and thirty-nine patients were enrolled. The mean follow-up period was 34.18 months. There were 99 (29.20%) cases of all-cause mortality. Total cholesterol levels after hip fracture were linearly associated with all-cause mortality in the elderly. Linear multivariate Cox regression models showed that TC levels were associated with mortality (hazard ratio (HR) = 0.67; 95% confidence interval (95% CI): 0.53–0.85; $p = 0.001$ after adjusting for confounding factors). Each 1 mmol/L increase in TC levels was associated with a 33% reduction in morbidity and mortality. Compared with the low-TC group, mortality was significantly lower in the middle-TC group (HR = 0.58; 95% CI: 0.35–0.94; $p = 0.027$) and high-TC group (HR = 0.45; 95% CI: 0.27–0.75; $p = 0.002$).

Conclusions. Total cholesterol levels were associated with mortality in geriatric hip fracture patients and could be considered a protective factor for all-cause mortality.

Key words: all-cause mortality, hip fractures, total cholesterol

Background

Hip fractures in elderly patients are one of the most common and severe types of osteoporotic fractures, occurring overwhelmingly in adults over the age of 70.¹ The incidence of hip fractures in the elderly increases with age, and is as high as 7% for those occurring within 10 years in the aging population aged 75–84 years.² The risk of death in older people with hip fractures is 6.8 times higher than that in people of the same age without fractures.³ It is predicted that by 2050, approx. 52% (3.3 million) of hip fracture cases worldwide will occur in Asian countries, particularly in China.^{4,5} The burden of hip fractures is expected to rise owing to the increase in the elderly population,⁶ and the resulting medical costs in China will reach 85 billion USD.³ Hip fractures pose a serious threat to the quality of life and life expectancy of the elderly population owing to their high prevalence and disability and mortality rates.⁷

In recent years, several scholars have analyzed the factors affecting the prognosis of hip fractures in elderly patients and concluded that sex, age, American Society of Anesthesiologists (ASA) classification, number of underlying medical conditions, preoperative waiting time, preoperative hemoglobin values, and albumin values are independent risk factors affecting the postoperative prognosis of elderly hip fracture patients.⁸

Total cholesterol (TC) levels represent the comprehensive level of human cholesterol metabolism, which is closely related to the nutritional status, metabolic level, disease development, and aging of the human body.⁹ Total cholesterol plays an important role in the maintenance of bodily functions, regulation of sexual functions, immune regulation, and in the development of organisms. Abnormal TC levels are an important risk factor for cardiovascular disease (CVD); therefore, TC is closely related to the development of many diseases,^{10,11} and is used as an important indicator of human blood lipid levels and overall health status. Current research suggests that lipids and other nutrient metabolites are associated with the incidences of osteoporosis and osteoporotic fractures.¹² Tankó et al. found that changes in hip bone mineral density (BMD) were closely related to TC levels and that these changes were a good predictor of atherosclerosis incidence.¹³ Related studies have shown that serum TC levels are positively correlated with overall bone density in the intertrochanteric space, greater trochanter, femoral neck, and hip.¹⁴ Other studies support the association between BMD in various parts of the hip and blood lipids.^{15,16} Few studies on lipid levels and hip BMD levels suggest that the conversion of nutrient metabolites *in vivo* may have an impact on the metabolism and deposition of bone mineral salts. In a study on independent risk factors for osteoporotic fractures of the hip, Yamaguchi et al. concluded that decreased TC levels were an independent risk factor for fracture.¹⁷ Dyslipidemia occurs when TC levels are elevated, possibly contributing

to the development of osteoporosis by inhibiting the expression of the osteogenic gene zinc finger structural transcription factor (Osterix) and dwarf-related transcription factor 2 (Runx2) through the BMP-Smad signaling pathway, and this mechanism reduces osteoblastic activity.¹⁸ Moreover, abnormal TC levels may differentiate stem cells in the bone marrow into lipogenic precursor cells, reduce the number of osteogenic precursor cells, and aggravate osteoporosis.¹⁹

Objectives

The relationship between serum TC levels and the prognosis of patients with hip fractures remains unclear. Therefore, the present study assessed the influence of serum TC levels on patient mortality over a long-term follow-up period. We hypothesized that there would be a linear association between TC levels and mortality. This prospective cohort study aimed to identify the role of TC levels in the incidence of hip fractures.

Materials and methods

Study design

We recruited elderly patients who had a hip fracture between January 1, 2015, and September 30, 2019, at the largest trauma center in Northwest China (Honghui Hospital in X'ian). This prospective study was approved by the Ethics Committee of Honghui Hospital (approval No. 202201009). All procedures involving human participants were performed in accordance with the 1964 Declaration of Helsinki and its later amendments. The study flow diagram is shown in Fig. 1.

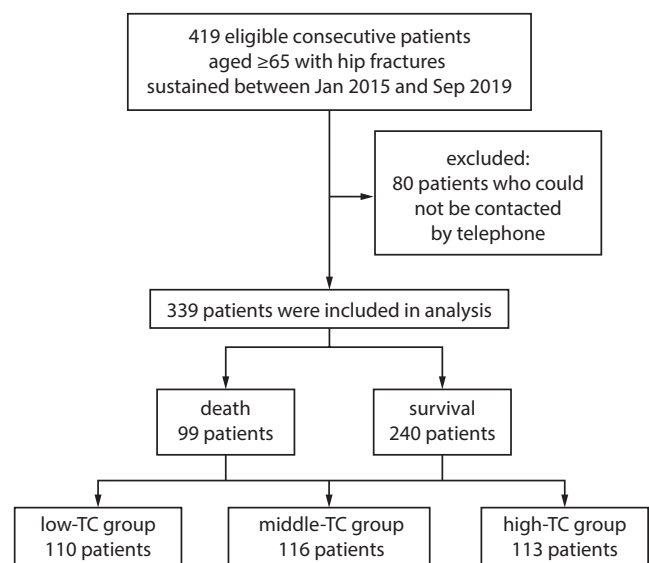


Fig. 1. Study flow diagram

Participants

The demographic and clinical data of patients were obtained from their original medical records. The inclusion criteria were as follows: 1) age ≥ 65 years, 2) radiographic or computed tomography (CT) diagnosis of a femoral neck, intertrochanteric or subtrochanteric fracture, 3) receiver of surgical or conservative treatment in a hospital, 4) availability of clinical data in the hospital, and 5) availability and ability to be contacted by telephone. Patients who could not be contacted were excluded.

Setting

Patients were examined using blood tests and ultrasonography during preparation for surgery. Intertrochanteric fractures are often managed with closed/open reduction and internal fixation (ORIF) using a proximal femoral nail anti-rotation implant. Femoral neck fractures were often treated with hemiarthroplasty or total hip arthroplasty, depending on the patient's age. Prophylaxis for deep vein thrombosis was initiated on admission. Upon discharge, the patients were asked to return monthly to assess the fracture union and orthopedic function.

Variables

Variables in our study were as follows: age, sex, occupation, history of allergy, injury mechanism, fracture classification, presence of hypertension, diabetes, coronary heart disease (CHD), arrhythmia, hemorrhagic stroke, ischemic stroke, cancer, multiple injuries, dementia, chronic obstructive pulmonary disease (COPD), hepatitis or gastritis, age-adjusted Charlson comorbidity index (aCCI), time from injury to admission, time from admission to operation, TC levels, operation time, blood loss, infusion, transfusion, treatment strategy, length in hospital stay, and length of follow-up.

Data sources and measurement

After discharge, the patient's family members were contacted by telephone from January 2022 to March 2022 to record data on the patient's survival, survival time and activities of daily life.

Bias

Follow-up was conducted by 2 medical professionals with 2 weeks of training and 1 year of experience. Patients who could not be contacted initially were attempted to be contacted 2 times more. When the family members of the patients did not respond, the patients were considered lost to follow-up.

Study size

We recruited elderly patients who had a hip fracture between January 1, 2015, and September 30, 2019.

Quantitative variables

Total cholesterol levels were defined using blood test results at admission. The dependent variable was all-cause mortality, whereas the independent variable was the TC level. The other variables were potential confounding factors. The endpoint event in this study was all-cause mortality after treatment. All-cause mortality was defined as mortality reported by the patient's family members.

Statistics analyses

Continuous variables were reported as mean \pm standard deviation ($M \pm SD$, Gaussian distribution) or median (range, skewed distribution). Categorical variables are presented as numbers with proportions. A χ^2 (categorical variables), one-way analysis of variance (ANOVA, normal distribution) or Kruskal–Wallis H test (skewed distribution) were used to detect the differences between TC levels. Proportional hazard assumptions were checked graphically and with the Schoenfeld residual test. Multicollinearity was checked using the variance inflation factor (VIF). Univariate and multivariate Cox proportional hazards regression models (3 models) were used to test the association between TC levels and mortality. Model 1 was not adjusted for covariates, model 2 was a minimally adjusted model, with adjusted sociodemographic variables, and model 3 was fully adjusted for all covariates (Table 1). For the Cox regression model, we used the concordance index to assess the goodness-of-fit. To test the robustness of our results, a sensitivity analysis was performed. We converted the TC levels into categorical variables according to the anemia criteria and calculated the p-value for the trend to verify the results. Since Cox proportional hazards regression model-based methods are often unable to study nonlinear models, the nonlinearity between TC levels and mortality was accounted for using a Cox proportional hazards regression model with cubic spline functions and smooth curve fitting (penalized spline method). In the spline analysis, a restricted cubic spline transformation of TC with 4 knots (25th, 50th, 75th, and 95th percentiles in all participants) was used to evaluate nonlinear associations. If nonlinearity was detected, we first calculated the inflection point using a recursive algorithm, and subsequently constructed a 2-piecewise Cox proportional hazards regression model on both sides of the inflection point.

All analyses were performed using statistical software packages R (R Foundation for Statistical Computing,

Table 1. The demographic and clinical characteristics of the study group (n = 339)

TC tertiles	Low	Middle	High	p-value
Number of participants	110	116	113	–
TC [mmol/L]	3.0 (2.8, 3.2)	3.8 (3.6, 4.0)	4.7 (4.5, 5.2)	<0.001*
Age [years]	81.0 (77.0, 86.0)	80.0 (76.0, 85.0)	79.0 (74.0, 83.0)	0.012*
Gender				
Male	55 (50%)	37 (31.90%)	20 (17.70%)	<0.001
Female	55 (50%)	79 (68.10%)	93 (82.30%)	
Injury mechanism				
Falling	104 (94.55%)	114 (98.28%)	112 (99.12%)	0.076*
Accident	4 (3.64%)	0 (0.00%)	1 (0.88%)	
Other	2 (1.82%)	2 (1.72%)	0 (0.00%)	
Fracture classification				
Intertrochanteric fracture	87 (79.09%)	84 (72.41%)	68 (60.18%)	0.031*
Femoral neck fracture	21 (19.09%)	30 (25.86%)	41 (36.28%)	
Subtrochanteric fracture	2 (1.82%)	2 (1.72%)	4 (3.54%)	
Hypertension				
No	52 (47.27%)	43 (37.07%)	48 (42.48%)	0.299
Yes	58 (52.73%)	73 (62.93%)	65 (57.52%)	
Diabetes				
No	93 (84.55%)	92 (79.31%)	84 (74.34%)	0.17
Yes	17 (15.45%)	24 (20.69%)	29 (25.66%)	
CHD				
No	52 (47.27%)	65 (56.03%)	56 (49.56%)	0.39
Yes	58 (52.73%)	51 (43.97%)	57 (50.44%)	
Arrhythmia				
No	62 (56.36%)	92 (79.31%)	87 (76.99%)	<0.001
Yes	48 (43.64%)	24 (20.69%)	26 (23.01%)	
Hemorrhagic stroke				
No	107 (97.27%)	114 (98.28%)	109 (96.46%)	0.71*
Yes	3 (2.73%)	2 (1.72%)	4 (3.54%)	
Ischemic stroke				
No	63 (57.27%)	78 (67.24%)	78 (69.03%)	0.142
Yes	47 (42.73%)	38 (32.76%)	35 (30.97%)	
Cancer				
No	107 (97.27%)	113 (97.41%)	110 (97.35%)	0.999*
Yes	3 (2.73%)	3 (2.59%)	3 (2.65%)	
Multiple injuries				
No	101 (91.82%)	111 (95.69%)	107 (94.69%)	0.443
Yes	9 (8.18%)	5 (4.31%)	6 (5.31%)	
Dementia				
No	103 (93.64%)	110 (94.83%)	107 (94.69%)	0.914
Yes	7 (6.36%)	6 (5.17%)	6 (5.31%)	

TC tertiles	Low	Middle	High	p-value
COPD				
No	104 (94.55%)	108 (93.10%)	109 (96.46%)	0.525
Yes	6 (5.45%)	8 (6.90%)	4 (3.54%)	
Hepatitis				
No	107 (97.27%)	114 (98.28%)	112 (99.12%)	0.536*
Yes	3 (2.73%)	2 (1.72%)	1 (0.88%)	
Gastritis				
No	107 (97.27%)	115 (99.14%)	110 (97.35%)	0.575*
Yes	3 (2.73%)	1 (0.86%)	3 (2.65%)	
aCCI	4.0 (4.0, 5.0)	4.0 (4.0, 5.0)	4.0 (4.0, 5.0)	0.14*
Treatment strategy				
Conservation	12 (10.91%)	3 (2.59%)	8 (7.08%)	0.02
ORIF	76 (69.09%)	83 (71.55%)	63 (55.75%)	
HA	22 (20.00%)	29 (25.00%)	41 (36.28%)	
THA	0 (0.00%)	1 (0.86%)	1 (0.88%)	
Time to admission [h]	24.0 (5.0, 72.0)	12.5 (4.0, 72.0)	13.0 (4.0, 24.0)	0.308*
Time to operation [days]	4.0 (3.0, 6.0)	4.0 (3.0, 6.0)	4.0 (3.0, 5.0)	0.355*
Operation time [min]	90.0 (75.0, 120.0)	90.0 (80.0, 120.0)	90.0 (77.5, 112.5)	0.372*
Blood loss [mL]	200.0 (150.0, 300.0)	200.0 (150.0, 300.0)	200.0 (150.0, 300.0)	0.973*
Infusion [mL]	1600 (1100, 1700)	1600 (1500, 1600)	1600 (1600, 1600)	0.725*
Transfusion [U]	2.0 (0.0, 2.0)	0.0 (0.0, 2.0)	0.0 (0.0, 2.0)	0.034*
Hospital stay [days]	8.0 (6.0, 10.1)	8.0 (6.7, 10.0)	7.8 (5.9, 9.4)	0.257*
Follow-up [months]	30.0 (21.9, 37.6)	35.5 (29.1, 44.8)	35.1 (29, 42.4)	0.001*
Mortality				
Survival	62 (56.36%)	88 (75.86%)	90 (79.65%)	<0.001
Death	48 (43.64%)	28 (24.14%)	23 (20.35%)	

Data are presented as median (Q1, Q3)/n (%). * For continuous variables, we used the Kruskal–Wallis rank-sum test, while Fisher's exact probability test was used for count variables with a theoretical number <10. TC – total cholesterol; CHD – coronary heart disease; COPD – chronic obstructive pulmonary disease; aCCI – age-adjusted Carlson comorbidity index; ORIF – open reduction and internal fixation; HA – hemiarthroplasty; THA – total hip arthroplasty.

Vienna, Austria), SAS 9.4 (SAS Institute Inc., Cary, USA) and EmpowerStats (X&Y Solutions Inc., Boston, USA). Hazard ratios (HRs) with 95% confidence intervals (95% CIs) were calculated. A 2-sided $p < 0.05$ was considered statistically significant.

Results

Patient characteristics

Three hundred and thirty-nine patients were enrolled in our study. The mean follow-up period was 34.18 months. There were 99 (29.20%) cases of all-cause mortality. The patients were divided into 3 groups according to TC levels: low-TC group, middle-TC group and high-TC group. Results of normality tests are presented in Supplementary Table 1; continuous variables were non-normally distributed according to the results of Shapiro–Wilk test. Table 1 lists the demographic and clinical characteristics of the patients, including their comorbidities, factors associated with injuries, and treatment.

Univariate analysis of the association between variates and mortality

We performed a univariate analysis to identify the potential confounding factors and the relationship between variables and mortality (Table 2). Owing to $p < 0.1$, the following variables were considered in the multivariate Cox regression analysis: age, CHD, arrhythmia, dementia, treatment strategy, and aCCI.

Multivariate analysis between TC and mortality

We used 3 models (Table 3) to correlate the TC levels and mortality. When the concentration of TC was variable, a linear regression was observed. The fully adjusted model showed a 33% decrease in the mortality risk when the TC concentration increased by 1 mmol/L after controlling for confounding factors (HR = 0.67; 95% CI: 0.53–0.85; $p = 0.001$). The concordance index was 0.70 (95% CI: 0.65–0.75), indicating that the Cox regression model was adequate. When the TC concentration was used as a categorical variable, there were statistically significant differences in TC levels among the 3 models ($p < 0.001$). Moreover, the p -value for the trend also showed a linear correlation in the 3 models ($p < 0.001$). The restricted cubic spline regression revealed no significant nonlinear associations between TC and mortality (Supplementary Fig. 1), and none of the predictors violated the proportional hazards assumption (Supplementary Table 2). The Kaplan–Meier survival curves in the 3 groups are depicted in Fig. 2.

Discussion

We found a linear correlation between TC levels and all-cause mortality after hip fracture in older adults. A higher TC was associated with lower mortality (HR = 0.67; 95% CI: 0.53–0.85; $p = 0.0012$), suggesting that each 1 mmol/L

increase in TC was associated with a 33% reduction in the mortality rate. Compared to the low-TC group, the middle-TC group had a significantly lower mortality rate (HR = 0.58; 95% CI: 0.35–0.94; $p = 0.027$), and the high-TC group had a significantly lower mortality rate (HR = 0.45; 95% CI: 0.27–0.75; $p = 0.002$). Moreover, the results were stable in the trend test (p -value for trend). In clinical practice, the patient's TC levels at admission could be used as a predictor of all-cause mortality in the mid-clinical course of hip fractures in elderly patients, and a higher TC level is associated with lower mortality.

Serum TC has been shown to be a protective factor not only for vascular-related diseases but also for osteoporotic fractures. An indirect association between TC and BMD has been demonstrated, and BMD is considered an important determinant of osteoporotic fractures.^{20–24} Total cholesterol concentration can be identified as an independent risk factor for osteoporotic fractures, and its predictive power increases over time.²⁵ Hypercholesterolemia has been reported to be a risk factor for atherosclerosis in patients with CHD.²⁶ It also increases bone loss in postmenopausal women.²⁷ Several studies have confirmed that elevated TC levels leading to hyperlipidemia may also induce bone loss and osteoporosis by affecting the function and differentiation of osteoblasts and osteoclasts.^{28,29} However, the interrelationship between serum cholesterol and osteoporosis fractures is still controversial.³⁰ This study is the first to prospectively examine the relationship between TC levels at admission and hip fracture prognosis.

Being a lipid-like substance, TC is an important component of the cell and organelle membranes, comprising approx. 30% of the cell membrane lipids, maintains the fluidity of the cell membrane, and facilitates the exchange of substances and information inside and outside the cell membrane. Simultaneously, TC is involved in the synthesis of bile acids and steroid hormones, and plays an important role in the formation and development of the nervous system. Importantly, the results of several studies have shown that low TC levels may cause mental and neurological symptoms such as irritability, cognitive impairment, memory impairment, dementia,^{31–33} and ultimately an increased risk of death.³⁴ In other words, the risk of death decreases with elevated TC levels. The relationship between abnormal serum lipid levels and cognition, memory and other functions in the elderly may result from amyloid deposition in the brain and the development of cerebrovascular disease.^{35–37} In contrast, high-density lipoprotein is a component of TC. A study by Yang et al. established a multivariate Cox regression model to analyze the 90-day postoperative all-cause mortality and reported that high-density lipoprotein (HDL) was an independent protective factor for postoperative death in elderly patients with intertrochanteric fractures (HR = 0.41).³⁸

Table 2. Effects of factors on mortality measured using univariate analysis (n = 339)

Factor	Statistics	HR (95% CI)	p-value
TC [mmol/L]	3.8 (3.2, 4.5)	0.60 (0.47, 0.77)	<0.001
Age [years]	80.0 (76.0, 85.0)	1.07 (1.04, 1.11)	<0.001
Sex			
Male	112 (33.04%)	1	–
Female	227 (66.96%)	0.74 (0.49, 1.11)	0.146
Injury mechanism			
Falling	330 (97.35%)	1	–
Accident	5 (1.47%)	0.60 (0.08, 4.32)	0.613
Other	4 (1.18%)	3.81 (1.20, 12.06)	0.023
Fracture classification			
Intertrochanteric fracture	239 (70.50%)	1	–
Femoral neck fracture	92 (27.14%)	0.74 (0.46, 1.19)	0.212
Subtrochanteric fracture	8 (2.36%)	0.68 (0.17, 2.76)	0.587
Hypertension			
No	143 (42.18%)	1	–
Yes	196 (57.82%)	0.76 (0.51, 1.13)	0.179
Diabetes			
No	269 (79.35%)	1	–
Yes	70 (20.65%)	1.18 (0.75, 1.87)	0.479
CHD			
No	173 (51.03%)	1	–
Yes	166 (48.97%)	1.62 (1.08, 2.42)	0.019
Arrhythmia			
No	241 (71.09%)	1	–
Yes	98 (28.91%)	1.95 (1.30, 2.90)	0.001
Hemorrhagic stroke			
No	330 (97.35%)	1	–
Yes	9 (2.65%)	0.29 (0.04, 2.07)	0.216
Ischemic stroke			
No	219 (64.60%)	1	–
Yes	120 (35.40%)	1.10 (0.73, 1.66)	0.6349

In addition to the linear relationship, we also speculated about the possibility of a curvilinear relationship based on a subgroup analysis and curve fitting. However, no inflection point on the curve was found in this study. Currently, in the context of this field, a linear relationship is more appropriate for explaining the relationship between TC and mortality.

To identify the confounding factors and draw reliable conclusions from this study, we first identified factors affecting the prognosis and TC levels. Age, sex, CHD, arrhythmia, dementia, and treatment strategy have been reported in previous studies as risk factors for hip fracture prognosis.^{39–43} Thus, we controlled for the vast majority of these confounding factors.

Factor	Statistics	HR (95% CI)	p-value
Cancer			
No	330 (97.35%)	1	–
Yes	9 (2.65%)	1.23 (0.39, 3.87)	0.729
Multiple injuries			
No	319 (94.10%)	1	–
Yes	20 (5.90%)	0.69 (0.25, 1.88)	0.467
Dementia			
No	320 (94.40%)	1	–
Yes	19 (5.60%)	2.60 (1.39, 4.87)	0.003
COPD			
No	321 (94.69%)	1	–
Yes	18 (5.31%)	1.00 (0.41, 2.46)	0.999
Hepatitis			
No	333 (98.23%)	1	–
Yes	6 (1.77%)	0.53 (0.07, 3.79)	0.526
Gastritis			
No	332 (97.94%)	1	–
Yes	7 (2.06%)	0.84 (0.21, 3.41)	0.806
aCCI	4.0 (4.0, 5.0)	1.38 (1.16, 1.63)	0.001
Time to admission [h]	19.0 (4.0, 72.0)	1.00 (1.00, 1.00)	0.791
Time to operation [days]	4.0 (3.0, 6.0)	0.97 (0.88, 1.07)	0.501
Treatment strategy			
Conservation	23 (6.78%)	1	–
ORIF	222 (65.49%)	0.25 (0.15, 0.44)	<0.001
HA	92 (27.14%)	0.25 (0.13, 0.48)	<0.001
THA	2 (0.59%)	0.00 (0.00, 0.00)	0.994
Operation time [min]	90.0 (80.0, 120.0)	1.00 (1.00, 1.01)	0.748
Blood loss [mL]	200.0 (150.0, 300.0)	1.00 (1.00, 1.00)	0.245
Infusion [mL]	1600 (1300, 1600)	1.00 (1.00, 1.00)	0.368
Transfusion [U]	0.0 (0.0, 2.0)	1.04 (0.88, 1.23)	0.653
Stay in hospital [days]	7.9 (6.1, 9.9)	1.02 (0.96, 1.09)	0.485

HR – hazard ratio; 95% CI – 95% confidence interval; TC – total cholesterol; CHD – coronary heart disease; COPD – chronic obstructive pulmonary disease; aCCI – age-adjusted Carlson comorbidity index; ORIF – open reduction and internal fixation; HA – hemiarthroplasty; THA – total hip arthroplasty.

Limitations of the study

This study has a few limitations. First, because our study was prospectively designed, a certain amount of loss to follow-up was unavoidable. To determine the prognosis of patients, we conducted several telephone follow-ups with patients or their family members when the patients did not respond the first time. Second, we were unable to determine the causal relationship between TC levels and prognosis, which needs to be confirmed in future studies. Third,

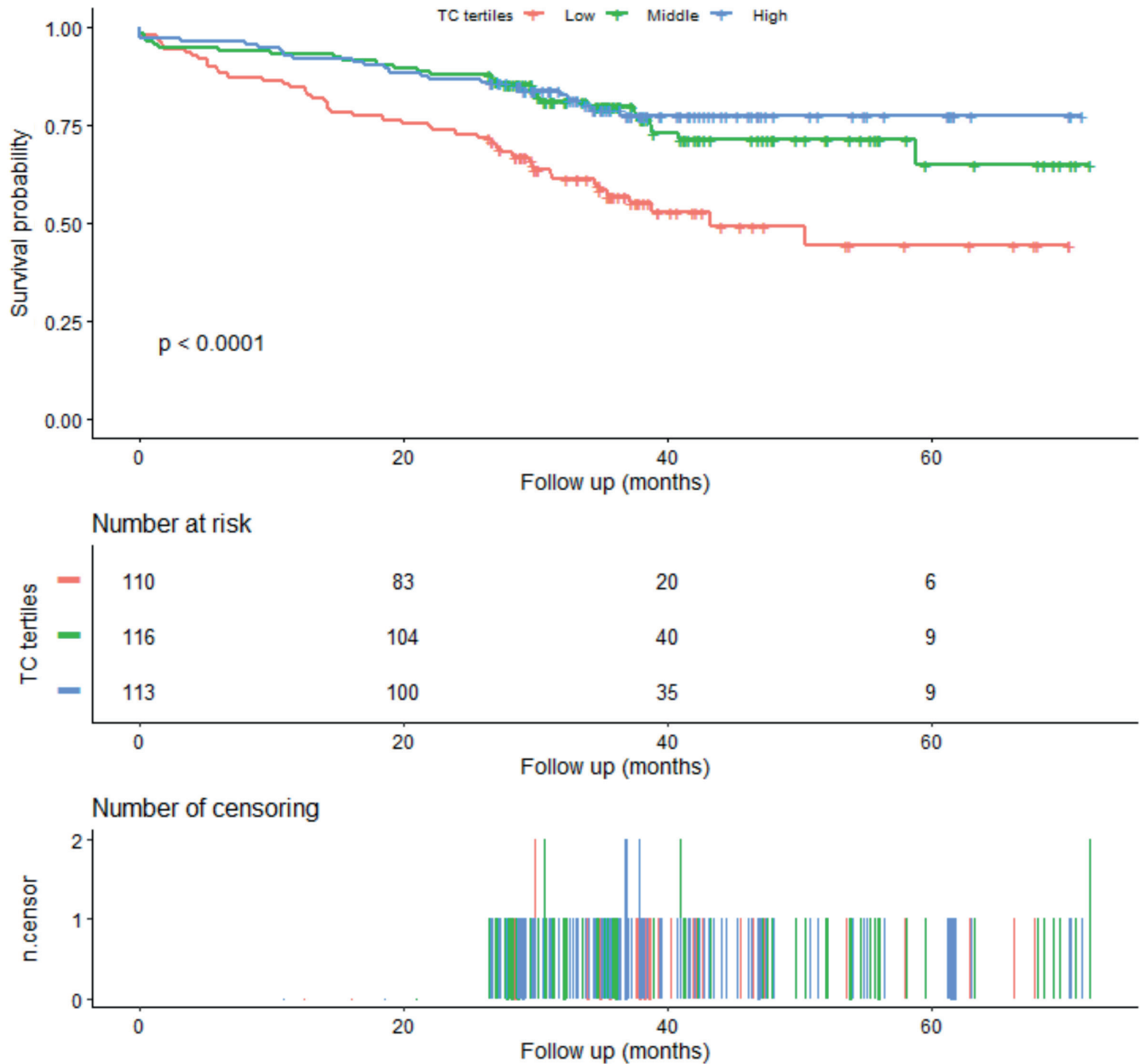


Fig. 2. Kaplan–Meier survival according to the levels of TC
TC – total cholesterol.

Table 3. Univariate and multivariate results following Cox regression (n = 339)

Exposure	Non-adjusted model	Minimally adjusted model	Fully adjusted model
TC	0.60 (0.47, 0.77); <math>< 0.001</math>	0.65 (0.50, 0.84); 0.001	0.67 (0.53, 0.85); 0.001
TC tertiles			
Low	Ref	Ref	Ref
Middle	0.45 (0.28, 0.73); 0.009	0.50 (0.31, 0.81); 0.005	0.58 (0.35, 0.94); 0.027
High	0.39 (0.24, 0.64); 0.002	0.46 (0.27, 0.79); 0.004	0.45 (0.27, 0.75); 0.002
p-value for trend	<math>< 0.001</math>	0.003	0.002

Data are presented as HR (95% CI) and p-value. The outcome variable was mortality, while the exposed variable was TC. Data were minimally adjusted for age and sex. Fully adjusted model was used for age, sex, CHD, arrhythmia, dementia, treatment strategy, and aCCI. HR – hazard ratio; 95% CI – 95% confidence interval; TC – total cholesterol; CHD – coronary heart disease; aCCI – age-adjusted Carlson comorbidity index.

our study population was from Western China, which has geographical and ethnic limitations. The generalizability of the conclusions of this study should be treated carefully.

Conclusions

In summary, TC levels were associated with all-cause mortality in patients with geriatric hip fractures and could be considered a protective factor for all-cause mortality.

Supplementary data

The Supplementary materials are available at <https://doi.org/10.5281/zenodo.8227882>. The package contains the following files:

Supplementary Fig. 1. Multivariable-adjusted HRs (black solid lines) and 95% CIs (dotted and dashed lines) for risk of all-cause mortality according to TC levels.

Supplementary Table 1. Results for Shapiro–Wilk test.

Supplementary Table 2. Test of the proportional hazards assumption for all covariates and mortality used in the Cox regression model.

ORCID iDs

Kun Li  <https://orcid.org/0000-0002-6165-6105>

Wen-Wen Cao  <https://orcid.org/0009-0001-7763-7056>

Shao-Hua Chen  <https://orcid.org/0009-0000-5068-1682>

Bin-Fei Zhang  <https://orcid.org/0000-0002-1135-6972>

Yu-Min Zhang  <https://orcid.org/0000-0003-2806-8448>

References

- Li L, Bennett-Brown K, Morgan C, Dattani R. Hip fractures. *Br J Hosp Med (Lond)*. 2020;81(8):1–10. doi:10.12968/hmed.2020.0215
- Prior JC, Langsetmo L, Lentle BC, et al. Ten-year incident osteoporosis-related fractures in the population-based Canadian Multicentre Osteoporosis Study: Comparing site and age-specific risks in women and men. *Bone*. 2015;71:237–243. doi:10.1016/j.bone.2014.10.026
- Pincus D, Ravi B, Wodchis WP. Wait time for hip fracture surgery and mortality: Reply. *JAMA*. 2018;319(21):2234. doi:10.1001/jama.2018.4426
- Cooper C, Campion G, Melton LJ. Hip fractures in the elderly: A worldwide projection. *Osteoporos Int*. 1992;2(6):285–289. doi:10.1007/BF01623184
- Zhang C, Feng J, Wang S, et al. Incidence of and trends in hip fracture among adults in urban China: A nationwide retrospective cohort study. *PLoS Med*. 2020;17(8):e1003180. doi:10.1371/journal.pmed.1003180
- Holvik K, Gjesdal CG, Tell GS, et al. Low serum concentrations of alpha-tocopherol are associated with increased risk of hip fracture: A NOREPOS study. *Osteoporos Int*. 2014;25(11):2545–2554. doi:10.1007/s00198-014-2802-6
- Xu BY, Yan S, Low LL, Vasanwala FF, Low SG. Predictors of poor functional outcomes and mortality in patients with hip fracture: A systematic review. *BMC Musculoskelet Disord*. 2019;20(1):568. doi:10.1186/s12891-019-2950-0
- Pioli G, Bendini C, Pignedoli P, Giusti A, Marsh D. Orthogeriatric co-management: Managing frailty as well as fragility. *Injury*. 2018;49(8):1398–1402. doi:10.1016/j.injury.2018.04.014
- Chimento A, Casaburi I, Avena P, et al. Cholesterol and its metabolites in tumor growth: Therapeutic potential of statins in cancer treatment. *Front Endocrinol (Lausanne)*. 2019;9:807. doi:10.3389/fendo.2018.00807
- Wong LH, Gatta AT, Levine TP. Lipid transfer proteins: The lipid commute via shuttles, bridges and tubes. *Nat Rev Mol Cell Biol*. 2019;20(2):85–101. doi:10.1038/s41580-018-0071-5
- Ikonen E. Mechanisms for cellular cholesterol transport: Defects and human disease. *Physiol Rev*. 2006;86(4):1237–1261. doi:10.1152/physrev.00022.2005
- Sivas F, Alemdaroğlu E, Elverici E, Kuluğ T, Özoran K. Serum lipid profile: Its relationship with osteoporotic vertebrae fractures and bone mineral density in Turkish postmenopausal women. *Rheumatol Int*. 2009;29(8):885–890. doi:10.1007/s00296-008-0784-4
- Tankó LB, Christiansen C, Cox DA, Geiger MJ, McNabb MA, Cummings SR. Relationship between osteoporosis and cardiovascular disease in postmenopausal women. *J Bone Miner Res*. 2005;20(11):1912–1920. doi:10.1359/JBMR.050711
- Leader A, Ayzefeldt RH, Lishner M, Cohen E, Segev D, Hermoni D. Thyrotropin levels within the lower normal range are associated with an increased risk of hip fractures in euthyroid women, but not men, over the age of 65 years. *J Clin Endocrinol Metab*. 2014;99(8):2665–2673. doi:10.1210/jc.2013-2474
- Tatsuno I, Terano T, Nakamura M, et al. Lifestyle and osteoporosis in middle-aged and elderly women: Chiba bone survey. *Endocr J*. 2013;60(5):643–650. doi:10.1507/endocrj.EJ12-0368
- Cui LH, Shin MH, Chung EK, et al. Association between bone mineral densities and serum lipid profiles of pre- and post-menopausal rural women in South Korea. *Osteoporos Int*. 2005;16(12):1975–1981. doi:10.1007/s00198-005-1977-2
- Yamaguchi T. Osteoporosis associated with the metabolic syndrome [in Japanese]. *Clin Calcium*. 2008;18(5):606–611. PMID:18445878.
- Wozney JM, Rosen V. Bone morphogenetic protein and bone morphogenetic protein gene family in bone formation and repair. *Clin Orthop Relat Res*. 1998;346(2):26–37. PMID:9577407.
- Ambrosi TH, Scialdone A, Graja A, et al. Adipocyte accumulation in the bone marrow during obesity and aging impairs stem cell-based hematopoietic and bone regeneration. *Cell Stem Cell*. 2017;20(6):771–784.e6. doi:10.1016/j.stem.2017.02.009
- Bagger YZ, Rasmussen HB, Alexandersen P, et al. Links between cardiovascular disease and osteoporosis in postmenopausal women: Serum lipids or atherosclerosis per se? *Osteoporos Int*. 2007;18(4):505–512. doi:10.1007/s00198-006-0255-2
- Yamaguchi T, Sugimoto T, Yano S, et al. Plasma lipids and osteoporosis in postmenopausal women. *Endocr J*. 2002;49(2):211–217. doi:10.1507/endocrj.49.211
- Tankó LB, Bagger YZ, Nielsen SB, Christiansen C. Does serum cholesterol contribute to vertebral bone loss in postmenopausal women? *Bone*. 2003;32(1):8–14. doi:10.1016/S8756-3282(02)00918-3
- Ahmed LA, Schirmer H, Berntsen GK, Fønnebo V, Joakimsen RM. Features of the metabolic syndrome and the risk of non-vertebral fractures: The Tromsø Study. *Osteoporos Int*. 2006;17(3):426–432. doi:10.1007/s00198-005-0003-z
- Hsu YH, Venners SA, Terwedow HA, et al. Relation of body composition, fat mass, and serum lipids to osteoporotic fractures and bone mineral density in Chinese men and women. *Am J Clin Nutr*. 2006;83(1):146–154. doi:10.1093/ajcn/83.1.146
- Trimppou P, Odén A, Simonsson T, Wilhelmsen L, Landin-Wilhelmsen K. High serum total cholesterol is a long-term cause of osteoporotic fracture. *Osteoporos Int*. 2011;22(5):1615–1620. doi:10.1007/s00198-010-1367-2
- Lampropoulos CE, Papaioannou I, D'Cruz DP. Osteoporosis: A risk factor for cardiovascular disease? *Nat Rev Rheumatol*. 2012;8(10):587–598. doi:10.1038/nrrheum.2012.120
- Tarakida A, Iino K, Abe K, et al. Hypercholesterolemia accelerates bone loss in postmenopausal women. *Climacteric*. 2011;14(1):105–111. doi:10.3109/13697137.2010.507888
- McFarlane SI, Muniyappa R, Shin JJ, Bahtiyar G, Sowers JR. Osteoporosis and cardiovascular disease. Brittle bones and boned arteries: Is there a link? *Endocrine*. 2004;23(1):1–10. doi:10.1385/ENDO.23:1:01
- Parhami F, Garfinkel A, Demer LL. Role of lipids in osteoporosis. *Arterioscler Thromb Vasc Biol*. 2000;20(11):2346–2348. doi:10.1161/01.ATV.20.11.2346
- Parhami F, Jackson SM, Tintut Y, et al. Atherogenic diet and minimal-ly oxidized low density lipoprotein inhibit osteogenic and promote adipogenic differentiation of marrow stromal cells. *J Bone Miner Res*. 1999;14(12):2067–2078. doi:10.1359/jbmr.1999.14.12.2067
- Golomb BA, Kane T, Dimsdale JE. Severe irritability associated with statin cholesterol-lowering drugs. *QJM*. 2004;97(4):229–235. doi:10.1093/qjmed/hch035

32. King DS, Wilburn AJ, Wofford MR, Harrell TK, Lindley BJ, Jones DW. Cognitive impairment associated with atorvastatin and simvastatin. *Pharmacotherapy*. 2003;23(12):1663–1667. doi:10.1592/phco.23.15.1663.31953
33. Wagstaff LR, Mitton MW, Arvik BM, Doraiswamy PM. Statin-associated memory loss: Analysis of 60 case reports and review of the literature. *Pharmacotherapy*. 2003;23(7):871–880. doi:10.1592/phco.23.7.871.32720
34. Alegre-López J, Cordero-Guevara J, Alonso-Valdivielso JL, Fernández-Melón J. Factors associated with mortality and functional disability after hip fracture: An inception cohort study. *Osteoporos Int*. 2005;16(7):729–736. doi:10.1007/s00198-004-1740-0
35. Reed B, Villeneuve S, Mack W, DeCarli C, Chui HC, Jagust W. Associations between serum cholesterol levels and cerebral amyloidosis. *JAMA Neurol*. 2014;71(2):195. doi:10.1001/jamaneurol.2013.5390
36. Gu X, Li Y, Chen S, et al. Association of lipids with ischemic and hemorrhagic stroke: A prospective cohort study among 267,500 Chinese. *Stroke*. 2019;50(12):3376–3384. doi:10.1161/STROKEAHA.119.026402
37. Aronow WS, Ahn C. Risk factors for new atherothrombotic brain infarction in older Hispanic men and women. *J Gerontol A Biol Sci Med Sci*. 2002;57(1):M61–M63. doi:10.1093/gerona/57.1.M61
38. Yang L, Yang H, Chen Q, Shen H, Wang Z. Analysis of risk factors for 90-day mortality after surgery in elderly patients with intertrochanteric fractures and a history of cardiovascular disease. *Ann Palliat Med*. 2022;11(1):155–162. doi:10.21037/apm-21-3625
39. Chang W, Lv H, Feng C, et al. Preventable risk factors of mortality after hip fracture surgery: Systematic review and meta-analysis. *Int J Surg*. 2018;52:320–328. doi:10.1016/j.ijsu.2018.02.061
40. Yong EL, Ganesan G, Kramer MS, et al. Risk factors and trends associated with mortality among adults with hip fracture in Singapore. *JAMA Netw Open*. 2020;3(2):e1919706. doi:10.1001/jamanetworkopen.2019.19706
41. Huetten P, Abou-Arab O, Djebara AE, et al. Risk factors and mortality of patients undergoing hip fracture surgery: A one-year follow-up study. *Sci Rep*. 2020;10(1):9607. doi:10.1038/s41598-020-66614-5
42. Ren Y, Hu J, Lu B, Zhou W, Tan B. Prevalence and risk factors of hip fracture in a middle-aged and older Chinese population. *Bone*. 2019;122:143–149. doi:10.1016/j.bone.2019.02.020
43. Sun T, Wang X, Liu Z, Chen X, Zhang J. Plasma concentrations of pro- and anti-inflammatory cytokines and outcome prediction in elderly hip fracture patients. *Injury*. 2011;42(7):707–713. doi:10.1016/j.injury.2011.01.010

An interpretable machine learning model to predict off-pump coronary artery bypass grafting-associated acute kidney injury

Zhihe Zeng^{A–D,F}, Xiao Tian^B, Lin Li^{A,C,D–F}, Yugang Diao^{E,F}, Tiezheng Zhang^{E,F}

Department of Anesthesiology, General Hospital of Northern Theater Command, Shenyang, China

A – research concept and design; B – collection and/or assembly of data; C – data analysis and interpretation; D – writing the article; E – critical revision of the article; F – final approval of the article

Advances in Clinical and Experimental Medicine, ISSN 1899–5276 (print), ISSN 2451–2680 (online)

Adv Clin Exp Med. 2024;33(5):473–481

Address for correspondence

Lin Li
E-mail: lilinlashofmine@qq.com

Funding sources

This study was supported by the Liaoning Provincial Key Research and Development Guidance Program (grant No. 2019JH8/10300083;2019010209) and Liaoning Provincial Key Research and Development Program (grant No. 2020JH2/10300121).

Conflict of interest

None declared

Received on July 24, 2022
Reviewed on June 2, 2023
Accepted on July 14, 2023

Published online on August 18, 2023

Cite as

Zeng Z, Tian X, Li L, Diao Y, Zhang T. An interpretable machine learning model to predict off-pump coronary artery bypass grafting-associated acute kidney injury. *Adv Clin Exp Med.* 2024;33(5):473–481. doi:10.17219/acem/169609

DOI

10.17219/acem/169609

Copyright

Copyright by Author(s)
This is an article distributed under the terms of the Creative Commons Attribution 3.0 Unported (CC BY 3.0) (<https://creativecommons.org/licenses/by/3.0/>)

Abstract

Background. Off-pump coronary artery bypass grafting-associated acute kidney injury (OPCAB-AKI) is related to 30-day perioperative mortality. Existing mathematical models cannot be applied to help clinicians make early diagnosis and intervention decisions.

Objectives. This study used an interpretable machine learning method to establish and screen an optimized OPCAB-AKI prediction model.

Materials and methods. Clinical data of 1110 patients who underwent OPCAB in the Department of Cardiac Surgery of General Hospital of Northern Theater Command (Shenyang, China) from January 2018 to December 2020 were collected retrospectively. Four machine learning models were used, including logistic regression (LR), decision tree (DT), random forest (RF), and eXtreme Gradient Boosting (XGBoost). The SHapley Additive exPlanation (SHAP) tool was used for explanatory analysis of the black-box model. The mean absolute value of the characteristic SHAP parameter was defined and sorted. The correlation between the characteristic parameters and OPCAB-AKI was determined based on the SHAP value. A quantitative analysis of a single characteristic and an interaction analysis of multiple characteristics were carried out for the main risk factors.

Results. The RF prediction model had the best performance, with an area under the curve (AUC) of 0.90, a precision rate of 0.80, an accuracy rate of 0.83, a recall rate of 0.74, and an F1 score of 0.78 for positive samples. The interpretation analysis of the SHAP model results showed that intraoperative urine volume contributed to the greatest extent to the RF model, and other parameters included intraoperative sufentanil dosage, intraoperative dexmedetomidine dosage, cyclic variation coefficient during the induction period, intraoperative hypotension duration, age, preoperative baseline serum creatinine, body mass index (BMI), and Acute Physiology, Age and Chronic Health Evaluation (APACHE) II score.

Conclusions. The model constructed by the RF ensemble learning algorithm predicted OPCAB-AKI, and indicators such as intraoperative urine volume were closely related to OPCAB-AKI.

Key words: coronary artery bypass grafting, acute kidney injury, machine learning, interpretability research

Background

Cardiac surgery-associated acute kidney injury (CSA-AKI) incidence is approx. 22–30%, of which 1% of cases must be treated with emergency dialysis.¹ Off-pump coronary bypass grafting (OPCAB) avoids the cardiopulmonary bypass risk factors of non-physiological perfusion and ischemia-reperfusion injury. However, circulatory fluctuations caused by surgical procedures can still cause cardiac and renal insufficiency, while low cardiac output syndrome further increases the risk of OPCAB-AKI. A previous study demonstrated that transient minor serum creatinine (sCr) elevation after cardiac surgery is associated with 30-day mortality.² Patients with stage I AKI have an increased risk of death by 56%, and patients with stage II or III AKI have a mortality risk of up to 3.5 times higher than in the general population. Even after curing CSA-AKI symptoms, the risk of progression to chronic kidney disease (CKD) and death remains increased.³ Early intervention could prevent AKI from progressing to a severe stage, which is crucial for reducing perioperative mortality.

Current mathematical models used to predict CSA-AKI are regression models based on preoperative data, including demographic variables, such as the European System for Cardiac Operative Risk Evaluation (EuroSCORE II) published in 2012, the Society of Thoracic Surgeons Score (STS score)⁴ published in 2008, and the Sino-System for Coronary Operative Risk Evaluation (SinoSCORE) published in 2009 in China.⁵ A common limitation of these models is that they only include the analysis of a few intraoperative risk factors. Since these factors correspond to multiple surgical types or complications, their single-risk prediction ability has to be improved. Clinicians must be able to understand and interpret the correlation between risk factors based on the accurate prediction of AKI risk to make correct decisions. However, achieving good predictability and interpretability is challenging because the computational process of most models is almost a “black-box” for researchers. Machine learning combined with SHapley Additive exPlanation (SHAP) could explain the output results of the prediction model, thereby solving this issue.^{6–9}

Objectives

This study combined preoperative features with various intraoperative clinical parameters, such as decisive surgical decisions and hemodynamic fluctuations. The aim of the study was to establish a risk prediction model including intraoperative features set as the primary objective variables, with OPCAB-AKI set as the sole outcome. The research hypothesized that the constructed OPCAB-AKI prediction model based on machine learning exhibits

good predictive performance, and the SHAP explanatory toolkit used to analyze the weight and clinical significance of single or multiple risk factors may be helpful for an accurate early prediction of OPCAB-AKI and precise clinical decision-making.

Materials and methods

Data collection

The Ethics Committee of the General Hospital of Northern Theater Command (Shenyang, China) approved the retrospective data analysis (approval No. k (2020) 01) and exempted it from informed consent. The clinical data of 1110 patients undergoing elective OPCAB in the above hospital from January 2018 to December 2020 were retrospectively collected on the Do-Care automatic anesthesia recording system and electronic medical record system (EMRS). Figure 1 illustrates the data collection process. Levels of sCr measured within the 24 h before surgery defined as the baseline. The single outcome was AKI within 7 days post-surgery. The diagnostic criteria were defined according to the Kidney Disease: Improving Global Outcomes (KDIGO) 2012 guidelines: 1) increased sCr level $\geq 26.5 \mu\text{mol/L}$ ($\geq 0.3 \text{ mg/dL}$) within 48 h, or 2) sCr level increased >1.5 times compared to the baseline value within 7 days, or 3) urine volume $<0.5 \text{ mL/kg/h}^{10}$ for 6 consecutive hours. The patients were divided into AKI-negative and AKI-positive groups according to whether AKI occurred after the operation.

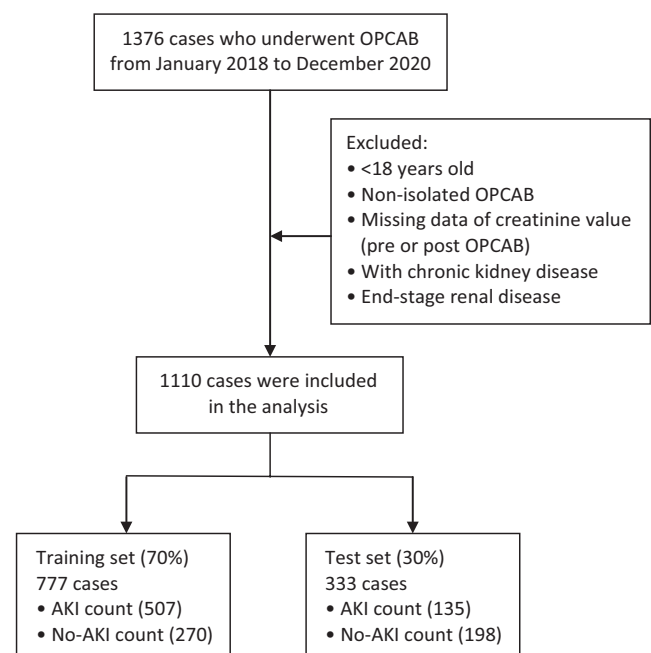


Fig. 1. Flowchart of data collection

OPCAB – off-pump coronary artery bypass grafting; AKI – acute kidney injury.

Statistical hypothesis testing and characteristic parameter selection

According to the EuroSCORE II value and the results of previous studies on CSA-AKI risk factors,^{11–14} 87 characteristic parameters were included and evaluated. Supplementary Table 1 provides a detailed description of the distribution of all parameters in different groups and datasets. Variance inflation factor (VIF) and the Box–Tidwell test verified predictors. Predictors of linear relationships with logit functions of outcomes and collinearity predictors were excluded. The remaining predictors were used to establish a logistic regression model, with 3 methods implemented to select feature predictors in the development cohort. First, predictors with $p < 0.05$ in the univariate analysis were chosen. Second, the least absolute shrinkage and selection operator (LASSO) regularization algorithm selected potential predictors with non-zero coefficients. Third, the random forest recursive feature elimination (RF-RFE) algorithm combined with backward stepwise selection produced a compact model. The χ^2 test was used to analyze categorical variables. The assessment of numerical variables used a Mann–Whitney U rank-sum test to conduct a univariate analysis of sample characteristics. The prediction performance of traditional logistic regression and machine learning models were then compared.

Data preprocessing

Treatment of vital signs in a perioperative time series

Two time windows were selected for the study: 1. Anesthesia induction duration (t_1) from the time when the patient entered the operation room to establish vital signs monitoring to 10 min after anesthesia induction; the assimilated indexes included heart rate (HR) and mean arterial pressure (MAP); 2. Operation duration (t_2) from skin incision to intravenous infusion of protamine; the collection indexes included HR, MAP and mean pulmonary artery pressure (mPAP). A polynomial curve function $Y(X,W) = W_0 + W_1X + W_2X^2 + W_3X^3 + \dots + W_MX^M$ was used to fit the continuous vital signs of patients (the collection interval was 1 min). In the formula, X was defined as the timepoint between the 2 time windows (t_1 and t_2) from the 1st minute till minute X , while Y specified the patient's vital signs (HR/MAP/mPAP) at the corresponding time point, and W was a coefficient of timepoint X in the polynomial function. The absolute values of each coefficient (W) of the function were summed to obtain 5 characteristic parameters (Supplementary Fig. 1): the coefficient of variation of HR during anesthesia induction, the coefficient of variation of MAP during anesthesia induction, the coefficient of variation of HR during the operation, the coefficient of variation of MAP during the operation, and the coefficient of variation of mPAP during the operation.

Acute hypotensive episodes (AHEs)¹⁵ and hypotension duration¹⁶ were defined and estimated according to the relevant literature: the total duration of $MAP < 65$ mm Hg from the moment of entering the operation room for establishing circulation monitoring to leaving the operating room and acute hypotension incidence ($MAP < 65$ mm Hg for >5 min).

Handling missing values

For characteristic parameters with a missing ratio $<10\%$, missing value interpolation did not effectuate any bias on the results.¹⁷ Deep learning technology was used to fill in the missing values.¹⁸ Ten parameters lacked values, and 3 had $\geq 10\%$ of values lacking, which were excluded from the models (Supplementary Table 2).

Characteristic parameter determination

After handling missing values, VIF and Box–Tidwell test were used to verify the remaining 84 predictors, resulting in the removal of 5 predictors of linear relationships or collinearity (Supplementary Table 3). The remaining 79 predictors were used to establish the logistic regression model. One-way analysis of variance (ANOVA) and Recursive Feature Elimination and LASSO regression were applied to select feature predictors in the development cohort. Finally, 39 predictors were selected to establish machine learning models (Supplementary Fig. 1 and Supplementary Table 4), and 21 statistically significant clinical characteristics were tested ($p < 0.05$).

Machine learning model establishment

This study examined a small sample high-dimensional dataset using 4 common machine learning algorithms simultaneously, including logistic regression (LR), classification decision tree (DT), RF, and eXtreme Gradient Boosting (XGBoost). The parameters (options activated) for each analysis are listed in Supplementary Table 5. The sample size of the dataset conformed to the rule of “10 events per variable” for characteristic parameters, which meets the sample size demands of machine learning. The `train_test_split` tool in the `sklearn` module randomly divided the preprocessed data into training and test sets at a ratio of 7:3, with 70% of the training sets included in the training model database. Cross-validation reduced the overfitting to some extent and allowed for obtaining critical information from the limited data. The training set data were randomly divided into 5 equal parts using the five-fold cross-validation method, with 4 used for the training model and 1 for model verification. The cycle was repeated 5 times. The model parameters were adjusted according to the area under the receiver operating characteristic (ROC) curve (AUC) to prevent overfitting of the modeling process, and the remaining 30% of the test sets were used for internal verification to evaluate the performance of the trained models on the new data.

Model performance evaluation

Accuracy, recall and precision rates evaluated the prediction results. The F1 score was used to balance the model precision and recall, and to evaluate the performance of the binary model. The F1 score ranges from 0 to 1, with larger values indicating better results. The ROC curve and AUC were also used to evaluate model performance, and the calibration curve was used to represent the accuracy of the model prediction probability.

Interpretive analysis

The interpretation analysis of the black-box model with the best predictive performance was done using the Python SHAP model interpretation package. Based on common theory and local interpretation, SHAP is a classic post-hoc interpretation framework that provides values to estimate the contribution of each characteristic. A SHAP value describes the weight or importance of a specific characteristic in predicting a particular data point by the model, which is the core of the parameter. Compared to traditional characteristic importance methods, SHAP has better consistency and presents a positive/negative correlation of each predictor relative to the target variable, which can be used for local and global interpretation. For local interpretability, each characteristic had its own set of Shapley values that might explain and quantify the contribution of each characteristic of each sample to the prediction, increasing the transparency and allowing clinicians to analyze the reliability of the prediction model. The global interpretation could be obtained based on the mean Shapley value of the corresponding variables in all samples as the significance value of the specific characteristic.

Results

Dataset description

After preprocessing the original electronic medical record data, 1110 samples were divided into AKI-positive (405 cases) and AKI-negative (705 cases) groups, according to whether AKI occurred postoperatively. The patients in the positive group had a higher mean age and a prolonged mean duration of intraoperative hypotension (MAP < 65 mm Hg). The incidence of abnormal preoperative sCr, preoperative electrocardiogram ventricular premature beat, intraoperative sudden atrial fibrillation, ventricular fibrillation, intraoperative use of intra-aortic balloon counterpulsation-assisted circulation, and intraoperative acute hypotension (MAP < 65 mm Hg for >5 min) was higher in the AKI-positive group than in the AKI-negative group. Dexmedetomidine dosage and urine volume were lower in the AKI-positive group than in the AKI-negative group.

Model prediction results and performance comparison

The test set ($n = 333$) results showed that the AUC of the RF model for positive samples (0.9, 95% confidence interval (95% CI): 0.86–0.94) was better than that for the other model groups (LR-AUC: 0.73, 95% CI: 0.67–0.79; DT-AUC: 0.75, 95% CI: 0.69–0.81; XGBoost-AUC: 0.86, 95% CI: 0.82–0.90) (Supplementary Table 6). However, the recall rate (0.74) and F1 score (0.78) performance indicators of the RF group did not differ significantly from the other integration algorithms (Supplementary Table 6 and Fig. 2A), and the calibration curve indicated that the prediction probability of the RF model was rather accurate (Fig. 2B). Compared with the traditional statistical binary logistic regression model (positive prediction accuracy: 0.71; AUC: 0.73, 95% CI: 0.70–0.76), the RF model and other integration algorithms showed better predictive ability for OPCAB-AKI (Fig. 3).

Interpretative analysis of the random forest model

The ranking results of the characteristic parameters showed that intraoperative urine volume contributed maximally to the RF model, followed by intraoperative sufentanil dosage, intraoperative dexmedetomidine dosage, the coefficient of variation of circulation during the induction period, the duration of intraoperative hypotension, age, preoperative baseline sCr, body mass index (BMI), and Acute Physiology, Age and Chronic Health Evaluation (APACHE) II scores (Fig. 4A).

Further analysis established a positive correlation between the coefficient of variation of circulation during the induction period, the dosage of sufentanil, duration of intraoperative hypotension, preoperative baseline sCr, APACHE II score, age, and postoperative AKI occurrence. As such, the higher the standard values corresponding to these characteristics, the greater the possibility of AKI in the model samples. On the other hand, intraoperative urine volume and intraoperative dexmedetomidine dosage correlated negatively with OPCAB-AKI incidence (Fig. 4B).

In the SHAP summary of the top 20 characteristics, the ordinate was characteristic and the abscissa was the SHAP value, sorted according to the mean absolute characteristic parameter value. The higher the SHAP value of the characteristic, the greater the OPCAB-AKI incidence. Each line represented a characteristic, a point represented a sample, and the color represented the characteristic value (red was high and blue was low). The positive/negative correlation between each characteristic and OPCAB-AKI was determined based on the distribution of the actual characteristic value and the SHAP value.

The SHAP value was used to analyze how the top-ranked characteristics in the RF black-box model affected

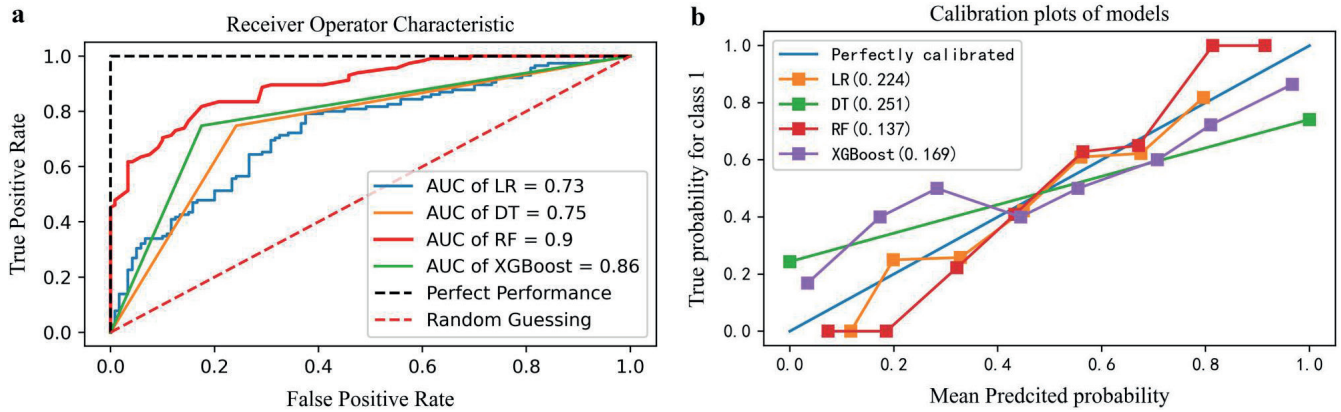


Fig. 2. Machine learning model performance

AUC – area under the curve; RF – random forest; XGBoost – extreme gradient boosting; LR – logistic regression; DT – decision tree.

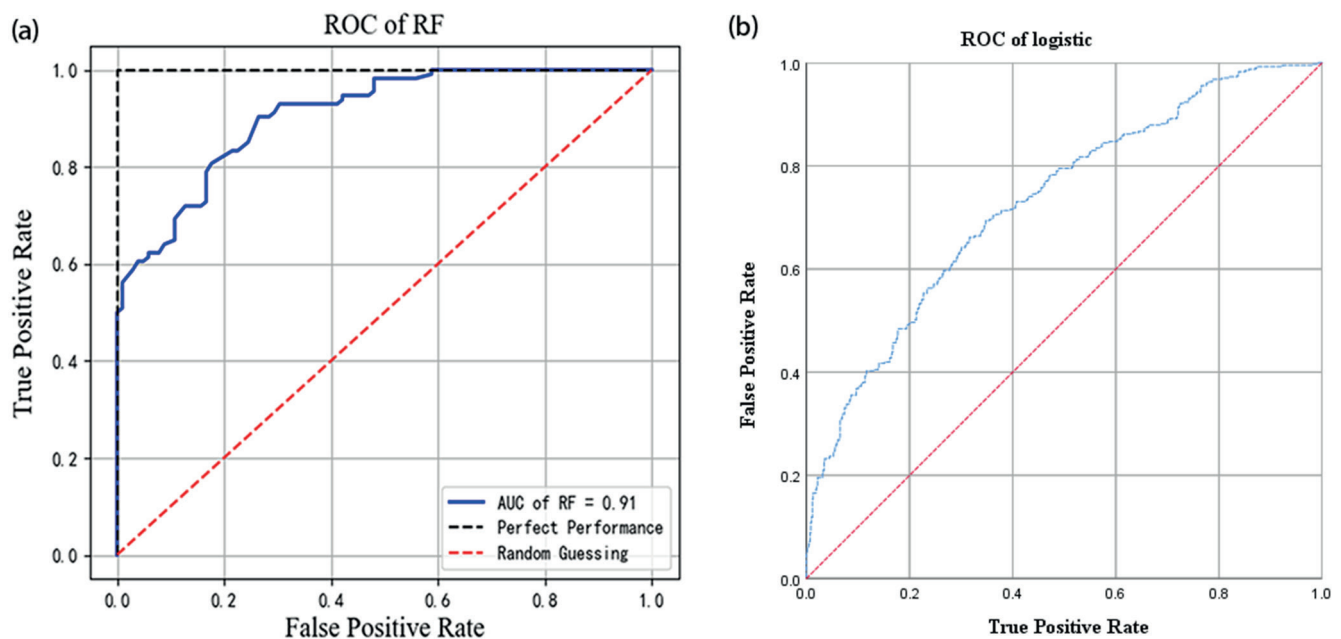


Fig. 3. Performance comparison between the random forest (RF) and binary logistic regression models

ROC – receiver operating characteristic; AUC – area under the curve.

the prediction results by comparing and quantifying the linear correlation between the SHAP values of each characteristic and the risk outcomes. The results showed that the OPCAB-AKI risk significantly increased when 3 consecutive characteristics reached specific thresholds: age >55 years, APACHE II score >19 points and BMI > 28 kg/m² (Fig. 5).

The SHAP dependency analysis revealed the importance and direction of the influence of the 2 pairs of characteristics on the model output, and their complex nonlinear effects were obtained and described. The results showed that the risk of OPCAB-AKI increased significantly with prolonged intraoperative hypotension duration and decreased intraoperative urine volume. Accordingly, the OPCAB-AKI risk was low at a short intraoperative hypotension duration (SHAP < 0) and high intraoperative urine volume (approx. 700 mL) (Fig. 6A). A high dexmedetomidine dose

was positively associated with increased intraoperative urine volume, which corresponded to a low risk of OPCAB-AKI (Fig. 6B).

Discussion

This retrospective cohort study employed a machine learning method to establish a risk prediction model for OPCAB-AKI using a small sample (1110 patients) of perioperative data collected from a single center over the course of 3 years. The results showed that the prediction effect of the integrated machine learning model was better than that of a traditional LR model, and the RF model showed the best prediction performance after integrating the intraoperative hemodynamic parameters (AUC = 0.9, 95% CI: 0.86–0.94). This helped the clinicians make an early

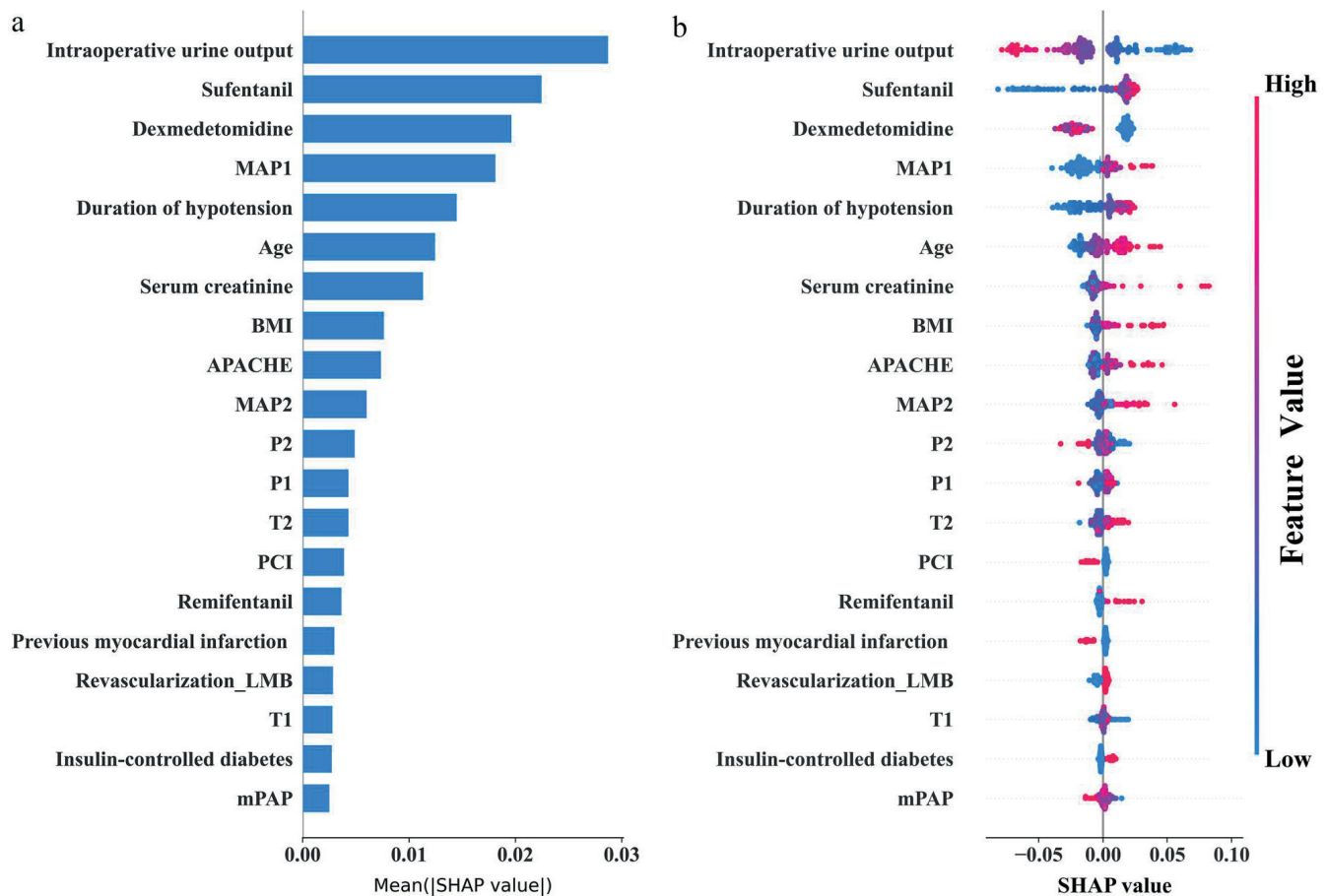


Fig. 4. Importance matrix diagram of the random forest model

MAP1 – coefficient of variation of mean arterial pressure during the induction period; BMI – body mass index; APACHE – Acute Physiology, Age and Chronic Health Evaluation; MAP2 – coefficient of variation of mean arterial pressure during the coronary artery bypass period; P2 – coefficient of variation of heart rate (HR) during the coronary artery bypass period; P1 – coefficient of variation of HR during the induction; T2 – operation time; PCI – percutaneous coronary intervention; T1 – skin incision-bypass time; mPAP – coefficient of variation of mean pulmonary arterial pressure during the coronary artery bypass period.

prediction and choose an appropriate AKI intervention before the end of surgery.

Among the screened OPCAB-AKI influencing factors, the top 5 items (intraoperative urine volume, intraoperative sufentanil dosage, intraoperative dexmedetomidine dosage, the coefficient of variation of MAP during the induction period, and intraoperative hypotension duration) are the intraoperative indicators that are not a primary concern in the classical prediction models, and the remaining items, such as age, preoperative baseline sCr, BMI, and APACHE II score, were the known CSA-AKI influencing factors.¹⁹ A single-center cohort study of patients undergoing any surgery showed that 40% of them were assessed as low risk for AKI by classical models but reassessed as high risk by machine learning models after incorporating intraoperative factors.²⁰ Compared to classical models, the results of this study highlight the impact of acute intraoperative pathophysiological reactions on renal function and the potential benefits of close monitoring and timely intervention.²¹

Intraoperative urine volume (with a mean SHAP value weight of 2.87%) was a major influencing factor in the OPCAB-AKI prediction model established in this

study. Previous studies on CSA-AKI have shown that urine volume predicts AKI after cardiopulmonary bypass surgery.²² This phenomenon is consistent with the results of the present study, suggesting that real-time monitoring and maintenance of adequate intraoperative urine volume could protect renal function in OPCAB patients.²³

Two other intraoperative influencing factors in the model were the coefficient of variation of circulation during induction and intraoperative hypotension duration. Some studies have shown that the risk of AKI is independently associated with intraoperative hypotension,^{24,25} and hemodynamic fluctuation is a major risk factor for inducing postoperative AKI.^{26–28} Perioperative supportive care for MAP could reduce the risk of postoperative complications such as AKI.²⁹ Off-pump coronary artery bypass grafting has unique hemodynamic characteristics and is prone to severe hemodynamic fluctuations during specific periods, such as anesthesia induction, fixation and compression of coronary arteries.³⁰ Since the blood pressure or HR at a single timepoint could not reflect the significance of the patient's hemodynamic fluctuations over time, this study used a polynomial higher-order function fitting

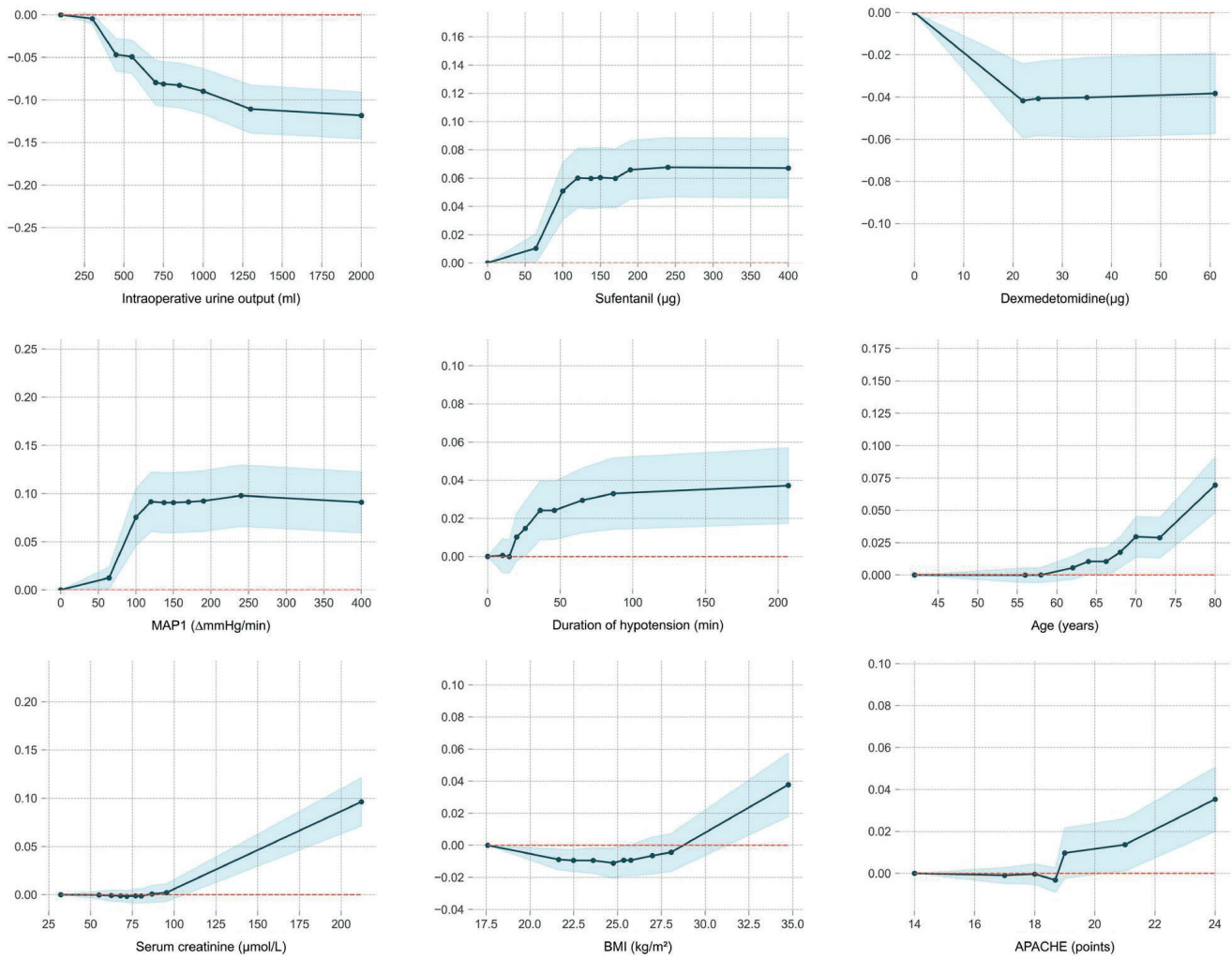


Fig. 5. Single characteristic quantitative analysis. The X-axis represents the actual value of the characteristic, and the Y-axis the corresponding SHapley Additive exPlanation (SHAP) value. When SHAP was >0, off-pump coronary artery bypass grafting-associated acute kidney injury (OPCAB-AKI) risk increased. MAP1 – the coefficient of variation of mean arterial pressure during the induction period; BMI – body mass index; APACHE – Acute Physiology, Age and Chronic Health Evaluation.

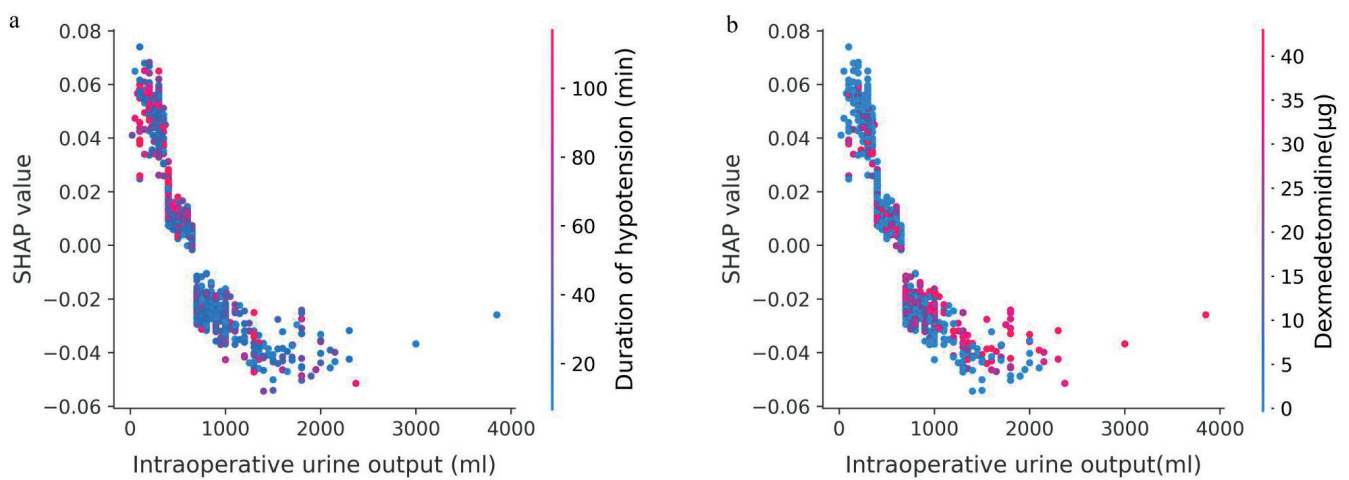


Fig. 6. Multi-characteristic interaction effects. The X-axis represents the actual value of the characteristic, the Y-axis is the corresponding SHapley Additive exPlanation (SHAP) value, and the blue to red colors on the right axis represent the size of the characteristic value (red was high and blue was low). A. Effects of intraoperative urine volume and intraoperative hypotension duration on model output; B. Effects of intraoperative urine volume and intraoperative dexmedetomidine dosage on model output

curve to represent continuous intraoperative circulation indicators. The results suggest that intraoperative hemodynamic fluctuations represented by the coefficient of variation of circulation can accurately predict OPCAB-AKI.

The impact of general anesthetics on postoperative AKI was rarely considered in previous models. In this study, dexmedetomidine was shown to be a critical influencing factor (negatively correlated) of OPCAB-AKI. A randomized controlled trial by Zhai et al. demonstrated that dexmedetomidine reduced CSA-AKI incidence and severity in patients undergoing cardiac surgery.³¹ Another meta-analysis concluded that dexmedetomidine infusion could be used as a preventive strategy for CSA-AKI. However, they did not specify the optimal dose or duration of intravenous dexmedetomidine infusion.³²

The model established in this study suggested that an excessive intraoperative sufentanil dosage might be a risk factor for inducing OPCAB-AKI. Based on the concept of Enhanced Recovery After Surgery (ERAS[®]), low-opioid anesthesia regimens have been widely accepted by clinicians.^{33,34} Although there was no evidence that low-opioid anesthesia reduced the risk of CSA-AKI or OPCAB-AKI, the results of the present study suggest that reducing intraoperative opioid dosage exerts a protective effect on the renal function of OPCAB patients.

Several studies have identified a high BMI and advanced age as major OPCAB-AKI risk factors.³⁵ Moreover, the APACHE II score is prognostic for critically ill patients immediately after admission to the intensive care unit (ICU), and was used in this study to replace laboratory indicators, such as hemoglobin, to predict postoperative AKI risk. After conducting the interpretive analysis of the black-box model with the use of the classic SHAP tool, the present study identified 3 continuous characteristics, including age, APACHE II score and BMI, that affected the critical threshold of the RF model for predicting the risk of OPCAB-AKI. These factors helped the clinicians to understand the influence of characteristics on the prediction outcome.

Although novel serum and urine biomarkers can predict AKI,³⁶ there are disadvantages to expensive tests, repeated tests during diagnosis and increased hospitalization costs. The main risk factors involved in this research model were routine items that were easy to collect and did not increase the medical burden.

The interaction analysis showed mutual influences among several OPCAB-AKI factors. For example, high intraoperative dexmedetomidine dosage and high intraoperative urine volume were associated with a low risk of postoperative AKI. Although the results cannot determine causality among factors, they suggested putative changing trends in specific environments, which were not captured by most analytical models. Combining this information with the clinical experience of the doctors aided in making individualized clinical decisions at an early stage.

The advantage of this study was that five-fold cross-validation was used to construct a stable performance

model. Predictive variables used in the study are readily available in clinical practice, ensuring model applicability. The model exhibits clinical interpretability and predictive reliability, which could help doctors understand the interaction between variables and targets as well as between 2 variables.

Limitations

The limitations of this study include its retrospective design, a small sample of subjects from the same tertiary general hospital, and lack of evaluation of different AKI stages. As such, the results require further external validation before they can be generalized, and additional prospective trials are needed to assess their clinical utility.

The major characteristics and inflection points found in this study could be used as early signs of OPCAB-AKI risk. However, whether these could act as a reference for clinical diagnosis in the recommended range needs further substantiation. If found to be externally valid, clinicians might incorporate the available web-based application into clinical practice to aid decision-making and optimize preoperative prevention efforts.

Conclusions

The ensemble learning algorithm represented by RF predicted OPCAB-AKI. Intraoperative urine volume, circulatory fluctuation during the induction period, intraoperative dexmedetomidine dosage, intraoperative hypotension duration, preoperative baseline sCr, APACHE II score, BMI, and age were the main factors influencing OPCAB-AKI. An explanatory framework increased model transparency, allowing clinicians to analyze the reliability of the predictive models.

Data availability statement

The datasets used and/or analyzed during the current study are available from the corresponding author upon reasonable request.

Supplementary data

The supplementary materials are available at <https://doi.org/10.5281/zenodo.8128783>. The package contains the following files:

Supplementary Fig. 1. Polynomial curve fitting of vital signs.

Supplementary Table 1. Distribution of each characteristic in the base dataset.

Supplementary Table 2. Parameters lacking values and parameters excluded from the models.

Supplementary Table 3. Predictors of linear relationships or collinearity that were removed.

Supplementary Table 4. Predictors selected and used in machine learning modeling.

Supplementary Table 5. The parameters (options activated) of each analysis.

Supplementary Table 6. Machine learning model performance results.

ORCID iDs

Zhihe Zeng  <https://orcid.org/0000-0003-2335-2300>

Xiao Tian  <https://orcid.org/0009-0002-9927-7191>

Lin Li  <https://orcid.org/0000-0001-7262-5788>

Yugang Diao  <https://orcid.org/0000-0003-4509-9035>

Tiezheng Zhang  <https://orcid.org/0000-0002-2228-1822>

References

- Rosner MH, Okusa MD. Acute kidney injury associated with cardiac surgery. *Clin J Am Soc Nephrol*. 2006;1(1):19–32. doi:10.2215/CJN.00240605
- Bernardi MH, Ristl R, Neugebauer T, Hiesmayr MJ, Druml W, Lassnigg A. Very early changes in serum creatinine are associated with 30-day mortality after cardiac surgery: A cohort study. *Eur J Anaesthesiol*. 2020;37(10):898–907. doi:10.1097/EJA.0000000000001214
- Brown JR, Hisey WM, Marshall EJ, et al. Acute kidney injury severity and long-term readmission and mortality after cardiac surgery. *Ann Thorac Surg*. 2016;102(5):1482–1489. doi:10.1016/j.athoracsurg.2016.04.020
- Ranucci M, Castelvechio S, Menicanti L, Frigiola A, Pelissero G. Risk of assessing mortality risk in elective cardiac operations: Age, creatinine, ejection fraction, and the law of parsimony. *Circulation*. 2009;119(24):3053–3061. doi:10.1161/CIRCULATIONAHA.108.842393
- Li Y, Zheng Z, Hu S; Chinese Coronary Artery Bypass Grafting Registry Study. The Chinese Coronary Artery Bypass Grafting Registry Study: Analysis of the national multicentre database of 9248 patients. *Heart*. 2009;95(14):1140–1144. doi:10.1136/hrt.2008.146563
- Yun D, Cho S, Kim YC, et al. Use of deep learning to predict acute kidney injury after intravenous contrast media administration: Prediction model development study. *JMIR Med Inform*. 2021;9(10):e27177. doi:10.2196/27177
- Kuno T, Mikami T, Sahashi Y, et al. Machine learning prediction model of acute kidney injury after percutaneous coronary intervention. *Sci Rep*. 2022;12(1):749. doi:10.1038/s41598-021-04372-8
- Ou SM, Lee KH, Tsai MT, Tseng WC, Chu YC, Tarng DC. Artificial intelligence for risk prediction of rehospitalization with acute kidney injury in sepsis survivors. *J Pers Med*. 2022;12(1):43. doi:10.3390/jpm12010043
- Ma P, Liu R, Gu W, et al. Construction and interpretation of prediction model of teicoplanin trough concentration via machine learning. *Front Med (Lausanne)*. 2022;9:808969. doi:10.3389/fmed.2022.808969
- Khawaja A. KDIGO clinical practice guidelines for acute kidney injury. *Nephron Clin Pract*. 2012;120(4):c179–c184. doi:10.1159/000339789
- Penny-Dimiri JC, Bergmeir C, Reid CM, Williams-Spence J, Cochrane AD, Smith JA. Machine learning algorithms for predicting and risk profiling of cardiac surgery-associated acute kidney injury. *Semin Thorac Cardiovasc Surg*. 2021;33(3):735–745. doi:10.1053/j.semtcvs.2020.09.028
- Guan C, Li C, Xu L, et al. Risk factors of cardiac surgery-associated acute kidney injury: Development and validation of a perioperative predictive nomogram. *J Nephrol*. 2019;32(6):937–945. doi:10.1007/s40620-019-00624-z
- Kristovic D, Horvatic I, Husedzinovic I, et al. Cardiac surgery-associated acute kidney injury: Risk factors analysis and comparison of prediction models. *Interact Cardiovasc Thorac Surg*. 2015;21(3):366–373. doi:10.1093/icvts/ivv162
- Thongprayoon C, Hansrivijit P, Bathini T, et al. Predicting acute kidney injury after cardiac surgery by machine learning approaches. *J Clin Med*. 2020;9(6):1767. doi:10.3390/jcm9061767
- Cherifa M, Blet A, Chambaz A, Gayat E, Resche-Rigon M, Pirracchio R. Prediction of an acute hypotensive episode during an ICU hospitalization with a super learner machine-learning algorithm. *Anesth Analg*. 2020;130(5):1157–1166. doi:10.1213/ANE.0000000000004539
- Lankadeva YR, May CN, Bellomo R, Evans RG. Role of perioperative hypotension in postoperative acute kidney injury: A narrative review. *Br J Anaesth*. 2022;128(6):931–948. doi:10.1016/j.bja.2022.03.002
- Chhabra G, Vashisht V, Ranjan J. A comparison of multiple imputation methods for data with missing values. *Indian J Sci Technol*. 2017;10(19):1–7. doi:10.17485/ijst/2017/v10i19/110646
- Tian T, Min MR, Wei Z. Model-based autoencoders for imputing discrete single-cell RNA-seq data. *Methods*. 2021;192:112–119. doi:10.1016/j.jymeth.2020.09.010
- Ortega-Loubon C, Fernández-Molina M, Pañeda-Delgado L, Jorge-Monjas P, Carrascal Y. Predictors of postoperative acute kidney injury after coronary artery bypass graft surgery. *Braz J Cardiovasc Surg*. 2018;33(4):323–329. doi:10.21470/1678-9741-2017-0251
- Adhikari L, Ozrazgat-Baslanti T, Ruppert M, et al. Improved predictive models for acute kidney injury with IDEA: Intraoperative Data Embedded Analytics. *PLoS One*. 2019;14(4):e0214904. doi:10.1371/journal.pone.0214904
- Tseng PY, Chen YT, Wang CH, et al. Prediction of the development of acute kidney injury following cardiac surgery by machine learning. *Crit Care*. 2020;24(1):478. doi:10.1186/s13054-020-03179-9
- Jiang YY, Kong XR, Xue FL, et al. Incidence, risk factors and clinical outcomes of acute kidney injury after heart transplantation: A retrospective single center study. *J Cardiothorac Surg*. 2020;15(1):302. doi:10.1186/s13019-020-01351-4
- Yilmaz M, Aksoy R, Kilic Yilmaz V, Balci C, Duzyol C, Tekeli Kunt A. Urine output during cardiopulmonary bypass predicts acute kidney injury after coronary artery bypass grafting. *Heart Surg Forum*. 2016;19(6):E289–E293. doi:10.1532/hsf.1495
- Liao P, Zhao S, Lyu L, et al. Association of intraoperative hypotension with acute kidney injury after liver resection surgery: An observational cohort study. *BMC Nephrol*. 2020;21(1):456. doi:10.1186/s12882-020-02109-9
- Davison E, Affleck A, Daratha KB. Intraoperative hypotension and acute kidney injury in non-cardiac surgery at a large tertiary care medical center. *AANA J*. 2022;90(1):58–63. PMID:35076385.
- Maheshwari K, Turan A, Mao G, et al. The association of hypotension during non-cardiac surgery, before and after skin incision, with postoperative acute kidney injury: A retrospective cohort analysis. *Anaesthesia*. 2018;73(10):1223–1228. doi:10.1111/anae.14416
- Tang Y, Zhu C, Liu J, et al. Association of intraoperative hypotension with acute kidney injury after noncardiac surgery in patients younger than 60 years old. *Kidney Blood Press Res*. 2019;44(2):211–221. doi:10.1159/000498990
- Sun LY, Wijesundera DN, Tait GA, Beattie WS. Association of intraoperative hypotension with acute kidney injury after elective non-cardiac surgery. *Anesthesiology*. 2015;123(3):515–523. doi:10.1097/ALN.0000000000000765
- Futier E, Lefrant JY, Guinot PG, et al. Effect of individualized vs standard blood pressure management strategies on postoperative organ dysfunction among high-risk patients undergoing major surgery: A randomized clinical trial. *JAMA*. 2017;318(14):1346–1357. doi:10.1001/jama.2017.14172
- Godoy LC, Rao V, Farkouh ME. Diabetes and multivessel disease: Coronary artery bypass grafting remains king. *Curr Opin Cardiol*. 2018;33(5):551–557. doi:10.1097/HCO.0000000000000550
- Zhai M, Kang F, Han M, Huang X, Li J. The effect of dexmedetomidine on renal function in patients undergoing cardiac valve replacement under cardiopulmonary bypass: A double-blind randomized controlled trial. *J Clin Anesth*. 2017;40:33–38. doi:10.1016/j.jclinane.2017.03.053
- Shi R, Tie HT. Dexmedetomidine as a promising prevention strategy for cardiac surgery-associated acute kidney injury: A meta-analysis. *Crit Care*. 2017;21(1):198. doi:10.1186/s13054-017-1776-0
- Loskutov O, Danchyna T, Kolesnykov V, Druzina A, Todurov B. Multimodal low-opioid anesthesia: A new approach to the issue of adequate intraoperative analgesia. *Georgian Med News*. 2019;(289):7–11. PMID:31215870.
- Nassif GJ, Miller TE. Evolving the management of acute perioperative pain towards opioid free protocols: A narrative review. *Curr Med Res Opin*. 2019;35(12):2129–2136. doi:10.1080/03007995.2019.1646001
- Wu L, Hu Y, Zhang X, Zhang J, Liu M. Development of a knowledge mining approach to uncover heterogeneous risk predictors of acute kidney injury across age groups. *Int J Med Inform*. 2021;158:104661. doi:10.1016/j.ijmedinf.2021.104661
- Rasmussen SR, Nielsen RV, Møgelvang R, Ostrowski SR, Ravn HB. Prognostic value of suPAR and hsCRP on acute kidney injury after cardiac surgery. *BMC Nephrol*. 2021;22(1):120. doi:10.1186/s12882-021-02322-0

Comparison of primary stability of used and unused self-tapping and self-drilling orthodontic mini-implants

Baris Baser^{1,A–F}, Mehmet Birol Ozel^{2,A,F}

¹ Department of Orthodontics, Faculty of Dentistry, Karadeniz Technical University, Trabzon, Turkey

² Department of Orthodontics, Faculty of Dentistry, Kocaeli University, Turkey

A – research concept and design; B – collection and/or assembly of data; C – data analysis and interpretation; D – writing the article; E – critical revision of the article; F – final approval of the article

Advances in Clinical and Experimental Medicine, ISSN 1899–5276 (print), ISSN 2451–2680 (online)

Adv Clin Exp Med. 2024;33(5):483–489

Address for correspondence

Baris Baser

E-mail: baris.baser@ktu.edu.tr

Funding sources

None declared

Conflict of interest

None declared

Received on February 20, 2023

Reviewed on March 20, 2023

Accepted on July 12, 2023

Published online on September 7, 2023

Abstract

Background. Skeletal anchorage has been the subject of study for many years. Recently, orthodontic mini-implants (MIs) were described as effective tools for anchorage and were named temporary anchorage devices (TADs). The success of MIs depends on their primary stability, which is defined as the lack of mobility in the bone after implant insertion, and the relevant factors affecting primary stability.

Objectives. This study aimed to compare the primary stability of used self-drilling (SD) and self-tapping (ST) MIs with unused ones by performing the insertion torque measurement, Periotest and pull-out test.

Materials and methods. Forty-six used (23 ST, 23 SD) and 46 unused (23 ST, 23 SD) MIs (1.5 mm × 8 mm) were inserted into a synthetic bone with the use of a digital screwdriver. Maximum insertion torque (MIT) values were recorded during the placement of MIs, and then Periotest measurements were made. Following the MIT and Periotest measurements, pull-out tests were performed on all MIs.

Results. The median MIT values (Ncm) of the MIs were as follows: used ST: 17.3, unused ST: 18.9, used SD: 24.1, unused SD: 25.2. The median values obtained after the Periotest were (±): used ST: 0, unused ST: –1, used SD: –3, unused SD: –3. Median pull-out values (N) were: used ST: 148.12, unused ST: 168.12, used SD: 173.12, unused SD: 203.20. Statistically, MIT and pull-out values of the used ST and SD implants were significantly lower compared to those of the unused ST and SD implants ($p < 0.05$).

Conclusions. Used orthodontic MIs showed poor performance compared with unused implants when they were inserted again in the in vitro conditions.

Key words: in vitro, self-tapping, primer stability, self-drilling, orthodontic mini-implant

Cite as

Baser B, Ozel MB. Comparison of primary stability of used and unused self-tapping and self-drilling orthodontic mini-implants. *Adv Clin Exp Med.* 2024;33(5):483–489. doi:10.17219/acem/169511

DOI

10.17219/acem/169511

Copyright

Copyright by Author(s)

This is an article distributed under the terms of the Creative Commons Attribution 3.0 Unported (CC BY 3.0) (<https://creativecommons.org/licenses/by/3.0/>)

Background

Skeletal anchorage has been the subject of study for many years.¹ Recently, orthodontic mini-implants (MIs) were described as effective tools for anchorage and were introduced as temporary anchorage devices (TADs).² These devices have some important advantages, including simple placement, less traumatic surgery, higher hygiene standards, and immediate loading.^{2–6}

The success of orthodontic MIs depends on their primary stability, which is defined as the lack of mobility in bone after MI insertion and some relevant factors that may affect stability.⁷ The MI design, the technique of implant placement, the insertion angle, and the diameter of the pilot drill are generally related to the primary stability of orthodontic MIs.^{8–10} Currently, 2 types of implants are predominantly used in orthodontic practice: self-tapping (ST) and self-drilling (SD) orthodontic MIs.¹¹ Self-tapping MIs require a pre-drilled hole with a diameter similar to the implant width, while self-drilling MIs have pointed tips and cutting threads that allow placement without drilling a pilot hole.¹² Many studies have compared the clinical success rate and superiority of these 2 placement techniques.^{13–16}

The literature also reports on invasive and non-invasive methods, such as pull-out strength (PS), Periotest and insertional torque (IT) tests, that have been introduced to measure the primary stability of orthodontic MIs.^{2,17,18} The IT is directly related to the biomechanical performance of MIs and is defined as the effect of frictional resistance between implant threads and bone.^{19–21} Periotest (Medizintechnik Gulden, Modautal, Germany) is an electronic device that was originally developed to express the physiologic or pathologic mobility of the periodontal tissues surrounding the natural tooth.²² The device has been used to measure the mobility of orthodontic implants. Periotest generates results that are shown digitally as a numeric value.²³ Low values indicate high stability, while high values indicate low stability of the implants.²⁴ Pull-out strength is another common indicator for evaluating the anchorage control of MIs.²⁵ Some studies have examined PS as the result of bone–thread integration failure and provided important information regarding primary stability.²⁶

The use of artificial bone blocks to evaluate the biomechanical performance of MIs has recently become popular due to ethical reasons.^{25,27} Specimens taken from cadavers may have homogeneity problems, although their characteristics are similar to those of *in vivo* tissues.²⁸ Some studies have described the use of synthetic materials that have mechanical features similar to the structure of human bone.^{29,30}

Despite the general use of orthodontic MIs as TADs and the successful results published in the literature, some studies have indicated changes in the MI surface after clinical use.³¹ The physical performance and sterility of orthodontic implants must also be ensured in cases of implant reuse. However, no consensus has been reached

regarding the effects of quality changes on the mechanical behavior of orthodontic MIs.²⁵ Although they are mostly discarded after clinical use, economic factors have led some orthodontists to reuse MIs, similar to orthodontic brackets and wires.^{32–34} Few studies have provided clinicians with valuable information regarding the reuse of MIs while also ensuring maximum cost–benefit ratio and efficiency for orthodontic practices.³ The physical performances of MIs after clinical use and the possible correlations among Periotest, IT and PS evaluations are lacking, although previous research has indicated a relationship between IT and PS values.³⁵

Objectives

The aim of this study was to compare the primary stability of re-used SD and ST orthodontic MIs with as-received ones using Periotest, IT and PS tests.

Materials and methods

Study design

A total of 92 ST and SD cylindrical orthodontic MIs (1.5-mm diameter, 8-mm thread shaft; BioMaterials Korea Inc., Seoul, South Korea) were used in this study. The MIs were divided into 2 main groups according to their condition: as-received (unused, $n = 46$) or retrieved (used, $n = 46$). Then, they were equally subdivided into 2 subgroups according to the placement technique: ST ($n = 23$) or SD ($n = 23$). In total, 46 implants were retrieved from patients after a successful service of between 3.5 and 5.5 months (average: 4.51 months) in a previous study,³¹ with no signs of early or late loss. After their removal, each implant was seated in a sterilizing machine (60 min at 134°C; Getinge 600; Getinge, Göteborg, Sweden) and then stored in a plastic container for reuse. No defects, cracks or corrosion could be established visually for the retrieved implants after the sterilization process. The other 46 MIs were used as received from the manufacturer.

Insertion of the orthodontic implants

A device was made to hold and secure a digital torque meter driver (Geratech TSD-50; Kartal Otomasyon, Kocaeli, Turkey) during the placement of the orthodontic MIs (Fig. 1A). This device allowed for the perpendicular insertion of the implants through a sliding mechanism (Fig. 1B). A total of 92 implantation points were marked on the artificial bone, with enough distance to allow Periotest measurements and the movement of the metal grip designed for the PS test. The self-drilling MIs were placed directly, without a pre-drilling phase. The self-tapping MIs were inserted after drilling a pilot hole (1.2 mm × 31 mm,

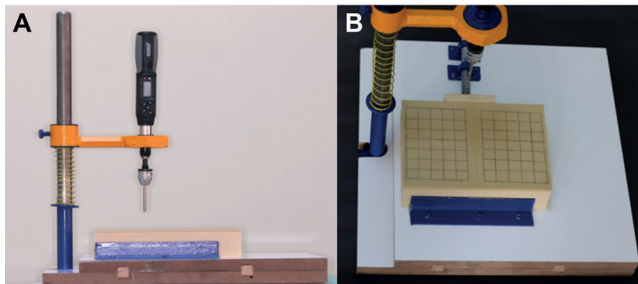


Fig. 1. A. A custom-made device for securing and stabilizing a digital torque meter driver; B. The sliding mechanism and overview of the device

BioMaterials Korea Inc.). The MIs were placed in a custom-made artificial bone block (solid rigid polyurethane foam, 180 mm in length, 13 mm in width and 43 mm in height; Sawbones Pacific Research Laboratories Inc., Vashon, USA) consisting of 2 layers that simulated cortical bone (3-mm thickness with a density of 50 pcf (0.80 g/cc)) and cancellous bone (40-mm thickness with a density of 30 pcf (0.48 g/cc)).^{29,36}

Data measurement

All MIs were placed manually by a single operator, and the maximum insertion torque (MIT) value of each implant was recorded in Ncm using a digital torque meter driver. The overinsertion and friction of the orthodontic MIs were avoided during placement by using a U-shaped metal stopper with a thickness of 1.2 mm to simulate soft tissue. After the placement of each MI, Periotest measurements were performed (Fig. 2A). The PS was evaluated by separating the synthetic bone into 2 equal parts and fastening it to a testing machine (Instron 1011; Instron Corp, Canton, USA) (Fig. 2B). A larger base with bilateral metal clamps was fabricated for the bone blocks to ensure full integration with the testing machine. Pull-out strength tests were performed with a loading rate of 1 mm/min using a grip fabricated for implant seizing that allowed vertical forces to be in the same direction as the long axis of the MIs. Maximum PS values for all MIs were recorded in newtons [N] until failure or rupture occurred. During all processes, the operator was blinded to all data, and a separate researcher recorded the values.



Fig. 2. A. Periotest measurement; B. The installed and separated synthetic bone block fastened to a testing machine for the pull-out test

Statistical analyses

Statistical analyses were performed using SPSS v. 17.0 software (SPSS Inc., Chicago, USA). Descriptive statistical methods (standard deviation, mean, median, minimum, and maximum values) were utilized to analyze the study data. At the data evaluation stage, the Shapiro–Wilk was conducted to assess the normality of the data. The Mann–Whitney U test was performed to determine the statistical significance of differences between the groups. Possible correlations between the MIT, Periotest and PS values were assessed using the Spearman test at the 95% confidence interval (95% CI) level. The level of significance for all statistical tests was predetermined at 0.05.

Results

All orthodontic MIs were placed in the bone without breakage or failure, and all tests were performed successfully. The median MIT of the ST implants was 17.3 Ncm in the retrieved group and 18.9 Ncm in the unused implant group. The median MIT was higher for the new SD implants (25.2 Ncm) than for the used SD implants (24.1 Ncm). The Mann–Whitney U test showed statistically significant differences between the MITs for the ST and SD MIs in both the retrieved ($z = -5.816$, $p = 0.001$) and unused implant groups ($z = -5.814$, $p = 0.001$).

The median values for the Periotest were (\pm) as follows: retrieved ST: 0, unused ST: -1, retrieved SD: -3, and unused SD: -3. A comparison of Periotest values for the different placement techniques revealed statistically significant differences only for the ST implant groups ($p = 0.001$). None of the SD groups showed any relevant differences, whether retrieved or new ($p > 0.05$).

The axial PS test was performed successfully in all groups. During the test, the SD MIs underwent only plastic deformation without any rupture, whereas 35 of the 46 ST orthodontic MIs detached from the head part. The median PS values for the retrieved ST and SD groups were 148.12 N and 173.12 N, respectively. The values for the unused ST and SD groups were 168.12 N and 203.20 N, respectively. All the PS values were higher for the new MIs than for the retrieved implants, and the differences in PS values were statistically significant for all implant types in both groups ($p = 0.001$). The medians, Q1, Q3, as well as Z- and p-values of the MIs for the MIT, PS and Periotest are listed in Table 1 and Table 2.

Statistically, the MIT and PS showed a positive correlation in all orthodontic implant groups. A comparison of the PS values for the different insertion techniques revealed a stronger correlation with MIT values in the retrieved ST group ($r = 0.791$, $p = 0.001$) than in the retrieved SD group ($r = 0.457$, $p = 0.028$). By contrast, the correlation between the MIT and PS values was stronger in the unused SD group ($r = 0.615$, $p = 0.002$) than in the unused

Table 1. The medians, Q1, Q3, Z- and p-values of the unused mini-implants for MIT, PS and Periotest

Measurement method	Self-tapping (n = 23)			Self-drilling (n = 23)			Unused implants (n = 46)	
	median	Q1	Q3	median	Q1	Q3	p-value	Z-value
MIT	18.90	18.10	20.10	25.20	24.90	25.90	0.001*	-5.814
Periotest	-1.00	-3.00	0.00	-3.00	-4.00	-3.00	0.001*	-3.752
PS	168.12	152.41	170.98	203.20	199.190	219.670	0.001*	-5.789

Mann-Whitney U test, * p = 0.001; Q1 – 25th percentile; Q3 – 75th percentile; MIT – maximum insertion torque; PS – pull-out strength.

Table 2. The medians, Q1, Q3, and Z- and p-values of the used mini-implants for MIT, PS and Periotest

Measurement method	Self-tapping (n = 23)			Self-drilling (n = 23)			Used implants (n = 46)	
	median	Q1	Q3	median	Q1	Q3	p-value	Z-value
MIT	17.30	16.90	19.10	24.10	23.70	24.90	0.001*	-5.816
Periotest	0.00	0.00	1.00	-3.00	-3.00	-2.00	0.001*	-5.959
PS	148.12	137.49	159.26	173.12	161.25	177.54	0.001*	-3.965

Mann-Whitney U test, * p = 0.001; Q1 – 25th percentile; Q3 – 75th percentile; MIT – maximum insertion torque; PS – pull-out strength.

Table 3. Correlations between used self-tapping and self-drilling mini-implants

Used implants	Self-tapping		Self-drilling	
	r	p-value	r	p-value
MIT-Periotest	-0.459	0.028*	-0.495	0.016*
MIT-Pull-Out	0.791	0.001**	0.457	0.028*
Periotest-Pull-Out	-0.530	0.009*	-0.389	0.066

r – Spearman's correlation; * p < 0.05; ** p = 0.001.

Table 4. Correlations between unused self-tapping and self-drilling mini-implants

Unused implants	Self-tapping		Self-drilling	
	r	p-value	r	p-value
MIT-Periotest	-0.466	0.025*	-0.625	0.001*
MIT-Pull-Out	0.548	0.007*	0.615	0.002*
Periotest-Pull-Out	-0.559	0.006*	-0.383	0.071

r – Spearman's correlation; * p < 0.05; ** p = 0.001

ST group (r = 0.548, p = 0.007). A negative correlation was found between the MIT and Periotest values of both the retrieved and new implant groups, regardless of the placement technique. The Periotest values were significantly and negatively correlated with PS for both the retrieved and new ST implants. However, according to the Spearman's rank test, the correlation between Periotest and PS values was not statistically significant for any of the SD implant groups (p > 0.05). The correlations between the different drilling types (ST or SD) and conditions (retrieved or new) for assessing MI stability are given in Table 3 and Table 4.

Discussion

The use of orthodontic MIs to achieve anchorage is becoming more common in orthodontic practice.³⁶ Their

properties and differences in use, such as their dimensions, designs and placement protocols, are also becoming more varied to allow clinicians to use them more efficiently.³⁷ Some studies have focused on the influence of the dimensions, insertion angles, cortical thickness, and density of bone on determining the success of MIs and decreasing their failure rate.²⁵ Although many studies have investigated the relationships between the physical properties of implants or the variations in bone and the primary stability of implants, only a few studies have explored the reuse of implants and their success after prior use.²⁵ In the present study, the implant placement protocol was the same as in a previous study³¹ that assessed the mechanical performance of ST compared to SD implants. The latter is currently the most common choice, given that the drilling phase is eliminated during placement. The MIs were also divided into groups to evaluate their mechanical performance according to their condition: as-received (control) or retrieved (experimental). This allowed for the assessment of each implant in terms of condition alone while maintaining all other characteristics.

Although the reuse of invasive medical devices, such as orthodontic MIs, in different patients can be seen as an ethical problem, the reuse of MIs in the same patient may be necessary for economic reasons.³¹ However, no studies focusing on the reuse of orthodontic MIs after their clinical use and how to ensure their primary stability while controlling all other conditions have been conducted. In our study, we examined MIs that had been retrieved and sterilized as our experimental treatment, while the control group received new implants of the same type and with the same properties as the ones used in a previous study.³¹ This raises the intriguing question of whether the condition of the orthodontic MI (retrieved compared to as-manufactured) or the placement technique is what ultimately determines the primary stability of the orthodontic implants.

Synthetic materials are more suitable testing materials than human and animal cadaver materials due to ethical reasons.²⁸ According to the American Society for Testing and Materials (ASTM) standards F1839-08, the homogeneity and consistent features of rigid polyurethane foam make it an ideal material for comparative testing of implants replacing specimens taken from human and animal cadavers.³⁸ Although the use of synthetic bone allowed us to recreate *in vitro* conditions and perform some tests, synthetic material cannot imitate the biological environment provided by organic models.²⁸ In our study, the use of a homogeneous and uniform artificial material overcame the variability of organic specimens. Our study was not intended to represent the biological response of bone tissue, such as osseointegration of dental implants, since the stability of MIs depends on mechanical locking with the bone. Some researchers have reported a density of the mandibular posterior area of 0.64 g/cc.³⁹ Based on these parameters, MIs were placed in a custom-made synthetic block with 2 layers that simulated the cortical bone (3-mm thickness, with a density of 50 pcf (0.80 g/cc)) and the cancellous bone (40-mm thickness with a density of 30 pcf (0.48 g/cc)).

In various studies, robotic systems equipped with machine drivers have been used for the placement of orthodontic MIs at the same angle, tour and speed for standardization.³⁶ In our study, the implants were inserted precisely and manually using a custom-made device that stabilized the digital torque meter driver to keep it vertical to the bone surface, as in previous studies.⁴⁰ The MIT values were lower for the retrieved and autoclaved MIs than for the unused implants, and statistically significant differences were detected between the MIT values of all MIs, regardless of the placement technique ($p = 0.005$, $p < 0.05$, $p = 0.001$). These findings indicate that the prior use or sterilization procedures significantly altered the MIT values of the implants. Similarly, the drilling phase before placement of a MI could decrease the insertion torque, although a technique that eliminates drilling enhances the stability of the thin MI.⁴¹ However, some studies have reported that the insertion torque had a weak relationship with implant stability.⁴²

The comparison of the Periotest values of all implants using different placement techniques revealed statistically significant differences for the ST implants only ($p = 0.001$). The unused and the retrieved SD implants did not show any statistically significant differences ($p > 0.05$). The statistical variation between the insertion techniques may be attributed to the intimate bone–implant contact achieved by the SD implants, which results in more stable values for the Periotest scores compared to the ST implants. These findings confirm that the Periotest scores were more stable for the new MIs than for the retrieved implants. This can be explained by changes in surface morphology due to cleaning and/or mechanical damage during prior placement and removal, as these changes could markedly alter osteoblastic growth and differentiation. Primary implant stability is known to be influenced by the microscopic and

macroscopic morphology of the implant.⁴³ However, our findings are in contrast with the results obtained by Kim et al.,⁴⁴ who found markedly lower Periotest values for SD orthodontic MIs. The differences in the Periotest values and reports might reflect the inconsistency of the Periotest measurements on implants.^{45,46}

In our study, the PS tests were performed by applying vertical forces oriented parallel to the long axis of the orthodontic MIs.³⁹ The application of pull-out tests in the axial direction does not provide a realistic reflection of the clinical situation because it is almost impossible to load MIs in the axial direction in a patient.⁴⁷ However, these tests are widely accepted as a method for comparing different types of implants in the orthopedic, maxillofacial surgery and orthodontic fields.⁴⁸ In our study, the pull-out values were significantly greater in all the unused implant groups than in the retrieved implant groups ($p = 0.001$). Moreover, the pull-out values for the unused implants, especially for the SD ones, were all substantially higher than the values for the unused MIs. The results regarding the PS values confirmed the importance of the implantation procedure and the implant condition in establishing primary stability since the results for the unused SD implants had the highest PS values (203.20 N).

For all implant groups, the Spearman's rank-order correlation performed for the MIT and PS values confirmed a strong, positive and statistically significant correlation between them. However, correlation assessments showed a negative relationship between the MIT and Periotest values for both the retrieved and new implant groups, regardless of the placement technique. The reason for this negative correlation is that lower Periotest values indicated higher implant stability. This finding suggests that the increase in MIT values and the corresponding decrease in Periotest values are evidence of increased primary stability.

Limitations

The stability of the orthodontic MIs might be affected by various biological and mechanical factors, such as bone density, soft tissue condition, oral hygiene, insertion method, and surface treatment.² Other factors, including the chemical composition, surface morphology, chemical composition of the saliva, biofilm formation, pH of the oral environment, protein adsorption, physical and chemical properties of foods, medicines taken by the patient, and oral hygiene habits, can affect the mechanical behavior of the MIs.^{49,50} However, such analysis was not the objective of this study. Nevertheless, these factors must be considered and evaluated in future studies. This study tested unused and used orthodontic MIs employing different placement techniques to compare primary stability based on MIT, PS and Periotest values. No other parameters were analyzed, such as removal torque, lateral displacement, surface alterations, histological analysis, or resonance frequency analysis. These parameters must also be considered and evaluated in further studies.

Conclusions

Used orthodontic MIs showed poor performance compared to unused implants inserted under in vitro conditions.

ORCID iDs

Baris Baser  <https://orcid.org/0000-0002-3052-9023>

Mehmet Birol Ozel  <https://orcid.org/0000-0002-2984-9468>

References

- Creekmore TD, Eklund MK. The possibility of skeletal anchorage. *J Clin Orthod.* 1983;17(4):266–269. PMID:6574142.
- Kim JW, Baek SH, Kim TW, Chang YI. Comparison of stability between cylindrical and conical type mini-implants: Mechanical and histological properties. *Angle Orthod.* 2008;78(4):692–698. doi:10.2319/0003-3219(2008)078[0692:COBCA]2.0.CO;2
- Akyalcin S, McIver HP, English JD, Ontiveros JC, Gallerano RL. Effects of repeated sterilization cycles on primary stability of orthodontic mini-screws. *Angle Orthod.* 2013;83(4):674–679. doi:10.2319/082612-685.1
- Iijima M, Muguruma T, Brantley WA, Okayama M, Yuasa T, Mizoguchi I. Torsional properties and microstructures of miniscrew implants. *Am J Orthod Dentofacial Orthop.* 2008;134(3):333.e1–333.e6. doi:10.1016/j.ajodo.2008.03.012
- Lim SA, Cha JY, Hwang CJ. Insertion torque of orthodontic miniscrews according to changes in shape, diameter and length. *Angle Orthod.* 2008;78(2):234–240. doi:10.2319/121206-507.1
- Papadopoulos MA, Tarawneh F. The use of miniscrew implants for temporary skeletal anchorage in orthodontics: A comprehensive review. *Oral Surg Oral Med Oral Pathol Oral Radiol Endod.* 2007;103(5):e6–e15. doi:10.1016/j.tripleo.2006.11.022
- Marquezan M, Mattos CT, Sant'Anna EF, De Souza MMG, Maia LC. Does cortical thickness influence the primary stability of miniscrews? A systematic review and meta-analysis. *Angle Orthod.* 2014;84(6):1093–1103. doi:10.2319/093013-716.1
- Baumgaertel S. Predrilling of the implant site: Is it necessary for orthodontic mini-implants? *Am J Orthod Dentofacial Orthop.* 2010;137(6):825–829. doi:10.1016/j.ajodo.2008.06.038
- Deguchi T, Nasu M, Murakami K, Yabuuchi T, Kamioka H, Takano-Yamamoto T. Quantitative evaluation of cortical bone thickness with computed tomographic scanning for orthodontic implants. *Am J Orthod Dentofacial Orthop.* 2006;129(6):721.e7–721.e12. doi:10.1016/j.ajodo.2006.02.026
- Mischkowski RA, Kneuert P, Florvaag B, Lazar F, Koebke J, Zöller JE. Biomechanical comparison of four different miniscrew types for skeletal anchorage in the mandibulo-maxillary area. *Int J Oral Maxillofac Surg.* 2008;37(10):948–954. doi:10.1016/j.ijom.2008.07.017
- Yi J, Ge M, Li M, et al. Comparison of the success rate between self-drilling and self-tapping miniscrews: A systematic review and meta-analysis. *Eur J Orthod.* 2017;39(3):287–293. doi:10.1093/ejo/cjw036
- Tepedino M, Masedu F, Chimenti C. Comparative evaluation of insertion torque and mechanical stability for self-tapping and self-drilling orthodontic miniscrews: An in vitro study. *Head Face Med.* 2017;13(1):10. doi:10.1186/s13005-017-0143-3
- Gupta N, Kotrashetti SM, Naik V. A comparative clinical study between self-tapping and drill free screws as a source of rigid orthodontic anchorage. *J Maxillofac Oral Surg.* 2012;11(1):29–33. doi:10.1007/s12663-011-0240-y
- Iwai H, Motoyoshi M, Uchida Y, Matsuoka M, Shimizu N. Effects of tooth root contact on the stability of orthodontic anchor screws in the maxilla: Comparison between self-drilling and self-tapping methods. *Am J Orthod Dentofacial Orthop.* 2015;147(4):483–491. doi:10.1016/j.ajodo.2014.12.017
- Lim HJ, Eun CS, Cho JH, Lee KH, Hwang HS. Factors associated with initial stability of miniscrews for orthodontic treatment. *Am J Orthod Dentofacial Orthop.* 2009;136(2):236–242. doi:10.1016/j.ajodo.2007.07.030
- Son S, Motoyoshi M, Uchida Y, Shimizu N. Comparative study of the primary stability of self-drilling and self-tapping orthodontic miniscrews. *Am J Orthod Dentofacial Orthop.* 2014;145(4):480–485. doi:10.1016/j.ajodo.2013.12.020
- Favero LG, Pisoni A, Paganelli C. Removal torque of osseointegrated mini-implants: An in vivo evaluation. *Eur J Orthod.* 2007;29(5):443–448. doi:10.1093/ejo/cjm062
- Huja SS, Litsky AS, Beck FM, Johnson KA, Larsen PE. Pull-out strength of monocortical screws placed in the maxillae and mandibles of dogs. *Am J Orthod Dentofacial Orthop.* 2005;127(3):307–313. doi:10.1016/j.ajodo.2003.12.023
- Chang CS, Lee TM, Chang CH, Liu JK. The effect of microrough surface treatment on miniscrews used as orthodontic anchors. *Clin Oral Implants Res.* 2009;20(10):1178–1184. doi:10.1111/j.1600-0501.2009.01728.x
- Wu J, Bai YX, Wang BK. Biomechanical and histomorphometric characterizations of osseointegration during mini-screw healing in rabbit tibiae. *Angle Orthod.* 2009;79(3):558–563. doi:10.2319/031108-138.1
- Zhao L, Xu Z, Yang Z, Wei X, Tang T, Zhao Z. Orthodontic mini-implant stability in different healing times before loading: A microscopic computerized tomographic and biomechanical analysis. *Oral Surg Oral Med Oral Pathol Oral Radiol Endod.* 2009;108(2):196–202. doi:10.1016/j.tripleo.2009.03.023
- Inaba M. Evaluation of primary stability of inclined orthodontic mini-implants. *J Oral Sci.* 2009;51(3):347–353. doi:10.2334/josnusd.51.347
- Atsumi M, Park SH, Wang HL. Methods used to assess implant stability: Current status. *Int J Oral Maxillofac Implants.* 2007;22(5):743–754. PMID:17974108.
- Çehrelci S, Arman-Özçırpıcı A. Primary stability and histomorphometric bone-implant contact of self-drilling and self-tapping orthodontic microimplants. *Am J Orthod Dentofacial Orthop.* 2012;141(2):187–195. doi:10.1016/j.ajodo.2011.07.020
- Meira TM, Tanaka OM, Ronsani MM, et al. Insertion torque, pull-out strength and cortical bone thickness in contact with orthodontic mini-implants at different insertion angles. *Eur J Orthod.* 2013;35(6):766–771. doi:10.1093/ejo/cjs095
- Pickard MB, Dechow P, Rossouw PE, Buschang PH. Effects of miniscrew orientation on implant stability and resistance to failure. *Am J Orthod Dentofacial Orthop.* 2010;137(1):91–99. doi:10.1016/j.ajodo.2007.12.034
- Chen CM, Wu JH, Lu PC, et al. Horizontal pull-out strength of orthodontic infrazygomatic mini-implant: An in vitro study. *Implant Dent.* 2011;20(2):139–145. doi:10.1097/ID.0b013e31820fb7d4
- Erbay Elibol FK, Oflaz E, Buğra E, Orhan M, Demir T. Effect of cortical bone thickness and density on pullout strength of mini-implants: An experimental study. *Am J Orthod Dentofacial Orthop.* 2020;157(2):178–185. doi:10.1016/j.ajodo.2019.02.020
- Cho KC, Baek SH. Effects of predrilling depth and implant shape on the mechanical properties of orthodontic mini-implants during the insertion procedure. *Angle Orthod.* 2012;82(4):618–624. doi:10.2319/080911-503.1
- Hung E, Oliver D, Kim KB, Kyung HM, Buschang PH. Effects of pilot hole size and bone density on miniscrew implants' stability. *Clin Implant Dent Relat Res.* 2012;14(3):454–460. doi:10.1111/j.1708-8208.2010.00269.x
- Mattos CT, Ruellas ACDO, Elias CN. Is it possible to re-use mini-implants for orthodontic anchorage? Results of an in vitro study. *Mat Res.* 2010;13(4):521–525. doi:10.1590/S1516-14392010000400015
- Pringle RA, Leman RB, Kratz JM, Gillette PC. An argument for pacemaker reuse: Pacemaker mortality in 169 patients over ten years. *Pacing Clin Electrophysiol.* 1986;9(6 Pt 2):1295–1298. doi:10.1111/j.1540-8159.1986.tb06711.x
- Schwartz Z, Lohmann CH, Blau G, et al. Re-use of implant coverscrews changes their surface properties but not clinical outcome. *Clin Oral Implants Res.* 2000;11(3):183–194. doi:10.1034/j.1600-0501.2000.011003183.x
- Sonis AL. Air abrasion of failed bonded metal brackets: A study of shear bond strength and surface characteristics as determined by scanning electron microscopy. *Am J Orthod Dentofacial Orthop.* 1996;110(1):96–98. doi:10.1016/S0889-5406(96)70094-X
- Boyle JM, Frost DE, Foley WL, Grady JJ. Torque and pullout analysis of six currently available self-tapping and "emergency" screws. *J Oral Maxillofac Surg.* 1993;51(1):45–50. doi:10.1016/S0278-2391(10)80389-1
- Heo YY, Cho KC, Baek SH. Angled-predrilling depth and mini-implant shape effects on the mechanical properties of self-drilling orthodontic mini-implants during the angled insertion procedure. *Angle Orthod.* 2012;82(5):881–888. doi:10.2319/100711-629.1

37. Hitchon PW, Brenton MD, Coppes JK, From AM, Torner JC. Factors affecting the pullout strength of self-drilling and self-tapping anterior cervical screws. *Spine (Phila Pa 1976)*. 2003;28(1):9–13. doi:10.1097/00007632-200301010-00004
38. Buhacoff G. An active seating system for prevention of pressure sores [doctoral thesis]. 1997. Cambridge, USA: Massachusetts Institute of Technology; 1997. <https://dspace.mit.edu/handle/1721.1/43599>.
39. Shah AH, Behrents RG, Kim KB, Kyung HM, Buschang PH. Effects of screw and host factors on insertion torque and pullout strength. *Angle Orthod*. 2012;82(4):603–610. doi:10.2319/070111-427.1
40. Pithon MM, Nojima MG, Nojima LI. In vitro evaluation of insertion and removal torques of orthodontic mini-implants. *Int J Oral Maxillofac Surg*. 2011;40(1):80–85. doi:10.1016/j.ijom.2010.09.013
41. Martinez H, Davarpanah M, Missika P, Celletti R, Lazzara R. Optimal implant stabilization in low density bone. *Clin Oral Implants Res*. 2001;12(5):423–432. doi:10.1034/j.1600-0501.2001.120501.x
42. Ozawa T, Takahashi K, Yamagata M, et al. Insertional torque of the lumbar pedicle screw during surgery. *J Orthop Sci*. 2005;10(2):133–136. doi:10.1007/s00776-004-0883-3
43. Meredith N, Friberg B, Sennerby L, Aparicio C. Relationship between contact time measurements and PTV values when using the Periotest to measure implant stability. *Int J Prosthodont*. 1998;11(3):269–275. PMID:9728122.
44. Kim JW, Ahn SJ, Chang YI. Histomorphometric and mechanical analyses of the drill-free screw as orthodontic anchorage. *Am J Orthod Dentofacial Orthop*. 2005;128(2):190–194. doi:10.1016/j.ajodo.2004.01.030
45. Elias JJ, Brunski JB, Scarton HA. A dynamic modal testing technique for noninvasive assessment of bone-dental implant interfaces. *Int J Oral Maxillofac Implants*. 1996;11(6):728–734. PMID:8990633.
46. Ramp LC, Reddy MS, Jeffcoat RL. Assessment of osseointegration by nonlinear dynamic response. *Int J Oral Maxillofac Implants*. 2000;15(2):197–208. PMID:10795452.
47. Carano A, Lonardo P, Velo S, Incorvati C. Mechanical properties of three different commercially available miniscrews for skeletal anchorage. *Prog Orthod*. 2005;6(1):82–97. PMID:15891787.
48. Brinley CL, Behrents R, Kim KB, Condoor S, Kyung HM, Buschang PH. Pitch and longitudinal fluting effects on the primary stability of mini-screw implants. *Angle Orthod*. 2009;79(6):1156–1161. doi:10.2319/103108-554R.1
49. Marigo G, Elias CN, Marigo M. Surface analysis of 2 orthodontic mini-implants after clinical use. *Am J Orthod Dentofacial Orthop*. 2016;150(1):89–97. doi:10.1016/j.ajodo.2015.12.012
50. Marigo M, Nouer DF, Genelhu MCS, et al. Evaluation of immunologic profile in patients with nickel sensitivity due to use of fixed orthodontic appliances. *Am J Orthod Dentofacial Orthop*. 2003;124(1):46–52. doi:10.1016/S0889-5406(03)00239-7

In vitro effects of deferoxamine on antibiotic susceptibility in Gram-negative bacteria

Mehmet Erinmez^{A–D,F}, Yasemin Zer^{A,C,E,F}

Department of Medical Microbiology, Faculty of Medicine, Gaziantep University, Turkey

A – research concept and design; B – collection and/or assembly of data; C – data analysis and interpretation; D – writing the article; E – critical revision of the article; F – final approval of the article

Advances in Clinical and Experimental Medicine, ISSN 1899–5276 (print), ISSN 2451–2680 (online)

Adv Clin Exp Med. 2024;33(5):491–497

Address for correspondence

Mehmet Erinmez

E-mail: mehmeterinmez92@hotmail.com

Funding sources

The Scientific Research Program of Gaziantep University provided funding for this study under grant No. TF.UT.21.28.

Conflict of interest

None declared

Acknowledgements

We would like to thank Prof. Seval Kul for providing statistical expertise.

Received on January 29, 2023

Reviewed on June 24, 2023

Accepted on July 19, 2023

Published online on August 18, 2023

Cite as

Erinmez M, Zer Y. In vitro effects of deferoxamine on antibiotic susceptibility in Gram-negative bacteria. *Adv Clin Exp Med*. 2024;33(5):491–497. doi:10.17219/acem/169794

DOI

10.17219/acem/169794

Copyright

Copyright by Author(s)

This is an article distributed under the terms of the Creative Commons Attribution 3.0 Unported (CC BY 3.0) (<https://creativecommons.org/licenses/by/3.0/>)

Abstract

Background. Iron is a vital element for the growth of bacteria. Bacteria use several strategies to scavenge iron, such as siderophores, which are thought to be important virulence components. The mammalian host uses various iron-binding substances to make iron unavailable for bacterial uptake. Deferoxamine (DFO) is a semi-synthetic iron chelator that has been licensed for medical use. Iron chelators like DFO may provide an alternative therapeutic technique for treating Gram-negative bacteria infections, which frequently display multidrug resistance.

Objectives. We assumed that iron deprivation or interactions with the cell membrane caused by DFO or increased siderophore synthesis may cause the inhibition or inactivation of proteins and enzymes necessary for critical processes in bacteria. Additionally, we proposed that these bacterial alterations might be the origin of synergistic interactions between DFO and several antibiotics.

Materials and methods. To test this hypothesis, we used disc diffusion, broth microdilution and checkerboard synergy testing methods on combinations of DFO with ceftriaxone, cefepime, meropenem, amikacin, levofloxacin, and tigecycline, respectively, in a total of 55 isolates (*Escherichia coli*, *Klebsiella pneumoniae*, *Pseudomonas aeruginosa*, *Acinetobacter baumannii*, and *Proteus mirabilis* strains – 11 isolates for each genus).

Results. No synergistic or antagonistic interactions were observed between DFO and the tested antibiotics in the *E. coli*, *K. pneumoniae*, *P. aeruginosa*, and *A. baumannii* isolates, while the addition of DFO significantly increased the inhibition zone diameters of cefepime, amikacin, meropenem, tigecycline, and levofloxacin in *P. mirabilis* isolates. According to the checkerboard synergy results, a synergistic interaction was found between DFO and tigecycline, cefepime and amikacin for *P. mirabilis* isolates.

Conclusions. Among the investigated bacteria, a synergy between antibiotics and DFO was only discovered against *P. mirabilis*. We do not believe that this entirely disproves our hypothesis, though. The production of siderophores triggered by the increased metabolic activity of actively proliferating bacteria at the infection site may provide better results. Therefore, expanding these investigations and developing infection models through animal testing would be advantageous.

Key words: deferoxamine, iron, *Proteus mirabilis*

Background

Antimicrobial resistance is a major public health concern and has an impact on many facets of medical practice.¹ Resistant bacterial strains pose a considerable obstacle to proper treatment, as few clinically available antibiotics maintain adequate action.² Gram-negative bacteria are intrinsically more resistant than Gram-positive bacteria because they have an outer membrane that acts as a permeation barrier.³ Resistance is very common among Gram-negative organisms such as *Klebsiella pneumoniae*, *Acinetobacter baumannii*, *Pseudomonas aeruginosa*, and *Escherichia coli*, which are hospital-acquired infectious agents.⁴

Iron, a vital element for growth, is necessary for the activity of numerous proteins and enzymes participating in various physiological pathways such as oxygen transportation, gene regulation and nitrogen fixation.⁵ In the mammalian host, the majority of intracellular iron is stored in ferritin or bound to heme or heme-containing substances, whereas extracellular iron is bound to transferrin, lactoferrin, hemopexin, and haptoglobin, making it unavailable for bacterial uptake.⁶ Bacteria use several strategies to scavenge essential elements such as iron and zinc; therefore, bacteria are in a constant race with the host for micronutrients.⁷ Siderophores are low-molecular weight iron binding substances that are secreted and imported by microorganisms for iron acquisition.⁸ During infection with bacterial and fungal pathogens, siderophores are thought to be important virulence components.⁹ Deferoxamine (DFO) is a semi-synthetic drug derived from the bacterial siderophore desferrioxamine B, which has been licensed for medical use for the treatment of iron excess.¹⁰ Iron chelators that have already withstood toxicity and preclinical testing in animals may provide an alternate therapeutic technique in the case of multidrug-resistant bacteria, where entire classes of antibiotics are no longer treatment options.¹¹ The siderophores may also serve as a facilitator for antibiotics to cross the cell membrane because of the increased permeability induced by iron deprivation.¹²

Objectives

We believe that iron deprivation or interactions with the cell membrane caused by DFO or increased siderophore synthesis may cause inhibition or inactivation of proteins and enzymes necessary for critical processes in bacteria, as well as exhibit synergy with several antibiotics.

Materials and methods

Bacterial isolates

According to the results of the power analysis, a total of 55 isolates were included in the study. Between May 2021

and December 2021, 11 strains of each of the following bacteria: *E. coli*, *K. pneumoniae*, *P. aeruginosa*, *A. baumannii*, and *Proteus mirabilis* were isolated from clinical samples that were randomly selected. While determining the isolates included in the study, resistance profiles and hospital ward or clinical sample type criteria were not used to ensure randomization. To prevent recurrence, only 1 sample from each patient was included in the study. Of the 55 isolates included in the study, 17 were recovered from the urine, 11 from blood, 10 from sputum, 8 from tracheal aspirates, 7 from wound swabs, and 2 from cerebrospinal fluid. The patients whose samples were included in the study were distributed by departments as follows: 18 from intensive care units, 12 from internal medicine clinics, 6 from pediatrics clinics, 4 from infectious diseases, 4 from urology, 2 from cardiology, 2 from neurosurgery, and 7 from other clinics. Of the isolates included in the study, 73% were susceptible to amikacin, 27% to levofloxacin, 62% to meropenem, 33% to cefepime, 40% to ceftriaxone, and 42% to tigecycline. *Escherichia coli* ATCC 25922 and *P. aeruginosa* ATCC 27853 were used as quality control strains. The Vitek2 (Biomérieux, Marcy-l'Étoile, France) system was used for bacterial identification.

Disc diffusion method

Using the disc diffusion method, we aimed to detect potential synergy between DFO and ceftriaxone, cefepime, meropenem, levofloxacin, amikacin, and tigecycline. Also, we aimed to evaluate changes in the resistance of bacteria to antibacterial drugs at increased iron levels, and investigate the synergistic effects of iron chelator and whether it is reversible with the addition of iron to the environment or not. *Escherichia coli*, *K. pneumoniae*, *P. aeruginosa*, *A. baumannii*, and *P. mirabilis* isolates kept in a skim milk storage medium at -20°C were thawed at room temperature and inoculated onto blood agar medium. Bacterial suspensions at a turbidity standard of 0.5 McFarland were prepared with the direct colony suspension method from colonies on agar plates incubated for 24 h. Inoculation was performed by spreading inoculum to the entire surface of the Mueller Hinton–Agar (MHA; Oxoid, Boston, USA) plate with a sterile swab. For each isolate, 6 MHA plates were used for different antibiotics (ceftriaxone, cefepime, meropenem, amikacin, levofloxacin, and tigecycline; Bioanalyse, Ankara, Turkey), and 4 discs were placed on these plates. Control antibiotic discs included a 10 μL antibiotic disc loaded with 10 mg/mL of DFO (Desferal; Novartis, East Hanover, USA), a 10 μL antibiotic disc loaded with ferric iron (Venofer; Vifor, St. Gallen, Switzerland), and a 10 μL antibiotic disc loaded with DFO+ferric iron. The MHA plates were incubated at $35 \pm 2^{\circ}\text{C}$ for 24 h and inhibition zones were measured. The European Antimicrobial Susceptibility Testing Committee (EUCAST) guidelines were followed for the evaluation of zone diameters.¹³

Broth microdilution method

Minimal inhibitory concentration (MIC) values of the commercially available antibacterial drugs ceftriaxone, cefepime, meropenem, levofloxacin, amikacin, and tigecycline and DFO for 55 Gram-negative isolates included in our study were determined with broth microdilution methods according to EUCAST standards (ISO 20776–1:2019). Stock solutions of ceftriaxone, cefepime, meropenem, levofloxacin, amikacin, and tigecycline (Carbosynth, Campton, UK) were prepared in accordance with the manufacturer’s instructions. Water was utilized as a solvent for ceftriaxone, meropenem, levofloxacin, amikacin, and tigecycline. The solvent for cefepime was phosphate buffer (pH 6.0, 0.1 mol/L). Twofold concentrations of antibiotics and DFO ranging between 0.06 µg/mL and 64 µg/mL (from 0.06 µg/mL to 512 µg/mL for DFO) were added to microplate wells filled with cation-adjusted Mueller–Hinton broth (CAMHB). Bacterial suspension at the concentration of 5×10⁵ CFU/mL was inoculated to the microplate wells. Inoculated microplates were incubated at 35 ±2°C for 24 h. The MIC was defined as the lowest antimicrobial drug concentration that inhibits the visible growth of the microorganism in the microdilution wells.

Checkerboard method

In our study, the checkerboard test, a reference method used for determining the efficacy of combinations of antimicrobial agents, was used to determine the fractional inhibitory concentration index (FIC_i) values of the combinations of DFO with ceftriaxone, cefepime, meropenem, amikacin, levofloxacin, and tigecycline antibiotics, and the results of the combinations for 55 Gram-negative bacterial isolates included in our study. In brief, serial twofold dilutions of the 1st compound (antibiotic) were performed across the columns, and serial twofold dilutions of the 2nd compound (DFO) were performed across the rows of a 96-well plate. Individual wells were inoculated with suspensions of overnight cultures in CAMHB

to provide a final inoculum density of 5×10⁵ CFU/mL. The plates were incubated for 24 h at 35 ±2°C. The FIC_i value takes into account the combination of antibiotics that produced the largest change from the MIC of each antibiotic. The following equation was used to quantify the interactions between the tested antibiotics (FIC_i):

$$A/MIC_A + B/MIC_B = FIC_A + FIC_B = FIC_i,$$

where A and B are the MIC of each antibiotic in combination (in a single well), and MIC_A and MIC_B are the MIC of each drug individually. If the FIC_i value was ≤0.5, it was considered synergy; values of greater than 0.5 but less than 1 were considered additive, values between 1 and 4 were interpreted as indifferent, and values >4 were considered antagonism.¹⁴ When a MIC for one of the test compounds was off-scale (greater than the highest concentration tested), the MIC was set to the next highest twofold concentration for calculation of the FIC (e.g., if the MIC was 32 µg/mL, the FIC was calculated based on a MIC of 64 µg/mL).¹⁵

Statistical analyses

Statistical analysis methods were used to evaluate the differences in inhibition zone diameters. The Kolmogorov–Smirnov test and Shapiro–Wilk test were used to test the normality of the subgroups, and the Levene’s test was used to evaluate the homogeneity of variance. Normality and variance homogeneity tests are presented in Supplementary Table 1. For statistical analysis, Student’s t-test and Wilcoxon rank sum test were used for normal and non-normal distributions, respectively. For descriptive statistics, mean ± standard deviation (M ±SD) were used for normal data, while median, 1st quartile (Q1) and 3rd quartile (Q3) values were used for non-normal data. Statistical analysis was carried out using IBM Statistical Package for Social Sciences (SPSS) for Windows v. 24.0 (IBM Corp., Armonk, USA), and p < 0.05 was considered statistically significant. Prior to the study, ethical approval was obtained from Gaziantep University Clinical Research Ethics Committee (approval No. 2021/11 issued on January 27, 2021).

Table 1. Changes in the inhibition zones of antibiotics against *Proteus mirabilis* with and without deferoxamine

Isolate (n = 11)	Antibiotics	Inhibition zone diameters [mm]				Mean increase of inhibition zone diameters (95% CI) control vs. DFO	p-value	t or Z
		control (n = 11)		+DFO (n = 11)				
		mean/median	SD/Q1, Q3	mean/median	SD/Q1, Q3			
<i>Proteus mirabilis</i>	ceftriaxone	28	24, 29	30	28, 33	2.4 (–5.5, 10.3)	0.116 ^W	–1.622
	meropenem	25	25, 26	28	28, 29	2.7 (2.0, 3.3)	<0.001 ^W	–3.914
	amikacin	21	16, 22	29	27, 30	4.8 (2.7, 6.8)	<0.001 ^W	–3.992
	levofloxacin	23	22, 26	28	27, 29	4.3 (1.3, 7.2)	0.004^W	–2.813
	tigecycline	9.5	±0.8	26.6	±2.1	17.1 (15.6, 18.5)	<0.001 ^t	24.559
	cefepime	18.7	±3.7	28.5	±1.8	9.8 (7.2, 12.3)	<0.001 ^t	7.831

DFO – deferoxamine; SD – standard deviation; Q1 – 1st quartile; Q3 – 3rd quartile; 95% CI – 95% confidence interval; ^W – Wilcoxon rank sum test; ^t – t-test. The p-values in bold are statistically significant.

Results

Disc diffusion rest results

No synergistic or antagonistic interactions were observed between DFO and the antibiotics ceftriaxone, cefepime, meropenem, amikacin, tigecycline, and levofloxacin in the *E. coli*, *K. pneumoniae*, *P. aeruginosa*, and *A. baumannii* isolates. No synergistic or antagonistic interactions were observed between DFO and ceftriaxone in *P. mirabilis* isolates, but the zone diameters of cefepime, amikacin, meropenem, tigecycline, and levofloxacin antibiotics increased statistically significantly with the addition of DFO (Table 1). The changes in the antimicrobial inhibition zone diameters of the isolates included in the study with iron supplementation, DFO supplementation and DFO+iron supplementation are shown in detail in Supplementary Table 2.

In *P. mirabilis* isolates, we observed a significant difference in inhibition zone diameters with the addition of the iron chelator. It was evaluated whether the synergistic effect observed between cefepime, amikacin, meropenem, tigecycline, and levofloxacin antibiotics and DFO was reversible by adding iron to the medium or not. The synergy between DFO and levofloxacin, cefepime, amikacin, meropenem, and tigecycline was reversed with

the addition of iron to the medium, while the inhibition zone diameters decreased significantly (Table 2). In addition, significant changes were observed in the inhibition zone diameters of cefepime, meropenem, amikacin, tigecycline, and levofloxacin against *P. mirabilis* isolates in iron-rich and iron-depleted environments (Table 3).

Broth microdilution and checkerboard test results

No bacteriostatic and bactericidal effects were observed in the ranges of human therapeutic doses of DFO (3 mg/kg/day) on the strains tested in our study. Antimicrobial susceptibility results determined using the broth microdilution method and disc diffusion test results were found to be compatible.

According to the checkerboard tests, while no significant synergy was detected in *E. coli*, *K. pneumoniae*, *P. aeruginosa*, and *A. baumannii* isolates, a synergistic interaction was found between tigecycline and cefepime antibiotics and DFO for all *P. mirabilis* isolates. In addition, a synergy between amikacin and DFO was detected in 72% of the *P. mirabilis* isolates included in the study. The results of the checkerboard synergy tests for *P. mirabilis* isolates are given in Table 4. Also, a comparison of the disc diffusion method and checkerboard synergy tests is presented

Table 2. Reversibility assay to determine whether iron supplementation eliminates the deferoxamine impact on inhibition zones in *Proteus mirabilis* isolates

Isolate (n = 11)	Antibiotic	Inhibition zone diameters [mm]				Mean increase of inhibition zone diameters (95% CI) DFO vs. DFO+iron	p-value	t or Z
		+DFO (n = 11)		DFO+iron (n = 11)				
		mean/median	SD/Q1, Q3	mean/median	SD/Q1, Q3			
<i>Proteus mirabilis</i>	ceftriaxone	30	28, 33	28	24, 29	-2.0 (-8.5, 4.5)	0.243 ^W	-1.230
	meropenem	28	28, 29	26	26, 27	-1.7 (-2.2, 1.1)	<0.001^W	-3.493
	amikacin	28.6	±1.8	24.8	±1.6	-3.8 (-5.3, -2.2)	<0.001^t	5.078
	levofloxacin	28	27, 29	26	24, 27	-2.0 (-4.3, 0.3)	<0.001^W	-3.607
	tigecycline	26.6	±2.1	22.8	±2.1	-3.8 (-5.6, -1.9)	0.001^t	4.126
	cefepime	29	27, 30	26	24, 27	-2.7 (-4.2, -1.1)	0.003^W	-2.896

DFO – deferoxamine; SD – standard deviation; Q1 – 1st quartile; Q3 – 3rd quartile; 95% CI – 95% confidence interval; ^W – Wilcoxon rank sum test; ^t – t-test. The p-values in bold are statistically significant.

Table 3. Evaluation of the activity of several different antibiotics against *Proteus mirabilis* isolates in iron-rich and iron-depleted environments

Isolate (n = 11)	Antibiotic	Inhibition zone diameters [mm]				Mean increase of inhibition zone diameters (95% CI) iron vs. DFO	p-value	t or Z
		+iron (n = 11)		+DFO (n = 11)				
		mean/median	SD/Q1, Q3	mean/median	SD/Q1, Q3			
<i>Proteus mirabilis</i>	ceftriaxone	26	22, 29	30	28, 33	-3.4 (-0.6, 7.4)	0.076 ^W	-1.782
	meropenem	26	25, 26	28	28, 29	-2.3 (-2.8, -1.7)	<0.001^W	-3.894
	amikacin	20.0	±2.5	28.6	±1.8	-8.6 (-10.4, -6.7)	<0.001^t	8.898
	levofloxacin	23	22, 26	28	27, 29	-4.4 (-7.3, -1.4)	0.004^W	-2.811
	tigecycline	9.5	±0.8	26.6	±2.1	-17.1 (-18.4, -15.7)	<0.001^t	24.559
	cefepime	18.7	±3.3	28.5	±1.8	-9.8 (-12.0, -7.5)	<0.001^t	8.439

DFO – deferoxamine; SD – standard deviation; Q1 – 1st quartile; Q3 – 3rd quartile; 95% CI – 95% confidence interval; ^W – Wilcoxon rank sum test; ^t – t-test. The p-values in bold are statistically significant.

Table 4. Broth microdilution and checkerboard synergy test results for *Proteus mirabilis* isolates

<i>P. mirabilis</i> isolates	DFO MIC [µg/mL]	Ceftriaxone MIC [µg/mL]	Ceftriaxone +DFO FIC _i and Int	Meropenem MIC [µg/mL]	Meropenem+ DFO FIC _i and Int	Amikacin MIC [µg/mL]	Amikacin+ DFO FIC _i and Int	Levofloxacin MIC [µg/mL]	Levofloxacin+ DFO FIC _i and Int	Tigecycline MIC [µg/mL]	Tigecycline+ DFO FIC _i and Int	Cefepime MIC [µg/mL]	Cefepime+ DFO FIC _i and Int
PM1	>512	1	0.53 indifferent	0.125	1.01 indifferent	2	0.26 synergy	1	0.53 indifferent	1	0.06 synergy	0.5	0.13 synergy
PM2	>512	0.25	1.01 indifferent	0.125	1.01 indifferent	1	0.51 indifferent	0.5	0.26 synergy	1	0.06 synergy	2	0.07 synergy
PM3	>512	0.5	0.51 indifferent	0.125	1.01 indifferent	1	0.13 synergy	0.125	1.01 indifferent	1	0.06 synergy	0.25	0.26 synergy
PM4	>512	0.25	1.01 indifferent	0.125	1.01 indifferent	0.5	0.13 synergy	2	1.12 indifferent	1	0.06 synergy	0.5	0.13 synergy
PM5	>512	0.25	1.01 indifferent	0.125	1.01 indifferent	1	0.51 indifferent	0.5	2.06 indifferent	1	0.06 synergy	1	0.13 synergy
PM6	>512	16	0.98 indifferent	0.125	1.01 indifferent	1	0.26 synergy	0.5	1.03 indifferent	1	0.06 synergy	4	0.26 synergy
PM7	>512	0.25	1.01 indifferent	0.125	1.01 indifferent	0.5	0.13 synergy	4	0.62 indifferent	1	0.06 synergy	0.5	0.13 synergy
PM8	>512	0.25	1.01 indifferent	0.125	1.01 indifferent	0.25	0.26 synergy	4	0.62 indifferent	2	0.03 synergy	0.25	0.26 synergy
PM9	>512	0.25	1.01 indifferent	0.125	1.01 indifferent	0.5	0.26 synergy	0.125	1.01 indifferent	1	0.06 synergy	0.5	0.13 synergy
PM10	>512	0.25	1.01 indifferent	0.125	1.01 indifferent	0.5	0.26 synergy	0.125	1.01 indifferent	2	0.03 synergy	16	0.13 synergy
PM11	>512	0.25	1.01 indifferent	0.125	1.01 indifferent	0.5	0.51 indifferent	1	0.53 indifferent	1	0.06 synergy	0.25	0.26 synergy

PM – *Proteus mirabilis*; Int – interpretation; DFO – deferroxamine; FIC_i – fractional inhibitory concentration index.

Table 5. Comparison of synergy testing with disc diffusion and checkerboard method

Antimicrobial agent	Synergy	
	checkerboard method	disc diffusion ^a
Tigecycline	+	+
Cefepime	+	+
Ceftriaxone	–	–
Amikacin	+*	+
Meropenem	–	+
Levofloxacin	–	+

* synergy was detected in 72% of the isolates; ^a synergy was defined as statistically significant increase in inhibition zone diameters.

in Table 5. Broth microdilution and checkerboard assay results for *E. coli*, *K. pneumoniae*, *P. aeruginosa*, and *A. baumannii* were not included in the paper due to negative results, but are available on request.

Discussion

A thorough understanding of host–bacteria relationships during Gram-negative bacterial infections can strengthen our dwindling arsenal of traditional antibiotics

with new strategies.¹⁶ Sequestration of iron by chelation may be a beneficial adjunct for the treatment of infections, given the relationship between iron excess or dietary iron supplementation and infection.¹⁷ Excess iron has been shown to aggravate the condition of the patient in various infections, including tuberculosis, malaria, invasive bacterial infections, cystitis, keratitis, and wound infections.¹⁸ We also observed that the in vitro bacterial activity was higher in an iron-rich environment since the inhibition zone diameters were lower when compared with inhibition zone diameters in an iron-depleted environment (Table 3). The overabundance of iron is hazardous to the host not just because of enhanced bacterial growth, but by inducing increased inflammatory activity and epithelial cell stress due to lysosomal damage.¹⁹ Iron is known to catalyze Fenton reactions, which generate highly reactive hydroxyl radicals that can compromise lysosomal membrane integrity, leading to the release of hydrolases and redox-active iron into the cytosol, and subsequent injury or cell death.²⁰ Similarly, lysosomal dysfunction induced by iron overload causes chronic liver injury through hepatocellular apoptosis, hepatic inflammation and liver fibrosis in mice fed with an iron-rich diet.²¹ The DFO, as an iron chelator, functions in aiding the host’s intrinsic iron-withholding systems, and appears to be a promising treatment option for local

infections.¹² Iron chelation with DFO improved host cell survival, reduced bacterial proliferation in urothelial cells and reduced autophagy.¹⁹ We have hypothesized that iron limitation conditions may result in increased production of siderophores, specific molecules for transporting iron. Siderophore secretion has the physical outcome of allowing molecules to diffuse away from producers, possibly preventing benefits from being returned to producer cells. Diffusion can still result in significant siderophore loss, putting bacterial fitness at risk.²² Conformational changes in the outer membrane of the bacteria during both increased secretion and uptake of siderophores may be responsible for vulnerabilities against antimicrobial activity. Moreover, under low iron concentrations, several physiological changes may occur in the bacterial pathogens, including a shift to a planktonic state.^{23,24} Bacteria in the planktonic state are known to be more susceptible to certain antimicrobials, suggesting a potential mechanism of iron chelation-induced sensitization to antimicrobials.¹ Because of the increased permeability induced by iron deprivation, siderophores may potentially serve as a facilitator for antibiotics across the cell membrane. Similarly, deprivation of iron reduces the activity of key proteins and enzymes such as cytochromes, which are examples of iron-dependent proteins that are crucial for energy metabolism, and ribonucleotide reductase, which is involved in DNA synthesis. If any of these get disrupted, the multiplication of the microorganism may be halted.¹² Our reversibility assay to determine if iron supplementation decreases the synergistic interaction between DFO and antibiotics revealed that iron supplementation significantly altered DFO's synergistic interaction with all antibiotics tested (Table 2). Therefore, a longer period may be required for permanent changes at a cellular level.

Previous reports revealed that *P. mirabilis* lacks detectable siderophore production.^{25,26} The absence of effective siderophores may explain the differences in *P. mirabilis* isolates in our study. Consistent with our study, in the study conducted by Marcelis et al., *Proteus* were the most susceptible bacteria to ethylenediamine-di-ortho-hydroxyphenylacetic acid (EDDA), a synthetic iron chelator, among Enterobacterales.²⁶ Based on these findings, we could hypothesize that bacteria incapable of producing effective siderophores will be potential targets for iron restriction and iron chelation therapy. Traditionally, siderophore production, or efficient siderophore production, has been considered to be characteristic of aerobic Gram-negative bacteria.²⁷ Anammox bacteria, which oxidize ammonium with nitrite as the terminal electron acceptor in the absence of oxygen, are anaerobic Gram-negative microorganisms within the phylum of planctomycetes and do not possess genes required for siderophore synthesis.^{28,29} Some researchers explain the poor efficacy of siderophore-conjugated antibacterial agents against Gram-positive bacteria with a lack of effective siderophore synthesis.³⁰ Certain Gram-positive bacteria, such

as *Staphylococcus lugdunensis* and *Streptococcus pyogenes*, have been demonstrated to lack endogenous siderophore synthesis.^{31,32} However, it is known that some Gram-positive bacteria can produce siderophores, such as staphyloferrins, bacillibactin and corynebactin.³³ Therefore, a species-level examination would be more useful than a general approach in determining iron chelation therapy targets. Furthermore, genetic modifications affect bacteria's ability to produce siderophores as well as their ability to thrive under iron-restricted conditions.³⁴ Therefore, it may be beneficial to identify genetic modifications at the species level in bacteria for which iron chelation therapy will be preferred in the near future.

Limitations of the study

For the strains included in the study, pulse-field gel electrophoresis may be accompanied by clone analysis, but our resources were limited. The disc diffusion method was unreliable because we lacked the knowledge of whether the disk was saturated with the desired amount of the tested compound. Furthermore, one of the limitations of our study is the inability to compare various bacterial species that lack the ability to produce siderophores.

Conclusions

No synergy was found between antibiotics and DFO against tested microorganisms other than *P. mirabilis*. However, we think that this does not completely rule out our hypothesis. Increased metabolic activities of actively growing bacteria at the site of infection may induce the synthesis of siderophores. We think that it would be beneficial to expand these studies and create infection models with animal experiments.

Supplementary data

The Supplementary materials are available at <https://doi.org/10.5281/zenodo.8132064>. The package contains the following files:

Supplementary Table 1. Tests of normality and variance homogeneity test for disc diffusion results.

Supplementary Table 2. Comparison of the changes in the inhibition zones of the antibiotics with iron supplementation and iron restriction.

ORCID iDs

Mehmet Erinmez  <https://orcid.org/0000-0002-3570-3510>

Yasemin Zer  <https://orcid.org/0000-0002-9078-9900>

References

1. Vinuesa V, McConnell MJ. Recent advances in iron chelation and gallium-based therapies for antibiotic resistant bacterial infections. *Int J Mol Sci.* 2021;22(6):2876. doi:10.3390/ijms22062876

2. Cassini A, Högberg LD, Plachouras D, et al. Attributable deaths and disability-adjusted life-years caused by infections with antibiotic-resistant bacteria in the EU and the European Economic Area in 2015: A population-level modelling analysis. *Lancet Infect Dis*. 2019;19(1):56–66. doi:10.1016/S1473-3099(18)30605-4
3. Zgurskaya HI, López CA, Gnanakaran S. Permeability barrier of Gram-negative cell envelopes and approaches to bypass it. *ACS Infect Dis*. 2015;1(11):512–522. doi:10.1021/acscinfed.5b00097
4. Bassetti M, Righi E. Multidrug-resistant bacteria: What is the threat? *Hematology*. 2013;2013(1):428–432. doi:10.1182/asheducation-2013.1.428
5. Andrews SC, Robinson AK, Rodríguez-Quiñones F. Bacterial iron homeostasis. *FEMS Microbiol Rev*. 2003;27(2–3):215–237. doi:10.1016/S0168-6445(03)00055-X
6. Braun V. Iron uptake mechanisms and their regulation in pathogenic bacteria. *Int J Med Microbiol*. 2001;291(2):67–79. doi:10.1078/1438-4221-00103
7. Cassat JE, Skaar EP. Iron in infection and immunity. *Cell Host Microbe*. 2013;13(5):509–519. doi:10.1016/j.chom.2013.04.010
8. Palmer LD, Skaar EP. Transition metals and virulence in bacteria. *Annu Rev Genet*. 2016;50(1):67–91. doi:10.1146/annurev-genet-120215-035146
9. Sassone-Corsi M, Chairatana P, Zheng T, et al. Siderophore-based immunization strategy to inhibit growth of enteric pathogens. *Proc Natl Acad Sci U S A*. 2016;113(47):13462–13467. doi:10.1073/pnas.1606290113
10. Byrne SL, Krishnamurthy D, Wessling-Resnick M. Pharmacology of iron transport. *Annu Rev Pharmacol Toxicol*. 2013;53(1):17–36. doi:10.1146/annurev-pharmtox-010611-134648
11. Thompson MG, Corey BW, Si Y, Craft DW, Zurawski DV. Antibacterial activities of iron chelators against common nosocomial pathogens. *Antimicrob Agents Chemother*. 2012;56(10):5419–5421. doi:10.1128/AAC.01197-12
12. Gokarn K, Pal R. Activity of siderophores against drug-resistant Gram-positive and Gram-negative bacteria. *Infect Drug Resist*. 2018;11:61–75. doi:10.2147/IDR.S148602
13. European Committee on Antimicrobial Susceptibility Testing (EUCAST). Breakpoint tables for interpretation of MICs and zone diameters. Version 12.0, 2022. Växjö, Sweden: EUCAST Development Laboratory. https://www.eucast.org/fileadmin/src/media/PDFs/EUCAST_files/Breakpoint_tables/v_12.0_Breakpoint_Tables.pdf
14. Davis H, Brown R, Ashcraft D, Pankey G. In vitro synergy with fosfomicin plus doxycyclin against linezolid and vancomycin-resistant *Enterococcus faecium*. *J Glob Antimicrob Resist*. 2020;22:78–83. doi:10.1016/j.jgar.2020.01.014
15. Thwaites M, Hall D, Stoneburner A, et al. Activity of plazomicin in combination with other antibiotics against multidrug-resistant Enterobacteriaceae. *Diagn Microbiol Infect Dis*. 2018;92(4):338–345. doi:10.1016/j.diagmicrobio.2018.07.006
16. Michels KR, Zhang Z, Bettina AM, et al. Hepcidin-mediated iron sequestration protects against bacterial dissemination during pneumonia. *JCI Insight*. 2017;2(6):e92002. doi:10.1172/jci.insight.92002
17. Carver PL. The battle for iron between humans and microbes. *Curr Med Chem*. 2018;25(1):85–96. doi:10.2174/0929867324666170720110049
18. Scott C, Arora G, Dickson K, Lehmann C. Iron chelation in local infection. *Molecules*. 2021;26(1):189. doi:10.3390/molecules26010189
19. Bauckman KA, Mysorekar IU. Ferritinophagy drives uropathogenic *Escherichia coli* persistence in bladder epithelial cells. *Autophagy*. 2016;12(5):850–863. doi:10.1080/15548627.2016.1160176
20. Terman A, Kurz T. Lysosomal iron, iron chelation, and cell death. *Antioxid Redox Signal*. 2013;18(8):888–898. doi:10.1089/ars.2012.4885
21. Lunova M, Goehring C, Kuscuoğlu D, et al. Hepcidin knockout mice fed with iron-rich diet develop chronic liver injury and liver fibrosis due to lysosomal iron overload. *J Hepatol*. 2014;61(3):633–641. doi:10.1016/j.jhep.2014.04.034
22. Kramer J, Özkaya Ö, Kümmerli R. Bacterial siderophores in community and host interactions. *Nat Rev Microbiol*. 2020;18(3):152–163. doi:10.1038/s41579-019-0284-4
23. Banin E, Brady KM, Greenberg EP. Chelator-induced dispersal and killing of *Pseudomonas aeruginosa* cells in a biofilm. *Appl Environ Microbiol*. 2006;72(3):2064–2069. doi:10.1128/AEM.72.3.2064-2069.2006
24. Hancock V, Dahl M, Klemm P. Abolition of biofilm formation in urinary tract *Escherichia coli* and *Klebsiella* isolates by metal interference through competition for fur. *Appl Environ Microbiol*. 2010;76(12):3836–3841. doi:10.1128/AEM.00241-10
25. Massad G, Zhao H, Mobley HL. *Proteus mirabilis* amino acid deaminase: Cloning, nucleotide sequence, and characterization of aad. *J Bacteriol*. 1995;177(20):5878–5883. doi:10.1128/jb.177.20.5878-5883.1995
26. Marcelis JH, Den Daas-Slagt HJ, Hoogkamp-Korstanje JAA. Iron requirement and chelator production of Staphylococci, *Streptococcus faecalis* and Enterobacteriaceae. *Antonie van Leeuwenhoek*. 1978;44(3–4):257–267. doi:10.1007/BF00394304
27. Ito A, Sato T, Ota M, et al. In vitro antibacterial properties of cefiderocol, a novel siderophore cephalosporin, against Gram-negative bacteria. *Antimicrob Agents Chemother*. 2018;62(1):e01454-17. doi:10.1128/AAC.01454-17
28. Kartal B, De Almeida NM, Maalcke WJ, Op Den Camp HJM, Jetten MSM, Keltjens JT. How to make a living from anaerobic ammonium oxidation. *FEMS Microbiol Rev*. 2013;37(3):428–461. doi:10.1111/1574-6976.12014
29. Strous M, Pelletier E, Mangenot S, et al. Deciphering the evolution and metabolism of an anaerobic bacterium from a community genome. *Nature*. 2006;440(7085):790–794. doi:10.1038/nature04647
30. Simner PJ, Patel R. Cefiderocol antimicrobial susceptibility testing considerations: The Achilles' heel of the Trojan horse? *J Clin Microbiol*. 2020;59(1):e00951-20. doi:10.1128/JCM.00951-20
31. Brozyna JR, Sheldon JR, Heinrichs DE. Growth promotion of the opportunistic human pathogen, *Staphylococcus lugdunensis*, by heme, hemoglobin, and coculture with *Staphylococcus aureus*. *MicrobiologyOpen*. 2014;3(2):182–195. doi:10.1002/mbo3.162
32. Eichenbaum Z, Muller E, Morse SA, Scott JR. Acquisition of iron from host proteins by the group A *Streptococcus*. *Infect Immun*. 1996;64(12):5428–5429. doi:10.1128/iai.64.12.5428-5429.1996
33. Sheldon JR, Heinrichs DE. Recent developments in understanding the iron acquisition strategies of Gram-positive pathogens. *FEMS Microbiol Rev*. 2015;39(4):592–630. doi:10.1093/femsre/fuv009
34. Niño-Liu DO, Ronald PC, Bogdanove AJ. *Xanthomonas oryzae* pathogens: Model pathogens of a model crop. *Mol Plant Pathol*. 2006;7(5):303–324. doi:10.1111/j.1364-3703.2006.00344.x

Human umbilical cord mesenchymal stem cell-derived exosomal miR-214-3p regulates the progression of gallbladder cancer by regulating ACLY/GLUT1

Luyao Liu^{1,A,B,D,F}, Wang Xiao^{2,B,C,E,F}, Zhulin Yang^{2,B,C,F}, Qunwei Wang^{2,A,C,F}, Jianing Yi^{3,A,C,E,F}

¹ Department of General Surgery, Hunan Provincial People's Hospital, The First Affiliated Hospital of Hunan Normal University, Changsha, China

² Department of General Surgery, The Second Xiangya Hospital of Central South University, Changsha, China

³ Department of Breast and Thyroid Gland Surgery, Hunan Provincial People's Hospital, The First Affiliated Hospital of Hunan Normal University, Changsha, China

A – research concept and design; B – collection and/or assembly of data; C – data analysis and interpretation; D – writing the article; E – critical revision of the article; F – final approval of the article

Advances in Clinical and Experimental Medicine, ISSN 1899–5276 (print), ISSN 2451–2680 (online)

Adv Clin Exp Med. 2024;33(5):499–510

Address for correspondence

Jianing Yi

E-mail: yijianing@hunnu.edu.cn

Funding sources

None declared

Conflict of interest

None declared

Received on November 11, 2022

Reviewed on February 14, 2023

Accepted on July 24, 2023

Published online on September 25, 2023

Cite as

Liu L, Xiao W, Yang Z, Wang Q, Yi J. Human umbilical cord mesenchymal stem cell-derived exosomal miR-214-3p regulates the progression of gallbladder cancer by regulating ACLY/GLUT1. *Adv Clin Exp Med.* 2024;33(5):499–510. doi:10.17219/acem/169976

DOI

10.17219/acem/169976

Copyright

Copyright by Author(s)

This is an article distributed under the terms of the Creative Commons Attribution 3.0 Unported (CC BY 3.0) (<https://creativecommons.org/licenses/by/3.0/>)

Abstract

Background. Human umbilical cord mesenchymal stem cell (hucMSC)-derived exosomes have been reported to be effective in the treatment of cancer. The miR-214-3p is a suppressor miRNA that has been extensively studied and has been proposed as a diagnostic and prognostic biomarker in some cancers.

Objectives. The aim of this study was to investigate whether the regulatory mechanism of hucMSC-derived exosomal miR-214-3p with GLUT1 and ACLY affects the proliferation and apoptosis of gallbladder cancer (GBC) cells.

Materials and methods. We found that the target genes of miR-214-3p on the TargetScan website contain GLUT1 and ACLY, and the targeting relationship was verified using luciferases. The GBC-SD cells overexpressing GLUT1 and ACLY were constructed to determine proliferation, apoptosis, migration, and other cellular activities.

Results. We identified hucMSCs and exosomes, and found that the exosomes contained miR-214-3p. Furthermore, TargetScan predicted that miR-214-3p had base interactions with ACLY. Dual luciferase assays showed that miR-214-3p could inhibit ACLY ($p < 0.05$). The results of quantitative reverse transcription polymerase chain reaction (RT-qPCR) and western blot showed that exosomal miR-214-3p could inhibit the expression of ACLY and GLUT1 ($p < 0.05$). Exosomal miR-214-3p can inhibit the proliferation, cloning and migration of GBC-SD cells ($p < 0.05$). The apoptosis of GBC-SD cells was increased ($p < 0.05$). The GBC-SD cells overexpressing ACLY and GLUT1 could reverse the efficacy of miR-214-3p.

Conclusions. Exosomal miR-214-3p can inhibit the downstream expression of ACLY and GLUT1. The ACLY and GLUT1 could affect the proliferation and apoptosis of GBC-SD cells.

Key words: GLUT1, exosomes, miR-214-3p, ACLY

Background

Gallbladder cancer (GBC) is an uncommon human malignancy that has a particular geographical distribution in Central and South America, Central and Eastern Europe, Japan, and Northern India.^{1,2} It is on the rise globally and its prognosis is very poor. Since GBCs are usually asymptomatic, early diagnosis may not be possible.³ Clinical evidence indicates that many GBC patients are diagnosed as inoperable, a state at which the tumor has already become invasive and metastatic.⁴ The overall prognosis of GBC is extraordinarily poor and the mean survival ranges from 13.2 to 19 months.⁵ Although some prognostic biomarkers in adenocarcinoma (ASC) have shown some promise, the clinical use of these proposed biomarkers has not yet been approved.^{6,7} Currently, there are no reliable or acceptable molecular markers associated with simple cholecystectomy (SC) or ASC progression and prognosis.

During oncogenesis, the metabolism of a tumor cell is reprogrammed to support rapid proliferation of tumor cells.⁸ Previous studies have reported that many metabolic genes play a significant role in the progression of cancer, and can be used as putative biomarkers for prognosis and targets for therapeutic agents. The basic metabolic processes of tumor cells are glycolysis and lipogenesis. It was discovered that most fatty acids in cancer come from lipogenesis.⁹ Glycolysis is a biochemical process. In cancer cells, adenosine triphosphate (ATP) is the main energy source.¹⁰ Moreover, the fatty acids synthesized in the process of adipogenesis are used as the main fuel for the rapid proliferation of cancer cells to produce cell membranes.¹¹ At present, at least 5 genes in the glycolysis and lipogenesis pathways are directly involved in tumorigenesis and tumor progression. The GLUT1 promotes increased glucose transport in tumor cells and maintains a high glycolysis rate in aerobic conditions. However, ACLY can convert citrate into acetyl-CoA for fat generation as a cell solute enzyme.⁹ Therefore, GLUT1 and ACLY are known as key enzymes in the rate-limiting first step of the metabolic pathway. In various tumors, such as breast cancer,^{12,13} colorectal cancer,^{14,15} gastric cancer,^{16,17} hepatocellular cancer,^{18,19} and prostate cancer,^{20–22} GLUT1 and ACLY are upregulated. In this regard, we further explored whether GLUT1 and ACLY play a role in the life activities of cholangiocarcinoma cells.

The human umbilical cord mesenchymal stem cell (hucMSC)-derived exosomes (hucMSC-exo) exert anti-inflammatory effects on human trophoblastic cells by transferring miRNAs.²³ The miR-214 was reported to be a member of a vertebrate-specific miRNA precursor involved in regulating glucose metabolism in the liver.²⁴ It also has an important role in skeletal diseases.²⁵ The miR-214-3p is a suppressor miRNA that has been extensively studied and has been proposed as a diagnostic and prognostic biomarker in some cancers.²⁶

Objectives

Therefore, the aim of the study was to investigate whether the regulatory mechanism of miR-214-3p with GLUT1 and ACLY affects the proliferation and apoptosis of GBC cells.

Materials and methods

Cell transfection

Human gallbladder carcinoma GBC-SD cells (BNCC100091) were purchased from Beina Biological Co., Ltd. (Beijing, China). The required si-RNA-negative control (NC), si-GLUT1 and si-ACLY were removed, and ice thawing was performed. Two of the 8 sterile centrifuges were taken, and 95 μ L of serum-free 1640 medium was added to each tube. Then, 5 μ L of i-RNA-NC and 5 μ L of Lipofectamine 2000 were added to the centrifuges, respectively. Another si-RNA was added to the corresponding centrifuge tube in the same way. The mixture was gently mixed and left to stand for 5 min at room temperature. Then, the 2 tubes were gently mixed and left to stand for 20 min at room temperature. Finally, the mixture was evenly added to the wells to be transfected and mixed. All plasmids were purchased from HonorGene Company (Changsha, China).

Separation of exosomes

The hucMSCs were obtained from the umbilical cord tissue of newborns. Five cell surface markers (CD105, CD90, CD34, CD14, and CD166) were evaluated to identify hucMSCs. The hucMSCs were counted to ensure that each cell suspension had more than 1×10^6 cells. The cells were incubated with human anti-CD105 (P-phycoerythrin (PE)), anti-CD90 (PE), anti-CD34 (PE), anti-CD14 (fluorescein isothiocyanate (FITC)), and anti-CD166 (FITC) (all from eBioscience, San Diego, USA), respectively, for 30 min at room temperature. Then, the cells were washed and suspended for flow cytometry analysis. Half the volume of an exosome separation solution was added to the supernatant, blown, mixed, and placed in the refrigerator at 4°C overnight. After 12 h, the supernatant was centrifuged for 1 h at 4°C. The supernatant solution was discarded, and the precipitate was retained. The precipitate was blown with phosphate-buffered saline (PBS) and fully mixed to form an exosome suspension. The concentration of exosomes was detected with bicinchoninic acid (BCA) protein concentration and stored at -80°C as reserve. The effective storage time of exosomes was 1 month.

Identification of exosomes

The exosomes were identified with transmission electron microscopy (TEM) (Tecnai™ G2 Spirit BIOTWIN; Thermo Fisher Scientific, Waltham, USA). A volume

of 20 μL of exosomes was dropped onto the copper mesh and left for 3 min. The cells were dried with an incandescent lamp, and pictures were taken under the TEM. The particle size analysis was performed using a nanoparticle tracking analysis (NS300; Malvern Panalytical, Malvern, UK). Western blot was utilized to identify the surface markers of exosomes. The protein content of the exosome suspension was measured with the use of a BCA kit (23227; Thermo Fisher Scientific), the sodium dodecyl-sulfate polyacrylamide gel electrophoresis (SDS-PAGE) gel was prepared, protein denaturation and electrophoresis were performed, and the membrane was transferred to detect the exosome-specific marker protein HSP70 (ab5439, 1:1000), CD63 (ab134045, 1:2000), CD81 (ab79559, 1:1000), and calnexin (ab22595, 1 $\mu\text{g}/\text{mL}$; Abcam, Cambridge, UK).

Alizarin red S assay

Oligodendrocyte Medium (OM) was used to culture 2×10^4 cells for 7 days. Then, the cells were stained with alizarin red and quantitatively analyzed. A nitro tetrazolium Blue chloride (NBT)/5-Bromo-4-chloro-3-indolyl phosphate (BCIP) staining kit (72091; MilliporeSigma, St. Louis, USA) was used for alizarin red staining after cell fixation. The alizarin red Active Colorimetric Quantitative Detection Kit was purchased from Nanjing Jiancheng Reagent Company (Nanjing, China). Depending on the instructions, the cells were collected, separated at 1000 rpm for 10 min, and observed with Triton-X100 or X400. The optical density (OD) of cells was measured at 520 nm. The experiment was repeated 3 times.

Oil Red O staining

Modified Oil Red O staining solution was used to stain 2×10^4 cells for 10–15 min in airtight conditions, protected from light. Mayer's hematoxylin staining solution was added to remove the stain, and the nuclei were restained for 5 min. The slices were blotted with filter paper and sealed with glycerol gelatin or gum arabic.

RT-qPCR

Total RNA was extracted from brain tissues using Trizol (15596026; Thermo Fisher Scientific).

About 500 μL of GBC-SD cells were collected into a new 1.5-mL centrifuge tube, and Trizol was supplemented to 1 mL after mixing, followed by chamber lysis for 3 min. Next, 200 μL of trichloromethane were added into the centrifuge tube, the tube was shaken vigorously for 15 s and then stood at room temperature for 3 min. The concentration was determined with a ultraviolet (UV) spectrophotometer, the absorbance (OD) value was measured at 260 nm and 280 nm, and the concentration and purity were calculated. Vortex oscillation mixing and temporary centrifugation were used for the wall of the solution

Table 1. Primer sequences

Gene	Sequence (5'-3')
<i>miR-214-3p</i>	F: CTGGCTGGACAGAGTTGTCAT
	R: GCTGTACAGGTGAGCGGATG
<i>GLUT1</i>	F: CTATGGGGAGAGCATCCTGC
	R: CCCAGTTTCGAGAAGCCAT
<i>ACLY</i>	F: CCTCAGCCATCCAGAATCGG
	R: CTCAGCCAGGACTTGACCC
β -actin	F: ACCCTGAAGTACCCCATCGAG
	R: AGCACAGCTGGATAGCAAC
<i>U6</i>	F: CTCGCTTCGGCAGCACA
	R: AACGCTTCACGAATTTGCCGT

to be collected at the bottom of the tube. The solution was incubated for 50 min at 50°C and 5 min at 85°C. Reaction conditions were as follows: 40 cycles of pre-denaturation at 95°C for 10 min, denaturation at 94°C for 15 s and annealing at 60°C for 30 s. After the reaction, the tubes were briefly centrifuged and cooled on ice. The internal reference primer was β -actin. The primer sequences are presented in Table 1. With 2 μg cDNA as template, the $2^{-\Delta\Delta\text{Ct}}$ relative quantitative method was used. The relative transcription level of the target gene was calculated as follows (Equation 1,2):

$$\Delta\Delta\text{Ct} = \Delta \text{ experimental group} - \Delta \text{ control group} \quad (1)$$

$$\Delta\text{Ct} = \text{Ct (target gene)} - \text{Ct (\beta-actin)} \quad (2)$$

Western blot

The GBC-SD cells were extracted using the Total Protein Extraction Solution RIPA kit (R0010; Beijing Solarbio Science & Technology Co., Ltd., Beijing, China). For primary antibodies, we used rabbit anti-p-mTOR (1:5000, ab109268), mouse anti-mTOR (1:10000, 66888-1-Ig), mouse t anti-p-AKT (1:5000, 66444-1-Ig), rabbit anti-AKT (1:1000, 10176-2-AP), rabbit anti-p-PI3K (0.5 $\mu\text{g}/\text{m}$, ab278545), mouse anti-PI3K (1:800, 67071-1-AP), mouse anti-Bax (1:10000, 60267-1-AP), mouse anti-Bcl-2 (1:1000, 60178-1-AP), rabbit anti-caspase 3 (1:5000, #9661, CSTO), and mouse anti- β -actin (1:5000, 66009-1-Ig). All antibodies were purchased from Proteintech Genomics (San Diego, USA). The membrane was immersed in Superecl Plus (k-12045-d50, Advansta, USA) for the development of luminescence. The β -actin was used as an internal reference. Image J software (NIH, USA) was utilized to analyze gray values.

CCK-8

Cells in each group were counted and inoculated into 96-well plates at a density of 5×10^3 cells/well, 100 μL per well. Each group was equipped with 3 multiple holes. After culture and adherence, the treatment was carried

out in accordance with the above method. After the corresponding time, 10 μ L of Cell Counting Kit-8 (CCK-8) (NU679; Dojindo Laboratories, Kumamoto, Japan) was added to each well, and the CCK-8 solution was prepared with a complete medium. Then, the drug-containing medium was removed and 100 μ L of CCK-8 medium was added to each well. The OD value at 450 nm was analyzed using the BioTek microplate analyzer (DSZ2000X; Cnmicro, Beijing, China) after further incubation at 37°C for 4 h at 5% CO₂, and the mean value was drawn as a histogram.

Wound healing assay

A flask of cells was taken and trypsinized, and after counting, approx. 5×10^5 cells were added to each well. After the cells were covered with the plate, the pipette tip was used to draw a horizontal line perpendicular to the previously drawn horizontal line. Cells were washed 3 times with sterile PBS, streaked cells were removed, and serum-free 1640 medium (R8758; Sigma-Aldrich, St. Louis, USA) was added. The scratches were photographed at 0 h, and 3 fields of view were taken at each timepoint. After culturing at 37°C and 5% CO₂ for 24 h and 48 h, pictures were taken again for recording.

Double luciferase activity

The target gene analysis of ACLY with miR-214-3p was performed using TargetScan website (https://www.targetscan.org/vert_80) to verify whether there is a targeting relationship between ACLY and miR-214-3p using the luciferase reporter gene assays. The target gene ACLY dual luciferase reporter gene vector and mutants with mutations of the binding site of miR-214-3p (pGL3-ACLY Wt and pGL3-ACLY Mut) were constructed, respectively. Two reporter plasmids were co-transfected with the overexpression of miR-214-3p into cells, and 24 h after transfection, the cells were lysed according to the TransDetect® Double-Luciferase Reporter Assay Kit procedure (FR201-01; full-form gold; Antipedia, Beijing, China), and the supernatant was collected. After that, 100 μ L of luciferase reporter gene activity (Renilla luciferase) was added to Reaction Reagent II and the ratio of firefly luciferase to sea kidney luciferase (FL/RL) was used to determine relative luciferase activity. Each experiment was repeated 3 times.

Cell colony formation

Cells from each group of the p-index growth phase were taken, digested with 0.25% trypsin, blown into individual cells, and suspended in a complete medium with 10% calf serum. The cells were incubated at 37°C in 5% CO₂ and saturated humidity for 2–3 weeks, with appropriate fluid changes. The culture medium was discarded, and the PBS solution (SH30256.01; HyClone, Logan, USA) was carefully washed twice. The 6-well plate was removed and soaked

with 1 mL of 10% acetic acid to decolorize. The absorbance was measured at 450 nm using a microplate reader (MB-530; Huisong Pharmaceuticals, Hangzhou, China).

Flow cytometry analysis

The cells were collected using digestion with ethylenediaminetetraacetic acid (EDTA)-free trypsin. They were washed twice with PBS and centrifuged at 2000 rpm for 5 min each time to collect approx. 3.2×10^5 cells. Next, 500 μ L of binding buffer was added to suspend the cells. After adding 5 μ L of Annexin V-APC, 5 μ L of propidium iodide (MBC0409; Meilunbio, Wuhan, China) was added, mixed at room temperature and protected from light. The reaction was performed for 10 min within 1 h and detected with flow cytometry.

The fixed sample was taken out, centrifuged at 800 rpm for 5 min, and the supernatant was discarded. Then, 1 mL of pre-cooled PBS was added to resuspend the cells, centrifuged at 800 rpm for 5 min, and the cells were collected by centrifugation. Next, 150 μ L of propidium iodide working solution was added and stained at 4°C for 30 min in the dark. The percentage of each cell cycle on the fluorescence histogram was analyzed.

Transwell assay

The cells treated above were digested with trypsin to form single cells, resuspended in serum-free medium to 2×10^6 cells/mL, and 100 μ L of cells were added to each well. The upper chamber was taken out and placed in a new well containing PBS. The pore size was 8 μ m. The samples were stained with 0.1% crystal violet (G1062; Beijing Solarbio Science & Technology Co., Ltd.) for 5 min, washed with water 5 times, placed on a glass slide, and photographed under a microscope (model DSZ2000X; Cnmicro). The cells on the outer surface of the upper chamber were observed under an inverted microscope (model DSZ2000X; Cnmicro), and 3 fields of view were taken for each. The chamber was taken out and soaked in 500 μ L of 10% acetic acid to decolorize, and the OD value was measured with a microplate reader (DSZ2000X; Cnmicro) at 550 nm.

Statistical analyses

All measurement data were expressed as mean \pm standard deviation (M \pm SD). The data were analyzed using GraphPad Prism v. 8.0 software (GraphPad Software, San Diego, USA). The Shapiro–Wilk test and F-test were used to compare variances and to evaluate whether the data conformed to a normal distribution and homogeneity of variance assumption. The unpaired Student's t-test was used to compare the data between 2 groups that did not have one-to-one correspondence. The Shapiro–Wilk test and the Brown–Forsythe test were used to analyze whether the data conformed to a normal distribution and

homogeneity of variance assumption. One-way analysis of variance (ANOVA) and Tukey’s post hoc test were used to compare data among 3 groups. The measurement data obeyed the normal distribution and homogeneity of variance. The degrees of freedom and p-values for normal distribution were used to present the results of the analysis. The difference was statistically significant at $p < 0.05$.

Results

Identification of hucMSCs and exosomes

First, we performed cultures on the purchased hucMSCs. The cells showed shuttle-shaped, swirling growth (Fig. 1A). Flow cytometry was used to detect the cell surface antigens CD14 (0.80%), CD34 (0.54%), CD90 (98.76%), CD105 (96.01%), and CD166 (97.03%) (Fig. 1B). The hucMSCs showed osteogenic capacity (Fig. 1C) and lipogenic capacity (Fig. 1D). Transmission electron microscopy was used to observe the secretion of exosomes by huc-MSCs (Tecnaï™ G2 Spirit BIOTWIN; Thermo Fisher Scientific). Exosomes were collected and were positive for exosome markers CD63, CD81 and HSP70, and negative for calnexin and elevated miR-214-3p expression (Fig. 1E–G). All raw data are presented in Supplementary Table 1. In short, hucMSCs can secrete exosomal miR-214-3p.

(96.01%), and CD166 (97.03%) (Fig. 1B). The hucMSCs showed osteogenic capacity (Fig. 1C) and lipogenic capacity (Fig. 1D). Transmission electron microscopy was used to observe the secretion of exosomes by huc-MSCs (Tecnaï™ G2 Spirit BIOTWIN; Thermo Fisher Scientific). Exosomes were collected and were positive for exosome markers CD63, CD81 and HSP70, and negative for calnexin and elevated miR-214-3p expression (Fig. 1E–G). All raw data are presented in Supplementary Table 1. In short, hucMSCs can secrete exosomal miR-214-3p.

Exosomal miR-214-3p can affect the proliferation of GBC-SD

The above results indicated the presence of miR-214-3p in hucMSC exosomes. To investigate the effect of exosomal miR-214-3p on the development of cholangiocarcinoma,

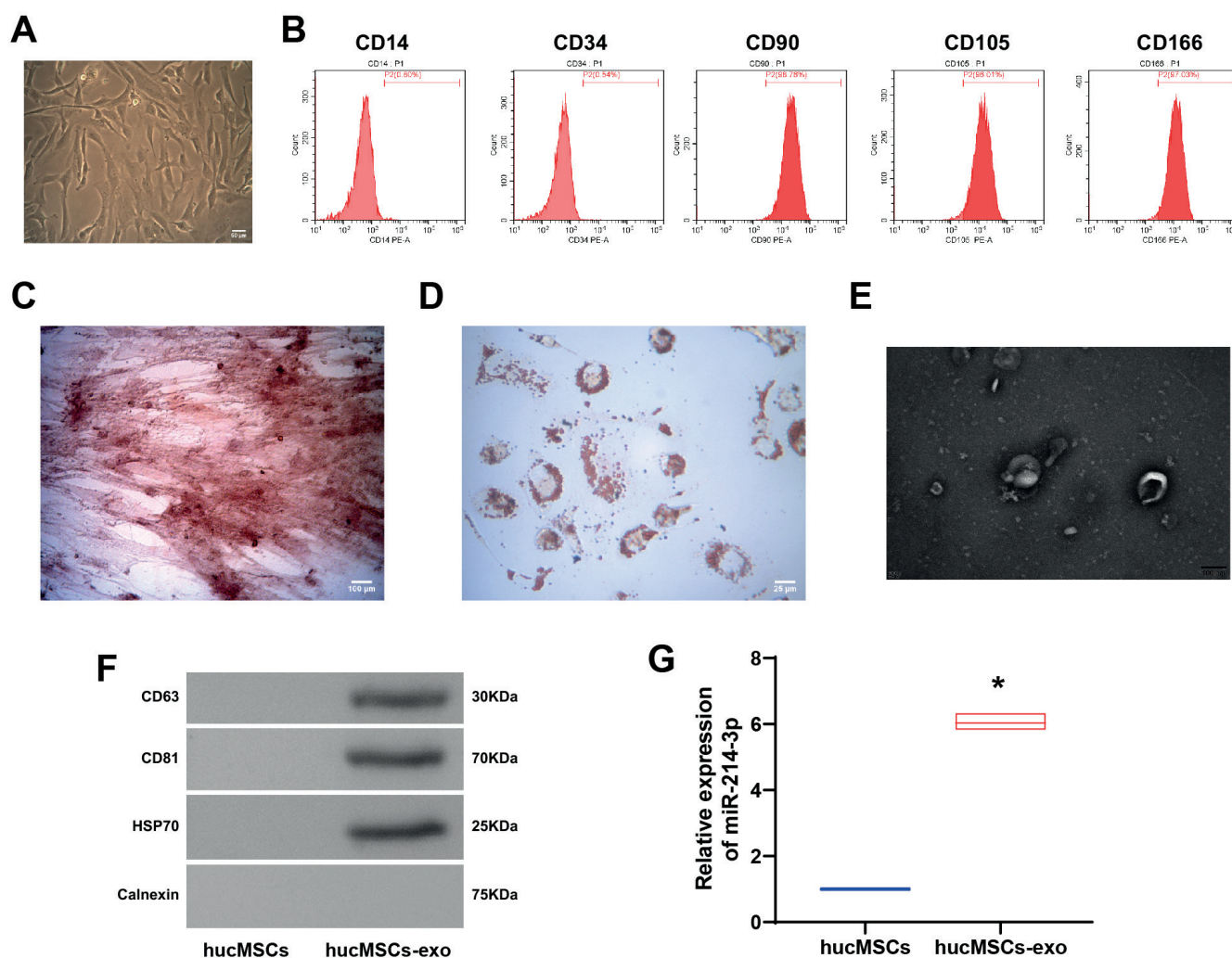


Fig. 1. Human umbilical cord mesenchymal stem cells (hucMSCs) can secrete exosomes. A. Fibrous appearance of hucMSCs; B. The ratio of markers indicates that the cells are hucMSCs; C. Alizarin red staining was used to observe the osteogenic ability of induced hucMSCs; D. Oil Red O staining was utilized to observe the ability to induce lipogenesis in hucMSCs; E. Transmission electron microscopy (TEM) recording of exosome images; F. Western blotting was used to detect hucMSC-derived exosomes (hucMSCs-exo) – CD63, HSP70, CD81, and calnexin; G. Quantitative reverse transcription polymerase chain reaction (RT-qPCR) was utilized to detect miR-214-3p expression in the hucMSC group and hucMSCs-exo group. The unpaired t-test was used to analyze comparisons between the 2 groups (n = 3)

* $p < 0.05$ compared to hucMSCs.

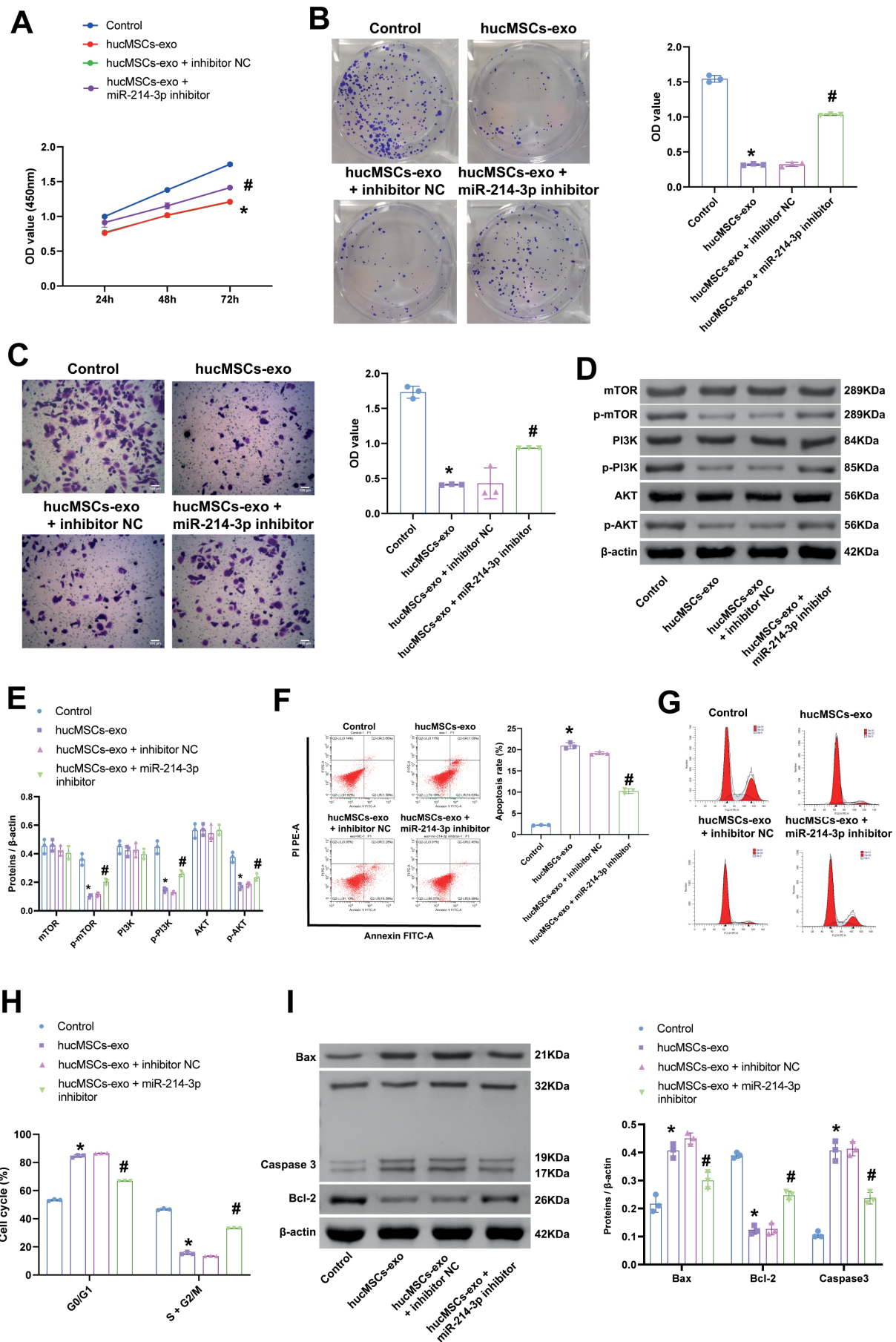


Fig. 2. Exosomal miR-214-3p can inhibit the proliferation of GBC-SD cells. A. Cell Counting Kit-8 (CCK-8) assays of GBC-SD cell proliferation at 24 h, 48 h and 72 h; B. Colony formation of GBC-SD cell clonal cell numbers; C. Transwell detection of GBC-SD cell invasion number; D,E. Western blot detection of proliferation-related pathway proteins (mTOR, p-mTOR, PI3K, p-PI3K, AKT, and p-AKT); F. Flow cytometry was used to detect the apoptosis rate of GBC-SD cells; G,H. Flow cytometry was utilized to detect the cycle of GBC-SD cells; I. The level of proteins (Bax, Bcl-2 and caspase 3). The comparisons among multiple groups were analyzed using one-way analysis of variance (ANOVA), followed by Tukey's post hoc test ($n = 3$)

* $p < 0.05$ compared to controls; # $p < 0.05$ compared to human umbilical cord mesenchymal stem cells (hucMSCs); OD – optical density; NC – negative control; GBC – gallbladder cancer; hucMSCs-exo – hucMSCs-derived exosomes.

the GBC-SD cell line was selected for subsequent experiments. The addition of exosomes in GBC-SD resulted in a decrease in cell proliferation (Fig. 2A), clonogenic ability (Fig. 2B), invasive ability (Fig. 2C), and an increase in the percentage of apoptosis (Fig. 2F) and G0/G1 phase (Fig. 2G,H). In contrast, after miR-214-3p silencing in GBC-SD, the proliferative, clonogenic and invasive capacities of the cells significantly increased after the addition of the exosomes in GBC-SD, while the percentage of apoptosis and S-phase decreased. The levels of p-mTOR, p-PI3K, p-AKT (Fig. 2D,E), and Bcl-2 decreased, and the expression of Bax and caspase 3 increased under exosome intervention. Silencing of miR-214-3p increased the levels of p-mTOR, p-PI3K, p-AKT, and Bcl-2, and inhibited the expression of Bax and caspase 3 (Fig. 2I). The data displayed in Fig. 2 are also presented in Supplementary Table 2. In short, miR-214-3p in exosomes was able to inhibit the proliferation of GBC-SD cells.

Exosomal miR-214-3p can regulate ACLY/GLUT1 to affect GBC-SD cells

The above experiments demonstrated that miR-214-3p can affect the proliferation and apoptosis of GBC-SD cells in exosomes. To investigate whether miR-214-3p can regulate the progression of GBC through ACLY/GLUT1, we constructed cell models overexpressing ACLY and GLUT1. The miR-214-3p expression levels were not affected by the overexpression of ACLY and GLUT1. Exosomal miR-214-3p inhibited ACLY and GLUT1 expression (Fig. 3A,B). The miR-214-3p was shown to have base interactions on the TargetScan website (<https://www.targetscan.org/>; Fig. 3C). Dual luciferase activity assays showed that miR-214-3p can target and inhibit the expression of ACLY (Fig. 3D). The data showed that exosome-competent miR-214-3p inhibited the proliferation of GBC-SD cells (Fig. 3E) and promoted their apoptosis (Fig. 3E), while the overexpression of ACLY and GLUT1 cells reversed this effect. The source data and analysis results of Fig. 3 are presented in Supplementary Table 3. In short, ACLY and GLUT1 can affect the proliferation and apoptosis of GBC-SD cells.

Inhibition of GLUT1 and ACLY can affect the proliferation of GBC-SD cells

The above results showed that GLUT1 and ACLY were associated with the prognosis of GBC patients. We planned to investigate whether GLUT1 and ACLY could affect the function of GBC-SD in vitro. Firstly, we constructed GBC-SD cells with the silencing of GLUT1 and ACLY. The data presented in Fig. 4A showed that the expression of GLUT1 and ACLY was inhibited in GBC-SD cells after silencing, indicating that the cell model was successfully constructed. Compared with the control and si-NC groups, the proliferative and clonogenic abilities of GBC-SD cells were reduced in the si-GLUT1 and si-ACLY groups, and the proliferative and clonogenic abilities of GBC-SD cells

were more significantly reduced in the si-GLUT1+si-ACLY group (Fig. 4B–D). Then, we examined the expression of proliferation-related genes, and the expression of p-mTOR, p-PI3K and p-AKT was significantly reduced in GBC-SD cells silenced with GLUT1 and ACLY (Fig. 4E). The results of the data analysis displayed in Fig. 4 are presented in Supplementary Table 4. In short, silencing of GLUT1 and ACLY inhibited the proliferative capacity of GBC-SD cells.

Inhibition of GLUT1 and ACLY can affect GBC-SD cell migration

The above results suggested that GLUT1 and ACLY can affect the proliferation of GBC-SD cells, thus whether silencing GLUT1 and ACLY can inhibit the proliferation of GBC-SD cells required further study. Transwell assays were used to detect the migration and invasion ability of GBC-SD cells. The experimental results demonstrated that the migration and invasion ability of GBC-SD cells were reduced in the si-GLUT1 and si-ACLY groups compared to the control and si-NC groups, and the reduction of migration and invasion ability of GBC-SD cells was more significant in the si-GLUT1+si-ACLY group (Fig. 5A,B). The scratch assays were performed to measure the migration distance, and the migration distance of GBC-SD cells silenced with GLUT1 and ACLY was significantly lower (Fig. 5C). The results displayed in Fig. 5 are presented in Supplementary Table 5. In conclusion, silencing of GLUT1 and ACLY inhibited the migratory ability of GBC-SD cells.

Inhibition of GLUT1 and ACLY can affect the apoptosis of GBC-SD cells

The above results suggested that GLUT1 and ACLY can affect the proliferation and migration of GBC-SD cells; thus, whether the silencing of GLUT1 and ACLY can promote apoptosis of GBC-SD cells required further investigation. Flow cytometry was used to detect the apoptosis rate of GBC-SD cells. Compared to the control and si-NC groups, the apoptosis rate of GBC-SD cells was elevated in the si-GLUT1 and si-ACLY groups, and the increase in the GBC-SD cell apoptosis rate was more significant in the si-GLUT1+si-ACLY group (Fig. 6A). The results of the data in Fig. 6B showed that the sum of S and G2/M phases of GBC-SD cells in the si-GLUT1 and si-ACLY groups were decreased compared to the control and si-NC groups, and the sum of S and G2/M phases of GBC-SD cells in the si-GLUT1+si-ACLY group was decreased more significantly. Western blot was utilized to analyze the expression of apoptosis-related proteins. The expression of Bax and caspase 3 was significantly increased, while the expression of Bcl-2 was significantly decreased in GBC-SD cells silenced with GLUT1 and ACLY (Fig. 6C). The results displayed in Fig. 6 are presented in Supplementary Table 6. All in all, silencing of GLUT1 and ACLY promoted apoptosis in GBC-SD cells.

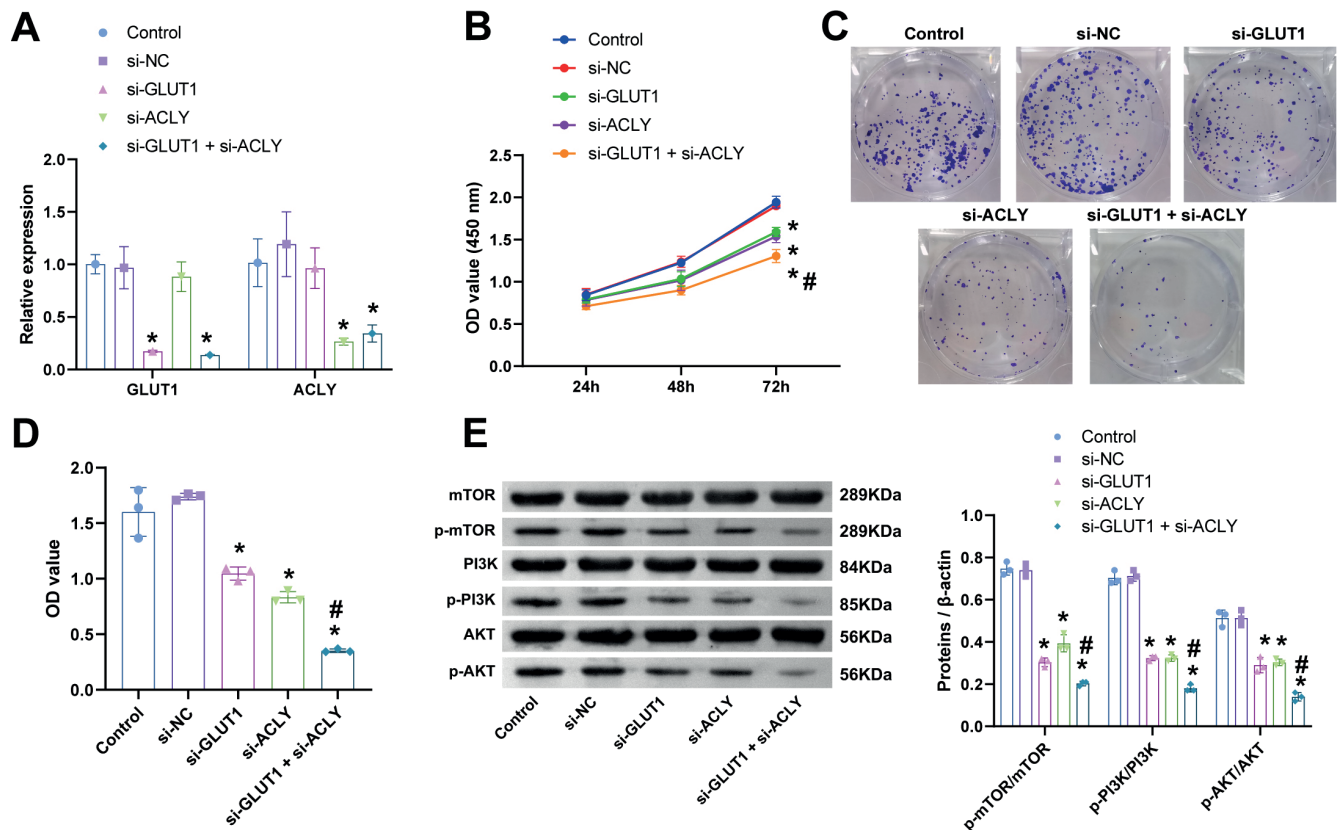


Fig. 4. GLUT1 and ACLY could inhibit the proliferation of GBC-SD cells. A. Quantitative reverse transcription polymerase chain reaction (RT-qPCR) was performed to detect the level of GLUT1 and ACLY; B. Cell Counting Kit-8 (CCK-8) was used to examine GBC-SD cell proliferation at 24 h, 48 h and 72 h; C,D. Clone formation was used to analyze the number of GBC-SD cloned cells; E. Western blot was utilized to detect the expression of proliferation-related pathway proteins (mTOR, p-mTOR, PI3K, p-PI3K, AKT, and p-AKT). Data were analyzed using one-way analysis of variance (ANOVA), followed by Tukey's post hoc test (n = 3)

*p < 0.05 compared to controls or si-NC; #p < 0.05 compared to si-GLUT1 or si-ACLY; OD – optical density; NC – negative control; GBC – gallbladder cancer; hucMSCs-exo – hucMSCs-derived exosomes.

Discussion

The understanding of clinicopathological characteristics of SC/ASC derives from studying the cases and analyzing small groups of patients. Therefore, more comprehensive studies are necessary to accurately understand SC/ASC tumors and adenocarcinoma differences. In malignant tumors of the gallbladder, the squamous differentiation incidence is at 1–12%.⁶ In this study, we observed that ACLY with GLUT1 reversed the inhibition of GBC-SD cell proliferation and migration by exosomal miR-214-3p.

Exosomes are subsets of naturally occurring particles inside the cells, with notable functions during physiological and pathological conditions.²⁷ Recent data revealed that exosomes facilitate paracrine cell-to-cell communication via the transfer of different biomolecules.²⁸ Evidence points to the fact that these nanoparticles can deliver numerous biotherapeutic agents to the target cells by using different fusion mechanisms and ligand–receptor interactions.²⁹ Exosomes can act as biological shuttles and can even treat neurological damage.³⁰ The SFB-miR-214-3p exosomes suppressed apoptosis and inflammation in chondrocytes.³¹ The overexpression of miR-214-3p repressed proliferation and cancer

cell stemness in vitro and in vivo in squamous cell lung cancer via targeting YAP1³² and fibroblast growth factor/MAPK signaling.³³ Han et al. suggested that miR-214-3p modulated breast cancer cell proliferation and apoptosis by targeting Survivin.³⁴ The miR-214-3p also interacted with TWIST1 to suppress the epithelial-to-mesenchymal transition of endometrial cancer cells.³⁵ In our study, exosomal miR-214-3p inhibited the proliferation and migration of GBC-SD cells and promoted their apoptosis. Exosomal miR-214-3p can reduce the activity of GBC-SD cells. This may have significant efficacy in treating the progressive development of GBC.

The ACLY is an enzyme that has recently been proven to be the key to the metabolism of cancer cells.^{8,36} The ACLY is the main source of acetyl-Coenzyme A, an important precursor for fatty acid, cholesterol, and isoprenoid biosynthesis, and it is also involved in protein acetylation.³⁷ The activation of ACLY signaling is linked to many cancers, such as prostate cancer, lung adenocarcinoma, leukemia, glioblastoma, ovarian cancer, and liver cancer.²¹ A positive expression of GLUT1 significantly predicts a poor prognosis in lung cancer patients. The GLUT1 may serve as a helpful biomarker and a potential target for the treatment strategies of lung cancer.³⁸ The blocking

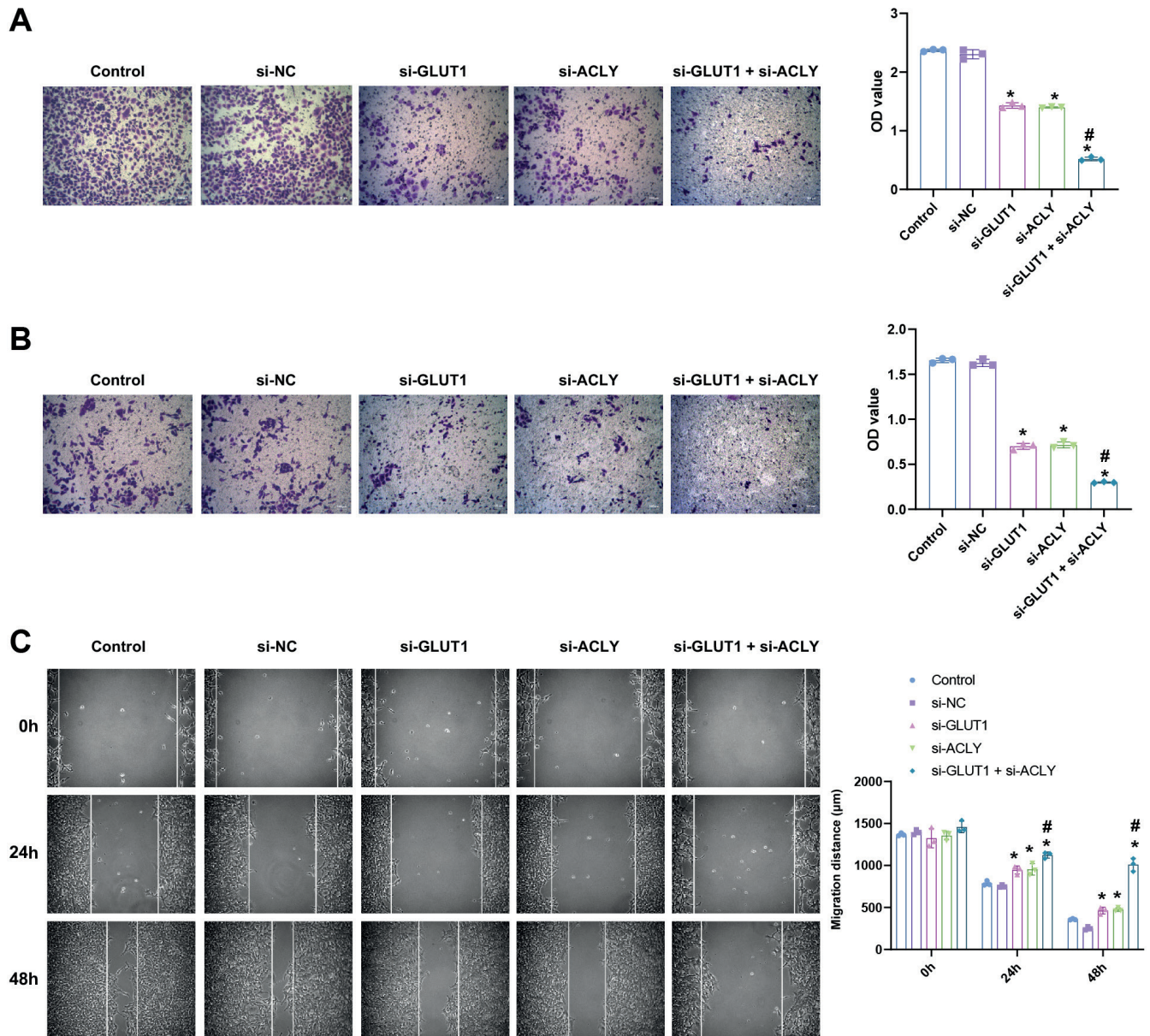


Fig. 5. GLUT1 and ACLY can inhibit the migration of GBC-SD cells. A,B. Transwell assay was used to test GBC-SD cell migration and invasion ability; C. The scratch assay was utilized to detect the migration distance of GBC-SD cells. The comparisons among multiple groups were analyzed using one-way analysis of variance (ANOVA) ($n = 3$)

* $p < 0.05$ compared to controls or si-NC; # $p < 0.05$ compared to si-GLUT1 or si-ACLY; OD – optical density; NC – negative control; GBC – gallbladder cancer; hucMSCs-exo – hucMSCs-derived exosomes.

of ACLY by siRNA can inhibit the Akt pathway, resulting in tumorigenicity loss in vitro. It is believed that blocking the ACLY pathway may have the potential to treat cancers. The results of this study showed that the knockdown of ACLY and GLUT1 inhibited the proliferation of GBC-SD cells and promoted apoptosis.

Limitations

It is thought that specific blocking of the GLUT1 and ACLY pathways may have the potential to treat human cancers. We will explore the effects of GLUT1 and ACLY on animal and human GBC in the future.

Conclusions

In conclusion, we found that exosomal miR-214-3p can target and inhibit ACLY. The miR-214-3p can inhibit the proliferation of GBC-SD cells. The overexpression of GLUT1 and ACLY promoted the proliferation of GBC-SD cells. In vitro experiments revealed that miR-214-3p can interfere with the activity of GBC-SD cells by inhibiting ACLY, which provided a basic theory for the treatment of GBC.

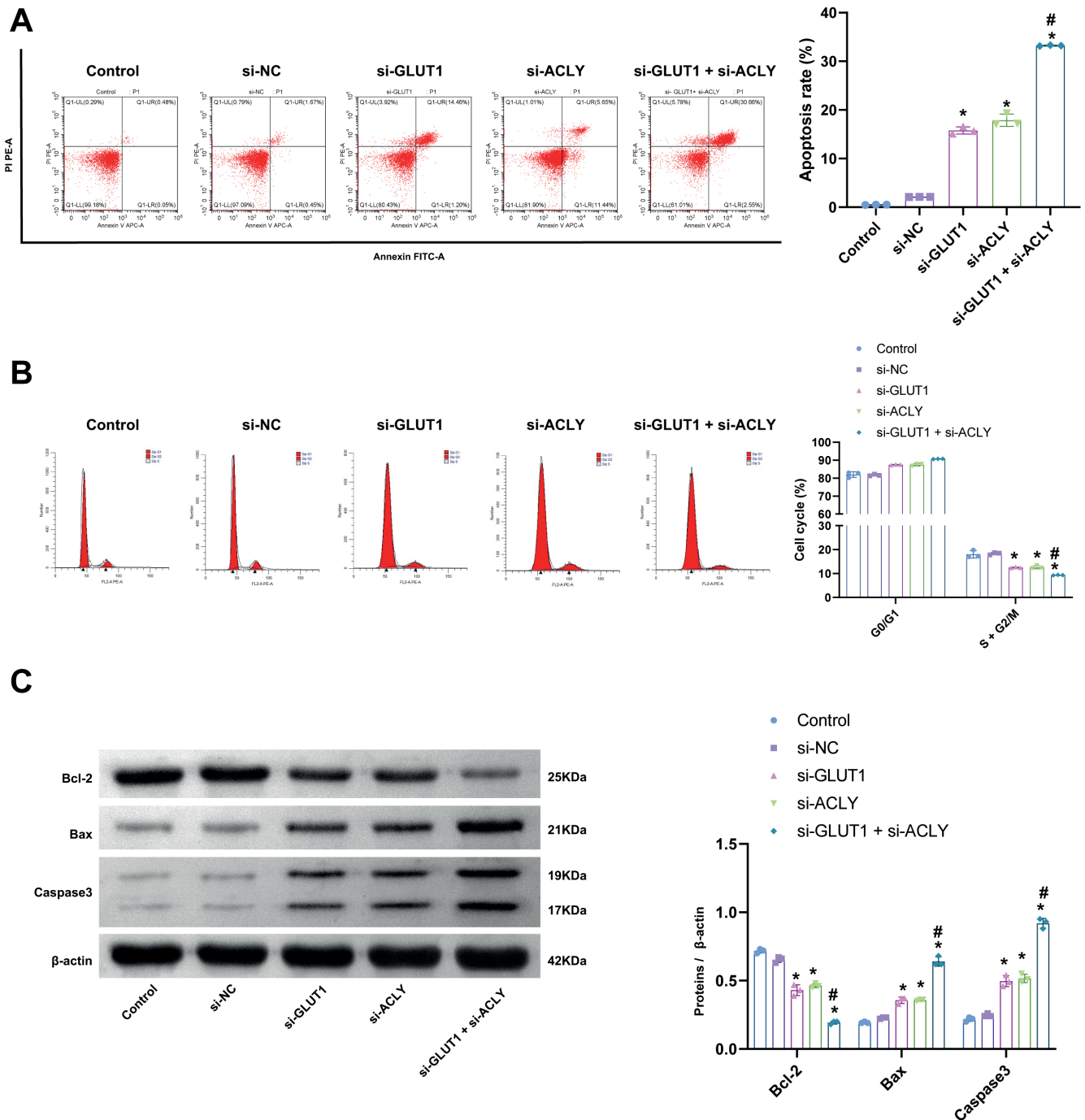


Fig. 6. GLUT1 and ACLY can promote the apoptosis of GBC-SD cells. **A.** GBC-SD cell apoptosis rate was promoted in the presence of GLUT1 and ACLY silencing; **B.** Flow cytometry was used to detect the GBC-SD cell cycle; **C.** Western blot was performed to detect the expression of apoptosis-related pathway proteins Bcl-2, Bax and caspase 3. Data were analyzed using one-way analysis of variance (ANOVA), followed by Tukey's post-hoc test (n = 3)

*p < 0.05 compared to controls or si-NC; #p < 0.05 compared to si-GLUT1 or si-ACLY; NC – negative control; GBC – gallbladder cancer; hucMSCs-exo – hucMSCs-derived exosomes.

Supplementary data

The supplementary materials are available at <https://doi.org/10.5281/zenodo.8161958>. The package contains the following files:

- Supplementary Table 1. The expression of miR-214-3p.
- Supplementary Table 2. The proliferation and apoptosis of GBC-SD cells.

Supplementary Table 3. miR-214-3p can regulate ACLY/ GLUT1 to affect GBC-SD cells.

Supplementary Table 4. Inhibition of GLUT1 and ACLY could affect the proliferation of GBC-SD cells.

Supplementary Table 5. GLUT1 and ACLY could inhibit the migratory ability of GBC-SD cells.

Supplementary Table 6. GLUT1 and ACLY could affect the apoptosis of GBC-SD cells.

ORCID iDs

Luyao Liu  <https://orcid.org/0000-0001-5241-967X>
 Wang Xiao  <https://orcid.org/0009-0002-9611-3845>
 Zhulin Yang  <https://orcid.org/0009-0000-3548-7961>
 Qunwei Wang  <https://orcid.org/0009-0001-3195-5665>
 Jianing Yi  <https://orcid.org/0000-0002-3282-3285>

References

- Torre LA, Bray F, Siegel RL, Ferlay J, Lortet-Tieulent J, Jemal A. Global cancer statistics, 2012. *CA Cancer J Clin.* 2015;65(2):87–108. doi:10.3322/caac.21262
- Sharma A, Sharma KL, Gupta A, Yadav A, Kumar A. Gallbladder cancer epidemiology, pathogenesis and molecular genetics: Recent update. *World J Gastroenterol.* 2017;23(22):3978. doi:10.3748/wjg.v23.i22.3978
- Wernberg JA, Lucarelli DD. Gallbladder cancer. *Surg Clin North Am.* 2014;94(2):343–360. doi:10.1016/j.suc.2014.01.009
- Mao W, Deng F, Wang D, Gao L, Shi X. Treatment of advanced gallbladder cancer: A SEER-based study. *Cancer Med.* 2020;9(1):141–150. doi:10.1002/cam4.2679
- Hu YP, Jin YP, Wu XS, et al. LncRNA-HGBC stabilized by HuR promotes gallbladder cancer progression by regulating miR-502-3p/SET/AKT axis. *Mol Cancer.* 2019;18(1):167. doi:10.1186/s12943-019-1097-9
- Liu L, Yang ZL, Wang C, et al. The expression of Notch 1 and Notch 3 in gallbladder cancer and their clinicopathological significance. *Pathol Oncol Res.* 2016;22(3):483–492. doi:10.1007/s12253-015-0019-4
- Liu DC, Yang ZL. MTDH and EphA7 are markers for metastasis and poor prognosis of gallbladder adenocarcinoma. *Diagn Cytopathol.* 2013;41(3):199–205. doi:10.1002/dc.21821
- Furuta E, Okuda H, Kobayashi A, Watabe K. Metabolic genes in cancer: Their roles in tumor progression and clinical implications. *Biochim Biophys Acta Rev Cancer.* 2010;1805(2):141–152. doi:10.1016/j.bbcan.2010.01.005
- Osugi J, Yamaura T, Muto S, et al. Prognostic impact of the combination of glucose transporter 1 and ATP citrate lyase in node-negative patients with non-small lung cancer. *Lung Cancer.* 2015;88(3):310–318. doi:10.1016/j.lungcan.2015.03.004
- Ganapathy-Kanniappan S, Geschwind JFH. Tumor glycolysis as a target for cancer therapy: Progress and prospects. *Mol Cancer.* 2013;12(1):152. doi:10.1186/1476-4598-12-152
- Li Z, Zhang H. Reprogramming of glucose, fatty acid and amino acid metabolism for cancer progression. *Cell Mol Life Sci.* 2016;73(2):377–392. doi:10.1007/s00018-015-2070-4
- Jang SM, Han H, Jang KS, et al. The glycolytic phenotype is correlated with aggressiveness and poor prognosis in invasive ductal carcinomas. *J Breast Cancer.* 2012;15(2):172. doi:10.4048/jbc.2012.15.2.172
- Khwaitrakpam A, Shyamananda M, Sailo B, et al. ATP citrate lyase (ACLY): A promising target for cancer prevention and treatment. *Curr Drug Targets.* 2015;16(2):156–163. doi:10.2174/1389450115666141224125117
- Mezheyeuski A, Nerovnya A, Bich T, Tur G, Ostman A, Portyanko A. Inter- and intra-tumoral relationships between vasculature characteristics, GLUT1 and budding in colorectal carcinoma. *Histol Histopathol.* 2015;30(10):1203–1211. doi:10.14670/HH-11-613
- Xie S, Zhou F, Wang J, et al. Functional polymorphisms of ATP citrate lyase gene predicts clinical outcome of patients with advanced colorectal cancer. *World J Surg Onc.* 2015;13(1):42. doi:10.1186/s12957-015-0440-x
- Kawamura T, Kusakabe T, Sugino T, et al. Expression of glucose transporter-1 in human gastric carcinoma: Association with tumor aggressiveness, metastasis, and patient survival. *Cancer.* 2001;92(3):634–641. doi:10.1002/1097-0142(20010801)92:3<634::AID-CNCR1364>3.0.CO;2-X
- Qian X, Hu J, Zhao J, Chen H. ATP citrate lyase expression is associated with advanced stage and prognosis in gastric adenocarcinoma. *Int J Clin Exp Med.* 2015;8(5):7855–7860. PMID:26221340. PMID:PMC4509285.
- Amann T, Hellerbrand C. GLUT1 as a therapeutic target in hepatocellular carcinoma. *Exp Opin Ther Targets.* 2009;13(12):1411–1427. doi:10.1517/14728220903307509
- Jiang H, Dai J, Huang X, et al. Genetic variants in de novo lipogenic pathway genes predict the prognosis of surgically-treated hepatocellular carcinoma. *Sci Rep.* 2015;5(1):9536. doi:10.1038/srep09536
- Xiao H, Wang J, Yan W, et al. GLUT1 regulates cell glycolysis and proliferation in prostate cancer. *Prostate.* 2018;78(2):86–94. doi:10.1002/pros.23448
- Gao Y, Islam MS, Tian J, Lui VWY, Xiao D. Inactivation of ATP citrate lyase by cucurbitacin B: A bioactive compound from cucumber, inhibits prostate cancer growth. *Cancer Lett.* 2014;349(1):15–25. doi:10.1016/j.canlet.2014.03.015
- Galbraith L, Leung HY, Ahmad I. Lipid pathway deregulation in advanced prostate cancer. *Pharmacol Res.* 2018;131:177–184. doi:10.1016/j.phrs.2018.02.022
- Qiu L, Wang J, Chen M, Chen F, Tu W. Exosomal microRNA-146a derived from mesenchymal stem cells increases the sensitivity of ovarian cancer cells to docetaxel and taxane via a LAMC2-mediated PI3K/Akt axis. *Int J Mol Med.* 2020;46(2):609–620. doi:10.3892/ijmm.2020.4634
- Li K, Zhang J, Yu J, et al. MicroRNA-214 suppresses gluconeogenesis by targeting activating transcriptional factor 4. *J Biol Chem.* 2015;290(13):8185–8195. doi:10.1074/jbc.M114.633990
- Li D, Liu J, Guo B, et al. Osteoclast-derived exosomal miR-214-3p inhibits osteoblastic bone formation. *Nat Commun.* 2016;7(1):10872. doi:10.1038/ncomms10872
- He GN, Bao NR, Wang S, Xi M, Zhang TH, Chen FS. Ketamine induces ferroptosis of liver cancer cells by targeting lncRNA PVT1/miR-214-3p/GPX4. *Drug Des Devel Ther.* 2021;15:3965–3978. doi:10.2147/DDDT.S332847
- Armstrong JPK, Holme MN, Stevens MM. Re-engineering extracellular vesicles as smart nanoscale therapeutics. *ACS Nano.* 2017;11(1):69–83. doi:10.1021/acsnano.6b07607
- Hassanpour M, Cheraghi O, Brazvan B, et al. Chronic exposure of human endothelial progenitor cells to diabetic condition abolished the regulated kinetics activity of exosomes. *Iran J Pharm Res.* 2018;17(3):1068–1080. PMID:30127829. PMID:PMC6094433.
- Heidarzadeh M, Gürsoy-Özdemir Y, Kaya M, et al. Exosomal delivery of therapeutic modulators through the blood-brain barrier: Promise and pitfalls. *Cell Biosci.* 2021;11(1):142. doi:10.1186/s13578-021-00650-0
- Shokrollahi E, Nourazarian A, Rahbarghazi R, et al. Treatment of human neuroblastoma cell line SH-5Y5 with HSP27 siRNA tagged-exosomes decreased differentiation rate into mature neurons. *J Cell Physiol.* 2019;234(11):21005–21013. doi:10.1002/jcp.28704
- Lai C, Liao B, Peng S, Fang P, Bao N, Zhang L. Synovial fibroblast-miR-214-3p-derived exosomes inhibit inflammation and degeneration of cartilage tissues of osteoarthritis rats. *Mol Cell Biochem.* 2023;478(3):637–649. doi:10.1007/s11010-022-04535-9
- Lu T, Yang Y, Li Z, Lu S. MicroRNA-214-3p inhibits the stem-like properties of lung squamous cell cancer by targeting YAP1. *Cancer Cell Int.* 2020;20(1):413. doi:10.1186/s12935-020-01506-2
- Yang Y, Li Z, Yuan H, et al. Reciprocal regulatory mechanism between miR-214-3p and FGFR1 in FGFR1-amplified lung cancer. *Oncogenesis.* 2019;8(9):50. doi:10.1038/s41389-019-0151-1
- Han LC, Wang H, Niu FL, Yan JY, Cai HF. Effect miR-214-3p on proliferation and apoptosis of breast cancer cells by targeting survivin protein. *Eur Rev Med Pharmacol Sci.* 2019;23(17):7469–7474. doi:10.26355/eurrev_201909_18856
- Fang YY, Tan MR, Zhou J, et al. miR-214-3p inhibits epithelial-to-mesenchymal transition and metastasis of endometrial cancer cells by targeting TWIST1. *Onco Targets Ther.* 2019;12:9449–9458. doi:10.2147/OTT.S181037
- Zaidi N, Swinnen JV, Smans K. ATP-citrate lyase: A key player in cancer metabolism. *Cancer Res.* 2012;72(15):3709–3714. doi:10.1158/0008-5472.CAN-11-4112
- Mashima T, Seimiya H, Tsuruo T. De novo fatty-acid synthesis and related pathways as molecular targets for cancer therapy. *Br J Cancer.* 2009;100(9):1369–1372. doi:10.1038/sj.bjc.6605007
- Zhang B, Xie Z, Li B. The clinicopathologic impacts and prognostic significance of GLUT1 expression in patients with lung cancer: A meta-analysis. *Gene.* 2019;689:76–83. doi:10.1016/j.gene.2018.12.006

Oridonin attenuated human PC-3 cell activity by modulating the Wnt/ β -catenin signaling

Shuling Zhang^{1,A,D,F}, Annamalai Vijayalakshmi^{2,A,D}, Lingjun Meng^{3,A,C,D,F}

¹ Department of Pharmacy, Tongchuan Hospital of Traditional Chinese Medicine, China

² Department of Biochemistry, Rabi Ammal Ahamed Maideen College for Women, Thiruvavur, India

³ Department of General Surgery, Tongchuan Hospital of Traditional Chinese Medicine, China

A – research concept and design; B – collection and/or assembly of data; C – data analysis and interpretation;

D – writing the article; E – critical revision of the article; F – final approval of the article

Advances in Clinical and Experimental Medicine, ISSN 1899–5276 (print), ISSN 2451–2680 (online)

Adv Clin Exp Med. 2024;33(5):511–518

Address for correspondence

Lingjun Meng

E-mail: menglingjuntc@outlook.com

Funding sources

None declared

Conflict of interest

None declared

Received on October 4, 2022

Reviewed on December 11, 2022

Accepted on July 14, 2023

Published online on January 23, 2024

Abstract

Background. Prostate cancer (PC) prevention is effectively achieved through its inhibition. Oridonin (ORD), an active diterpenoid isolated from *Rabdosia rubescens*, has been shown to have an inhibitory effect on PC cells, although its impact on PC is unknown.

Objectives. The present work investigated the actions and probable mechanisms of ORD on cellular proliferation, apoptosis, PC, and the wingless-type MMTV integration site family member 2 (Wnt)/ β -catenin signaling pathway using the androgen-independent PC-3 cell line.

Materials and methods. In this study, cell viability was analyzed with MTT assay method, apoptotic morphology determined using DAPI dye method, while protein (CD133, OCT-4, Nanog, SOX-2 & Aldh1A1) and mRNA expressions were analyzed with western blotting and real time polymerase chain reaction (PCR).

Results. We demonstrated a concentration-dependent ORD inhibition of PC-3 cell proliferation and inhibition of induction apoptosis. Furthermore, ORD decreased PC-3 Wnt-2, phosphorylated glycogen synthase kinase-3 (p-GSK3), and β -catenin protein levels and downregulated *cyclin-D1* and *c-myc* messenger ribonucleic acid (mRNA).

Conclusions. Oridonin inhibited proliferation and induced apoptosis in PC-3 cells, with the findings suggesting that it acted via the Wnt/ β -catenin pathway to exert its effects. This study demonstrates that ORD may impact PC.

Key words: apoptosis, oridonin, prostate cancer, Wnt/ β -catenin signaling, PC-3 cells

Cite as

Zhang S, Vijayalakshmi A, Meng L. Oridonin attenuated human PC-3 cell activity by modulating the Wnt/ β -catenin signaling. *Adv Clin Exp Med.* 2024;33(5):511–518. doi:10.17219/acem/175519

DOI

10.17219/acem/175519

Copyright

Copyright by Author(s)

This is an article distributed under the terms of the Creative Commons Attribution 3.0 Unported (CC BY 3.0) (<https://creativecommons.org/licenses/by/3.0/>)

Background

The world's most prevalent malignancy, prostate cancer (PC), accounts for 30% of all malignant tumors in men.¹ Prostate cancer contributes to 10% of all mortality and ranks as the 2nd major risk of cancer-associated deaths in western countries,² with the USA reporting 191,930 new cases and 33,330 deaths in 2020.³ Prostate cancer mortality results from bone and lymph node metastasis and mortality rate of cancer progression through androgen-dependent to androgen-independent prostatic growth reversion.⁴ The PC androgen-dependent phase can be effectively treated with androgen withdrawal therapy, resulting in prostate gland involution due to cellular proliferation subdual and apoptosis activation.⁵ Although hormonal excision typically works as a first-line treatment against localized tumors, degeneration occurs in most patients after some years, and once the PC becomes androgen-independent, a highly metastatic tumor resistant to irradiation and chemotherapy develops.^{1,6} Unfortunately, most patients eventually progress to the androgen-independent stage, for which there is no efficient life-extending management strategy.^{7,8}

Androgen-independent cancer progression, and its molecular mechanisms, are poorly understood. Therefore, research is required to better understand androgen-independent pathophysiology and identify beneficial treatment strategies for PC. Hence, a drug capable of controlling the signaling pathways involved in tumor progression without impacting hormone receptor expression could significantly improve metastatic PC therapy.

Oridonin (ORD) is an ent-kaurane diterpenoid sequestered from the aromatic plant *Rabdosia rubescens*, extensively used in traditional Chinese medicine.⁹ In vitro trials revealed that ORD stimulates apoptosis in various tumor cells such as acute leukemia, gliomas, non-small cell lung cancer, melanoma, and prostate cancer, with these studies showing that ORD promotes cell death, enhances phagocytosis, and prevents cell cycle progression.^{10,11} Previous research has also demonstrated ORD apoptotic and anti-proliferative properties in several malignant cells, such as colorectal, mammary and liver cancer.^{12–14} Furthermore, several in vitro and in vivo studies have reported ORD growth inhibition of many human malignancies, including oral cancer,^{15,16} gallbladder carcinoma,¹⁷ glioblastoma,¹⁸ pancreatic tumors,¹⁹ cervical cancer,²⁰ and esophageal cancer.²¹ In addition, recent research showed ORD supplementation to restrict growth and trigger apoptosis in PC cells (PCCs).^{22–24} However, the precise role of ORD anti-tumor activity remains unknown.

Several human cancer-derived cell lines with tumor cell characteristics have been recognized for genetic, chemoresistance and therapeutic drug studies.²⁵ The latest method in cancer treatment is cancer cell (CC) targeting since breast cancer cells MCF7 participate in growth, metastasis, drug resistance, and cancer recurrence.²⁶ The PCC

markers, such as CD133, aldehyde dehydrogenase 1 family member A1 (ALDH1A1), Nanog, octamer-binding transcription factor 4 (Oct-4), and SRY-box transcription factor 2 (Sox2), are well-established and used to recognize the cells and assess their actions.²⁷ Thus, CC targeting is likely the optimal tumor prevention and management strategy.

Recently, researchers have identified the wingless-type MMTV integration site family member 2 (Wnt)/ β -catenin signaling pathway as vital in controlling PCC activities.^{28,29} Triggering of Wnt/ β -catenin signaling is governed at the β -catenin level and regulated by glycogen synthase kinase-3 beta (GSK3 β), which mediates β -catenin phosphorylation to trigger β -catenin deprivation. Inactivation of β -catenin through GSK3 β phosphorylation leads to its degradation, accumulation in the cytosol, and nuclear translocation to promote downstream gene targets such as *cyclin-D1* and *c-myc* to act as transcription factors that control CC activity.³⁰

Among PCCs, the androgen-independent PC-3 cell line has higher metastatic potential than others.³¹ Hence, the current study aimed to investigate ORD anti-proliferative action on PC-3 cells and explore its potential to induce apoptotic signaling pathways.

Objectives

The current research aimed to demonstrate, for the first time, ORD-driven suppression of CC markers and PC. Furthermore, we aimed to establish ORD attenuation of PCCs through the Wnt/ β -catenin pathway.

Materials and methods

Chemicals

Oridonin, Dulbecco's modified Eagle's medium (DMEM), fetal bovine serum (FBS), antibiotics (CD133, ALDH1A1, OCT-4, Nanog, Sox2, Wnt-2, β -catenin, GSK3 β , *c-myc*, *cyclin-D1*, and GAPDH), phosphate-buffered saline (PBS), 3-(4,5-dimethylthiazol-2-yl)-2,5-diphenyltetrazolium bromide (MTT), 4',6-diamidino-2-phenylindole (DAPI), dimethyl sulfoxide (DMSO), and sodium dodecyl sulfate (SDS) were obtained from Gibco (Thermo Fisher Scientific, Waltham USA). The antibodies for western blot analysis were acquired from Beyotime Biotechnology (Shanghai, China).

Cell culture

The human PC-3 cell line was procured from the Chinese Academy of Medical Sciences (Beijing, China). The cells were grown and preserved in DMEM containing FBS (10%), penicillin (100 U/mL), and streptomycin (100 U/mL) at 37°C with 5% CO₂ and less than 95% humidified air.

Cell cytotoxicity assay

An MTT assay determined the influence of ORD on PC-3 cellular proliferation.³² PC-3 cells were seeded onto 96-well plates at a density of 3000 cells/well, incubated overnight in DMEM media, and then treated with different ORD dosages (10–60 μ M) for 1 day at 37°C. An aliquot of MTT (10 μ L) was added to each well and incubated at 37°C for 4 h to allow the conversion of MTT into insoluble formazan crystals through mitochondrial dehydrogenase. The subsequent formazan crystals were dissolved by adding 150 μ L DMSO to the culture medium. Each experiment was repeated thrice, with cells grown in a culture medium containing DMSO used as a control. Optical density (OD) was determined at 490 nm using a microplate reader (PerkinElmer EnVision; PerkinElmer, Waltham, USA) to assess proliferation, which was calculated as a percentage of untreated PC-3 cell proliferation (100%). Half maximal inhibitory concentration (IC50) (drug concentration that caused a 50% reduction in the MTT assay) was also calculated.

Apoptosis exploration using DAPI staining

Human PC-3 cells treated with ORD (20 μ M/mL, 30 μ M/mL or 40 μ M/mL) in 96-well plates were fixed with paraformaldehyde (4%) at 37°C for 10 min, and then stained using DAPI for 10 min to analyze the cellular changes associated with apoptosis.³³ Finally, all slides were fixed on a glass slide and observed using fluorescence microscope (Nikon Eclipse TS100; Nikon Corp., Tokyo, Japan).

Western blot study

Human PC-3 cells were treated with ORD (20 μ M/mL, 30 μ M/mL or 40 μ M/mL) and incubated for 24 h. Cell lysates were prepared using an ice-cold lysis buffer containing protease inhibitors and then used for western blot analysis. Protein content measurement utilized a Protein BCA Assay Kit (Pierce Chemical, Rockford, USA). The western blot experiment involved electrophoretically dispersing the proteins and relocating them to a polyvinylidene difluoride (PVDF) film that was blocked overnight at 4°C using a probe before being treated with diluted (1:1000) primary antibodies, including anti-CD133, anti-Oct-4, anti-ALDH1A1, anti-Sox2, anti-Nanog, anti-Wnt-2, anti- β -catenin, anti-phosphorylated(p)-GSK3 β (ser9), anti-c-myc, anti-cyclin-D1 and anti-glyceraldehyde 3-phosphate dehydrogenase (GAPDH), and incubated overnight at 4°C. Appropriate secondary antibodies (1:5000) were then added to the films, with GAPDH used as an internal control. Proteins were visualized using a LI-COR Odyssey imaging system (LI-COR Biosciences, Lincoln, USA).

Determination of messenger ribonucleic acid levels using quantitative real-time polymerase chain reaction

Total ribonucleic acid (RNA) was extracted from human cells PC-3 using TRIzol[®] reagent (Abcam, Cambridge, USA), according to the manufacturer's instructions. The isolated RNA was converted to complementary deoxyribonucleic acid (cDNA) through reverse transcription using a high-capacity cDNA Reverse Transcription kit (Beyotime Biotechnology), following the manufacturer's protocol. Then, the Fast Start SYBR Green Master Mix (Abcam) was employed to explore the cDNAs, according to the manufacturer's protocol. The band intensity was scrutinized using 1.5% agarose gel electrophoresis. Finally, the band intensity was measured using ImageJ 1.48 software (National Institutes of Health, Bethesda, USA). A comparative threshold cycle (Ct) method was used to calculate the fold changes in the expression of each gene using the formula $2^{-\Delta\Delta C_t}$. The quantitative real-time polymerase chain reaction (qPCR) primer sequences are presented in Table 1.

Table 1. Primer sequences used in the study

Primer	Sequence
CD133	forward: 5'-GGAGGACGTGTACGATGATGT-3'
	reverse: 5'-GCTTGTGCATAACAGGATTGTGAA-3'
ALDH1A1	forward: 5'-ATCAAAGAAGCTGCCGGGAA-3'
	reverse: 5'-GCATTGTCCAAGTCGGCATC-3'
OCT-4	forward: 5'-GATGGGAGCCACTGGTTCAC-3'
	reverse: 5'-GGTCCAGATCCTCCAGGGTAT-3'
Nanog	forward: 5'-CTCCAACAT CCTGAACCT-3'
	reverse: 5'-GTCACAC CATTGCTATTCTT-3'
Sox2	forward: 5'-AAAATCCCATCCCCACAGCAA-3'
	reverse: 5'-AAAATAGTCCCCAAAAGAAGTCC-3'
GAPDH	forward: 5'-CTTCTTTTTCGTC GCCAGCCGA-3'
	reverse: 5'-ACCAGGCGCCAATACGACCAA-3'

Statistical analyses

All experiments were independently conducted in triplicate (n = 3) and repeated 3 times, with data expressed as mean \pm standard deviation (M \pm SD). Statistical analysis employed GraphPad Prism v. 8.0.1 (GraphPad Software, San Diego, USA) and IBM Statistical Package for Social Sciences (SPSS) v. 25 (IBM Corp., Armonk, USA) software. The Shapiro–Wilk test assessed the normality of data distribution and demonstrated a non-normal distribution, perhaps due to the small sample size. As such, the subsequent analysis used the nonparametric Kruskal–Wallis test followed by Dunn's post hoc comparison of intergroup variables (control: n = 6; 20 μ M/mL: n = 6; 30 μ M/mL: n = 6; and 40 μ M/mL: n = 6). Differences were considered statistically significant when p < 0.05.

Results

Table 2 and Table 3 show the results of comparing variables among groups.

Table 2. Oridonin (ORD) cytotoxic action on PC-3 cells

Variables	MTT	p-value
Control (n = 6)	100.00 (91.00, 109.00)	p < 0.001
10 μ M ORD (n = 6)	80.73 (73.43, 87.95)	
20 μ M ORD (n = 6)	69.23 (62.97, 75.43)	
30 μ M ORD (n = 6)	51.37 (46.73, 55.97)	
40 μ M ORD (n = 6)	38.08 (34.63, 41.49)	
50 μ M ORD (n = 6)	25.91 (23.57, 28.23)	
60 μ M ORD (n = 6)	17.04 (15.50, 18.56)	

Data were presented as median (minimum and maximum). The p-value was obtained using Kruskal–Wallis test.

Cytotoxic effects of ORD on human PC-3 cells

The cytotoxicity of a range of ORD concentrations (10 μ M/mL, 20 μ M/mL, 30 μ M/mL, 40 μ M/mL, 50 μ M/mL, and 60 μ M/mL) on human PC-3 cells was determined

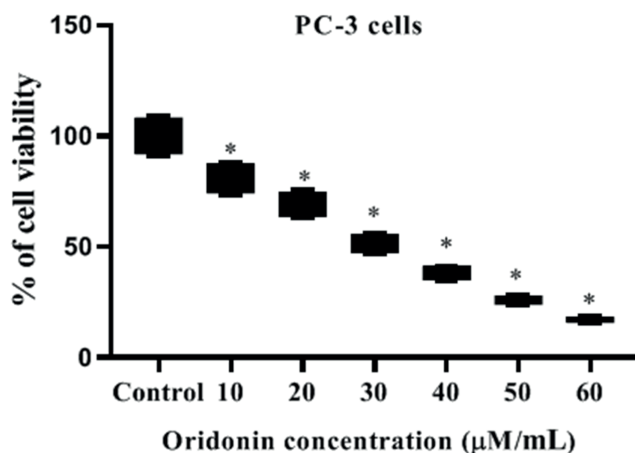


Fig. 1. Oridonin inhibits human PC-3 cell proliferation. Human PC-3 cells were treated with various oridonin (ORD) dosages (10–60 μ M/mL) for 24 h, with cell viability then assessed using a 3-(4,5-dimethylthiazol-2-yl)-2,5-diphenyltetrazolium bromide (MTT) assay. The data are presented as mean \pm standard deviation (M \pm SD) for triplicate tests. The significance is denoted by *p < 0.05 compared to the untreated control

Table 3. Oridonin (ORD) action on mRNA expression quantification values.

Variables	Control (n = 6)	20 μ M ORD (n = 6)	30 μ M ORD (n = 6)	40 μ M ORD (n = 6)	p-value
CD133	1 (0.91, 1.09)	0.85 (0.77, 0.93)	0.73 (0.66, 0.80)	0.59 (0.54, 0.64)	p < 0.001
ALDH1A1	1 (0.91, 1.09)	0.77 (0.70, 0.84)	0.64 (0.58, 0.70)	0.53 (0.48, 0.53)	p < 0.001
OCT-4	1 (0.91, 1.09)	0.63 (0.57, 0.69)	0.51 (0.46, 0.56)	0.36 (0.33, 0.39)	p < 0.001
Nanog	1 (0.91, 1.09)	0.78 (0.71, 0.85)	0.53 (0.48, 0.58)	0.31 (0.28, 0.34)	p < 0.001
Sox2	1 (0.91, 1.09)	0.80 (0.73, 0.87)	0.71 (0.65, 0.77)	0.64 (0.58, 0.70)	p < 0.001

Data were presented as median (minimum and maximum). The p-value was obtained using Kruskal–Wallis test.

using the MTT assay. The results revealed that ORD had a concentration-dependent anti-proliferative action on PC-3 cells. Untreated control cells did not experience any anti-proliferative effect and showed 100% PC-3 cell proliferation. However, 10 μ M, 20 μ M, 30 μ M, and 40 μ M ORD dosages substantially (p < 0.05) inhibited PC-3 viability compared to the untreated control. Furthermore, viability was inhibited further by administering a high dosage of ORD (50 μ M and 60 μ M), leading to cellular damage.

Results of the MTT assay showed that the ORD IC₅₀ was 30 μ M. Therefore, to avoid the damaging effects of high ORD concentrations (20 μ M/mL, 30 μ M/mL and 40 μ M/mL), ORD was used for subsequent experiments (Fig. 1).

Oridonin triggered apoptosis in DAPI-stained PC-3 cells

Assessment of ORD (20 μ M/mL, 30 μ M/mL and 40 μ M/mL) on PC-3 cell morphological apoptotic features utilized DAPI staining. Control cells stained with DAPI were viable with normal nuclei. In contrast, ORD-treated PC-3 cells appeared apoptotic, based on nuclear morphology and body disintegration. Furthermore, PC-3 cells exposed to ORD (20 μ M/mL, 30 μ M/mL or 40 μ M/mL) displayed chromatin condensation, membrane blebbing, nuclear envelop impairment, fragmentation, and cellular collapse in a concentration-dependent manner. These results demonstrated that ORD exhibits anti-proliferative and apoptotic activity on PC-3 cells in a dose-dependent way (Fig. 2).

Oridonin suppressed PCC protein and messenger RNA expression

We evaluated the effect of ORD on the protein and mRNA levels of PCC markers. Western blot and qPCR assays indicated that ORD attenuated the levels of protein and messenger (m)RNA of CD133, Oct-4, Sox2, ALDH1A1, and Nanog in a concentration-dependent manner (Fig. 3,4). These findings demonstrated that ORD could suppress PCC activity.

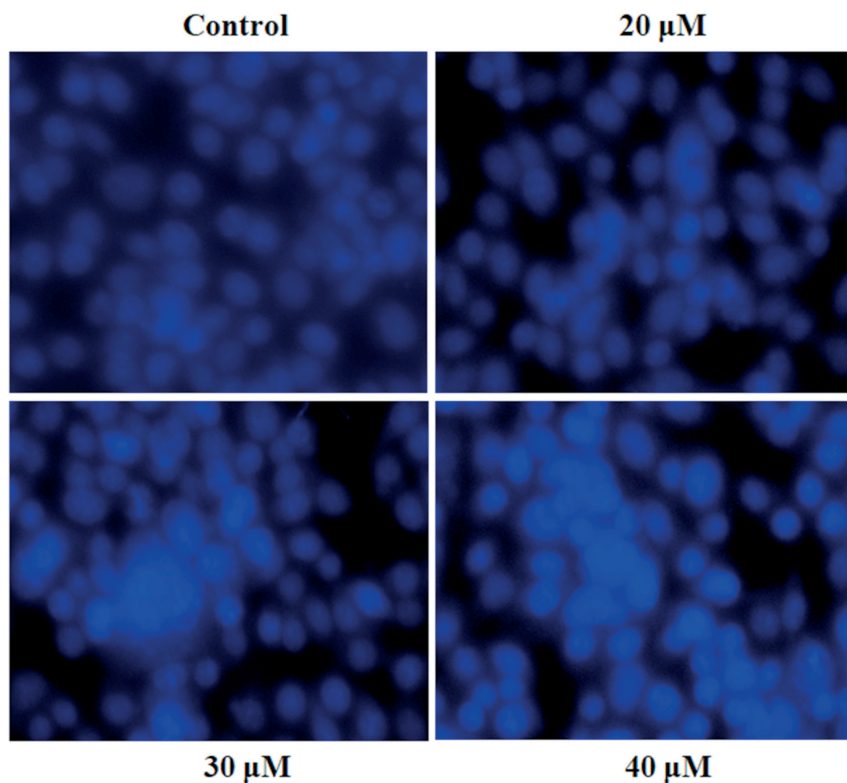


Fig. 2. The influence of oridonin on human PC-3 cell apoptosis. PC-3 cancer cells were exposed to oridonin ORD (20 μM/mL, 30 μM/mL or 40 μM/mL) for 24 h. Apoptosis was highlighted with 4',6-diamidino-2-phenylindole (DAPI) staining and assessed using fluorescence microscopy

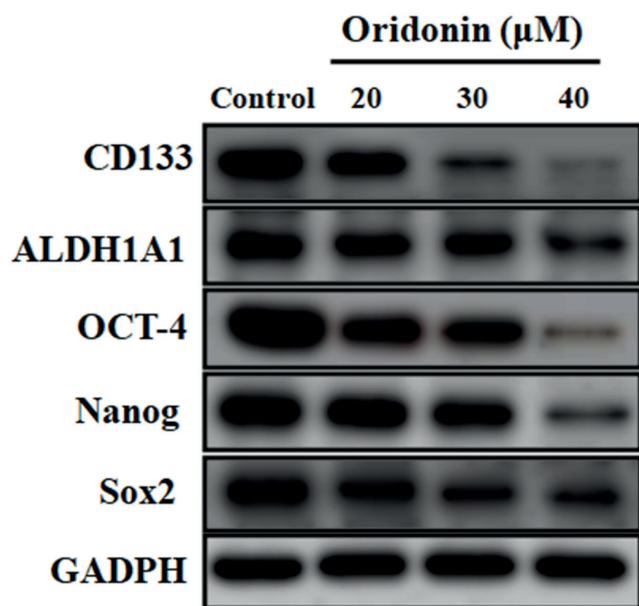


Fig. 3. Effects of oridonin on human PC-3 cell pancreatic cancer cell markers. Human PC-3 cells were exposed to 20 μM/mL, 30 μM/mL or 40 μM/mL oridonin (ORD) for 24 h. The expression of pancreatic cancer cell (PCC) proteins and glyceraldehyde 3-phosphate dehydrogenase (GAPDH) was investigated using western blot

Oridonin inhibited Wnt/β-catenin signaling in PC-3 cells

Wnt/β-catenin signaling is a crucial pathway for controlling PC-3 cell actions. Accordingly, we investigated whether the anti-proliferative activities of ORD on PC-3 cells were facilitated by the Wnt/β-catenin pathway.

The findings indicated that ORD repressed Wnt-2, β-catenin and p-GSK3β protein levels, and attenuated *cyclin-D1* and *c-myc* genes (Fig. 5).

Discussion

Prostate cancer remains the most commonly diagnosed malignancy in males and the 2nd leading source of tumor-associated deaths in American men.^{1,3} Metastatic PC is the end-phase and leads to most tumor-related deaths. Moreover, metastatic PC sufferers are at a higher risk of emerging bone metastasis, which ultimately results in skeletal illness.⁴ The U.S. Food and Drug Administration (FDA)-approved chemotherapeutic drugs docetaxel and cabazitaxel are used for metastatic PC treatment. However, these medicines have serious and potentially lethal side effects.^{34,35} Regardless of recent research on putative therapeutics, our knowledge of PC is still limited, including its source and signaling pathways.^{5,6} Nonetheless, PCCs are regarded as a cause of sustained prostate carcinogenesis.²⁶ Thus, finding PCC-targeted medications might lead to their removal and produce beneficial effects.²⁷

Oridonin’s anti-tumor capabilities include reducing viability and promoting apoptosis in various malignant cells.^{10,11} Moreover, numerous research has reported that ORD suppressed cell growth and induction of cell-cycle arrest in a range of CCs.^{12,14} Several mechanisms have been postulated to take part in the anti-cancer ability of ORD, such as proliferation inhibition, apoptosis

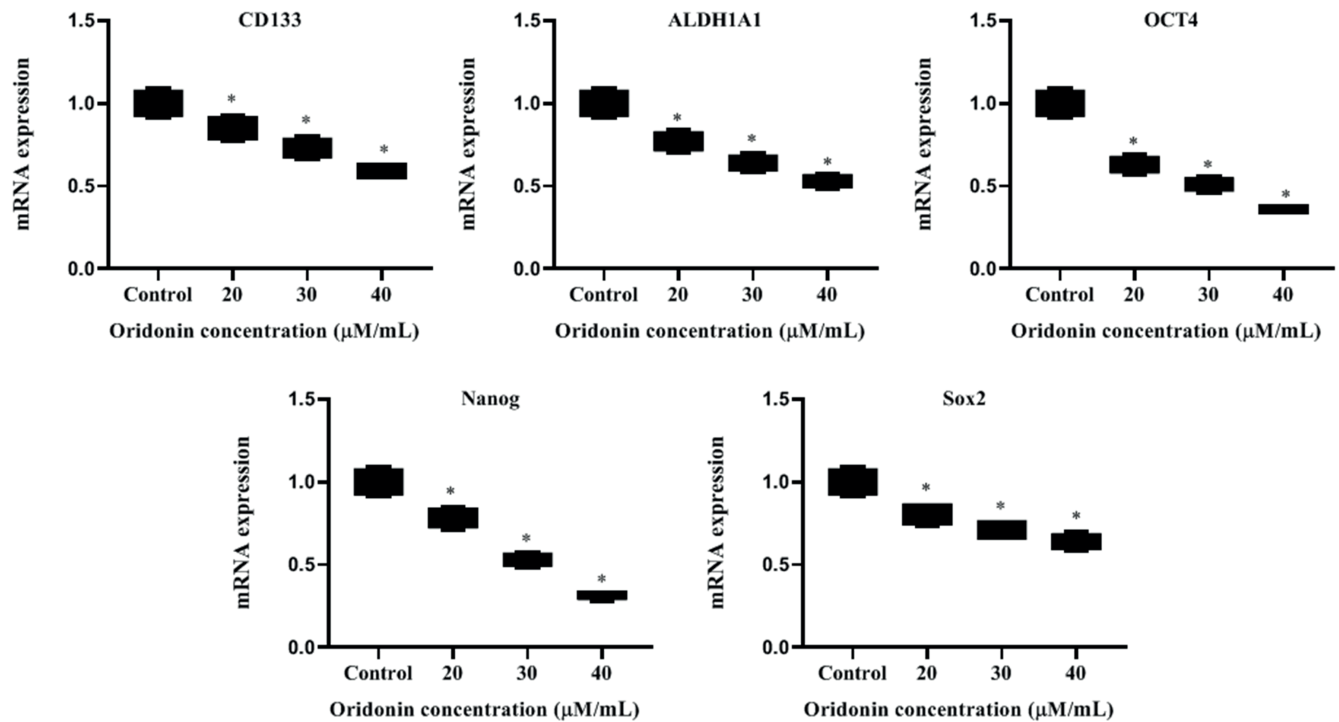


Fig. 4. The influence of oridonin on PC-3 cell messenger ribonucleic acid levels. PC-3 cells were treated with 20 μM /mL 30 μM /mL or 40 μM /mL oridonin (ORD) for 24 h. Pancreatic cancer cell PCC marker messenger ribonucleic acid (mRNA) expression was measured using quantitative real-time polymerase chain reaction (qPCR). Results are presented as mean \pm standard deviation ($M \pm SD$) for triplicate trials. Significant differences compared to the untreated control are denoted by * ($p < 0.05$)

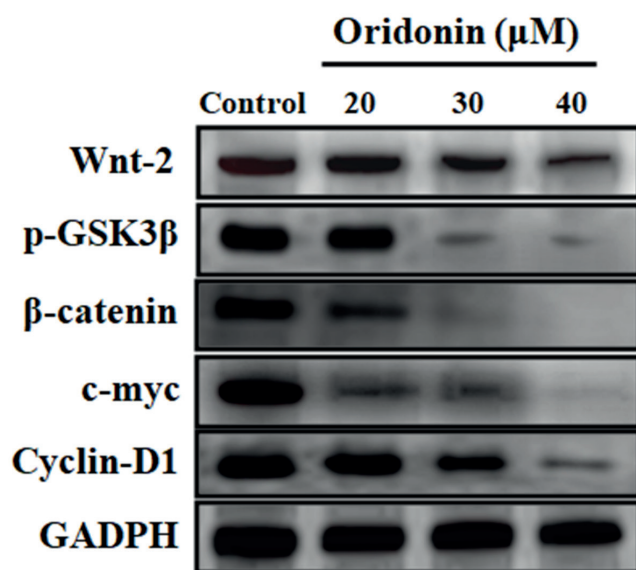


Fig. 5. Effects of oridonin on wingless-type MMTV integration site family member 2/ β -catenin signaling in PC-3 cells. Human PC-3 cells were treated with 20 μM /mL, 30 μM /mL or 40 μM /mL oridonin (ORD) for 24 h. The levels of wingless-type MMTV integration site family member 2 (Wnt-2), β -catenin, glycogen synthase kinase-3 beta (GSK3 β), c-myc, cyclin-D1, and glyceraldehyde 3-phosphate dehydrogenase (GAPDH) proteins were assessed using western blot

triggering, cell cycle arrest, caspase activation, reactive oxygen species (ROS) generation, and subdual of protein kinase B (Akt) signaling and other pathways.^{15,21} Indeed, ORD decreases cell proliferation through death receptor 5 over-stimulation and mammalian target of rapamycin

(mTOR) phosphorylation attenuation in ovarian and breast cancer cells.¹² However, the effects of ORD in human PC are still uncertain, with limited information on the signaling pathways and mechanisms responsible for its pathophysiology.

In the current study, we established the anti-proliferative activity of ORD on human androgen-independent PC-3 cells, with the results showing that ORD blocked PCC proliferation and the Wnt/ β -catenin pathway and induced apoptosis in a concentration-dependent manner. These outcomes are in agreement with the previous findings on ORD in leukemia cells and others.^{10,11} Apoptosis is a well-categorized cell death program that can be triggered by various anti-tumor mediators through communal pathways.⁵ Several studies have documented that the anti-cancer properties of ORD are due to its apoptosis stimulation effects.^{15,21} In agreement with these findings, our results revealed that ORD could initiate apoptosis in PC-3 cells.

Cancer cells are a small population of cells with stem cell features, including self-regeneration, multipotent diversity, increased tumorigenicity, and drug resistance.^{25,26} Many dietary compounds, such as curcumin,³⁶ koenimbin,²⁶ sulforaphane,³⁷ and synthetic compounds comprising monobenzylin Schiff base complex,³⁸ have demonstrated the chemopreventive actions of CCs. These cells are recognized as the tumor source and have a crucial role in driving PC development.³⁹ Targeted PCC intermediation may be the ultimate approach to PC prevention and treatment. In this regard, ORD could inhibit tumor conversion and

PCC metastasis.⁴⁰ However, the effects of ORD on PCCs have not been investigated yet. The current study established a concentration-dependent ORD PC-3 cell inhibition and downregulation of markers such as CD133, Oct-4, Nanog, ALDH1A1, and Sox2. These outcomes indicate that ORD could reduce the PCC action and may be proposed as a potential PCC-targeting agent. Indeed, the results from this research highlight the potential role and mechanisms of ORD on PCCs for the first time. Furthermore, we established that ORD anti-proliferative and apoptotic actions on PCCs may be mediated via the Wnt/ β -catenin pathway.

Wnt/ β -catenin signaling plays an essential role in the growth and expansion of PC cells.²⁸ Also, previous experiments demonstrated that androgen-independent PCC lines, namely the extremely invasive PC-3 cells, display higher Wnt/ β -catenin signaling levels than androgen-dependent PC cells.⁴¹ The Wnt/ β -catenin pathway has been documented to be vital for controlling the action of CCs in PC.^{28,29} Zhang et al. demonstrated that the Wnt/ β -catenin pathway and its target genes *c-myc* and *cyclin-D1* were stimulated in PCCs.⁴² In the present research, we investigated if Wnt/ β -catenin signaling is involved in the anti-cancer effects of ORD on PCCs. We found that ORD suppressed GSK3 β phosphorylation and the expression of β -catenin, *c-myc* and *cyclin-D1*, and inhibited β -catenin nuclear translocation. These findings suggest that stimulation of apoptosis and cell cycle arrest by ORD were complemented by the suppression of Wnt/ β -catenin signaling. As such, it appears that the proposed anti-cancer actions of ORD on PCCs were mediated through Wnt/ β -catenin signaling.

Limitations

The current study determined the anti-proliferative actions of ORD on PC-3 cells, highlighted its potent apoptosis-inducing effects, and showed that ORD could suppress CC markers and restrict PC. However, we were unable to uncover novel insights into the molecular mechanisms of ORD in PC.

Conclusions

Oridonin inhibited PC-3 cell proliferation and induced apoptosis in a concentration-dependent way. Moreover, the Wnt/ β -catenin signaling pathway appears to be a promising target through which ORD facilitates apoptosis in PC-3 cells. In the current study, we found, for the first time, that ORD controlled Wnt/ β -catenin signaling and attenuated PCC activity. According to our findings, ORD has the potential to be a future chemotherapeutic drug, which may decrease drug resistance and PC degeneration by triggering apoptosis in CCs. The findings of this research provide novel insight into the contribution and underlying molecular mechanisms of ORD in PC.

Supplementary data

The supplementary materials are available at <https://doi.org/10.5281/zenodo.8045766>. The package contains the following files:

Supplementary Fig. 1. Results of Kruskal–Wallis test as presented in Fig. 1.

Supplementary Fig. 2. Results of Kruskal–Wallis test as presented in Fig. 5.

ORCID iDs

Shulong Zhang  <https://orcid.org/0009-0004-9551-4270>

Annamalai Vijayalakshmi  <https://orcid.org/0000-0002-2436-8956>

Lingjun Meng  <https://orcid.org/0000-0002-6590-4284>

References

- Crawford ED, Eisenberger MA, McLeod DG, et al. A controlled trial of leuprolide with and without flutamide in prostatic carcinoma. *N Engl J Med*. 1989;321(7):419–424. doi:10.1056/NEJM198908173210702
- Ferlay J, Soerjomataram I, Dikshit R, et al. Cancer incidence and mortality worldwide: Sources, methods and major patterns in GLOBOCAN 2012. *Int J Cancer*. 2015;136(5):E359–E386. doi:10.1002/ijc.29210
- Siegel RL, Miller KD, Jemal A. Cancer statistics, 2020. *CA Cancer J Clin*. 2020;70(1):7–30. doi:10.3322/caac.21590
- Sartor O, Coleman R, Nilsson S, et al. Effect of radium-223 dichloride on symptomatic skeletal events in patients with castration-resistant prostate cancer and bone metastases: Results from a phase 3, double-blind, randomised trial. *Lancet Oncol*. 2014;15(7):738–746. doi:10.1016/S1470-2045(14)70183-4
- Schrecengost R, Knudsen KE. Molecular pathogenesis and progression of prostate cancer. *Semin Oncol*. 2013;40(3):244–258. doi:10.1053/j.seminoncol.2013.04.001
- Eisenberger MA, Simon R, O'Dwyer PJ, Wittes RE, Friedman MA. A reevaluation of nonhormonal cytotoxic chemotherapy in the treatment of prostatic carcinoma. *J Clin Oncol*. 1985;3(6):827–841. doi:10.1200/JCO.1985.3.6.827
- Fiñones RR, Yeargin J, Lee M, et al. Early human prostate adenocarcinomas harbor androgen-independent cancer cells. *PLoS One*. 2013;8(9):e74438. doi:10.1371/journal.pone.0074438
- Santos JI, Teixeira AL, Dias F, et al. Restoring TGF β 1 pathway-related microRNAs: Possible impact in metastatic prostate cancer development. *Tumour Biol*. 2014;35(7):6245–6253. doi:10.1007/s13277-014-1887-z
- Marks LS, DiPaola RS, Nelson P, et al. PC-SPEs: Herbal formulation for prostate cancer. *Urology*. 2002;60(3):369–375. doi:10.1016/S0090-4295(02)01913-1
- Hsieh TC, Wijeratne EK, Liang JY, Gunatilaka AL, Wu JM. Differential control of growth, cell cycle progression, and expression of NF- κ B in human breast cancer cells MCF-7, MCF-10A, and MDA-MB-231 by ponidicin and oridonin, diterpenoids from the Chinese herb *Rabdosia rubescens*. *Biochem Biophys Res Commun*. 2005;337(1):224–231. doi:10.1016/j.bbrc.2005.09.040
- Ikezoe T, Yang Y, Bandobashi K, et al. Oridonin, a diterpenoid purified from *Rabdosia rubescens*, inhibits the proliferation of cells from lymphoid malignancies in association with blockade of the NF- κ B signal pathways. *Mol Cancer Ther*. 2005;4(4):578–586. doi:10.1158/1535-7163.MCT-04-0277
- Dong Y, Zhang T, Li J, et al. Oridonin inhibits tumor growth and metastasis through anti-angiogenesis by blocking the Notch signaling. *PLoS One*. 2014;9(12):e113830. doi:10.1371/journal.pone.0113830
- Jin H, Tan X, Liu X, Ding Y. Downregulation of *AP-1* gene expression is an initial event in the oridonin-mediated inhibition of colorectal cancer: Studies in vitro and in vivo. *J Gastroenterol Hepatol*. 2011;26(4):706–715. doi:10.1111/j.1440-1746.2010.06500.x
- Wang H, Ye Y, Pan SY, et al. Proteomic identification of proteins involved in the anticancer activities of oridonin in HepG2 cells. *Phyto-medicine*. 2011;18(2–3):163–169. doi:10.1016/j.phymed.2010.06.011

15. Oh HN, Seo JH, Lee MH, et al. Oridonin induces apoptosis in oral squamous cell carcinoma probably through the generation of reactive oxygen species and the p38/JNK MAPK pathway. *Int J Oncol*. 2018;52(5):1749–1759. doi:10.3892/ijo.2018.4319
16. Yang J, Ren X, Zhang L, Li Y, Cheng B, Xia J. Oridonin inhibits oral cancer growth and PI3K/Akt signaling pathway. *Biomed Pharmacother*. 2018;100:226–232. doi:10.1016/j.biopha.2018.02.011
17. Bao R, Shu Y, Wu X, et al. Oridonin induces apoptosis and cell cycle arrest of gallbladder cancer cells via the mitochondrial pathway. *BMC Cancer*. 2014;14:217. doi:10.1186/1471-2407-14-217
18. Lin TY, Lee CC, Chen KC, Lin CJ, Shih CM. Inhibition of RNA transportation induces glioma cell apoptosis via downregulation of Ran-GAP1 expression. *Chem Biol Interact*. 2015;232:49–57. doi:10.1016/j.cbi.2015.02.019
19. Liermann J, Naumann P, Fortunato F, et al. Phytotherapeutics oridonin and ponidicin show additive effects combined with irradiation in pancreatic cancer in vitro. *Radiol Oncol*. 2017;51(4):407–414. doi:10.1515/raon-2017-0048
20. Cui Q, Tashiro SI, Onodera S, Minami M, Ikejima T. Oridonin induced autophagy in human cervical carcinoma HeLa cells through Ras, JNK, and P38 regulation. *J Pharmacol Sci*. 2007;105(4):317–325. doi:10.1254/jphs.FP0070336
21. Pi J, Cai H, Jin H, et al. Qualitative and quantitative analysis of ROS-mediated oridonin-induced oesophageal cancer KYSE-150 cell apoptosis by atomic force microscopy. *PLoS One*. 2015;10(10):e0140935. doi:10.1371/journal.pone.0140935
22. Zhang Z, Zhang X, Xue W, et al. Effects of oridonin nanosuspension on cell proliferation and apoptosis of human prostatic carcinoma PC-3 cell line. *Int J Nanomedicine*. 2010;5:735–742. doi:10.2147/IJN.S13537
23. Yang H, Ping Dou Q. Targeting apoptosis pathway with natural terpenoids: Implications for treatment of breast and prostate cancer. *Curr Drug Targets*. 2010;11(6):733–744. doi:10.2174/138945010791170842
24. Li X, Li X, Wang J, Ye Z, Li JC. Oridonin up-regulates expression of P21 and induces autophagy and apoptosis in human prostate cancer cells. *Int J Biol Sci*. 2012;8(6):901–912. doi:10.7150/ijbs.4554
25. Kamalidehghan B, Houshmand M, Kamalidehghan F, et al. Establishment and characterization of two human breast carcinoma cell lines by spontaneous immortalization: Discordance between estrogen, progesterone and HER2/neu receptors of breast carcinoma tissues with derived cell lines. *Cancer Cell Int*. 2012;12(1):43. doi:10.1186/1475-2867-12-43
26. Ahmadipour F, Ibrahim Noordin M, Mohan S, et al. Koenimbins, a natural dietary compound of *Murraya koenigii* (L) Spreng: Inhibition of MCF7 breast cancer cells and targeting of derived MCF7 breast cancer stem cells (CD44⁺/CD24⁻/low). An in vitro study. *Drug Des Devel Ther*. 2015;9:1193–1208. doi:10.2147/DDDT.S72127
27. Sharpe B, Beresford M, Bowen R, Mitchard J, Chalmers AD. Searching for prostate cancer stem cells: Markers and methods. *Stem Cell Rev Rep*. 2013;9(5):721–730. doi:10.1007/s12015-013-9453-4
28. Holland JD, Klaus A, Garratt AN, Birchmeier W. Wnt signaling in stem and cancer stem cells. *Curr Opin Cell Biol*. 2013;25(2):254–264. doi:10.1016/j.ccb.2013.01.004
29. Kypta RM, Waxman J. Wnt/ β -catenin signalling in prostate cancer. *Nat Rev Urol*. 2012;9(8):418–428. doi:10.1038/nrurol.2012.116
30. Zhan T, Rindtorff N, Boutros M. Wnt signaling in cancer. *Oncogene*. 2017;36(11):1461–1473. doi:10.1038/onc.2016.304
31. Tilley WD, Wilson CM, Marcelli M, McPhaul MJ. Androgen receptor gene expression in human prostate carcinoma cell lines. *Cancer Res*. 1990;50(17):5382–5386. PMID:2386943.
32. Mosmann T. Rapid colorimetric assay for cellular growth and survival: Application to proliferation and cytotoxicity assays. *J Immunol Methods*. 1983;65(1–2):55–63. doi:10.1016/0022-1759(83)90303-4
33. Grimm D, Bauer J, Kossmehl P, et al. Simulated microgravity alters differentiation and increases apoptosis in human follicular thyroid carcinoma cells. *FASEB J*. 2002;16(6):604–606. doi:10.1096/fj.01-0673fje
34. Schweizer MT, Gulati R, Mostaghel EA, et al. Docetaxel-related toxicity in metastatic hormone-sensitive and metastatic castration-resistant prostate cancer. *Med Oncol*. 2016;33(7):77. doi:10.1007/s12032-016-0793-1
35. Bahl A, Masson S, Malik Z, et al. Final quality of life and safety data for patients with metastatic castration-resistant prostate cancer treated with cabazitaxel in the UK Early Access Programme (EAP) (NCT01254279). *BJU Int*. 2015;116(6):880–887. doi:10.1111/bju.13069
36. Hewlings S, Kalman D. Curcumin: A review of its effects on human health. *Foods*. 2017;6(10):92. doi:10.3390/foods6100092
37. Li Y, Zhang T, Korkaya H, et al. Sulforaphane, a dietary component of broccoli/broccoli sprouts, inhibits breast cancer stem cells. *Clin Cancer Res*. 2010;16(9):2580–2590. doi:10.1158/1078-0432.CCR-09-2937
38. Fani S, Kamalidehghan B, Lo KM, et al. Anticancer activity of a monobenzyln complex C1 against MDA-MB-231 cells through induction of apoptosis and inhibition of breast cancer stem cells. *Sci Rep*. 2016;6:38992. doi:10.1038/srep38992
39. Harris KS, Kerr BA. Prostate cancer stem cell markers drive progression, therapeutic resistance, and bone metastasis. *Stem Cells Int*. 2017;2017:8629234. doi:10.1155/2017/8629234
40. Lu J, Chen X, Qu S, et al. Oridonin induces G2/M cell cycle arrest and apoptosis via the PI3K/Akt signaling pathway in hormone-independent prostate cancer cells. *Oncol Lett*. 2017;13(4):2838–2846. doi:10.3892/ol.2017.5751
41. Cayrol C, Knibiehler M, Ducommun B. p21 binding to PCNA causes G1 and G2 cell cycle arrest in p53-deficient cells. *Oncogene*. 1998;16(3):311–320. doi:10.1038/sj.onc.1201543
42. Zhang K, Guo Y, Wang X, et al. WNT/ β -catenin directs self-renewal symmetric cell division of hTERT^{high} prostate cancer stem cells. *Cancer Res*. 2017;77(9):2534–2547. doi:10.1158/0008-5472.CAN-16-1887

Wnt signaling pathway and sclerostin in the development of atherosclerosis and vascular calcification

Piotr Kocełak^{1,A–D}, Monika Puzianowska-Kuźnicka^{2,3,C,E}, Magdalena Olszanecka-Glinianowicz^{4,A,E,F}, Jerzy Chudek^{5,A,C,F}

¹ Pathophysiology Unit, Department of Pathophysiology, Faculty of Medical Sciences, Medical University of Silesia, Katowice, Poland

² Department of Geriatrics and Gerontology, Medical Centre of Postgraduate Education, Warsaw, Poland

³ Department of Human Epigenetics, Mossakowski Medical Research Institute, Polish Academy of Sciences, Warsaw, Poland

³ Health Promotion and Obesity Management Unit, Department of Pathophysiology, Faculty of Medical Sciences in Katowice, Medical University of Silesia, Poland

⁴ Department of Internal Medicine and Oncological Chemotherapy, Faculty of Medical Sciences in Katowice, Medical University of Silesia, Poland

A – research concept and design; B – collection and/or assembly of data; C – data analysis and interpretation;

D – writing the article; E – critical revision of the article; F – final approval of the article

Advances in Clinical and Experimental Medicine, ISSN 1899–5276 (print), ISSN 2451–2680 (online)

Adv Clin Exp Med. 2024;33(5):519–532

Address for correspondence

Piotr Kocełak

E-mail: pkocelak@sum.edu.pl

Funding sources

None declared

Conflict of interest

None declared

Received on August 2, 2022

Reviewed on June 21, 2023

Accepted on July 13, 2023

Published online on September 7, 2023

Abstract

Atherosclerosis is a complex process involving endothelial dysfunction, vascular inflammation, vascular smooth muscle cell (VSMC) proliferation, angiogenesis, and calcification. One of the pathomechanisms of atherosclerosis is the upregulation of Wnt signaling. This study aimed to summarize the current knowledge regarding the role of Wnt signaling and sclerostin in atherosclerosis, vascular calcification, aneurysms, and mortality based on the PubMed database. We followed the Preferred Reporting Items for Systematic Reviews and Meta-Analyses (PRISMA) recommendation and identified 160 papers that were included in this systematic review. The published data highlight that the upregulation of Wnt components facilitates the initiation and progression of atherosclerosis, arterial remodeling, VSMCs proliferation and phenotypic transition to the osteoblastic lineage in the arterial wall. This results in protein secretion, cell migration, calcification, fibrosis and aneurysm formation. The transformation of VSMCs into osteoblast-like cells that is observed in atherosclerosis results in sclerostin expression inhibiting the Wnt pathway. Furthermore, it was shown that sclerostin, expressed in atherosclerotic plaques, inhibits aneurysm formation in a mouse model. However, in humans, while the antisclerostin antibody romosozumab inhibits bone resorption, biochemical parameters of endothelial activation and inflammation are not affected, and the incidence of aneurysms is not increased. It was suggested that detecting sclerostin in the calcified aortic atherosclerotic plaques reflects a defense mechanism against Wnt activation and inhibition of atherosclerosis, although this has only been shown in animal models. Moreover, an increased number of vascular cells converted to osteogenic phenotypes results in increased plasma sclerostin concentrations. Therefore, plasma sclerostin derived from bone limits its importance as a global marker of vascular calcification.

Key words: atherosclerosis, aneurysm, cardiovascular disease, sclerostin, WNT-signaling

Cite as

Koceleak P, Puzianowska-Kuźnicka M, Olszanecka-Glinianowicz M, Chudek J. Wnt signaling pathway and sclerostin in the development of atherosclerosis and vascular calcification. *Adv Clin Exp Med.* 2024;33(5):519–532. doi:10.17219/acem/169567

DOI

10.17219/acem/169567

Copyright

Copyright by Author(s)

This is an article distributed under the terms of the Creative Commons Attribution 3.0 Unported (CC BY 3.0) (<https://creativecommons.org/licenses/by/3.0/>)

Introduction

Cardiovascular disease (CVD) is one of the most common causes of mortality worldwide,¹ the most frequent form of which is coronary artery disease (CAD) associated with atherosclerosis, and its acute form (myocardial infarction) is responsible for most deaths. Atherosclerosis is a complex process that consists of several pathological traits, including endothelial dysfunction, vascular inflammation, vascular smooth muscle cell (VSMC) proliferation, plaque angiogenesis, and calcification.^{2,3} Moreover, all these processes are associated with the Wnt signaling pathway.^{2,4}

The process of arterial calcification stems from the transformation of VSMCs localized in the intima-media into osteoblast-like cells,^{5,6} thereby switching functions from contractile to synthetic. The shift in VSMC phenotype is primarily related to runt-related transcription factor 2 (RUNX2) expression regulated by the Wnt pathway.^{6,7} The increase in mechanical load within arteries likely releases proteins to strengthen the action on the RUNX2 factor and facilitates the action of the Wnt-enhancing calcification.⁸ This process can be driven by soft tissue injury, resulting in the disruption of homeostasis and the initiation of bone matrix development, leading to ectopic calcification and mineralization of soft tissues.⁹

The main functions of Wnt signaling are the regulation of cell migration and polarity, organogenesis, fate determination, and proliferation of cells during embryonic development. Wnt signaling is also involved in the proliferation of stem cells into progenitor cells, which can subsequently differentiate into several cell types, including cardiac muscle, VSMC and endothelial cells. Therefore, the Wnt pathway is crucial during embryonic development and plays a role in the homeostasis of the adult organism. Moreover, the Wnt pathway is ubiquitous and controls many fundamental cellular processes, including osteogenesis, integrating multiple receptors, growth factors and cellular connections to transcription factors that affect gene expression.⁴

Sclerostin (SOST), an inhibitor of bone formation and calcification secreted by osteocytes,^{10,11} is also a soluble inhibitor of the Wnt canonical signaling pathway. Sclerostin is involved in bone tissue homeostasis, inhibits osteogenesis and calcification, and is a modulator of bone homeostasis.^{10,11} Its mechanism of action is to bind the LRP5 receptors and disrupt the canonical Wnt pathway.

Numerous studies have reported the involvement of sclerostin in the development of atherosclerosis^{11,12} and its complications,^{13,14} including arterial stenosis,¹⁴ and clinical presentation in the form of ischemic heart disease,¹⁵ cerebral ischemia^{16,17} and peripheral artery disease,¹⁸ but also more advanced complications such as vascular calcification^{19–22} and aneurysm development.²² The results of some studies suggest that sclerostin could potentially play a positive role and inhibit the progression of atherosclerosis.²³

Moreover, it has been shown that sclerostin may be locally produced in calcified tissue and may act as a counter mechanism against enhanced calcification in arterial beds. It seems that sclerostin may constitute the intermediary between bone homeostasis and the development of vessel calcification and atherosclerosis.

Objectives

As the induction of calcification is an important element in atherosclerosis, we aimed to summarize the knowledge on the role of Wnt signaling and sclerostin in the development of atherosclerosis and vascular calcification.

Methodology

Data on the role of Wnt signaling and sclerostin in the development of atherosclerosis, arterial aneurysm and mortality presented in the article are based on published studies available in the PubMed database. Our search was based on the keywords “Wnt signaling”, “sclerostin”, “atherosclerosis”, “vascular calcification”, “aneurysm”, and “cardiovascular mortality”, and we initially identified 652 articles. Following a review by 2 of the authors, 160 studies were included in the article. Duplicated articles, as well as papers without full-text availability, were excluded from the review. The review included a broad range of articles, from basic molecular studies to clinical outcome investigations. The Preferred Reporting Items for Systematic Reviews and Meta-Analyses (PRISMA) flow diagram is presented in Fig. 1.

The Wnt pathway: general overview

The ‘Wnt’ name comes from the combination of the Wingless segment polarity gene name in *Drosophila* and its vertebrate homolog int-1 (integrated). This highly conserved signaling pathway is activated by membrane receptors.²⁴ The Wnt signaling pathway consists of at least 19 proteins and is involved in numerous biological processes, including embryonic development, organogenesis, stem cell development, cell proliferation, differentiation, migration and polarity, tissue homeostasis, and glucose and lipid metabolism.^{24–27} Furthermore, Wnt signaling participates in bone formation, vascular and valvular calcification,^{2,3,19,28,29} and angiogenesis.³⁰ In the process of angiogenesis, Wnt signaling regulates endothelial cell proliferation and survival,³¹ and proliferation, migration and survival of VSMCs via the Wnt/ β -catenin pathway.^{2,28–30}

Alterations in Wnt signaling appear to be directly involved in the increase of cardiovascular risk. For example, in mouse models, mutations of the co-receptors of Frizzled

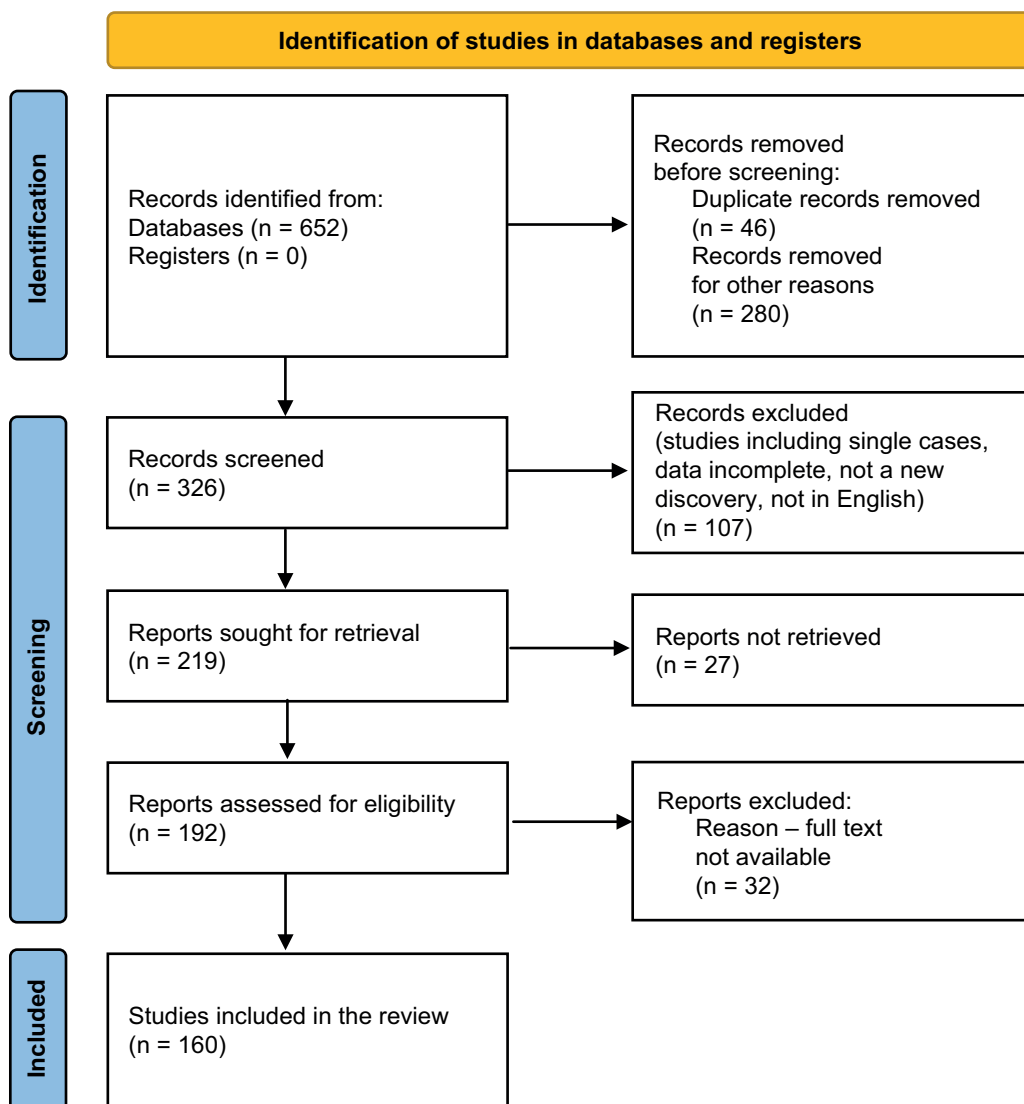


Fig. 1. Preferred Reporting Items for Systematic Reviews and Meta-Analyses (PRISMA) flow diagram

(Fz), a receptor in the Wnt pathway (e.g., low-density lipoprotein receptor-related protein 6 (LRP6)), are associated with an increase in morphogenesis and differentiation of adipocytes,³² enhancement of monocyte adhesion to endothelial cells, the proliferation of VSMCs,³⁰ vascular calcification,³³ hypercholesterolemia and, consequently, hypertension, type 2 diabetes mellitus (T2DM) and premature CAD.³⁴ The current literature also shows that enhanced Wnt signaling, due to gain-of-function mutations of all elements of this signaling pathway, is associated with alterations in vascular development.^{35,36}

The Wnt pathway: mechanism of action

The Wnt proteins secreted by epithelial cells bind to the extracellular domain of the Fz surface receptor family. The Wnt ligand and the Fz receptor require LRP5/6 as co-receptors for the transduction of the signal into the cells.²⁴ Other ligands that can activate LRP5/6

receptors include parathormone (PTH)³⁷ and G-protein-coupled ligands such as isoproterenol (β -mimetic), adenosine and glucagon.³⁸ Furthermore, LRP5/6 are also co-receptors for a platelet-derived growth factor (PDGF) and the transforming growth factor- β (TGF- β) receptor.³⁹ The complex of Wnt protein/Fz receptor with LRP5/6 co-receptors transduces the signal to cytoplasmic phosphoprotein Dishevelled (Dsh/Dvl). Moreover, Wnt signaling activates 3 different pathways: canonical, planar cell polarity (PCP) and the Wnt/Ca.²⁴

The canonical pathway

The canonical pathway comprises Dsh signaling to protein complexes which, in the absence of Wnt ligands, promotes the ubiquitination and finally degradation of β -catenin,²⁴ while the Wnt ligand and activation of the Fz-LRP5/6 receptor complex inhibits this degradation, resulting in the translocation of β -catenin from the cytoplasm into the nucleus. Finally, β -catenin interacts

with T-cell factor (TCF)/lymphoid-enhancer binding factor (LEF), which activates the transcription of Wnt-related genes that encode cyclin D1, PPAR and c-Myc, all of which are responsible for cell growth, proliferation and survival.²⁴

The non-canonical pathways

The non-canonical pathways comprise the PCP pathway, which regulates the cytoskeletal organization and cell polarization,²⁴ and the Wnt/Ca pathway responsible for the regulation of cell movement and adhesion.²⁴ In these pathways, the Wnt signal is mediated through Fz receptors independent from the LRP5/6 co-receptor. The co-receptors for this pathway are likely mediated through tyrosine-protein kinase transmembrane receptor (ROR2),⁴⁰ neurotrophin-related protein 1 (NRH1),⁴¹ receptor tyrosine kinase (Ryk),⁴² and protein tyrosine kinase 7 (PTK).⁴³

The transduction of the non-canonical signaling leads to the activation of cytoplasmic Dsh, which is similar to the activation of the canonical pathway, but the PCP pathway utilizes the PDZ and DEP domains of Dsh, and ultimately activates the small GTPases Rho and Rac.⁴⁴ One branch of this pathway acts through Daam 1 (Dishevelled-associated activator of morphogenesis 1), which binds to the central PDZ domain of Dsh and activates Rho GTPase through WGEF (weak-similarity GEF).⁴⁵

Active Rho GTPase can stimulate Rho-associated kinase (ROCK)⁴⁶ and myosin,⁴⁷ resulting in the modification of actin and cytoskeletal organization.

The other signaling branch depends on the C-terminal DEP domain of Dsh and stimulates Rac GTPase activity.⁴⁸ Rac triggers c-Jun N-terminal kinase (JNK)⁴⁹ in a Daam-independent manner. Both Rho and Rac GTPases can regulate transcription and alter cell organization and polarity.⁵⁰

The 2nd arm of non-canonical Wnt signaling, the Wnt/Ca pathway, is responsible for an increase in intracellular calcium levels through trimeric G protein signaling.^{51,52} Increased calcium stimulates calcium-sensitive kinases, including phospholipase C, and protein kinase C (PKC).⁵³ Moreover, the Wnt/Ca pathway is thought to stimulate the canonical and PCP pathways^{54,55} by utilizing the PDZ and DEP domains of the Dsh protein. However, in the non-canonical pathway, the Dsh protein is localized at the cell membrane and not in the cytoplasm as in the canonical Wnt signaling pathway.⁵⁶ Finally, the Wnt/Ca pathway is essential in embryonic development, cell adhesion, tissue orientation, and organ formation.⁵¹

Numerous factors, such as secreted frizzled-related proteins (sFRPs)⁵⁷ and Wnt inhibitory factor-1 (WIF-1),⁵⁸ may inhibit the Wnt pathways by directly binding to Wnt and preventing its connection with the receptor. In addition, sclerostin⁵⁹ and Dickkopf (Dkk) family members⁶⁰ inhibit the transduction of the signal by binding to LRP5/6. The Wnt signaling pathways are highlighted in Fig. 2.

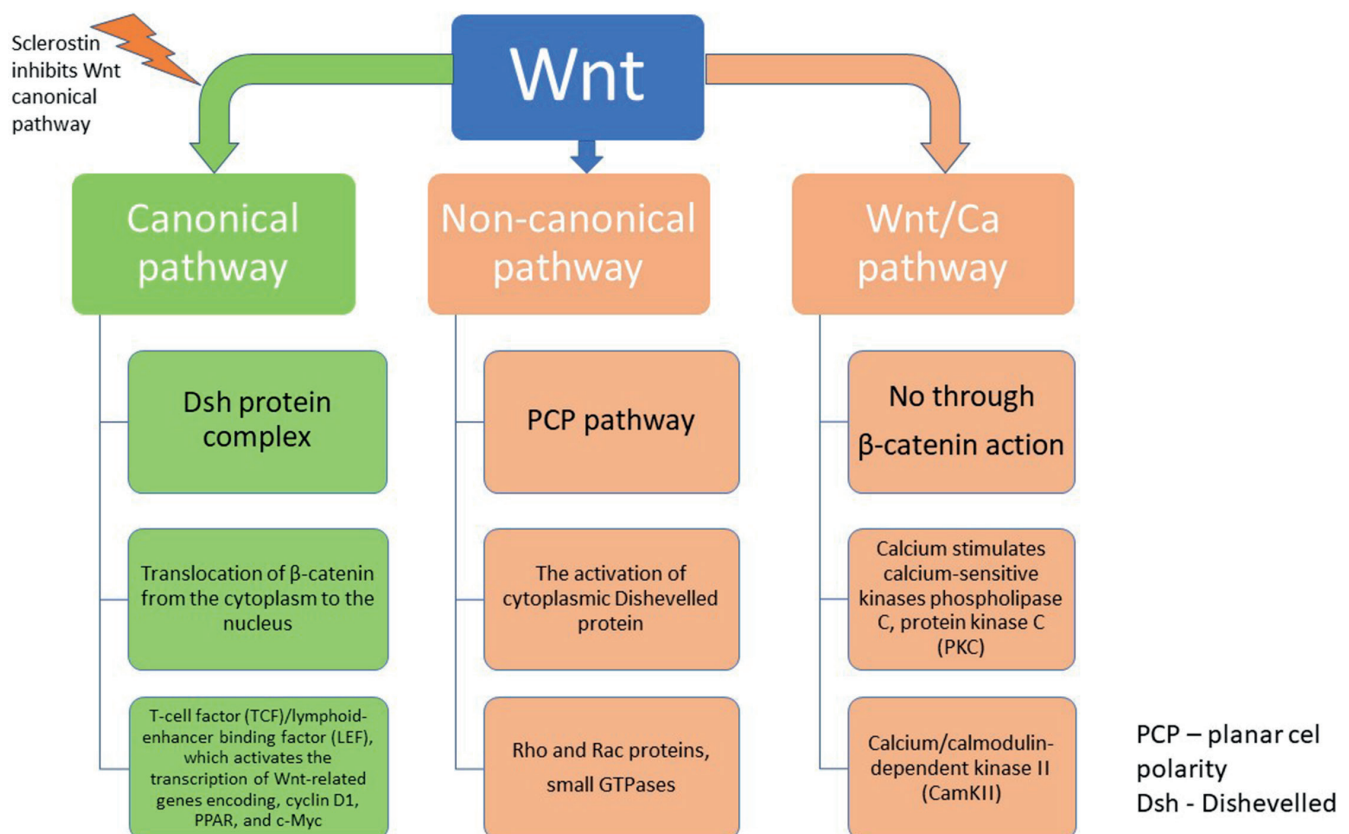


Fig. 2. Wnt signaling

Wnt signaling and bone formation

Wnt signaling participates in bone formation by increasing the transformation of mesenchymal stem cells (MSCs) to osteoblasts while inhibiting osteoclast differentiation.^{61,62}

Bone cells, including osteoblasts, osteocytes, chondrocytes and bone marrow cells, produce many Wnt ligands.⁶³ In the mouse, these are secreted from osteoblasts in an autocrine manner and participate in their mineralization and maturation. Moreover, Wnt16 induces osteoprotegerin expression in osteoblasts via the Wnt- β -catenin pathway⁶⁴ and inhibits osteoclasts formation independent from osteoprotegerin (OPG) action.⁶⁵ Furthermore, the Wnt5a ligand involved in the non-canonical signaling pathway is responsible for osteoblast lineage formation from mesenchymal precursors and can inhibit adipocyte differentiation.⁶⁶ Even though the receptor for Wnt5a is the tyrosine kinase orphan receptor 2 (Ror2), its action results in enhancement in LRP5/6, which activates β -catenin and enhances the expression of OPG, and promotes osteoblast differentiation.⁶⁶

Wnt3a, a Wnt ligand in the canonical signaling pathway, inhibits calcitriol-induced, but not Rankl-induced osteoclast formation induced by OPG expression in osteoblasts.⁶⁷ Moreover, Wnt16 secreted from osteoblasts inhibits human and mouse osteoclast formation by disrupting Rankl in a Wnt-independent manner.⁶⁴ This is achieved through inhibiting Rankl-induced activation of NF- κ B and calcitriol-induced mice osteoclast formation.⁶⁸ Wnt4 is also expressed in osteoblasts and inhibits osteoclasts formation independently from the Wnt pathway by enhancing OPG expression.⁶⁹

Wnt5a enhances LRP5/6 expression in osteoblasts and simultaneously promotes Wnt10b and activates the Wnt/ β -catenin pathway to induce osteoclasts formation. The interplay between Wnt5a and Wnt16 may also regulate osteoclastogenesis and osteolysis, and it is known that Wnt5a mediates osteoclast formation by binding to and stimulating Ror-2 receptors.⁷⁰ Conditions such as arthritis with a high level of Wnt5a may reverse the inhibitory effect of Wnt16 on osteoclast formation.^{66,70}

In summary, secreted Wnt signaling ligands regulate osteoblast and osteoclast differentiation, and their interplay defines the balance between bone formation and bone resorption. The surrounding environmental conditions determine the induction of different Wnt ligands and the regulation of bone homeostasis.

Wnt signaling and atherosclerosis

All aspects of Wnt signaling are closely associated with the initiation and progression of atherosclerosis.^{26,30} The upregulation of Wnt signaling (increased expression of the components of Wnt signaling, including WNT5a,

WNT5b and WNT11) was detected in human aortic calcified atherosclerotic lesions and related aneurysms.^{23,71} Furthermore, shear stress appears to be the primary mechanism that triggers the upregulation of Wnt signaling.⁷² In addition, upregulated Wnt signaling affects endothelial cell proliferation and survival, enhances monocyte adhesion and transendothelial migration,^{3,73} and results in dysregulation of proliferation and apoptosis of VSMCs.²⁸ Wnt signaling participates in bone formation by increasing the transformation of MSCs to osteoblasts and inhibiting differentiation to osteoclasts.^{61,62} Therefore, inappropriate activation of the Wnt signaling pathway may play a role in osteoblastic transition into the arterial wall⁷⁴ and vascular calcification.³⁰ It appears that the link between atherosclerosis and bone loss is mediated through the canonical Wnt signaling pathway.¹¹

Atherosclerosis development is associated with the proliferation and migration of VSMCs and endothelial dysfunction.⁷⁵ The canonical Wnt/ β -catenin signaling pathway results in the upregulation of proliferation genes, such as *cyclin D1* responsible for VSMCs proliferation.⁷⁴ Some of the *WNT* family genes encoding proteins such as *WNT1*^{74,76} and *WNT5a*⁷⁷ in VSMCs and macrophages from atherosclerotic plaques have been identified as the initiators of VSMCs proliferation and release of pro-inflammatory cytokines. Additionally, overexpression of Wnt inhibitors like sFRPs has been shown to constrain VSMC proliferation.⁷⁶ In contrast, Wnt3a exerts an anti-inflammatory effect by modulating NF κ B-related gene expression in a mouse model.⁷⁸ Moreover, an increased DKK-1 level promotes pro-inflammatory cytokine release,⁷⁹ and the Wnt co-receptor LRP5 is responsible for enhancing lipid uptake, transforming macrophages into foam cells, and macrophage migration through enhanced regulation of Wnt-related proteins such as osteopontin (OPN), bone morphogenetic protein 2 (BMP2), cyclin D1, c-jun, lymphoid enhancer factor 1 (LEF1), and β -catenin.⁸⁰

The Wnt pathway regulates the expression of OPG and OPN associated with extracellular matrix mineralization.⁸¹ Osteopontin has pro-inflammatory properties⁸² and activates the proteolytic activity of metalloproteinases,⁸³ while OPG expressed in endothelial cells and VSMCs⁸⁴ plays a role in the pathogenesis of atherosclerosis and the progression of aortic aneurysms.⁸⁵

Wnt signaling is also involved in the process of fibrogenesis through TGF- β activation.⁸⁶ Pathological activation of the canonical Wnt pathway has been detected in pulmonary,⁸⁷ dermal,⁸⁸ renal,⁸⁹ and myocardial infarction-related fibrosis,⁹⁰ and in muscles of mice from a model of musculoskeletal dystrophy.⁹¹ The DKK proteins are thought to play a significant role in inhibiting the Wnt canonical pathway by either binding to the LRP5/6 receptor and its co-receptor Kremen-1/2, internalizing the receptor and facilitating its degradation, or by disrupting the interaction between WNT and the LRP5/6 and Fz co-receptor complex.⁹² In cultured human fibroblasts, TGF- β signaling

led to lower DKK-1 expression, which in turn activated the Wnt pathway. Both lower expression of DKK-1 and the use of DKK-1-neutralizing antibodies resulted in aggravation of fibrosis, whereas overexpression of DKK-1 prevented the initiation of fibrosis in the skin obtained from patients with systemic sclerosis.⁹¹ Overexpression of Wnt proteins in fibroblasts has been detected in enhanced generalized dermal fibrosis mouse models.⁹¹ This evidence demonstrates that the interrelation of the TGF- β pathway and Wnt signaling plays a pivotal role in the pathogenesis of fibrosis.⁹¹

During atherosclerosis, fibrosis is present in the wall of the artery and heart valves. WNT5b and WNT11 proteins were detected in aortic valvular interstitial cells with extensive fibrosis, underscoring the role of the canonical Wnt pathway in the development and exacerbation of atherosclerosis in humans.⁷¹

Wnt signaling and vascular calcification

The involvement of Wnt signaling in physiological bone turnover may be the herald of calcification, as the process of calcifying smooth muscle cells resembles the process of osteogenesis. Vascular calcification is one of the most common locations of ectopic soft tissue calcification and represents the congregation of hydroxyapatite preferentially in the tunica media⁹ during diabetes and chronic kidney disease (CKD), and contributes to the development of hypertension and cardiovascular complications.⁹³ The primary pathological process is that of the transition of mesenchymal VSMCs into a single-lineage osteogenic cell type.⁹⁴ In the presence of calcified arterial plaques, a loss of elasticity increases the constant strain exerted on arteries resulting in VSMC proliferation and differentiation.⁶ In transformed VSMCs, osteogenic genes have been found, albeit their mRNA expression is significantly lower than in osteoblasts.⁹⁵ Moreover, high plasma levels of calcium and phosphate initiate the process of calcium deposition in arteries by changing the phenotype of VSMCs and increasing the expression of osteogenic proteins.^{96,97} The main regulatory mechanism involved in the process of calcification and plaque formation is the canonical Wnt signaling pathway.⁹⁸ The target gene of the Wnt cascade is the transcription factor RUNX2 responsible for the phenotypic change of VSMC,⁷ osteoblast differentiation and initiation of calcification.²⁴

The arterial Wnt signaling pathway is induced by hypercalcemia and hyperphosphatemia, RUNX2, BMP-2 and -4, and stress or injury, which results in the upregulation of Wnt-related genes.⁹⁹ The Wnt signaling pathway induces vascular calcification by promoting the expression of genes responsible for VSMC differentiation like *RUNX2* (osteogenic differentiation),¹⁰⁰ *VCAN* (cell proliferation and migration due to vessel injury),¹⁰¹ *OPG* to inhibit osteoclast

formation,¹⁰² and *RANKL* (responsible for the recruitment of osteoblast-like precursors).¹⁰⁰

Wnt3a has been shown to activate β -catenin and RUNX2 expression, thereby increasing arterial calcium deposition and osteocalcin expression resulting in the promotion of VSMC calcification¹⁰³ as well as migration by increased adherence to type 1 collagen fibrils.¹⁰⁴ Moreover, Wnt7b plays a role in the development of neo-vasculature via the Wnt signaling pathway,¹⁰⁵ while Wnt16 has been implicated in changing the phenotype of VSMCs from contractile to osteogenic lineage.¹⁰⁶

Sclerostin: mechanism of action

Sclerostin, the product of the *SOST* gene¹⁰⁷ and secreted by osteocytes,¹⁰ acts mainly in an autocrine and paracrine manner. The physiological role of sclerostin is the inhibition of bone formation and calcification,¹¹ and it has been suggested that the serum concentration of sclerostin reflects the pool of mature osteocytes.¹⁰⁷ Its expression was also detected in many other tissues, including the heart, lungs and cancers.¹⁰⁸ The mechanisms of sclerostin action are summarized in Table 1.

Sclerostin is a soluble inhibitor of the canonical Wnt signaling pathway and therefore regulates the proliferation and differentiation of osteoblasts and bone formation.¹¹⁷ It antagonizes BMP signaling, thus stimulating osteoblast and osteocyte apoptosis.^{118,119} The autocrine action of sclerostin also involves stimulating RANKL expression in osteocytes, thus supporting osteoclast activity and bone resorption.¹²⁰ In addition, the paracrine action of sclerostin on osteoblasts and osteoclasts by the LRP5 receptor inhibits bone formation.¹²¹

Sclerostin signaling is modulated by numerous factors, including calcitriol, which facilitates its action by modulating the expression of LRP5/6, the sclerostin receptor. In addition, as shown in mice models, calcitriol enhances the expression of *Dkk-1* and secretion of frizzled-related protein 2 (*Sfrp2*), which are antagonists of the Wnt signaling pathway.¹²² Other factors modulating the action of sclerostin are PTH,¹²³ tumor necrosis factor alpha (TNF- α)¹¹⁰ and glucocorticoids.¹¹¹

Thus, the physiological role of sclerostin in the regulation of bone mineralization is the inhibition of the canonical Wnt/ β -catenin pathway via LRP5/6 binding¹⁰⁹ It also enhances the degradation of β -catenin, resulting in the inhibition of osteoblast differentiation and proliferation.

As mentioned above, numerous studies have shown the essential role of the Wnt signaling pathway in vascular development and remodeling.³⁰ An anti-calcification effect related to the inhibition of the Wnt pathway was demonstrated in carotid plaques and calcified aortas.¹¹² Thus, the presence of sclerostin in human arteries is not unexpected.¹²⁴ Some studies have also reported sclerostin and DKK-1 expression in calcified human aortas and carotid plaques.¹²⁴

Table 1. Mechanisms of sclerostin action

Models	Genes mutation	Effects or results
In vitro human, mice osteoblast ^{11,109}	–	sclerostin and Dickkopf family bind to LRP5/6 receptors and suppress osteogenesis
A human with atherosclerosis and heart valves calcifications ²¹	–	sclerostin has been identified in vascular smooth muscle cells and aortic valves
A human with chronic kidney disease ²²	–	sclerostin is produced locally in calcified arteries
In vitro mice, cell osteoblasts culture incubated with TNF- α ¹¹⁰	–	decreased sclerostin levels
Mice osteocytes culture incubated with glucocorticoids ¹¹¹	–	increased sclerostin levels
In vitro and ex vivo mice VSMC arterial cells with atherosclerosis and calcifications ¹¹²	<i>Enpp1</i> ^{-/-} mouse	sclerostin expression identified in mature osteocyte – VSMC of aortic tissue
A human with sclerosteosis and VBD ¹¹³	gene chromosome 17q12-q21 of sclerostin	loss of sclerostin function in bones
Mice limb bud ¹¹⁴	<i>SOST</i> gain of function mutations	loss of Wnt pathway in limbs
A human with bone overgrowth ¹¹⁵	<i>LRP4</i> genes: mutations – R1170W, W1186S	loss of function of LRP4 – sclerostin receptor in bone
Postmenopausal women treated with calcitriol ¹¹⁶	–	enhanced serum sclerostin levels

VSMC – vascular smooth muscle cells; VBD – Van Buchem's disease; TNF- α – tumor necrosis factor alpha.

Sclerostin expression in VSMCs likely reflects their transition to osteoblast-like cells.¹¹² This hypothesis is supported by a positive correlation between serum sclerostin concentration and the severity of aortic calcification.^{21,125} In addition, it was shown that β -catenin activity is crucial in initiating VSMC proliferation and neointima formation, processes essential in arterial physiology. Reactive oxygen species (ROS) are among the factors that can enhance β -catenin activity.⁷⁴ Sclerostin and DKK-1 inhibit the β -catenin-dependent Wnt signaling pathway, and therefore a high sclerostin level may indicate a defensive mechanism against enhanced Wnt pathway stimulation by ROS.³³ The process of vascular calcification resembles that of bone morphogenesis.¹²⁶ Wnt signaling mediates the differentiation of progenitor and VSMCs into an osteo/chondro phenotype.¹²⁷ This was seen in cultured rat VSMCs, in which *Dkk-1* acts as a potent inhibitor of the canonical Wnt signaling pathway reducing the expression of *Runx2*, an essential transcription factor for osteogenic differentiation.¹⁰³ In human knee chondrocytes, the incubation with sclerostin resulted in a decrease of *RUNX-2* mRNA.¹²⁸ Therefore, both sclerostin and *Dkk-1* proteins may neutralize the process of vascular calcification and modify arterial stiffness and arteriosclerotic plaque stability.¹²⁹

Sclerostin and atherosclerosis

Interestingly, a higher sclerostin concentration was found in the media compared to the intima of atherosclerotic plaques of patients undergoing carotid endarterectomy, and a similar finding was demonstrated for VSMCs when compared to infiltrating macrophages.¹³⁰ Sclerostin was also found in the aorta of patients undergoing aortic

valve surgery and was upregulated in calcifying VSMCs and calcified valvular plaques.²¹ Serum sclerostin levels have been associated with the presence of thoracic aortic calcification (TAC), the severity of calcification, and sclerostin expression in the vessel wall.¹³¹ Numerous studies have shown associations between sclerostin levels and aortic or carotid plaques and vascular calcifications in patients with T2DM and CVD and in postmenopausal women.^{12,132,133} In addition, sclerostin levels were higher in elderly patients with peripheral arterial disease (PAD) than in patients with a normal value of the ankle-brachial index (ABI), and higher sclerostin levels were shown to be an independent predictor of PAD.¹⁸ Therefore, it seems that sclerostin may be considered a surrogate marker of vascular calcification, and may even be a surrogate of vascular disturbances in patients with CKD.¹³⁴ Previous literature also suggests that increased sclerostin levels in VSMCs may protect against excessive vascular calcification in dialysis patients.¹³³ However, this mechanism has limited efficacy.

The increased sclerostin concentrations observed during the course of atherosclerosis in a clinical setting seem to be ineffective in exerting protective anti-calcification effects in damaged vessels. Moreover, clinical studies show sex-related differences in sclerostin concentrations, which are higher in men, and in the frequency and course of CVD. However, even higher serum sclerostin concentrations in men do not prevent the occurrence and progression of atherosclerosis, suggesting that the levels of circulating sclerostin are not effective in inhibiting the pathological process in vessels.¹³⁵

Sclerostin is independently positively associated with increased carotid intima-media thickness (CIMT) and with the risk of carotid plaque presence and aortic calcification.¹² However, Gaudio et al. showed higher sclerostin and DKK-1 concentrations in postmenopausal women with

T2DM than in healthy controls and a negative correlation with CIMT only in the T2DM group.¹¹ Thus, sclerostin concentration was an independent predictor of CIMT in T2DM patients. In patients with T2DM, sclerostin was likely higher due to the presence of atherosclerotic lesions and the presence of cells derived from an osteogenic lineage inside the arterial wall, which may be the source of circulating sclerostin.¹³⁶ Therefore, higher sclerostin levels in patients with CVD may reflect the advanced progression of atherosclerosis and plaque calcification.

Sclerostin and vascular calcification

Recently, it was shown that *SOST* knockout mice or the administration of anti-sclerostin antibodies resulted in enhanced bone formation and mineralization.^{137,138} However, the data describing the role of sclerostin as an important risk factor for vascular calcification raise doubt.¹³⁹ It has been found that induction of renal failure in *SOST* knockout mice resulted in the development of vascular calcification.¹⁴⁰ However, while low levels of sclerostin increased bone formation,^{141,142} this process did not prevent increased vascular mineralization.¹³⁸ In addition, in DBA/2J mice that are more susceptible to the development of ectopic calcifications without renal failure,¹⁴³ treatment with anti-sclerostin antibodies and a diet that included warfarin resulted in the development of aortic and renal arteries calcifications.¹³⁸ Thus, these results suggest that sclerostin prevents vessel calcification in the aorta, kidney and cardiac arteries. This hypothesis seems to be supported by observations that expression of sclerostin mRNA and protein occurs in calcified vessels in both mice and humans,¹⁴⁴ and plasma sclerostin levels are inversely associated with mortality among patients with CKD.¹⁴⁵ It seems that locally produced sclerostin in the calcified tissues may act as a counter mechanism against further ectopic calcification. The mechanism may be similar to bones in that sclerostin binds to LRP5 receptors and inhibits the Wnt pathway in VSMCs. It seems that sclerostin may also act by indirect stimulation of FGF-23,¹⁴⁶ resulting in urinary phosphate excretion, which lowers the plasma phosphate level.

Sclerostin and aneurysms

Under physiological conditions, VSMCs produce collagen and elastin, which are responsible for the strength and elasticity of arteries and the aorta. However, during atherosclerosis, the phenotype of VSMCs is modified, and they start producing matrix metalloproteinases (MMPs) that are involved in the degradation of the extracellular matrix, which in turn contributes to the development of aneurysms.¹¹²

A study by Kirshna et al. reported the downregulation of sclerostin and activation of the Wnt/ β -catenin pathway in abdominal aortic aneurysms (AAA)²³ in both mouse and human aortas. Upregulation of Wnt target genes was also detected in that arterial intima and media during the aging processes.¹⁴⁷ The development of an aneurysm may stem from epigenetic changes in several genes, including excessive methylation of one of the CpG islands in the *SOST* promoter and subsequent inhibition of gene activity by up to 75%, as shown in human osteocytes.^{148,149}

Physiologically, collagen and elastin fibers maintain arterial width and elasticity. During the development of an aneurysm, fragmentation of collagen and elastin fibers occurs, resulting in decreased arterial wall strength.¹⁵⁰ Results of studies performed on mouse fibroblasts indicate that by inhibiting the Wnt pathway, sclerostin enhances the expression of genes encoding extracellular matrix proteins responsible for maintaining the aorta structure.¹⁵¹

It is known that Wnt signaling controls the expression of OPG and OPN. Osteopontin activates proteolytic pathways and MMP-9 activity,⁸¹ and is engaged in the promotion of inflammation.⁸⁰ In a mouse model, low OPN levels limited the development of AAA,¹⁵² and it is interesting to note that OPG promotes the MMP-2 and MMP-9 release and activity from monocytes and VSMCs,^{153,154} leading to instability of the arterial wall. Furthermore, OPG concentration correlated positively with AAA progression¹⁴⁸ and was positively associated with aortic diameter, MMP-2 and MMP-9 activity, cathepsin activity, and the number of lymphocytes inside the wall of aortic aneurysms, all being well-established parameters of AAA pathogenesis and severity.^{83,85} Moreover, OPG deficiency protected against aortic angiotensin II-induced aneurysm development and rupture in mice.¹⁵⁵

In a study performed in a mouse model, results showed that sclerostin overexpression or administration inhibited angiotensin II-induced aneurysm formation in the thoracic and abdominal aorta and the development of atherosclerosis.²³ In line with this finding, inhibition of the Wnt pathway by sclerostin protected against the AAA development by downregulation of pro-aneurysmal genes in mice.²³ Potentially, the inhibition of Wnt signaling may decrease the expression of OPN, OPG and MMP-9, and thus attenuate aortic wall inflammation and extracellular matrix degradation.²³

Sclerostin and mortality

An investigation by Zeng et al. found a U-shaped association between sclerostin levels and vascular calcification and mortality.¹⁵⁶ Even though atherosclerosis progresses with aging, it was shown that sclerostin concentrations did not predict the occurrence of cardiovascular events during a 15-year observational period in a population-based prospective study, whereas DKK-1 level was such a predictor.¹⁵⁷ Moreover, some data has shown that DKK-1

Table 2. Association of sclerostin expression with cardiac and vascular pathologies

Models	Material	Results
Human – postmenopausal type 2 diabetic women with atherosclerosis ¹²	serum	Serum sclerostin level positively correlates with plaque volume and vascular calcifications.
Humans over 65 years ¹⁸	serum	Serum sclerostin levels were higher in patients with PAD than in patients with normal ABI.
Human – Afro-Caribbean men ¹⁹	serum	Serum sclerostin levels positively correlate with coronary and aortic calcifications.
Human with atherosclerosis ²¹	calcified and atherosclerotic aorta wall	Upregulated expression of sclerostin was detected in VSMCs.
Human with atherosclerosis ²¹	serum	Serum sclerostin level positively correlates with aortic calcification.
Human with atherosclerosis ¹²⁴	aorta wall, atherosclerotic plaques	Sclerostin expressions were detected in the heart, calcified aorta and atherosclerotic plaques.
Human with atherosclerosis ¹³⁰	atherosclerotic plaques and aortic calcifications	Sclerostin expressions were detected in aortic calcifications and plaques. Higher levels of sclerostin in the media than in the intima.

VSMC – vascular smooth muscle cells; PAD – peripheral arterial disease; ABI – ankle-to-brachial index.

is released mainly from endothelial cells⁷⁹ and can activate platelets,¹⁵⁸ causes endothelial cell apoptosis and enhances the expression of molecules including pentraxin-3 and plasminogen activator inhibitor type 1, which contributes to inflammation and inhibits fibrinolysis.¹⁵⁹

The effects of inhibition of sclerostin in the vasculature

Locally enhanced sclerostin production can potentially inhibit vascular calcification at the site in the arterial wall, although at the same time may exert a negative effect on the bones by increasing bone resorption and inhibiting bone formation after being released into the circulation.¹²⁰ Administration of the sclerostin inhibitor romosozumab, an anti-sclerostin antibody used to treat osteoporosis, resulted in a decrease in bone resorption and an increase in bone formation.¹⁶⁰ The results of the ARCH study involving postmenopausal women with osteoporosis revealed a higher frequency of severe cardiovascular adverse events in the group treated with romosozumab than in patients treated with alendronate (2.5% compared to 1.9%).¹⁶¹ The most common cardiovascular events were myocardial infarctions and stroke. However, the results of another large study, FRAME, did not find an increase in cardiovascular risk between romosozumab and placebo groups.¹⁶² Several nonclinical studies have also been performed to elucidate the potential biological mechanisms mediating the increase in adverse cardiovascular events. It has been shown that romosozumab did not induce vasoconstriction in isolated human coronary artery cultures,¹⁶³ and did not have any impact on cardiovascular or respiratory function in monkeys.¹⁶⁴ Moreover, it did not initiate or exacerbate the process of arterial calcification in the absence of atherosclerosis in rats, even during lifetime exposure to this drug.¹⁶⁵ In mouse models of atherosclerosis, administration of anti-sclerostin antibodies did not result in changes to plaque

volume or mineralization, and histopathological examination of the aortas did not reveal increased hemorrhages, thrombosis or necrosis in a high-fat diet model of atherosclerosis due to treatment with romosozumab.¹⁶³ Therapeutic anti-sclerostin antibodies did not increase the incidence of aneurysms²³ and did not change biochemical parameters, platelet and endothelial activation or markers of inflammation in mouse models of the aortic aneurysm.²³

Thus, the studies in animal models have not shown a significant effect of anti-sclerostin antibodies on the cardiovascular system. Furthermore, the data did not show evidence of the detrimental effects of sclerostin inhibition on the development of inflammation or exacerbation of atherosclerosis. The summary of findings concerning sclerostin levels in different clinical conditions is presented in Table 2.

Summary

Emerging data suggest there are similarities between bone homeostasis and vascular pathologies.¹⁶⁶ Bone constitutes the buffering capacity for calcium and phosphorus, although the conditions of hypercalcemia and hyperphosphatemia result in stimulation of the arterial Wnt pathway. This Wnt pathway enhancement results in the initiation of transdifferentiation of VSMCs into a phenotype that secretes proteins, migrates, and induces mineralization and atherosclerosis. The Wnt pathway also stimulates the release and activity of other signaling regulators and growth factors, exacerbating RUNX2 expression and resulting in vascular calcification.

Conclusions

Sclerostin and DKK-1 detection in the calcified aorta in carotid plaques supports the hypothesis that upregulation of Wnt pathway inhibitors may be a defensive mechanism

to restrain atherosclerosis. However, these methods have so far only been demonstrated under specific laboratory conditions and in animal models. It is also suggested that serum sclerostin concentrations mirror the advancement of arterial remodeling and vessel wall calcification, and it may represent the increased number of vascular cells transformed into osteogenic phenotypes. Indeed, higher serum sclerostin concentrations are observed in patients with atherosclerosis and vessel calcification when compared to healthy subjects. However, the value of serum sclerostin levels as a marker of advancement of global vascular calcification is lowered by the fact that they reflect 2 pools of sclerostin; one released by VSMCs due to their pathogenic transition to the osteogenic-like phenotype in arterial walls and a second that is derived physiologically from the bones.

ORCID iDs

Piotr Kocełak  <https://orcid.org/0000-0001-8135-8482>

Monika Puzianowska-Kuźnicka

 <https://orcid.org/0000-0001-5295-3848>

Magdalena Olszanecka-Glinianowicz

 <https://orcid.org/0000-0001-5632-5590>

Jerzy Chudek  <https://orcid.org/0000-0002-6367-7794>

References

- Centers for Disease Control and Prevention (CDC). *About Underlying Cause of Death, 1999–2020*. Atlanta, USA: Centers for Disease Control and Prevention; 2018. <https://wonder.cdc.gov/ucd-icd10.html>. Accessed September 2, 2016.
- Tsaousi A, Williams H, Lyon CA, et al. Wnt4/ β -catenin signaling induces VSMC proliferation and is associated with intimal thickening. *Circ Res*. 2011;108(4):427–436. doi:10.1161/CIRCRESAHA.110.233999
- Arderiu G, Espinosa S, Peña E, Aledo R, Badimon L. Monocyte-secreted Wnt5a interacts with FZD5 in microvascular endothelial cells and induces angiogenesis through tissue factor signaling. *J Mol Cell Biol*. 2014;6(5):380–393. doi:10.1093/jmcb/mju036
- Du J, Li J. The role of Wnt signaling pathway in atherosclerosis and its relationship with angiogenesis. *Exp Ther Med*. 2018;16(3):1975–1981. doi:10.3892/etm.2018.6397
- Stegemann JP, Nerem RM. Altered response of vascular smooth muscle cells to exogenous biochemical stimulation in two- and three-dimensional culture. *Exp Cell Res*. 2003;283(2):146–155. doi:10.1016/S0014-4827(02)00041-1
- Tang X, Liu Y, Xiao Q, et al. Pathological cyclic strain promotes proliferation of vascular smooth muscle cells via the ACTH/ERK/STAT3 pathway. *J Cell Biochem*. 2018;119(10):8260–8270. doi:10.1002/jcb.26839
- Lin ME, Chen T, Leaf EM, Speer MY, Giachelli CM. Runx2 expression in smooth muscle cells is required for arterial medial calcification in mice. *Am J Pathol*. 2015;185(7):1958–1969. doi:10.1016/j.ajpath.2015.03.020
- Du J, Zu Y, Li J, et al. Extracellular matrix stiffness dictates Wnt expression through integrin pathway. *Sci Rep*. 2016;6:20395. doi:10.1038/srep20395
- Giachelli CM. Ectopic calcification: Gathering hard facts about soft tissue mineralization. *Am J Pathol*. 1999;154(3):671–675. doi:10.1016/S0002-9440(10)65313-8
- Sevetson B, Taylor S, Pan Y. Cbfa1/RUNX2 directs specific expression of the sclerostin gene (*SOST*). *J Biol Chem*. 2004;279(14):13849–13858. doi:10.1074/jbc.M306249200
- Gaudio A, Privitera F, Pulvirenti I, Canzonieri E, Rapisarda R, Fiore CE. The relationship between inhibitors of the Wnt signalling pathway (sclerostin and Dickkopf-1) and carotid intima-media thickness in postmenopausal women with type 2 diabetes mellitus. *Diab Vasc Dis Res*. 2014;11(1):48–52. doi:10.1177/1479164113510923
- Morales-Santana S, García-Fontana B, García-Martín A, et al. Atherosclerotic disease in type 2 diabetes is associated with an increase in sclerostin levels. *Diabetes Care*. 2013;36(6):1667–1674. doi:10.2337/dc12-1691
- Chen A, Sun Y, Cui J, et al. Associations of sclerostin with carotid artery atherosclerosis and all-cause mortality in Chinese patients undergoing maintenance hemodialysis. *BMC Nephrol*. 2018;19(1):264. doi:10.1186/s12882-018-1046-7
- Scimeca M, Anemona L, Granaglia A, et al. Plaque calcification is driven by different mechanisms of mineralization associated with specific cardiovascular risk factors. *Nutr Metab Cardiovasc Dis*. 2019;29(12):1330–1336. doi:10.1016/j.numecd.2019.08.009
- Frysz M, Gergei I, Scharnagl H, et al. Circulating sclerostin levels are positively related to coronary artery disease severity and related risk factors. *J Bone Miner Res*. 2022;37(2):273–284. doi:10.1002/jbmr.4467
- Zhao B, Chen A, Wang H, et al. The relationship between sclerostin and carotid artery atherosclerosis in patients with stage 3–5 chronic kidney disease. *Int Urol Nephrol*. 2020;52(7):1329–1336. doi:10.1007/s11255-020-02495-x
- He XW, Wang E, Bao YY, et al. High serum levels of sclerostin and Dickkopf-1 are associated with acute ischaemic stroke. *Atherosclerosis*. 2016;253:22–28. doi:10.1016/j.atherosclerosis.2016.08.003
- Teng IC, Wang JH, Lee CJ, Hou JS, Hsu BG. Serum sclerostin as an independent marker of peripheral artery disease in elderly persons. *Int J Clin Exp Pathol*. 2018;11(5):2816–2821. PMID:31938401. PMID:PMC6958239.
- Kuipers AL, Miljkovic I, Carr JJ, et al. Association of circulating sclerostin with vascular calcification in Afro-Caribbean men. *Atherosclerosis*. 2015;239(1):218–223. doi:10.1016/j.atherosclerosis.2015.01.010
- Morena M, Jausent I, Dupuy AM, et al. Osteoprotegerin and sclerostin in chronic kidney disease prior to dialysis: Potential partners in vascular calcifications. *Nephrol Dial Transplant*. 2015;30(8):1345–1356. doi:10.1093/ndt/gfv081
- Koos R, Brandenburg V, Mahnken AH, et al. Sclerostin as a potential novel biomarker for aortic valve calcification: An in-vivo and ex-vivo study. *J Heart Valve Dis*. 2013;22(3):317–325. PMID:24151757.
- Brandenburg VM, Kramann R, Koos R, et al. Relationship between sclerostin and cardiovascular calcification in hemodialysis patients: A cross-sectional study. *BMC Nephrol*. 2013;14:219. doi:10.1186/1471-2369-14-219
- Krishna SM, Seto SW, Jose RJ, et al. Wnt signaling pathway inhibitor sclerostin inhibits angiotensin II-induced aortic aneurysm and atherosclerosis. *Arterioscler Thromb Vasc Biol*. 2017;37(3):553–566. doi:10.1161/ATVBAHA.116.308723
- Komiya Y, Habas R. Wnt signal transduction pathways. *Organogenesis*. 2008;4(2):68–75. doi:10.4161/org.4.2.5851
- Endo M, Nishita M, Fujii M, Minami Y. Insight into the role of Wnt5a-induced signaling in normal and cancer cells. *Int Rev Cell Mol Biol*. 2015;314:117–148. doi:10.1016/bs.ircmb.2014.10.003
- Dejana E. The role of Wnt signaling in physiological and pathological angiogenesis. *Circ Res*. 2010;107(8):943–952. doi:10.1161/CIRCRESAHA.110.223750
- Kühl M, Sheldahl LC, Park M, Miller JR, Moon RT. The Wnt/Ca²⁺ pathway: A new vertebrate Wnt signaling pathway takes shape. *Trends Genet*. 2000;16(7):279–283. doi:10.1016/S0168-9525(00)02028-X
- Couffignal T, Dufourcq P, Duplâa C. Beta-catenin nuclear activation: Common pathway between Wnt and growth factor signaling in vascular smooth muscle cell proliferation? *Circ Res*. 2006;99(12):1287–1289. doi:10.1161/01.RES.0000253139.82251.31
- Wang X, Xiao Y, Mou Y, Zhao Y, Blankesteyn WM, Hall JL. A role for the beta-catenin/T-cell factor signaling cascade in vascular remodeling. *Circ Res*. 2002;90(3):340–347. doi:10.1161/hh0302.104466
- Marinou K, Christodoulides C, Antoniadou C, Koutsilieris M. Wnt signaling in cardiovascular physiology. *Trends Endocrinol Metab*. 2012;23(12):628–636. doi:10.1016/j.tem.2012.06.001
- Clevers H. Wnt/ β -catenin signaling in development and disease. *Cell*. 2006;127(3):469–480. doi:10.1016/j.cell.2006.10.018
- Christodoulides C, Lagathu C, Sethi JK, Vidal-Puig A. Adipogenesis and WNT signalling. *Trends Endocrinol Metab*. 2009;20(1):16–24. doi:10.1016/j.tem.2008.09.002
- Shao JS, Cheng SL, Pingsterhaus JM, Charlton-Kachigian N, Loewy AP, Towler DA. Mx2 promotes cardiovascular calcification by activating paracrine Wnt signals. *J Clin Invest*. 2005;115(5):1210–1220. doi:10.1172/JCI24140
- Mani A, Radhakrishnan J, Wang H, et al. LRP6 mutation in a family with early coronary disease and metabolic risk factors. *Science*. 2007;315(5816):1278–1282. doi:10.1126/science.1136370

35. Corada M, Nyqvist D, Orsenigo F, et al. The Wnt/beta-catenin pathway modulates vascular remodeling and specification by upregulating Dll4/Notch signaling. *Dev Cell*. 2010;18(6):938–949. doi:10.1016/j.devcel.2010.05.006
36. Duarte A, Hirashima M, Benedito R, et al. Dosage-sensitive requirement for mouse Dll4 in artery development. *Genes Dev*. 2004;18(20):2474–2478. doi:10.1101/gad.1239004
37. Wan M, Yang C, Li J, et al. Parathyroid hormone signaling through low-density lipoprotein-related protein 6. *Genes Dev*. 2008;22(21):2968–2979. doi:10.1101/gad.1702708
38. Wan M, Li J, Herbst K, et al. LRP6 mediates cAMP generation by G protein-coupled receptors through regulating the membrane targeting of Gα(s). *Sci Signal*. 2011;4(164):ra15. doi:10.1126/scisignal.2001464
39. Johnson BG, Ren S, Karaca G, et al. Connective tissue growth factor domain 4 amplifies fibrotic kidney disease through activation of LDL receptor-related protein 6. *J Am Soc Nephrol*. 2017;28(6):1769–1782. doi:10.1681/ASN.2016080826
40. Nishita M, Yoo SK, Nomachi A, et al. Filopodia formation mediated by receptor tyrosine kinase Ror2 is required for Wnt5a-induced cell migration. *J Cell Biol*. 2006;175(4):555–562. doi:10.1083/jcb.200607127
41. Sasai N, Nakazawa Y, Haraguchi T, Sasai Y. The neurotrophin-receptor-related protein NRH1 is essential for convergent extension movements. *Nat Cell Biol*. 2004;6(8):741–748. doi:10.1038/ncb1158
42. Lu W, Yamamoto V, Ortega B, Baltimore D. Mammalian Ryk is a Wnt coreceptor required for stimulation of neurite outgrowth. *Cell*. 2004;119(1):97–108. doi:10.1016/j.cell.2004.09.019
43. Lu X, Borchers AGM, Jolicoeur C, Rayburn H, Baker JC, Tessier-Lavigne M. PTK7/CCK-4 is a novel regulator of planar cell polarity in vertebrates. *Nature*. 2004;430(6995):93–98. doi:10.1038/nature02677
44. Wallingford JB, Habas R. The developmental biology of Dishevelled: An enigmatic protein governing cell fate and cell polarity. *Development*. 2005;132(20):4421–4436. doi:10.1242/dev.02068
45. Tanegashima K, Zhao H, Dawid IB. WGEF activates Rho in the Wnt–PCP pathway and controls convergent extension in *Xenopus* gastrulation. *EMBO J*. 2008;27(4):606–617. doi:10.1038/emboj.2008.9
46. Marlow F, Topczewski J, Sepich D, Solnica-Krezel L. Zebrafish Rho kinase 2 acts downstream of Wnt11 to mediate cell polarity and effective convergence and extension movements. *Curr Biol*. 2002;12(11):876–884. doi:10.1016/S0960-9822(02)00864-3
47. Weiser DC, Pyati UJ, Kimelman D. Gravin regulates mesodermal cell behavior changes required for axis elongation during zebrafish gastrulation. *Genes Dev*. 2007;21(12):1559–1571. doi:10.1101/gad.1535007
48. Habas R, Dawid IB, He X. Coactivation of Rac and Rho by Wnt/Frizzled signaling is required for vertebrate gastrulation. *Genes Dev*. 2003;17(2):295–309. doi:10.1101/gad.1022203
49. Li L, Yuan H, Xie W, et al. Dishevelled proteins lead to two signaling pathways: Regulation of LEF-1 and c-Jun N-terminal kinase in mammalian cells. *J Biol Chem*. 1999;274(1):129–134. doi:10.1074/jbc.274.1.129
50. Keller R, Davidson LA, Shook DR. How we are shaped: The biomechanics of gastrulation. *Differentiation*. 2003;71(3):171–205. doi:10.1046/j.1432-0436.2003.710301.x
51. Slusarski DC, Pelegri F. Calcium signaling in vertebrate embryonic patterning and morphogenesis. *Dev Biol*. 2007;307(1):1–13. doi:10.1016/j.ydbio.2007.04.043
52. Slusarski DC, Corces VG, Moon RT. Interaction of Wnt and a Frizzled homologue triggers G-protein-linked phosphatidylinositol signalling. *Nature*. 1997;390(6658):410–413. doi:10.1038/37138
53. Sheldahl LC, Slusarski DC, Pandur P, Miller JR, Kühl M, Moon RT. Dishevelled activates Ca²⁺ flux, PKC, and CamKII in vertebrate embryos. *J Cell Biol*. 2003;161(4):769–777. doi:10.1083/jcb.200211094
54. Kühl M, Sheldahl LC, Malbon CC, Moon RT. Ca²⁺/calmodulin-dependent protein kinase II is stimulated by Wnt and Frizzled homologs and promotes ventral cell fates in *Xenopus*. *J Biol Chem*. 2000;275(17):12701–12711. doi:10.1074/jbc.275.17.12701
55. Miller JR, Hocking AM, Brown JD, Moon RT. Mechanism and function of signal transduction by the Wnt/β-catenin and Wnt/Ca²⁺ pathways. *Oncogene*. 1999;18(55):7860–7872. doi:10.1038/sj.onc.1203245
56. Axelrod JD, Miller JR, Shulman JM, Moon RT, Perrimon N. Differential recruitment of Dishevelled provides signaling specificity in the planar cell polarity and Wingless signaling pathways. *Genes Dev*. 1998;12(16):2610–2622. doi:10.1101/gad.12.16.2610
57. Hoang BH, Thomas JT, Abdul-Karim FW, et al. Expression pattern of two Frizzled-related genes, *Frzb-1* and *Sfrp-1*, during mouse embryogenesis suggests a role for modulating action of Wnt family members. *Dev Dyn*. 1998;212(3):364–372. doi:10.1002/(SICI)1097-0177(199807)212:3<364::AID-AJA4>3.0.CO;2-F
58. Hsieh JC, Kodjabachian L, Rebbert ML, et al. A new secreted protein that binds to Wnt proteins and inhibits their activities. *Nature*. 1999;398(6726):431–436. doi:10.1038/18899
59. Li X, Zhang Y, Kang H, et al. Sclerostin binds to LRP5/6 and antagonizes canonical Wnt signaling. *J Biol Chem*. 2005;280(20):19883–19887. doi:10.1074/jbc.M413274200
60. Glinka A, Wu W, Delius H, Monaghan AP, Blumenstock C, Niehrs C. Dickkopf-1 is a member of a new family of secreted proteins and functions in head induction. *Nature*. 1998;391(6665):357–362. doi:10.1038/34848
61. Rodda SJ, McMahon AP. Distinct roles for Hedgehog and canonical Wnt signaling in specification, differentiation and maintenance of osteoblast progenitors. *Development*. 2006;133(16):3231–3244. doi:10.1242/dev.02480
62. Glass DA, Bialek P, Ahn JD, et al. Canonical Wnt signaling in differentiated osteoblasts controls osteoclast differentiation. *Dev Cell*. 2005;8(5):751–764. doi:10.1016/j.devcel.2005.02.017
63. Kim JB, Leucht P, Lam K, et al. Bone regeneration is regulated by Wnt signaling. *J Bone Miner Res*. 2007;22(12):1913–1923. doi:10.1359/jbmr.070802
64. Movérare-Skrktic S, Henning P, Liu X, et al. Osteoblast-derived WNT16 represses osteoclastogenesis and prevents cortical bone fragility fractures. *Nat Med*. 2014;20(11):1279–1288. doi:10.1038/nm.3654
65. Zhong Z, Zylstra-Diegel CR, Schumacher CA, et al. Wntless functions in mature osteoblasts to regulate bone mass. *Proc Natl Acad Sci USA*. 2012;109(33):E2197–E2204. doi:10.1073/pnas.1120407109
66. Okamoto M, Udagawa N, Uehara S, et al. Noncanonical Wnt5a enhances Wnt/β-catenin signaling during osteoblastogenesis. *Sci Rep*. 2014;4:4493. doi:10.1038/srep04493
67. Yamane T, Kunisada T, Tsukamoto H, et al. Wnt signaling regulates hemopoiesis through stromal cells. *J Immunol*. 2001;167(2):765–772. doi:10.4049/jimmunol.167.2.765
68. Kobayashi Y, Thirukonda GJ, Nakamura Y, et al. Wnt16 regulates osteoclast differentiation in conjunction with Wnt5a. *Biochem Biophys Res Commun*. 2015;463(4):1278–1283. doi:10.1016/j.bbrc.2015.06.102
69. Yu B, Chang J, Liu Y, et al. Wnt4 signaling prevents skeletal aging and inflammation by inhibiting nuclear factor-κB. *Nat Med*. 2014;20(9):1009–1017. doi:10.1038/nm.3586
70. Maeda K, Kobayashi Y, Udagawa N, et al. Wnt5a-Ror2 signaling between osteoblast-lineage cells and osteoclast precursors enhances osteoclastogenesis. *Nat Med*. 2012;18(3):405–412. doi:10.1038/nm.2653
71. Albanese I, Yu B, Al-Kindi H, et al. Role of noncanonical Wnt signaling pathway in human aortic valve calcification. *Arterioscler Thromb Vasc Biol*. 2017;37(3):543–552. doi:10.1161/ATVBAHA.116.308394
72. Lee DK, Nathan Grantham R, Trachte AL, Mannion JD, Wilson CL. Activation of the canonical Wnt/β-catenin pathway enhances monocyte adhesion to endothelial cells. *Biochem Biophys Res Commun*. 2006;347(1):109–116. doi:10.1016/j.bbrc.2006.06.082
73. Souilhol C, Serbanovic-Canic J, Fragiadaki M, et al. Endothelial responses to shear stress in atherosclerosis: A novel role for developmental genes. *Nat Rev Cardiol*. 2020;17(1):52–63. doi:10.1038/s41569-019-0239-5
74. Quasnicka H, Slater SC, Beeching CA, Boehm M, Sala-Newby GB, George SJ. Regulation of smooth muscle cell proliferation by beta-catenin/T-cell factor signaling involves modulation of cyclin D1 and p21 expression. *Circ Res*. 2006;99(12):1329–1337. doi:10.1161/01.RES.0000253533.65446.33
75. Libby P, Ridker PM, Hansson GK. Progress and challenges in translating the biology of atherosclerosis. *Nature*. 2011;473(7347):317–325. doi:10.1038/nature10146
76. Ezan J, Leroux L, Barandon L, et al. FrzA/sFRP-1, a secreted antagonist of the Wnt-Frizzled pathway, controls vascular cell proliferation in vitro and in vivo. *Cardiovasc Res*. 2004;63(4):731–738. doi:10.1016/j.cardiores.2004.05.006
77. Kim J, Kim J, Kim DW, et al. Wnt5a induces endothelial inflammation via beta-catenin-independent signaling. *J Immunol*. 2010;185(2):1274–1282. doi:10.4049/jimmunol.1000181

78. Yang D, Li S, Duan X, et al. TLR4 induced Wnt3a-Dvl3 restrains the intensity of inflammation and protects against endotoxin-driven organ failure through GSK3 β / β -catenin signaling. *Mol Immunol.* 2020;118:153–164. doi:10.1016/j.molimm.2019.12.013
79. Ueland T, Otterdal K, Lekva T, et al. Dickkopf-1 enhances inflammatory interaction between platelets and endothelial cells and shows increased expression in atherosclerosis. *Arterioscler Thromb Vasc Biol.* 2009;29(8):1228–1234. doi:10.1161/ATVBAHA.109.189761
80. Borrell-Pagès M, Romero JC, Juan-Babot O, Badimon L. Wnt pathway activation, cell migration, and lipid uptake is regulated by low-density lipoprotein receptor-related protein 5 in human macrophages. *Eur Heart J.* 2011;32(22):2841–2850. doi:10.1093/eurheartj/ehr062
81. Viñas JL, Sola A, Jung M, et al. Inhibitory action of Wnt target gene osteopontin on mitochondrial cytochrome c release determines renal ischemic resistance. *Am J Physiol Renal Physiol.* 2010;299(1):F234–F242. doi:10.1152/ajprenal.00687.2009
82. Denhardt DT, Noda M, O'Regan AW, Pavlin D, Berman JS. Osteopontin as a means to cope with environmental insults: Regulation of inflammation, tissue remodeling, and cell survival. *J Clin Invest.* 2001;107(9):1055–1061. doi:10.1172/JCI12980
83. Lai CF, Seshadri V, Huang K, et al. An osteopontin-NADPH oxidase signaling cascade promotes pro-matrix metalloproteinase 9 activation in aortic mesenchymal cells. *Circ Res.* 2006;98(12):1479–1489. doi:10.1161/01.RES.0000227550.00426.60
84. Li Y, Toraldo G, Li A, et al. B cells and T cells are critical for the preservation of bone homeostasis and attainment of peak bone mass in vivo. *Blood.* 2007;109(9):3839–3848. doi:10.1182/blood-2006-07-037994
85. Koole D, Hurks R, Schoneveld A, et al. Osteoprotegerin is associated with aneurysm diameter and proteolysis in abdominal aortic aneurysm disease. *Arterioscler Thromb Vasc Biol.* 2012;32(6):1497–1504. doi:10.1161/ATVBAHA.111.243592
86. Akhmetshina A, Palumbo K, Dees C, et al. Activation of canonical Wnt signalling is required for TGF- β -mediated fibrosis. *Nat Commun.* 2012;3:735. doi:10.1038/ncomms1734
87. Königshoff M, Balsara N, Pfaff EM, et al. Functional Wnt signaling is increased in idiopathic pulmonary fibrosis. *PLoS One.* 2008;3(5):e2142. doi:10.1371/journal.pone.0002142
88. Colwell AS, Krummel TM, Longaker MT, Lorenz HP. Wnt-4 expression is increased in fibroblasts after TGF- β 1 stimulation and during fetal and postnatal wound repair. *Plast Reconstr Surg.* 2006;117(7):2297–2301. doi:10.1097/01.prs.0000218708.16909.31
89. He W, Dai C, Li Y, Zeng G, Monga SP, Liu Y. Wnt/ β -catenin signaling promotes renal interstitial fibrosis. *J Am Soc Nephrol.* 2009;20(4):765–776. doi:10.1681/ASN.2008060566
90. He W, Zhang L, Ni A, et al. Exogenously administered secreted frizzled related protein 2 (Sfrp2) reduces fibrosis and improves cardiac function in a rat model of myocardial infarction. *Proc Natl Acad Sci U S A.* 2010;107(49):21110–21115. doi:10.1073/pnas.1004708107
91. Trenz F, Haroun S, Cloutier A, Richter MV, Grenier G. A muscle resident cell population promotes fibrosis in hindlimb skeletal muscles of mdx mice through the Wnt canonical pathway. *Am J Physiol Cell Physiol.* 2010;299(5):C939–C947. doi:10.1152/ajpcell.00253.2010
92. Semenov MV, Zhang X, He X. DKK1 antagonizes Wnt signaling without promotion of LRP6 internalization and degradation. *J Biol Chem.* 2008;283(31):21427–21432. doi:10.1074/jbc.M800014200
93. Giachelli CM. Vascular calcification mechanisms. *J Am Soc Nephrol.* 2004;15(12):2959–2964. doi:10.1097/01.ASN.0000145894.57533.C4
94. Donoghue PS, Sun T, Gadegaard N, Riehle MO, Barnett SC. Development of a novel 3D culture system for screening features of a complex implantable device for CNS repair. *Mol Pharm.* 2014;11(7):2143–2150. doi:10.1021/mp400526n
95. Patel JJ, Bourne LE, Davies BK, et al. Differing calcification processes in cultured vascular smooth muscle cells and osteoblasts. *Exp Cell Res.* 2019;380(1):100–113. doi:10.1016/j.yexcr.2019.04.020
96. Persy V, D'Haese P. Vascular calcification and bone disease: The calcification paradox. *Trends Mol Med.* 2009;15(9):405–416. doi:10.1016/j.molmed.2009.07.001
97. Campbell GR, Campbell JH. Smooth muscle phenotypic changes in arterial wall homeostasis: Implications for the pathogenesis of atherosclerosis. *Exp Mol Pathol.* 1985;42(2):139–162. doi:10.1016/0014-4800(85)90023-1
98. Saidak Z, Le Henaff C, Azzi S, et al. Wnt/ β -catenin signaling mediates osteoblast differentiation triggered by peptide-induced α 5 β 1 integrin priming in mesenchymal skeletal cells. *J Biol Chem.* 2015;290(11):6903–6912. doi:10.1074/jbc.M114.621219
99. Skalka N, Caspi M, Caspi E, Loh YP, Rosin-Arbesfeld R. Carboxypeptidase E: A negative regulator of the canonical Wnt signaling pathway. *Oncogene.* 2013;32(23):2836–2847. doi:10.1038/onc.2012.308
100. Giachelli CM. The emerging role of phosphate in vascular calcification. *Kidney Int.* 2009;75(9):890–897. doi:10.1038/ki.2008.644
101. Rahmani M, Read JT, Carthy JM, et al. Regulation of the versican promoter by the β -catenin-T-cell factor complex in vascular smooth muscle cells. *J Biol Chem.* 2005;280(13):13019–13028. doi:10.1074/jbc.M411766200
102. Spencer GJ, Utting JC, Etheridge SL, Arnett TR, Genever PG. Wnt signalling in osteoblasts regulates expression of the receptor activator of NF κ B ligand and inhibits osteoclastogenesis in vitro. *J Cell Sci.* 2006;119(Pt 7):1283–1296. doi:10.1242/jcs.02883
103. Cai T, Sun D, Duan Y, et al. WNT/ β -catenin signaling promotes VSMCs to osteogenic transdifferentiation and calcification through directly modulating *Runx2* gene expression. *Exp Cell Res.* 2016;345(2):206–217. doi:10.1016/j.yexcr.2016.06.007
104. Wu X, Wang J, Jiang H, et al. Wnt3a activates β 1-integrin and regulates migration and adhesion of vascular smooth muscle cells. *Mol Med Rep.* 2014;9(4):1159–1164. doi:10.3892/mmr.2014.1937
105. Wang Z, Shu W, Lu MM, Morrissey EE. Wnt7b activates canonical signaling in epithelial and vascular smooth muscle cells through interactions with Fzd1, Fzd10, and LRP5. *Mol Cell Biol.* 2005;25(12):5022–5030. doi:10.1128/MCB.25.12.5022-5030.2005
106. Behrmann A, Zhong D, Sabaeifard P, Goodarzi M, Lemoff A, Towler D. Wnt16 regulates vascular matrix metabolism and arterial stiffness in the *Ldlr*^{-/-} mouse model of diet-induced metabolic syndrome. *Arterioscler Thromb Vasc Biol.* 2020;40:A331. doi: 10.1161/CIRCRESAHA.119.316141.
107. Durosier C, Van Lierop A, Ferrari S, Chevalley T, Papapoulos S, Rizzoli R. Association of circulating sclerostin with bone mineral mass, microstructure, and turnover biochemical markers in healthy elderly men and women. *J Clin Endocrinol Metab.* 2013;98(9):3873–3883. doi:10.1210/jc.2013-2113
108. Caporilli S, Latinkic BV. Ventricular cell fate can be specified until the onset of myocardial differentiation. *Mech Dev.* 2016;139:31–41. doi:10.1016/j.mod.2016.01.001
109. Li X, Liu P, Liu W, et al. Dkk2 has a role in terminal osteoblast differentiation and mineralized matrix formation. *Nat Genet.* 2005;37(9):945–952. doi:10.1038/ng1614
110. Vincent C, Findlay DM, Welldon KJ, et al. Pro-inflammatory cytokines TNF-related weak inducer of apoptosis (TWEAK) and TNF α induce the mitogen-activated protein kinase (MAPK)-dependent expression of sclerostin in human osteoblasts. *J Bone Miner Res.* 2009;24(8):1434–1449. doi:10.1359/jbmr.090305
111. Sato AY, Cregor M, Delgado-Calle J, et al. Protection from glucocorticoid-induced osteoporosis by anti-catabolic signalling in the absence of *Sost/sclerostin*. *J Bone Miner Res.* 2016;31(10):1791–1802. doi:10.1002/jbmr.2869
112. Zhu D, Mackenzie NCW, Millán JL, Farquharson C, MacRae VE. The appearance and modulation of osteocyte marker expression during calcification of vascular smooth muscle cells. *PLoS One.* 2011;6(5):e19595. doi:10.1371/journal.pone.0019595
113. Van Hul W, Balemans W, Van Hul E, et al. Van Buchem disease (hyperostosis corticalis generalisata) maps to chromosome 17q12-q21. *Am J Hum Genet.* 1998;62(2):391–399. doi:10.1086/301721
114. Collette NM, Genetos DC, Murugesu D, Harland RM, Loots GG. Genetic evidence that *SOST* inhibits WNT signaling in the limb. *Dev Biol.* 2010;342(2):169–179. doi:10.1016/j.ydbio.2010.03.021
115. Leupin O, Piters E, Halleux C, et al. Bone overgrowth-associated mutations in the *LRP4* gene impair sclerostin facilitator function. *J Biol Chem.* 2011;286(22):19489–19500. doi:10.1074/jbc.M110.190330
116. Cheng Q, Wu X, Du Y, et al. Levels of serum sclerostin, FGF-23, and intact parathyroid hormone in postmenopausal women treated with calcitriol. *Clin Interv Aging.* 2018;13:2367–2374. doi:10.2147/CLIA.S186199
117. Kubota T, Michigami T, Ozono K. Wnt signaling in bone. *Clin Pediatr Endocrinol.* 2010;19(3):49–56. doi:10.1297/cpe.19.49

118. Evenepoel P, D'Haese P, Brandenburg V. Sclerostin and DKK1: New players in renal bone and vascular disease. *Kidney Int.* 2015;88(2):235–240. doi:10.1038/ki.2015.156
119. Reddi AH. Initiation and promotion of endochondral bone formation by bone morphogenetic proteins: Potential implications for avian tibial dyschondroplasia. *Poult Sci.* 2000;79(7):978–981. doi:10.1093/ps/79.7.978
120. Wijenayaka AR, Kogawa M, Lim HP, Bonewald LF, Findlay DM, Atkins GJ. Sclerostin stimulates osteocyte support of osteoclast activity by a RANKL-dependent pathway. *PLoS One.* 2011;6(10):e25900. doi:10.1371/journal.pone.0025900
121. Wang JS, Mazur CM, Wein MN. Sclerostin and osteocalcin: Candidate bone-produced hormones. *Front Endocrinol.* 2021;12:584147. doi:10.3389/fendo.2021.584147
122. Cianferotti L, Demay MB. VDR-mediated inhibition of DKK1 and SFRP2 suppresses adipogenic differentiation of murine bone marrow stromal cells. *J Cell Biochem.* 2007;101(1):80–88. doi:10.1002/jcb.21151
123. Keller H, Kneissel M. *SOST* is a target gene for PTH in bone. *Bone.* 2005;37(2):148–158. doi:10.1016/j.bone.2005.03.018
124. Didangelos A, Yin X, Mandal K, Baumert M, Jahangiri M, Mayr M. Proteomics characterization of extracellular space components in the human aorta. *Mol Cell Proteomics.* 2010;9(9):2048–2062. doi:10.1074/mcp.M110.001693
125. Hampson G, Edwards S, Conroy S, Blake GM, Fogelman I, Frost ML. The relationship between inhibitors of the Wnt signalling pathway (Dickkopf-1(DKK1) and sclerostin), bone mineral density, vascular calcification and arterial stiffness in post-menopausal women. *Bone.* 2013;56(1):42–47. doi:10.1016/j.bone.2013.05.010
126. Sage AP, Tintut Y, Demer LL. Regulatory mechanisms in vascular calcification. *Nat Rev Cardiol.* 2010;7(9):528–536. doi:10.1038/nrcardio.2010.115
127. Shao JS, Cai J, Towler DA. Molecular mechanisms of vascular calcification: Lessons learned from the aorta. *Arterioscler Thromb Vasc Biol.* 2006;26(7):1423–1430. doi:10.1161/01.ATV.0000220441.42041.20
128. Wu J, Ma L, Wu L, Jin Q. Wnt- β -catenin signaling pathway inhibition by sclerostin may protect against degradation in healthy but not osteoarthritic cartilage. *Mol Med Rep.* 2017;15(5):2423–2432. doi:10.3892/mmr.2017.6278
129. Pikilidou M, Yavropoulou M, Antoniou M, Yovos J. The contribution of osteoprogenitor cells to arterial stiffness and hypertension. *J Vasc Res.* 2015;52(1):32–40. doi:10.1159/000381098
130. Leto G, D'Onofrio L, Lucantoni F, et al. Sclerostin is expressed in the atherosclerotic plaques of patients undergoing carotid endarterectomy. *Diabetes Metab Res Rev.* 2019;35(1):e3069. doi:10.1002/dmrr.3069
131. Li M, Zhou H, Yang M, Xing C. Relationship between serum sclerostin, vascular sclerostin expression and vascular calcification assessed by different methods in ESRD patients eligible for renal transplantation: A cross-sectional study. *Int Urol Nephrol.* 2019;51(2):311–323. doi:10.1007/s11255-018-2033-4
132. Register TC, Hruska KA, Divers J, et al. Sclerostin is positively associated with bone mineral density in men and women and negatively associated with carotid calcified atherosclerotic plaque in men from the African American-Diabetes Heart Study. *J Clin Endocrinol Metab.* 2014;99(1):315–321. doi:10.1210/jc.2013-3168
133. Claes KJ, Viaene L, Heye S, Meijers B, d'Haese P, Evenepoel P. Sclerostin: Another vascular calcification inhibitor? *J Clin Endocrinol Metab.* 2013;98(8):3221–3228. doi:10.1210/jc.2013-1521
134. Thambiah S, Roplekar R, Manghat P, et al. Circulating sclerostin and Dickkopf-1 (DKK1) in predialysis chronic kidney disease (CKD): Relationship with bone density and arterial stiffness. *Calcif Tissue Int.* 2012;90(6):473–480. doi:10.1007/s00223-012-9595-4
135. Catalano A, Pintauro B, Morabito N, et al. Gender differences in sclerostin and clinical characteristics in type 1 diabetes mellitus. *Eur J Endocrinol.* 2014;171(3):293–300. doi:10.1530/EJE-14-0106
136. García-Martín A, Rozas-Moreno P, Reyes-García R, et al. Circulating levels of sclerostin are increased in patients with type 2 diabetes mellitus. *J Clin Endocrinol Metab.* 2012;97(1):234–241. doi:10.1210/jc.2011-2186
137. Poole KES, Van Bezooijen RL, Loveridge N, et al. Sclerostin is a delayed secreted product of osteocytes that inhibits bone formation. *FASEB J.* 2005;19(13):1842–1844. doi:10.1096/fj.05-4221fje
138. De Maré A, Opdebeeck B, Neven E, D'Haese PC, Verhulst A. Sclerostin protects against vascular calcification development in mice. *J Bone Miner Res.* 2022;37(4):687–699. doi:10.1002/jbmr.4503
139. McClung M, Grauer A. Romosozumab in postmenopausal women with osteopenia. *N Engl J Med.* 2014;370(17):1664–1665. doi:10.1056/NEJMc1402396
140. Van Lierop AH, Moester MJC, Hamdy NAT, Papapoulos SE. Serum Dickkopf 1 levels in sclerostin deficiency. *J Clin Endocrinol Metab.* 2014;99(2):E252–E256. doi:10.1210/jc.2013-3278
141. Li X, Ominsky MS, Niu QT, et al. Targeted deletion of the sclerostin gene in mice results in increased bone formation and bone strength. *J Bone Miner Res.* 2008;23(6):860–869. doi:10.1359/jbmr.080216
142. Kaesler N, Verhulst A, De Maré A, et al. Sclerostin deficiency modifies the development of CKD-MBD in mice. *Bone.* 2018;107:115–123. doi:10.1016/j.bone.2017.11.015
143. Krüger T, Oelenberg S, Kaesler N, et al. Warfarin induces cardiovascular damage in mice. *Arterioscler Thromb Vasc Biol.* 2013;33(11):2618–2624. doi:10.1161/ATVBAHA.113.302244
144. De Maré A, Maudsley S, Azmi A, et al. Sclerostin as regulatory molecule in vascular media calcification and the bone-vascular axis. *Toxins (Basel).* 2019;11(7):428. doi:10.3390/toxins11070428
145. Lips L, De Roij Van Zuijdewijn CLM, Ter Wee PM, et al. Serum sclerostin: Relation with mortality and impact of hemodiafiltration. *Nephrol Dial Transplant.* 2017;32(7):1217–1223. doi:10.1093/ndt/gfw246
146. Ryan ZC, Ketha H, McNulty MS, et al. Sclerostin alters serum vitamin D metabolite and fibroblast growth factor 23 concentrations and the urinary excretion of calcium. *Proc Natl Acad Sci U S A.* 2013;110(15):6199–6204. doi:10.1073/pnas.1221255110
147. Marchand A, Atassi F, Gaaya A, et al. The Wnt/beta-catenin pathway is activated during advanced arterial aging in humans. *Aging Cell.* 2011;10(2):220–232. doi:10.1111/j.1474-9726.2010.00661.x
148. Moran CS, Clancy P, Biros E, et al. Association of PPARgamma allelic variation, osteoprotegerin and abdominal aortic aneurysm. *Clin Endocrinol (Oxf).* 2010;72(1):128–132. doi:10.1111/j.1365-2265.2009.03615.x
149. Delgado-Calle J, Sañudo C, Bolado A, et al. DNA methylation contributes to the regulation of sclerostin expression in human osteocytes. *J Bone Miner Res.* 2012;27(4):926–937. doi:10.1002/jbmr.1491
150. Isenburg JC, Simionescu DT, Starcher BC, Vyavahare NR. Elastin stabilization for treatment of abdominal aortic aneurysms. *Circulation.* 2007;115(13):1729–1737. doi:10.1161/CIRCULATIONAHA.106.672873
151. Hamburg-Shields E, DiNuoscio GJ, Mullin NK, Lafyatis R, Atit RP. Sustained β -catenin activity in dermal fibroblasts promotes fibrosis by upregulating expression of extracellular matrix protein-coding genes. *J Pathol.* 2015;235(5):686–697. doi:10.1002/path.4481
152. Bruemmer D, Collins AR, Noh G, et al. Angiotensin II-accelerated atherosclerosis and aneurysm formation is attenuated in osteopontin-deficient mice. *J Clin Invest.* 2003;112(9):1318–1331. doi:10.1172/JCI200318141
153. Moran CS, McCann M, Karan M, Norman P, Kethesuan N, Golledge J. Association of osteoprotegerin with human abdominal aortic aneurysm progression. *Circulation.* 2005;111(23):3119–3125. doi:10.1161/CIRCULATIONAHA.104.464727
154. Bennett BJ, Scatena M, Kirk EA, et al. Osteoprotegerin inactivation accelerates advanced atherosclerotic lesion progression and calcification in older ApoE^{-/-} mice. *Arterioscler Thromb Vasc Biol.* 2006;26(9):2117–2124. doi:10.1161/01.ATV.0000236428.91125.e6
155. Moran CS, Jose RJ, Biros E, Golledge J. Osteoprotegerin deficiency limits angiotensin II-induced aortic dilatation and rupture in the apolipoprotein E-knockout mouse. *Arterioscler Thromb Vasc Biol.* 2014;34(12):2609–2616. doi:10.1161/ATVBAHA.114.304587
156. Zeng C, Guo C, Cai J, Tang C, Dong Z. Serum sclerostin in vascular calcification and clinical outcome in chronic kidney disease. *Diab Vasc Dis Res.* 2018;15(2):99–105. doi:10.1177/1479164117742316
157. Klingenschmid G, Tschiderer L, Himmler G, et al. Associations of serum Dickkopf-1 and sclerostin with cardiovascular events: Results from the prospective Bruneck study. *J Am Heart Assoc.* 2020;9(6):e014816. doi:10.1161/JAHA.119.014816
158. Di M, Wang L, Li M, et al. Dickkopf1 destabilizes atherosclerotic plaques and promotes plaque formation by inducing apoptosis of endothelial cells through activation of ER stress. *Cell Death Dis.* 2017;8(7):e2917. doi:10.1038/cddis.2017.277

159. Pontremoli M, Brioschi M, Baetta R, Ghilardi S, Banfi C. Identification of DKK-1 as a novel mediator of statin effects in human endothelial cells. *Sci Rep*. 2018;8(1):16671. doi:10.1038/s41598-018-35119-7
160. Chavassieux P, Chapurlat R, Portero-Muzy N, et al. Bone-forming and antiresorptive effects of romosozumab in postmenopausal women with osteoporosis: Bone histomorphometry and micro-computed tomography analysis after 2 and 12 months of treatment. *J Bone Miner Res*. 2019;34(9):1597–1608. doi:10.1002/jbmr.3735
161. Saag KG, Petersen J, Brandi ML, et al. Romosozumab or alendronate for fracture prevention in women with osteoporosis. *N Engl J Med*. 2017;377(15):1417–1427. doi:10.1056/NEJMoa1708322
162. Cosman F, Crittenden DB, Adachi JD, et al. Romosozumab treatment in postmenopausal women with osteoporosis. *N Engl J Med*. 2016;375(16):1532–1543. doi:10.1056/NEJMoa1607948
163. Turk JR, Deaton AM, Yin J, et al. Nonclinical cardiovascular safety evaluation of romosozumab, an inhibitor of sclerostin, for the treatment of osteoporosis in postmenopausal women at high risk of fracture. *Regul Toxicol Pharmacol*. 2020;115:104697. doi:10.1016/j.yrtph.2020.104697
164. Ominsky MS, Boyd SK, Varela A, et al. Romosozumab improves bone mass and strength while maintaining bone quality in variectomized cynomolgus monkeys. *J Bone Miner Res*. 2017;32(4):788–801. doi:10.1002/jbmr.3036
165. Chouinard L, Felx M, Mellal N, et al. Carcinogenicity risk assessment of romosozumab: A review of scientific weight-of-evidence and findings in a rat lifetime pharmacology study. *Regul Toxicol Pharmacol*. 2016;81:212–222. doi:10.1016/j.yrtph.2016.08.010
166. Towler DA. Commonalities between vasculature and bone: An osseocentric view of arteriosclerosis. *Circulation*. 2017;135(4):320–322. doi:10.1161/CIRCULATIONAHA.116.022562

Transcriptome analysis of immune-inflammatory regulation in *Tremella fuciformis*-derived polysaccharide reeducated B16 cells: A subcutaneous model

Xiumin Li^{A–F}, Qiaoling Su^{C,E}, Yutian Pan^{A,F}

The Engineering Technological Center of Mushroom Industry, Minnan Normal University, Zhangzhou, China

A – research concept and design; B – collection and/or assembly of data; C – data analysis and interpretation; D – writing the article; E – critical revision of the article; F – final approval of the article

Advances in Clinical and Experimental Medicine, ISSN 1899–5276 (print), ISSN 2451–2680 (online)

Adv Clin Exp Med. 2024;33(5):533–542

Address for correspondence

Xiumin Li
E-mail: lixiumins06@163.com

Funding sources

The study was financially supported by the Natural Science fund of Fujian Province (grant No. 2021J011012), Science and Technology project of Zhangzhou city in Fujian Province (grant No. zz2021J44) and Scientific Research and Nurturing Projects of Minnan Normal University (grant No. MSPY2021).

Conflict of interest

None declared

Received on September 13, 2023

Reviewed on March 24, 2024

Accepted on April 23, 2024

Published online on May 22, 2024

Cite as

Li X, Su Q, Pan Y. Transcriptome analysis of immune-inflammatory regulation in *Tremella fuciformis*-derived polysaccharide reeducated B16 cells: A subcutaneous model. *Adv Clin Exp Med*. 2024;33(5):533–542. doi:10.17219/acem/187877

DOI

10.17219/acem/187877

Copyright

Copyright by Author(s)

This is an article distributed under the terms of the Creative Commons Attribution 3.0 Unported (CC BY 3.0) (<https://creativecommons.org/licenses/by/3.0/>)

Abstract

Background. Circulating cancer cells have characteristics of tumor self-targeting. Modified circulating tumor cells may serve as tumor-targeted cellular drugs. *Tremella fuciformis*-derived polysaccharide (TFP) is related to immune regulation and tumor inhibition, so could B16 cells reeducated by TFP be an effective anti-tumor drug?

Objectives. To evaluate the intrinsic therapeutic potential of B16 cells exposed to TFP and clarify the therapeutic molecules or pathways altered by this process.

Materials and methods. RNA-seq technology was used to study the effect of TFP-reeducated B16 cells on the immune and inflammatory system by placing the allograft subcutaneously in C57BL/6 mice.

Results. *Tremella fuciformis*-derived polysaccharide-reeducated B16 cells recruited leukocytes, neutrophils, dendritic cells (DCs), and mast cells into the subcutaneous region and promoted the infiltration of several cytokines such as tumor necrosis factor alpha (TNF- α), interleukin 6 (IL-6), interleukin 1 β (IL-1 β), and interleukin 1 (IL-1). Tumor necrosis factor alpha also activated Th17 lymphocytes to secrete interleukin 17 (IL-17) and interferon gamma (IFN- γ). The co-expression of IFN- γ and IL-17 was favorable for tumor immunity to shrink tumors. In short, TFP-reeducated B16 cells activated the innate and adaptive immune responses, especially Th17 cell differentiation and IFN- γ production, as well as the TNF- α signaling pathway, which re-regulated the inflammatory and immune systems.

Conclusions. B16 cells subcutaneously exposed to TFP in mice induced an immune and inflammatory response to inhibit tumors. The study of the function of TFP-reeducated B16 cells to improve cancer immunotherapy may be of particular research interest. This approach could be an alternative and more efficient strategy to deliver cytokines and open up new possibilities for long-lasting, multi-level tumor control.

Key words: IL-17, TNF- α , *Tremella fuciformis*-derived polysaccharide, reeducated B16 melanoma, RNA-seq technology

Background

A tumor is the result of a complex interaction between malignant and normal cells, including immune cells. Immune evasion and tumor-promoting inflammation are hallmarks of cancer.^{1,2}

The immune system is divided into 2 primary branches: innate and adaptive immunity. These branches provide comprehensive cellular and molecular protection from a wide range of diseases, including infectious diseases and cancer.³ In the early stages of carcinogenesis, innate immune cells (macrophages, neutrophils, dendritic cells (DCs), and natural killer (NK) cells) provide a robust 1st line of defense against cancer cell-associated “danger signals” through an acute inflammatory response to initiate cancer recognition, the secretion of pro-inflammatory cytokines, and elimination of cancer cells by innate immune cells.^{4,5} The innate immune response is of critical importance for the formation of an effective anti-tumor adaptive immune response.⁶ The adaptive immune response occurs subsequent to the innate immune response. Dendritic cells migrate, present tumor antigens, and activate tumor-specific CD4⁺ and CD8⁺ T cells. These specific T cells migrate to the tumor site and facilitate killing of tumor cells to prevent the occurrence and development of a tumor.⁷ Cancer cells modulate the functions of immune cells surrounding the tumor.⁸ The formation and development of tumors are the result of complex interactions between cancer cells and immune cells. Each immune cell type has a dual effect of immune promotion and immune suppression, making immunity present a double-edged sword: they hinder cancer progression or promote tumor activity.^{3,9}

Immune cell populations co-evolve with cancer cells, sculpt the progression of the tumor and produce sustained inflammatory pathways.¹⁰ Inflammation has been proven to be closely related to all stages of most cancers. Inflammation processes are driven by immune cells and molecules released by immune cells, which mediate the interactions between these cells.¹¹ The communication at the cellular and molecular levels ensures a balance between immune response activation and inhibition.⁸ More and more evidence suggests that the tumor microenvironment (TME) is one of the main obstacles to cancer immunotherapy, with chronic inflammation playing a major role in tumor cell proliferation and immune suppression,¹² but acute inflammation caused by certain therapies can reeducate tumor-promoting TMEs to re-enter the anti-tumor immune microenvironment.^{13–15}

Tumor necrosis factor alpha (TNF- α) is mainly produced by macrophages, monocytes, T cells, NK cells, B cells, and fibroblasts.¹⁶ It is a pleiotropic cytokine that plays an important role in host defenses and acute and chronic inflammation. Tumor necrosis factor alpha stimulates many pro-inflammatory cytokines, including interleukin 6 (IL-6), IL-8 and TNF- α itself, as well as adhesion molecules, chemokines and metalloproteinases.¹⁷ On the other hand,

TNF- α promotes the synthesis of anti-inflammatory factors and limits the secretion of inflammatory cytokines. It is also an essential signaling protein in the innate and adaptive immune systems,¹⁸ which can promote the recruitment of immune cells such as neutrophils, monocytes and lymphocytes to inflammatory sites.¹⁹

T cells are activated during the inflammatory process and differentiate into Th17 cells under conditions of IL-1 β , tumor growth factor beta (TGF- β) and IL-6.²⁰ Th17 cells have been recognized to play a dual role in tumor development. According to Zhao et al., Th17 cells have the effects of promoting and suppressing tumors.²¹ High levels of Th17 cells are associated with an improved prognosis.²² Th17 cells have been shown to recruit immune cells into tumors, activate effector CD8⁺ T cells, directly convert them into Th1 phenotype, and produce interferon gamma (IFN- γ) to kill tumor cells.²¹ Melanoma patients who exhibit an increase in the number of Th17 cells have been reported to have a higher survival rate.²³ Some studies have shown that if Th17 cells are the only immune cells, they can promote cancer, but have protective function in the presence of other immune cells.²⁴ The presence of other immune cells promotes the protective role of Th17 cells dependent on IFN- γ , and its co-expression with IL-17 is beneficial to shrink the tumor.²⁵ Interferon gamma exerts its anti-cancer effect by tumor angiogenesis inhibition, cytokine secretion, anti-proliferative activity, and stimulating anti-tumor immunity in the TME.²⁶

Tumor necrosis factor alpha is also one of the major effector cytokines secreted by pathogenic Th17 cells, initiating the production and release of IL-1, IL-6, IL-8, and IL-17.²⁷ Interleukin 17 is known to stimulate TNF- α , IL-6 and IL-1 β production, while IL-1 β acts synergistically with IL-6 to induce pro-inflammatory Th 17 cell differentiation.²⁸ Studies have shown that the presence of TNF- α and IL-1 β is required for the maximum effects of IL-17.²⁹ Interleukin 17 can cooperate with TNF- α to induce a synergistic response.³⁰ Tumor necrosis factor alpha and IFN- γ accelerate NF- κ B-mediated cell apoptosis.²⁶

The effect of TNF- α on inducing cancer cell death or survival depends on the cellular microenvironment.²⁶ Many efforts have been made to enhance the anti-tumor effect and reduce the systemic toxicity of TNF- α , including cell-based therapy. A recent study showed that systemically administered TNF-expressing tumor cells can localize tumors, release TNF- α locally and induce cancer cell apoptosis, reducing the growth of both primary tumors and metastatic colonies in immunocompetent mice.³¹

Cancer cells can educate innate immune cells to exert tumor protection and immunosuppressive activities.³² *Tremella fuciformis*-derived polysaccharide-reeducated B16 cells (TFP-B16 cells) may locally activate the TNF- α signaling pathway, Th17 cell differentiation and pro-inflammatory cytokines release, promote cytokine-cytokine interactions, induce immune-inflammatory profile changes, and may possess therapeutic potential by engineering them to attack melanoma cells.

Objectives

This study used RNA-seq technology to investigate the effects of TFP-B16 cells on the immune and inflammatory systems of C57 BL/6 mice after subcutaneous transplantation. Additionally, the study evaluated the therapeutic potential of B16 cell exposure to TFP and the therapeutic molecules or pathways activated by these cells.

Materials and methods

Cell culture and mice treatment

B16 cells were provided by Stem Cell Bank of Chinese Academy of Sciences (Beijing, China), and were cultured at 37°C under 5% CO₂ in Dulbecco's modified Eagle's medium (DMEM) medium supplemented with 10% fetal bovine serum (FBS). The C57BL/6 mice (6–8 weeks, 18–20 g) were purchased from the Shanghai Experimental Animal Center (Shanghai, China). They were housed in a temperature- and humidity-controlled environment (25°C, 30–40%), kept on a 12-h light/dark cycle, and provided with an unrestricted amount of rodent chow (corn 40–43%, bran 26%, soybean cake 29%, salt 1%, bone meal 1%, lysine 1%, vitamins 1%) and water. After 1 week of acclimatization, the mice were randomly divided into 2 groups: the model group and the TFP group. After exposure to 5 mg/mL of TFP for 24 h, B16 cells were washed 3 times with phosphate-buffered saline (PBS), and 1×10⁶ cells were subcutaneously inoculated into the right flank of the mice. For the vehicle control, the same amount of B16 cells were subcutaneously inoculated as described.

RNA extraction, library construction and RNA-seq analysis

Six tumor tissues from the model and TFP groups were used for RNA-seq analysis. Total RNA was extracted using a Trizol reagent kit (Invitrogen, Waltham, USA) according to the manufacturer's protocol. mRNA enriched using Oligo (dT) beads was fragmented into short fragments and reverse-transcribed into cDNA. The purified double-stranded cDNA fragments were end-repaired, poly (A) added, ligated to adaptors, and screened for approx. 200 bp cDNA using AMPure XP beads (Beckman Coulter, Brea, USA) After polymerase chain reaction (PCR) amplification, the cDNA library was built and sequenced using Illumina Novaseq 6000 (Gene Denovo Biotechnology Co.; Guangzhou, China).

Sequencing data processing and interpretation

Raw reads containing adapters reads containing more than 10% known nucleotides (N) and low-quality reads

containing more than 50% low-quality (Q-value ≤10) bases were filtered using fastp³³ from the raw data. The rRNA reads were removed from the clean data to obtain effective data using Bowtie2.³⁴ The remaining clean reads were further used in assembly and gene abundance calculations. The final clean data were mapped to the *Mus musculus* genome (Ensembl release104) using HISAT2.³⁵ The sequenced data reported in this study was archived in the Sequence Read Archive (SRA) with the BioProject ID PRJNA772896.

Identification of differentially expressed genes and enrichment analysis

The mapped reads of each sample were assembled using StringTie (<https://ccb.jhu.edu/software/stringtie/index.shtml>)^{36,37} in a reference-based approach. Gene abundances and variations were analyzed using RSEM software (<http://deweylab.github.io/RSEM/>)³⁸ and normalized by fragment per kilobase of transcript per million mapped reads. The RNA differential expression analysis was performed using DESeq2 (<https://www.bioconductor.org/packages/release/bioc/html/DESeq2.html>)³⁹ software for the 2 groups. The genes identified using the parameters of a false discovery rate (FDR) below 0.05 and absolute fold change ≥2 were considered significant DEGs.

Gene Ontology (GO) enrichment of the differentially expressed genes (DEGs) was performed. All DEGs were mapped to GO terms in the GO database (<http://www.geneontology.org>), gene numbers were calculated for every term, and significantly enriched GO terms in DEGs compared to the background genome were defined using the hypergeometric test. The calculated p-value went through FDR correction, using FDR ≤ 0.05 as the threshold. The biological pathways of the DEGs were enriched to the Kyoto Encyclopedia of Genes and Genomes (KEGG; <http://www.kegg.jp>) using the same hypergeometric test as used for GO term enrichment. Gene Set Enrichment Analysis (GSEA) was used to identify whether a set of genes in specific GO terms\KEGG pathways showed significant differences between the 2 groups (<http://software.broadinstitute.org/gsea/index.jsp>).

Results

The TFP-B16 cells stimulated immune cell activation

To detect the overall gene expression changes of allografts, we conducted RNA-seq analysis on the model and TFP groups. Figure 1A shows that TFP extensively regulates gene expression, with more upregulated genes (113) than downregulated genes (17), indicating that TFP mainly plays a role by promoting gene transcription.

To characterize immune states, GSEA analysis was used to identify the immune system response in the TFP

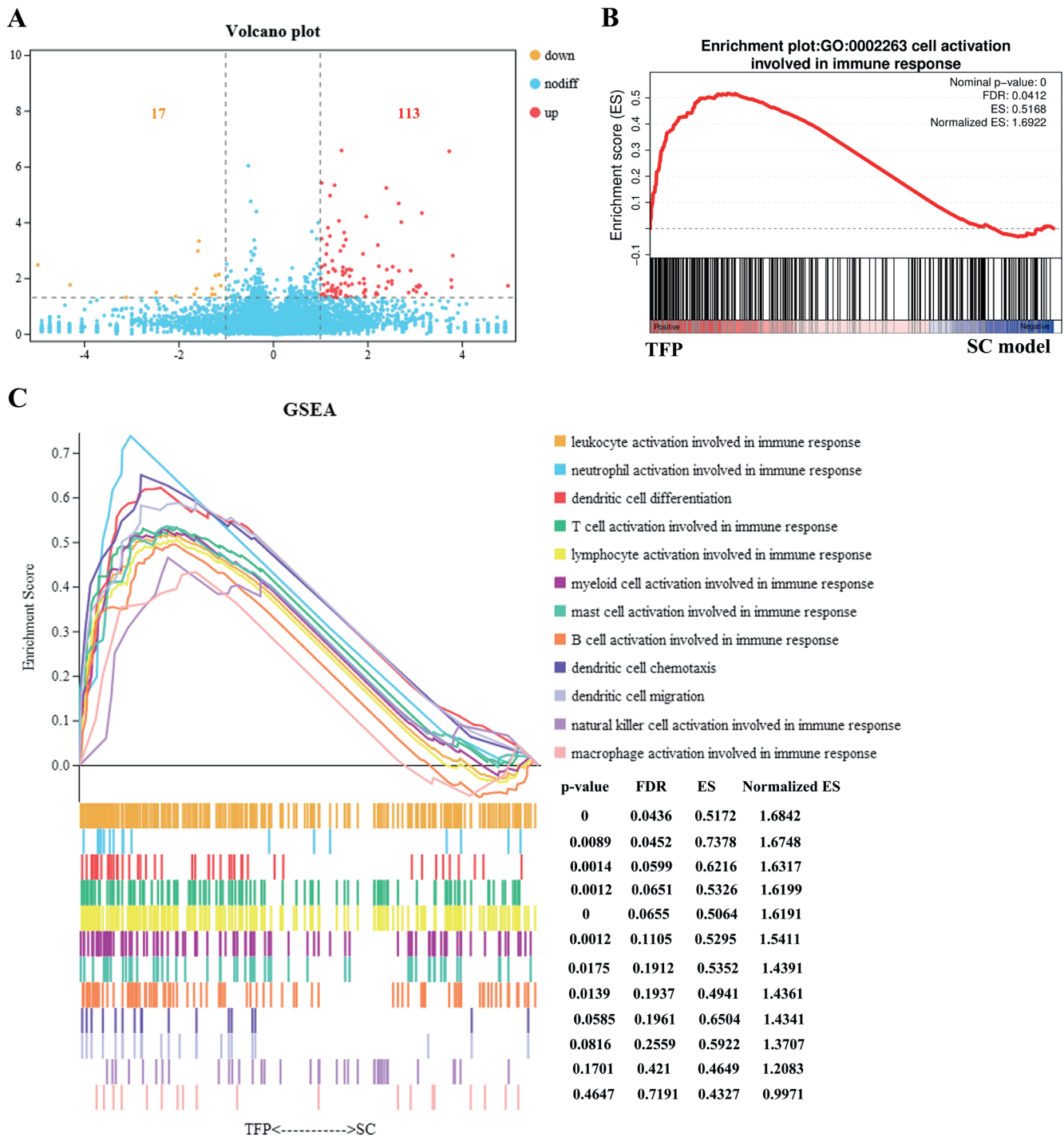


Fig. 1. The TFP-B16 cells regulated more upregulated genes (113) than downregulated genes (17), as well as promoted “cell activation involved in immune response” such as leukocytes, neutrophils, lymphocytes, and mast cells, but not NK cells and macrophages. A. Volcano plot; B. The GSEA analysis of cell activation involved immune response; C. The many kinds of immune cells activated during the immune response

TFP – *Tremella fuciformis*-derived polysaccharide; TFP-B16 cells – TFP-reeducated B16 cells; SC – subcutaneous; GO – Gene Ontology; GSEA – Gene Set Enrichment Analysis; FDR – false discovery rate; ES – enrichment score, the highest point of the curve is the ES value. When the ES value is positive, it indicates that a certain set of functional genes are enriched at the front of the sorting sequence. When the ES value is negative, it indicates that a certain set of functional genes are enriched at the back of the sorting sequence. The higher the ES value, the smaller the FDR value, indicating a higher degree of enrichment and reliable results.

group. The data showed that the TFP-B16-treated group was positive for “cell activation involved in immune response,” as shown in Fig. 1B. Leukocytes, neutrophils, lymphocytes (T cells and B cells), and mast cells were activated in the immune response, but NK cell and macrophage

activation were not significantly increased, as shown in Fig. 1C. Dendritic cells underwent significant differentiation. These data show that TFP-B16 cells promote more immune cell infiltration into the allograft compared to the model group.

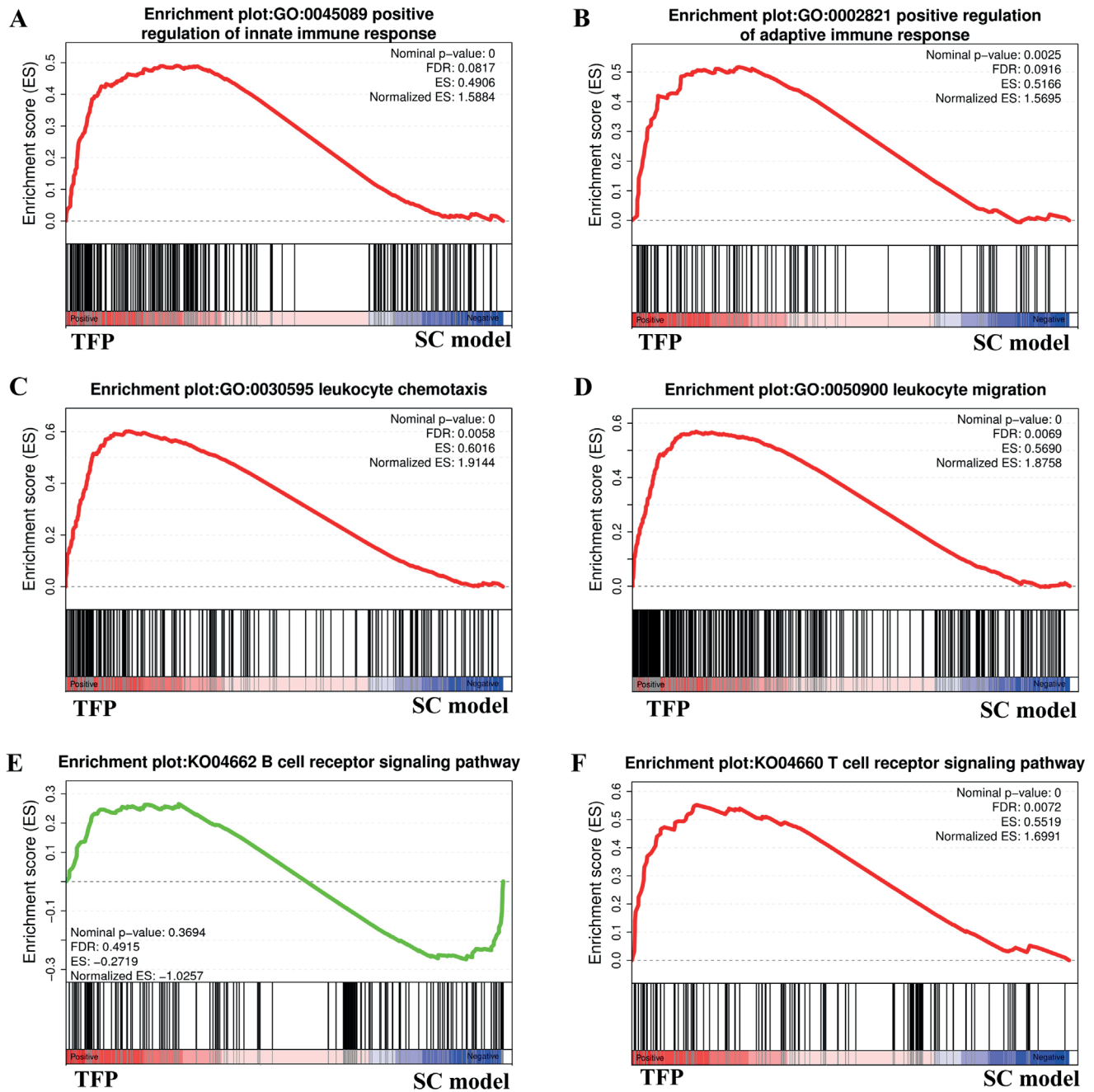


Fig. 2. The TFP-B16 cells activated the innate and adaptive immune system, infiltrating adaptive immune system cells, which were primarily T lymphocytes, and activating T cells receptor signaling pathways. A. Enrichment plot of positive regulation of innate immune system; B. Enrichment plot of positive regulation of adaptive immune system; C. Enrichment plot of leukocyte chemotaxis; D. Enrichment plot of leukocyte migration; E. Enrichment plot of B cell receptor signaling pathways; F. Enrichment plot of T cell receptor signaling pathways

TFP – *Tremella fuciformis*-derived polysaccharide; TFP-B16 cells – TFP-reeducated B16 cells; SC – subcutaneous; GO – Gene Ontology; KO – KEGG orthology; KEGG – Kyoto Encyclopedia of Genes and Genomes.

TFP-B16 cells activated innate and adaptive immune response

The GSEA showed that there were significant differences in the “positive regulation of innate immune response” (Fig. 2A) and “positive regulation of adaptive immune response” (Fig. 2B) gene sets between the TFP-B16 and SC groups, and most of the genes in the 2 pathway gene sets were upregulated in the TFP-B16 group.

In the early stage of immunity, leukocyte synthesis, migration and release of TNF- α and IL-1 cytokines have been found to promote pro-inflammatory effects.²¹ The TFP-B16 cells in the treatment group showed positive results in “leukocyte chemotaxis” and “leukocyte migration,” as shown in Fig. 2C and Fig. 2D. These data indicate that TFP-B16 cells activated innate immunity which has an important role in the early phases of anti-tumorigenesis.

Dendritic cells can process foreign antigens and present them to T lymphocytes, initiating a specific adaptive immune response.⁴⁰ Activated adaptive immune cells, including T and B lymphocytes, are known to further amplify the initial inflammatory response. The “T cell receptor signaling pathway” was activated but not the “B cell receptor signaling pathway,” as shown in Fig. 2E and Fig. 2F. This data indicated that the infiltrating adaptive immune system cells are primarily T lymphocytes, and the T cell receptor signaling pathways were activated.

TFP-B16 cells induce inflammation via TNF- α and IL-17 pathway activation

To further uncover the effects of TFP-B16 cells on the immune-inflammatory environment, the KEGG pathway enrichment analysis showed that TNF- α and IL-17 signaling pathways were significantly altered by the TFP-B16 cell group. Furthermore, as shown in Fig. 3A, TFP significantly altered NF- κ B signaling pathways and cytokine–cytokine receptor interactions. Tumor necrosis factor alpha-induced NF- κ B needs to convert immature DCs into functionally mature effector cells and then stimulate naïve T-cells to initiate antigen-specific T-cell responses.

Tumor necrosis factor alpha signaling pathways via TNFR1 mainly trigger pro-inflammatory and apoptotic effects.⁴¹ The TFP-B16 cells promoted leukocyte recruitment and inflammatory cytokine secretion, negatively regulated intercellular signaling, and remodeled the extracellular matrix, as shown in Fig. 3B. The TFP-B16 cells also promoted chemokines, cytokines and inflammatory genes and remodeling of the extracellular matrix via IL-17 through the IL-17 receptor, as shown in Fig. 3C.

The GSEA showed that more pathways related to acute inflammation were significantly increased in the TFP-B16 cells as shown in Fig. 3D. Acute inflammation is the initial response to harmful stimuli,⁴² while chronic inflammation promotes the development, progression and metastasis of tumors. This data suggested that TFP-B16 cells activated the acute inflammatory response, which had an important role in the early phase of anti-tumorigenesis.

The GSEA of IFN- γ showed that IFN- γ production and response to IFN- γ was significantly upregulated by TFP-B16 cells, as shown in Fig. 3E, which suggested that IFN- γ plays an important role in immune regulation. The use of TFP-B16 cells is a novel strategy to modulate TNF- α and IFN- γ pathways; such an approach would have the benefit of triggering protective immunity.

The interplay of TFP-B16 cells on the immune-inflammatory system

The most significant impacts by TFP-B16 cells were seen on the “immune system process ($p = 1.39e-17$),” “regulation of the immune system process ($p = 7.26e-15$),”

“immune response ($p = 1.19e-15$),” and “defense response ($p = 3.52e-17$).” The impact on “cell activation ($p = 1.19e-11$),” “leukocyte activation ($p = 2.10e-11$),” “positive regulation of immune system process ($p = 1.35e-13$),” “response to external stimulus ($p = 8.51e-13$),” and “inflammation response ($p = 9.53e-14$)” was followed by the impact on “positive regulation of response to stimulus ($p = 1.15e-11$),” and these GO terms were all in the top 10. This data confirmed that TFP-B16 cells regulate immune and inflammation responses and can influence the immune response, as shown in Fig. 4.

Discussion

The complex immunosuppressive networks formed by inflammatory cells, tumor cells and their secreted cytokines in the TME play a pivotal role in tumor immune escape.⁴³ The cytokine content can tip the balance between immunosuppressive and immune-activating factors within tumors.⁴⁴ The specific blockade of inhibition pathways in the TME is expected to effectively prevent immune escape and tumor tolerance.

The ineffectiveness of traditional cytokine therapy is primarily attributed to the presence of numerous immunosuppressive cytokines and chemokines in the TME.⁴³ Several studies have directed cytokines specifically to tumors using engineered cytokine-producing T-cells or targeted nanoparticle systems.⁴⁵ Advances in polysaccharide-based nanosystems have the potential to enhance the local delivery of immunotherapeutic agents, reprogram immune regulatory cells, promote inflammatory cytokines, and block immune checkpoints in addition to receptor-mediated active targeting.⁴⁶

Attracting tumor-specific immune cells or immunomodulatory factors directly to tumor sites⁴⁷ rather than stimulating the entire leukocyte population non-specifically has the potential to address systemic toxicity and adverse side effects.⁴³ Tumor cells manipulated in vitro circulate through the blood, creating the potential for efficient direct targeting of immune cell proliferation and providing a source for self-amplification of appropriate immunity, and can serve as a unique and effective carrier for delivering bioactive cytokines to the parental tumor through their homing characteristics, especially in highly metastatic cells.³¹

There are few reports on the use of polysaccharide-modified tumor cells for the treatment of tumors. In this study, inflammatory and immune responses in the subcutaneous region induced by the TFP-B16 cells were explored using transcriptome analysis.

The immune and inflammation process induced by subcutaneous injection of TFP-B16 cells begins with a local cellular response to an extracellular stimulus and the activation of innate (leukocytes, neutrophils, myeloid cells, mast cells, DCs) and adaptive immune cells (T and B cells).

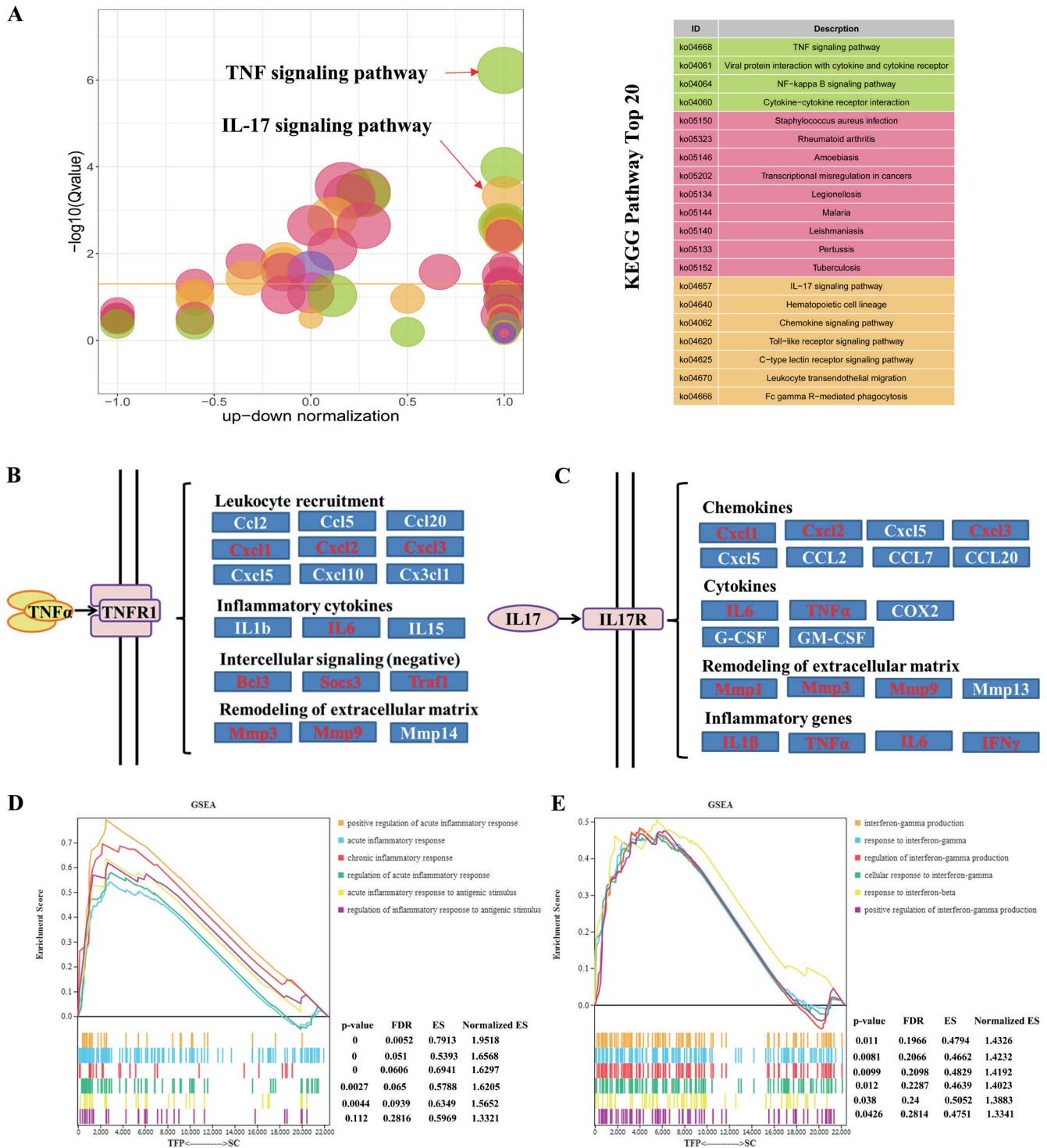


Fig. 3. The TFP-B16 cells activated inflammation via TNF- α and IL-17 signaling pathways. A. Top 20 KEGG pathways; B. The functional regulation of TNF- α signaling pathways; C. The functional regulation of IL-17 signaling pathways; D. The acute or chronic inflammatory responses were induced; E. Interferon production was induced

TFP – *Tremella fuciformis*-derived polysaccharide; TFP-B16 cells – TFP-reeducated B16 cells; KEGG – Kyoto Encyclopedia of Genes and Genomes; GSEA – Gene Set Enrichment Analysis; TNF- α – tumor necrosis factor alpha; IL-17 – interleukin 17.

Cytokines and chemokines such as IL-1, IL-6, IL-8, IL-17, and TNF- α are produced to amplify the local inflammatory process after immune cell migration and adaptive immune response initiation. Tumor necrosis factor alpha has been identified as one of the most effective molecules

for mediating important anti-tumor immune effects that disrupt tumors.⁴⁸ Systemic administration of TNF- α can lead to significant off-target toxicities, thereby limiting the administrable concentration and resulting in lower efficacy.⁴⁹ The methods to stimulate endogenous TNF- α

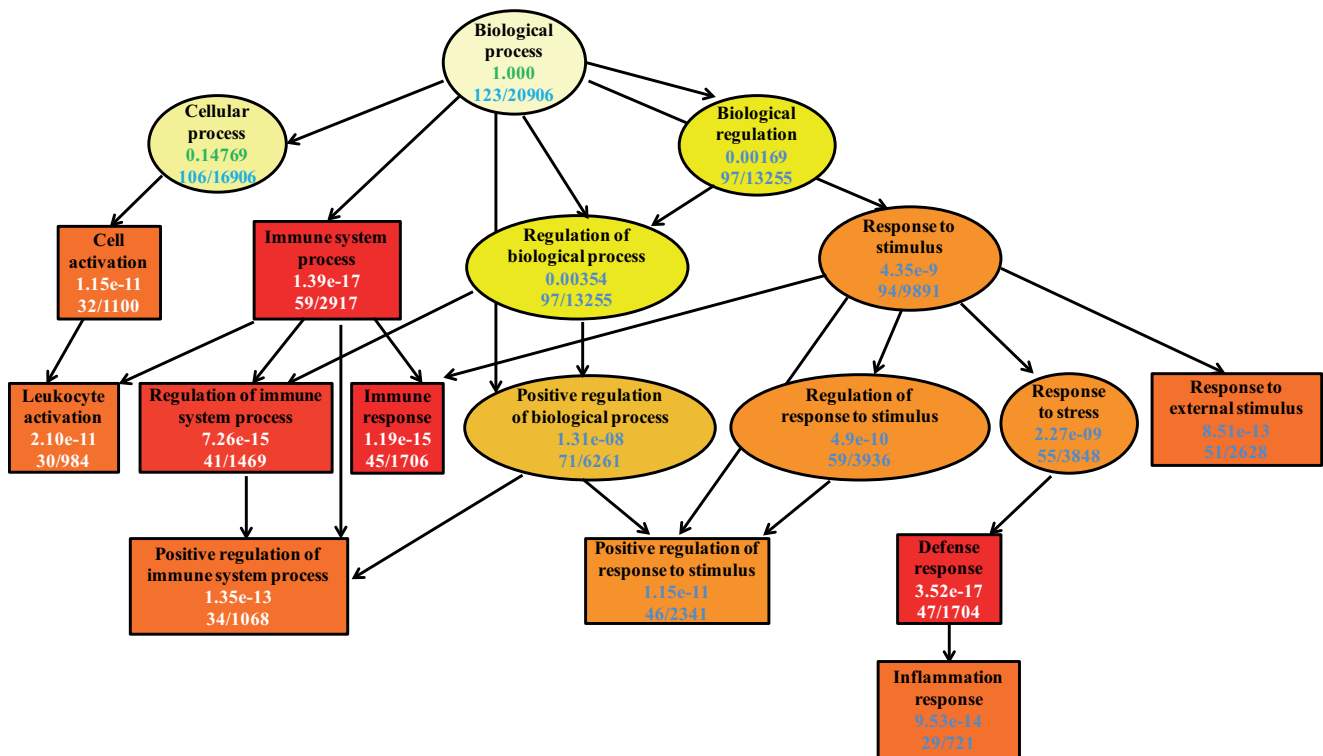


Fig. 4. The interplay of TFP-B16 cells on the immune-inflammatory system. TFP-B16 cells had the most significant impact on “immune system process and response”, and “defense response,” followed by their effects on “cell activation,” “leukocyte activation,” “positive regulation of immune system process,” and “inflammation response”, and finally by their impact on “response to external stimulus”. The arrow indicates the relationship between the upper and lower layers of GO Term. The ellipse represents GO terms with enrichment not in the top 10. The box represents GO terms with enrichment in the top 10. The darker the color, the more significant the enrichment level. Black words indicate the function description in GO terms. The 1st line numbers indicate the p-value obtained by enrichment analysis. The 2nd line numbers indicate the ratio of significant genes in this term and the total number of genes in GO terms

TFP – *Tremella fuciformis*-derived polysaccharide; TFP-B16 cells – TFP-reeducated B16 cells; GO – Gene Ontology.

release are currently being evaluated as a long-term regulatory immune intervention.⁵⁰ The TFP-B16 cells elevated TNF- α , which constitutes a TME signal that biases recruited immune cells toward anti-tumor and pro-inflammatory activities. Tumor necrosis factor alpha has cytotoxic effects and induces the secretion of other cytokines, such as IL-1 β and IL-6. This reaction results in cytokine- and chemokines-mediated damage to target tissues.

Moreover, TFP-B16 cells and their tumor environment not only provide soluble cytokines but also provide unknown cell–cell contact signaling for the expansion of Th17 cells. The TFP-B16 cells upregulated IL-17 production by Th17 cells. Interleukin 17 stimulates CXCL2 and CXCL3 production, attracts IFN- γ anti-tumor neutrophils in vivo, and inhibits tumor growth.⁵¹ Several studies have shown that tumor-specific Th17 polarized cells reduce the advancement of B16 melanoma in a mouse model, and this process heavily depends on IFN- γ production.⁵²

The results revealed heterogeneity in the content of the factors produced by B16 cells and in their impact on the expression of inflammatory and immunity traits. Through these interactions, TFP-B16 cells reshaped the immune and inflammatory microenvironment and may thus inhibit tumor progression.

Limitations

There are some limitations to the present study. First, due to the crucial importance of tumor cells expressing TNF- α for anti-tumor activity, further detection of TNF- α expression in tumor or blood circulation is necessary. Second, the anti-tumor effect and mechanism of B16 cells reprogrammed by TFP are needed in the future mouse models of tumor cells.

Conclusions

Administration of TFP-B16 cells could lead to activation of anti-tumor mechanisms locally and reduced counter-regulatory mechanisms through modification by TFP. This approach would be an alternative and more efficient strategy to deliver cytokines and open up new possibilities for long-term and multi-level tumor control.

Supplementary data

The Supplementary materials are available at <https://doi.org/10.5281/zenodo.10992031>. The package includes the following files:

Supplementary Table 1. Statistical table of data filtering.
Supplementary Table 2. Statistical table of base information.

Supplementary Table 3. Statistical table of ribosomal comparison.

Supplementary Table 4. Statistical table of reference comparison.

Supplementary Table 5. The original data of Fig. 3A.

Supplementary Table 6. The original data of Fig 4.

Data availability

The datasets generated and/or analyzed during the current study are available from the corresponding author on reasonable request.

Consent for publication

Not applicable.

ORCID iDs

Xiumin Li  <https://orcid.org/0000-0002-5296-2960>

Qiaoling Su  <https://orcid.org/0009-0000-1772-8450>

Yutian Pan  <https://orcid.org/0000-0001-9842-9320>

References

- Shalapour S, Karin M. Immunity, inflammation, and cancer: An eternal fight between good and evil. *J Clin Invest*. 2015;125(9):3347–3355. doi:10.1172/JCI80007
- Hanahan D, Weinberg RA. Hallmarks of cancer: The next generation. *Cell*. 2011;144(5):646–674. doi:10.1016/j.cell.2011.02.013
- Di Lorenzo A, Bolli E, Tarone L, Cavallo F, Conti L. Toll-like receptor 2 at the crossroad between cancer cells, the immune system, and the microbiota. *Int J Mol Sci*. 2020;21(24):9418. doi:10.3390/ijms21249418
- Dunn GP, Bruce AT, Ikeda H, Old LJ, Schreiber RD. Cancer immunoediting: From immunosurveillance to tumor escape. *Nat Immunol*. 2002;3(11):991–998. doi:10.1038/ni1102-991
- Pastò A, Consonni FM, Sica A. Influence of innate immunity on cancer cell stemness. *Int J Mol Sci*. 2020;21(9):3352. doi:10.3390/ijms21093352
- Gerada C, Ryan KM. Autophagy, the innate immune response and cancer. *Mol Oncol*. 2020;14(9):1913–1929. doi:10.1002/1878-0261.12774
- Wyatt A, Levy D. Modeling the effect of memory in the adaptive immune response. *Bull Math Biol*. 2020;82(9):124. doi:10.1007/s11538-020-00798-9
- Zadka Ł, Grybowski DJ, Dzięgiel P. Modeling of the immune response in the pathogenesis of solid tumors and its prognostic significance. *Cell Oncol*. 2020;43(4):539–575. doi:10.1007/s13402-020-00519-3
- Fein MR, He XY, Almeida AS, et al. Cancer cell CCR2 orchestrates suppression of the adaptive immune response. *J Exp Med*. 2020;217(10):e20181551. doi:10.1084/jem.20181551
- Law AMK, Lim E, Ormandy CJ, Gallego-Ortega D. The innate and adaptive infiltrating immune systems as targets for breast cancer immunotherapy. *Endocr Relat Cancer*. 2017;24(4):R123–R144. doi:10.1530/ERC-16-0404
- Irimia D, Wang X. Inflammation-on-a-chip: Probing the immune system ex vivo. *Trends Biotechnol*. 2018;36(9):923–937. doi:10.1016/j.tibtech.2018.03.011
- Greten FR, Grivennikov SI. Inflammation and cancer: Triggers, mechanisms, and consequences. *Immunity*. 2019;51(1):27–41. doi:10.1016/j.immuni.2019.06.025
- Singh R, Mishra MK, Aggarwal H. Inflammation, immunity, and cancer. *Mediators Inflamm*. 2017;2017:6027305. doi:10.1155/2017/6027305
- Velazquez-Caldelas TE, Alcalá-Corona SA, Espinal-Enríquez J, Hernandez-Lemus E. Unveiling the link between inflammation and adaptive immunity in breast cancer. *Front Immunol*. 2019;10:56. doi:10.3389/fimmu.2019.00056
- Grivennikov SI, Greten FR, Karin M. Immunity, inflammation and cancer. *Cell*. 2010;140(6):883–899. doi:10.1016/j.cell.2010.01.025
- Bradley J. TNF-mediated inflammatory disease. *J Pathol*. 2008;214(2):149–160. doi:10.1002/path.2287
- Bonizzi G, Karin M. The two NF- κ B activation pathways and their role in innate and adaptive immunity. *Trends Immunol*. 2004;25(6):280–288. doi:10.1016/j.it.2004.03.008
- Yang S, Wang J, Brand DD, Zheng SG. Role of TNF–TNF receptor 2 signal in regulatory T cells and its therapeutic implications. *Front Immunol*. 2018;9:784. doi:10.3389/fimmu.2018.00784
- Pasparakis M, Alexopoulou L, Episkopou V, Kollias G. Immune and inflammatory responses in TNF alpha-deficient mice: A critical requirement for TNF alpha in the formation of primary B cell follicles, follicular dendritic cell networks and germinal centers, and in the maturation of the humoral immune response. *J Exp Med*. 1996;184(4):1397–1411. doi:10.1084/jem.184.4.1397
- Cerboni S, Gehrman U, Preite S, Mitra S. Cytokine-regulated Th17 plasticity in human health and diseases. *Immunology*. 2021;163(1):3–18. doi:10.1111/imm.13280
- Zhao H, Wu L, Yan G, et al. Inflammation and tumor progression: Signaling pathways and targeted intervention. *Sig Transduct Target Ther*. 2021;6(1):263. doi:10.1038/s41392-021-00658-5
- Haghshenas MR, Khademi B, Faghieh Z, Ghaderi A, Erfani N. Immune regulatory cells and IL17-producing lymphocytes in patients with benign and malignant salivary gland tumors. *Immunol Lett*. 2015;164(2):109–116. doi:10.1016/j.imlet.2015.02.008
- Kryczek I, Banerjee M, Cheng P, et al. Phenotype, distribution, generation, and functional and clinical relevance of Th17 cells in the human tumor environments. *Blood*. 2009;114(6):1141–1149. doi:10.1182/blood-2009-03-208249
- Martin-Orozco N, Dong C. The IL-17/IL-23 axis of inflammation in cancer: Friend or foe? *Curr Opin Investig Drugs*. 2009;10(6):543–549. PMID:19513943.
- Guéry L, Dubrot J, Lippens C, et al. Ag-presenting CpG-activated pDCs prime Th17 cells that induce tumor regression. *Cancer Res*. 2014;74(22):6430–6440. doi:10.1158/0008-5472.CAN-14-1149
- Shen J, Xiao Z, Zhao Q, et al. Anti-cancer therapy with TNF α and IFN γ : A comprehensive review. *Cell Prolif*. 2018;51(4):e12441. doi:10.1111/cpr.12441
- Papadakis KA, Targan SR. Tumor necrosis factor: Biology and therapeutic inhibitors. *Gastroenterology*. 2000;119(4):1148–1157. doi:10.1053/gast.2000.18160
- Muranski P, Restifo NP. Essentials of Th17 cell commitment and plasticity. *Blood*. 2013;121(13):2402–2414. doi:10.1182/blood-2012-09-378653
- Bystrom J, Taher TE, Muhyaddin MS, et al. Harnessing the therapeutic potential of Th17 cells. *Mediators Inflamm*. 2015;2015:205156. doi:10.1155/2015/205156
- Sparna T, Rétey J, Schmic K, et al. Genome-wide comparison between IL-17 and combined TNF-alpha/IL-17 induced genes in primary murine hepatocytes. *BMC Genomics*. 2010;11(1):226. doi:10.1186/1471-2164-11-226
- Dondossola E, Dobroff AS, Marchiò S, et al. Self-targeting of TNF-releasing cancer cells in preclinical models of primary and metastatic tumors. *Proc Natl Acad Sci U S A*. 2016;113(8):2223–2228. doi:10.1073/pnas.1525697113
- Schreiber RD, Old LJ, Smyth MJ. Cancer immunoediting: Integrating immunity's roles in cancer suppression and promotion. *Science*. 2011;331(6024):1565–1570. doi:10.1126/science.1203486
- Chen S, Zhou Y, Chen Y, Gu J. fastp: An ultra-fast all-in-one FASTQ preprocessor. *Bioinformatics*. 2018;34(17):i884–i890. doi:10.1093/bioinformatics/bty560
- Langmead B, Salzberg SL. Fast gapped-read alignment with Bowtie 2. *Nat Methods*. 2012;9(4):357–359. doi:10.1038/nmeth.1923
- Kim D, Langmead B, Salzberg SL. HISAT: A fast spliced aligner with low memory requirements. *Nat Methods*. 2015;12(4):357–360. doi:10.1038/nmeth.3317

36. Pertea M, Pertea GM, Antonescu CM, Chang TC, Mendell JT, Salzberg SL. StringTie enables improved reconstruction of a transcriptome from RNA-seq reads. *Nat Biotechnol.* 2015;33(3):290–295. doi:10.1038/nbt.3122
37. Pertea M, Kim D, Pertea GM, Leek JT, Salzberg SL. Transcript-level expression analysis of RNA-seq experiments with HISAT, StringTie and Ballgown. *Nat Protoc.* 2016;11(9):1650–1667. doi:10.1038/nprot.2016.095
38. Li B, Dewey CN. RSEM: Accurate transcript quantification from RNA-Seq data with or without a reference genome. *BMC Bioinformatics.* 2011;12(1):323. doi:10.1186/1471-2105-12-323
39. Love MI, Huber W, Anders S. Moderated estimation of fold change and dispersion for RNA-seq data with DESeq2. *Genome Biol.* 2014; 15(12):550. doi:10.1186/s13059-014-0550-8
40. Suresh R, Mosser DM. Pattern recognition receptors in innate immunity, host defense, and immunopathology. *Adv Physiol Educ.* 2013; 37(4):284–291. doi:10.1152/advan.00058.2013
41. Mercogliano MF, Bruni S, Mauro F, Elizalde PV, Schillaci R. Harnessing tumor necrosis factor alpha to achieve effective cancer immunotherapy. *Cancers (Basel).* 2021;13(3):564. doi:10.3390/cancers13030564
42. Kumar R, Clermont G, Vodovotz Y, Chow CC. The dynamics of acute inflammation. *J Ther Biol.* 2004;230(2):145–155. doi:10.1016/j.jtbi.2004.04.044
43. Gao S, Yang D, Fang Y, et al. Engineering nanoparticles for targeted remodeling of the tumor microenvironment to improve cancer immunotherapy. *Theranostics.* 2019;9(1):126–151. doi:10.7150/thno.29431
44. Zhang M, Kim JA, Huang AYC. Optimizing tumor microenvironment for cancer immunotherapy: β -glucan-based nanoparticles. *Front Immunol.* 2018;9:341. doi:10.3389/fimmu.2018.00341
45. Waldman AD, Fritz JM, Lenardo MJ. A guide to cancer immunotherapy: From T cell basic science to clinical practice. *Nat Rev Immunol.* 2020;20(11):651–668. doi:10.1038/s41577-020-0306-5
46. Saeed M, Gao J, Shi Y, Lammers T, Yu H. Engineering nanoparticles to reprogram the tumor immune microenvironment for improved cancer immunotherapy. *Theranostics.* 2019;9(26):7981–8000. doi:10.7150/thno.37568
47. Zeng Y, Xiang Y, Sheng R, et al. Polysaccharide-based nanomedicines for cancer immunotherapy: A review. *Bioact Mater.* 2021;6(10): 3358–3382. doi:10.1016/j.bioactmat.2021.03.008
48. Laha D, Grant R, Mishra P, Nilubol N. The role of tumor necrosis factor in manipulating the immunological response of tumor microenvironment. *Front Immunol.* 2021;12:656908. doi:10.3389/fimmu.2021.656908
49. Siurala M, Havunen R, Saha D, et al. Adenoviral delivery of tumor necrosis factor- α and interleukin-2 enables successful adoptive cell therapy of immunosuppressive melanoma. *Mol Ther.* 2016;24(8): 1435–1443. doi:10.1038/mt.2016.137
50. Steeland S, Libert C, Vandenbroucke RE. A new venue of TNF targeting. *Int J Mol Sci.* 2018;19(5):1442. doi:10.3390/ijms19051442
51. Vitiello GA, Miller G. Targeting the interleukin-17 immune axis for cancer immunotherapy. *J Exp Med.* 2020;217(1):e20190456. doi:10.1084/jem.20190456
52. Ye J, Livergood RS, Peng G. The role and regulation of human Th17 cells in tumor immunity. *Am J Pathol.* 2013;182(1):10–20. doi:10.1016/j.ajpath.2012.08.041

Is there a role of calprotectin testing in the diagnosis of surgical site infections after total hip and knee arthroplasty? A preliminary study

Dariusz Grzelecki^{1,A–D,F}, Dariusz Marczał^{1,C,E}, Piotr Dudek^{1,B,E}, Tomasz Okoń^{1,B,E}, Bartłomiej Kordasiewicz^{2,C,E}, Jacek Kowalczewski^{1,A,E,F}

¹ Department of Orthopedics and Rheumorthopedics, Centre of Postgraduate Medical Education, Otwock, Poland

² Idea Ortopedia, Warsaw, Poland

A – research concept and design; B – collection and/or assembly of data; C – data analysis and interpretation; D – writing the article; E – critical revision of the article; F – final approval of the article

Advances in Clinical and Experimental Medicine, ISSN 1899–5276 (print), ISSN 2451–2680 (online)

Adv Clin Exp Med. 2024;33(5):543–548

Address for correspondence

Dariusz Grzelecki

E-mail: dariuszgrzelecki@gmail.com

Funding sources

This study was supported by the Ministry of Science and Higher Education subsidy to preserve the research potential of the Postgraduate Medical Education Center (No. 501-1-17-29-18, No. 501-1-17-29-19).

Conflict of interest

None declared

Received on October 2, 2023

Reviewed on February 18, 2024

Accepted on April 9, 2024

Published online on May 14, 2024

Cite as

Grzelecki D, Marczał D, Dudek P, Okoń T, Kordasiewicz B, Kowalczewski J. Is there a role of calprotectin testing in the diagnosis of surgical site infections after total hip and knee arthroplasty? A preliminary study. *Adv Clin Exp Med.* 2024;33(5):543–548. doi:10.17219/acem/186958

DOI

10.17219/acem/186958

Copyright

Copyright by Author(s)

This is an article distributed under the terms of the Creative Commons Attribution 3.0 Unported (CC BY 3.0) (<https://creativecommons.org/licenses/by/3.0/>)

Abstract

Background. Recent studies have revealed the usefulness of synovial calprotectin (CLP) in diagnosing chronic periprosthetic joint infections (PJIs). However, there is still a lack of evidence to support the use of serum CLP in the diagnosis of early PJIs and surgical site infections (SSIs) after total joint arthroplasties (TJAs).

Objectives. The primary aim of this study is to investigate the standard kinetics of CLP concentrations in the blood during the very early postoperative period after non-complicated total hip arthroplasty (THA) and total knee arthroplasty (TKA). The secondary aim was to perform a preliminary comparison of CLP concentrations between non-infected patients and patients with recognized SSIs.

Materials and methods. A total of 64 consecutive patients who underwent primary THA and TKA were included in this prospective research. Sixty patients (30 THA and 30 TKA) were scheduled to determine the standard shape of the blood CLP curve and the expected concentrations during the first 5 postoperative days after non-complicated TJAs. In 4 additional patients, early SSI was confirmed, and they were included in a separate SSI subgroup.

Results. Calprotectin demonstrated a linear increase during the first 5 postoperative days. Statistically significant differences in CLP concentrations between non-infected cases and SSIs were not observed. The preoperative median results with interquartile range (Q1–Q3) were 0.52 (0.39–0.64) mg/dL and 0.5 (0.47–0.52) mg/dL ($p = 0.77$), while post operation they were as follows: on postoperative day 1: 0.88 (0.53–1.3) mg/dL and 0.86 (0.62–1.1) mg/dL ($p = 0.84$), on postoperative day 3: 1.77 (1.29–2.08) mg/dL and 1.85 (1.70–1.95) mg/dL ($p = 0.72$), and on postoperative day 5: 2.32 (1.79–2.67) mg/dL and 2.56 (2.25–2.83) mg/dL ($p = 0.55$), respectively.

Conclusions. Serial CLP measurements during the early postoperative period revealed a linear (statistically significant) increase in concentration to postoperative day 5 without an evident point of decrease. A significant difference in median values and the course of curve patterns between the non-complicated and SSI groups was not observed.

Key words: calprotectin, periprosthetic joint infection, surgical site infection, total hip arthroplasty, total knee arthroplasty

Background

A surgical site infection (SSI) is a serious early complication of total joint arthroplasty (TJA) with a reported incidence of up to 3.68%.^{1,2} This complication is associated with multiple perioperative factors and comorbidities, e.g., type of surgery (primary or revision), diabetes, obesity, rheumatoid arthritis, and smoking.^{1,3} Despite the availability of guidelines that can help to recognize SSIs,⁴ the diagnosis of infection in the early postoperative period after TJA is challenging due to the different expressions of clinical symptoms, their intensification and overlap following surgical trauma, and a wide fluctuation of laboratory marker concentrations in specific patients.^{5,6} Current concepts propose the use of clinical symptoms together with single or serial measurements of biochemical blood markers such as C-reactive protein (CRP), white blood cell (WBC) count and interleukin 6 (IL-6).⁷⁻⁹ However, these biomarkers have shown non-univocal interpretations in the septic scenario. Thus, there is a need to investigate other diagnostic markers with potential value in diagnosing SSI during the early postoperative period.

Calprotectin (CLP) is a zinc and calcium-binding protein that reduces superoxide dismutase and inhibits bacterial defense mechanisms against oxygenation. This heterodimer is released to body fluids from activated granulocytes and monocytes during inflammation and infection.¹⁰ Currently, CLP has been helpful in the diagnosis of inflammatory bowel diseases, monitoring the biological treatment of rheumatoid arthritis^{10,11} and diagnosing chronic periprosthetic joint infections (PJIs).¹²⁻¹⁴ However, there is still a lack of evidence to support the use of serum samples of this marker in the diagnosis of early infection and SSIs after TJA.

Objectives

The primary aim of this preliminary study was to reveal the standard kinetics of CLP concentrations in the blood during the early postoperative period after non-complicated total hip arthroplasty (THA) and total knee arthroplasty (TKA) and to compare this curve shape with curves of CRP and IL-6. The secondary aim was to compare blood CLP concentrations between non-infected patients and patients with recognized early infections/SSIs.

Materials and methods

This study has received Postgraduate Medical Education Center Ethical Committee approval No. 104/PB/2018.

Blood samples from 64 consecutive patients (25 men and 39 women) who underwent primary THA and TKA between January 2019 and December 2019 were tested. Initially, this study aimed to analyze data collected from

60 patients (30 THA and 30 TKA) to determine the standard shape for the concentration curve of blood CLP during the first 5 days after the surgery. Despite the fact that in this study, patients after TKA and THA were analyzed, in terms of the examined markers these groups were homogenous and were combined as 1. Patients followed the standard protocol of observation and postoperative rehabilitation used routinely in the authors' department and were discharged on the 5th postoperative day. All patients in the non-infected group were observed for a minimum of 2 years postoperatively, and there were no misdiagnosed cases. During the collection of the samples on the appointed days, in 4 patients (1 after THA and 3 after TKA), SSIs following Centers for Disease Control and Prevention (CDC) criteria were recognized.⁴ These patients were enrolled in a separate subgroup to conduct the additional analysis. Patients with chronic inflammatory diseases (e.g., rheumatoid arthritis, ankylosing spondylitis), with active or previous oncological treatment, patients with preoperative CRP concentration in blood >10 mg/L, those who have undergone surgical procedures on the knee joint in the past or were treated due to septic arthritis or PJIs, and those who underwent THA after femoral neck fractures were excluded from this study.

The CLP concentrations in blood were measured with an immunoturbidimetric Calprotectin Immunoassay (GCal; Gentian, Moss, Norway). Blood samples were collected at 7 AM from patients at 4 time points: the day before surgery, during admission to the hospital, and on postoperative days 1, 3 and 5. All samples were collected in test tubes with lithium heparin. Afterward, the quantitative analysis was done with the use of a Mindray BS-400 analyzer (Diamond Diagnostics Inc., Holliston, USA). Additionally, serum CRP (CRP Ultra; Cormay, Łomianki, Poland) and serum IL-6 (Interleukin 6 ELISA kit; Roche, Basel, Switzerland) concentrations were measured from the same blood samples.

Statistical analysis was performed with Statistica v. 13.1 (TIBCO Software Inc., Palo Alto, USA). The Shapiro–Wilk test was utilized to check the normality of the data. For dichotomous data, the Fisher's exact test was performed. For continuous variables, Mann–Whitney U tests were employed, and results were presented as medians with interquartile ranges (Q1–Q3). For repeated variables, non-parametric Friedman's analysis of variance (ANOVA) was performed. To assess a trend for analyzed markers in subsequent days, the Page test was used. A p-value < 0.05 was considered significant.

Results

Demographic and clinical data of the study groups are presented in Table 1. Statistically significant differences between the medians (Q1–Q3) for CLP concentrations in TKA and THA groups were observed between: 1) preoperative

Table 1. Demographic and clinical data

Parameters	Non-infected (n = 60)	SSI (n = 4)	Total (n = 64)	p-value	z	U
Male/female	24/36	1/3	25/39	>0.999*	–	–
Hip/knee	30/30	1/3	31/33	0.614*	–	–
Age [years]	64.50 (59.0–72.00)	64.00 (62.50–65.50)	64.50 (59.75–72.00)	0.820**	–0.361	107
Weight [kg]	82.00 (74.50–94.25)	77.00 (69.50–87.25)	82.00 (72.75–94.25)	0.529**	–0.625	96.5
BMI [kg/m ²]	30.12 (27.32–33.77)	27.90 (25.92–31.34)	29.94 (26.82–33.77)	0.718**	–0.388	106
Time of surgery [min]	60.00 (50.00–70.00)	70.00 (68.75–73.75)	60.00 (52.25–70.00)	0.083**	–1.763	57
Postoperative hospital stay [days]	6.00 (5.00–7.00)	9.50 (8.00–14.00)	6.00 (5.75–7.00)	<0.002**	–3.097	12
Blood transfusions (THA/TKA)	20	1	21	>0.999*	–	–
Transfusions per patient ratio	0.33	0.25	0.32	0.925**	–0.163	116
Diabetes	9	1	10	>0.999*	–	–

SSI – surgical site infection; BMI – body mass index; THA – total hip arthroplasty; TKA – total knee arthroplasty. *Fisher's exact test (2×2); **Mann–Whitney U test; z – value of Mann–Whitney U test; U – Mann–Whitney U test. The values are presented as a median and interquartile range (Q1–Q3)

measurements and postoperative day 3; 2) preoperative measurements and postoperative day 5; 3) postoperative day 1 and postoperative day 3; and 4) postoperative day 1 and postoperative day 5 (Mann–Whitney U test: $p < 0.001$ for all comparisons). A statistically significant increasing trend of CLP concentrations after TKA (Page test: $p < 0.001$) and THA (Page test: $p < 0.001$) was observed. Statistically significant differences in median (Q1–Q3) CLP concentrations between THA and TKA from preoperative and postoperative measurements were not observed (Fig. 1A).

In consecutively operated patients after primary THA and TKA, a SSI was confirmed in 4/64 patients (6.25%). In this group, 3 cases (1 THA and 2 TKA) presented with superficial infection secondary to wound healing issues without joint capsule perforation, for which surgical debridement and irrigation were performed. In 1 patient (after TKA), according to CDC criteria, deep space/organ SSI (early PJI) was recognized, and debridement, antibiotics and implant retention with a mobile elements exchange (DAIR) procedure were administered. Statistically significant differences in CLP concentrations between non-infected cases and SSI were not observed (Fig. 1B).

For CRP, statistically significant differences between non-infected and SSI groups were noted only on postoperative day 5 (95.55 (70.95–125.40) mg/L vs 202.50 (174.63–232.13) mg/L; Mann–Whitney U test: $p = 0.005$). However, for preoperative measurements, on postoperative day 1 and postoperative day 3, significant differences were not observed (Fig. 1C).

For IL-6 concentrations, significant differences were noted on postoperative day 3 (64.10 (47.05–100.40) pg/mL vs 118.75 (91.43–146.53) pg/mL; Mann–Whitney U test: $p = 0.047$) and postoperative day 5 (29.10 (19.28–48.55) pg/mL vs 64.40 (60.48–91.50) pg/mL;

Mann–Whitney U test: $p = 0.016$). Values of IL-6 concentrations measured preoperatively and on postoperative day 1 did not differ significantly (Fig. 1D). Median values with Q1–Q3 are presented in the Table 2.

Discussion

In our study, we assessed the usefulness of the serum CLP marker, which recently showed a high usefulness in the diagnosis of chronic PJIs when it is determined in synovial fluid.^{12,13,15} Unfortunately, the potential value of CLP in the diagnosis of early PJIs and SSIs after primary TJAs was not investigated before, and to our knowledge, this is the first report that revealed a standard pattern for the kinetic curve of CLP after non-complicated THA and TKA. We have revealed a constant, linear increase during the first 5 postoperative days. In this pilot study, we did not reveal significant differences between non-infected and SSI cases in terms of the CLP concentration values on corresponding postoperative days.

In relation to blood CRP, after major orthopedic operations such as THA and TKA, in non-complicated cases, concentrations increase with a peak after 2 or 3 days, followed by a rapid decrease.^{8,16} Larsson et al. reported the highest CRP values are seen 48–72 h after THA and TKA. Moreover, they revealed that normal or close to normal CRP levels returned by 14–21 days after surgery.⁸ This was also confirmed by Waśko et al., who also observed a wide range of blood CRP concentrations from 100 mg/L to 260 mg/L on the 3rd day after THA and TKA procedures.⁷ Based on the standard kinetics of CRP in the postoperative period, different studies were

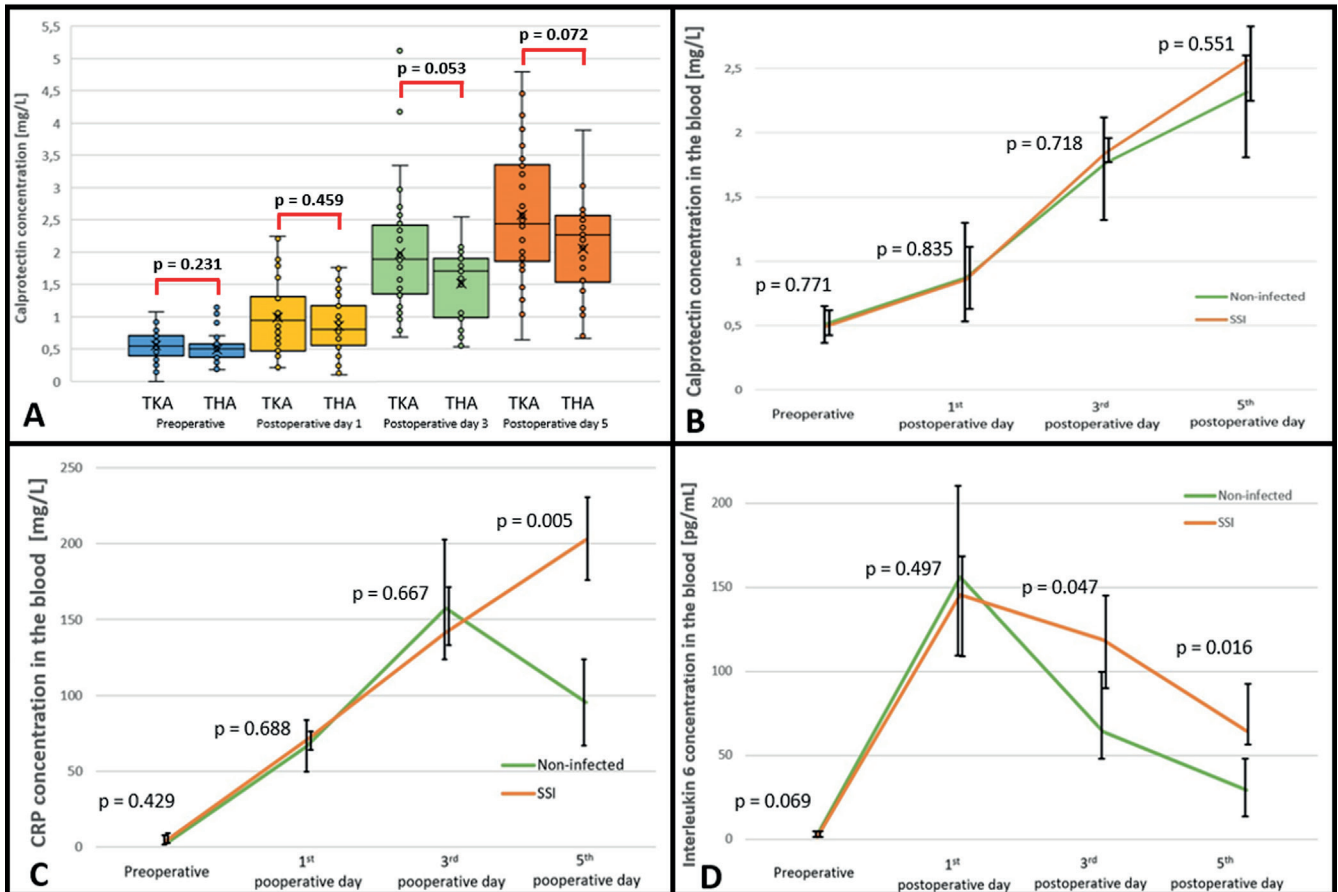


Fig. 1. A. Box plot of calprotectin concentrations at 4 timepoints in patients who underwent total hip arthroplasty (THA) and total knee arthroplasty (TKA) included in the non-infected group. Significant differences in preoperative and postoperative measurements were not observed. A line graph of blood calprotectin (CLP) (B), C-reactive protein (CRP) (C) and interleukin 6 (IL-6) (D) during the perioperative period (preoperative and postoperative days 1, 3 and 5) for all patients (THA and TKA combined) in the non-infected (green line) and surgical site infection (SSI) (orange line) groups. Results of marker concentrations are presented as median (Q1–Q3). Significant differences in the Mann–Whitney U test between groups were observed for CRP on day 5 ($p = 0.005$), IL-6 on day 3 ($p = 0.047$) and IL-6 on day 5 ($p = 0.016$)

Table 2. Median concentrations with interquartile range (Q1–Q3) of calprotectin (CLP), C-reactive protein (CRP) and interleukin 6 (IL-6) in the perioperative period for both total hip arthroplasty (THA) and total knee arthroplasty (THA) in the non-infected and surgical site infection (SSI) groups. Friedman’s analysis of variance (ANOVA) test was performed to check the relationship between variables

Variable	Preoperative	Postoperative day 1	Postoperative day 3	Postoperative day 5	Friedman ANOVA p-value	df1	df2	F
Non-infected								
CLP [mg/dL]	0.52 (0.39–0.64)	0.88 (0.53–1.30)	1.77 (1.29–2.08)	2.32 (1.79–2.67)	<0.001	3	177	157.344
CRP [mg/L]	2.45 (1.20–3.93)	66.30 (49.03 – 80.55)	157.60 (123.03–207.75)	95.55 (70.95–125.40)	<0.001	3	177	293.399
IL-6 [pg/mL]	2.60 (1.58–3.96)	156.00 (110.65–214.33)	64.10 (47.05–100.40)	29.10 (19.28–48.55)	<0.001	3	177	138.831
SSI								
CLP [mg/dL]	0.50 (0.47–0.52)	0.86 (0.62–1.10)	1.85 (1.70–1.95)	2.56 (2.25–2.83)	0.007	3	9	78.312
CRP [mg/L]	4.05 (2.63–5.10)	70.20 (67.35–72.78)	141.63 (127.95–167.55)	202.50 (174.63–232.13)	0.007	3	9	31.653
IL-6 [pg/mL]	1.50 (1.50–1.75)	145.55 (112.38–170.75)	118.75 (91.43–146.53)	64.40 (60.48–91.50)	0.026	3	9	14.461

df – degrees of freedom; F – Friedman test.

conducted to assess whether the increase in CRP correlates with the risk of developing PJIs. Despite this fact, there is still no consensus about the usefulness of serial CRP measurements after TJA in diagnosing early PJIs.¹⁷ Niskanen et al. concluded that the rise in CRP levels at 1 or 2 weeks after TJA may be an indicator of a serious complication.¹⁶ Similarly, Kim et al. concluded that elevated CRP levels may indicate postoperative infection; however, they emphasized that there is a need to differentiate between non-infection causes and other site infections.¹⁸ On the other hand, Rohe et al. and Windish et al. revealed that serial measurements of CRP have no predictive value in diagnosing early PJIs after THA and TKA.^{19,20} We are aware that this requires further investigation. However, we believe that serial measurements and the observation of the curve pattern are currently the best and widely available laboratory methods to diagnose an early postoperative infection. Due to the wide range of the received values of CRP, there is a need to compare the obtained results with those measured on the day of the concentration peak.

In the case of IL-6, our results also agree with those reported by the other authors. Compared to the curve trajectory of CRP, higher values of IL-6 are expected earlier. In non-complicated TJAs, the IL-6 concentration curve presents different kinetic patterns than CLP and CRP, with a maximum, rapid increase on the 1st postoperative day, and a more dynamic decrease in the following days. Maniar et al. reported that the IL-6 concentration increased rapidly, with a peak at 12 h after TKA, and returned to a level in the range of 3–14 pg/mL within 2 weeks.²¹ Waśko et al., in the study mentioned above, observed that IL-6 reaches the highest value during the first 24 h after TJA and decreases over the following postoperative days.⁷ Despite this fact, we observed significantly higher concentrations of IL-6 on days 3 and 5 between SSI and non-complicated cases and agreed with Aichmair et al. that the increased serum values of this marker cannot predict an early onset PJI.²²

Limitations

This study has some limitations which should be considered before data analysis. First, although this is a prospective study, the SSI group (4 patients) was significantly smaller than the non-infected group (60 patients). Second, the analysis covered only a short postoperative period (the 5th postoperative day to the day of the patient's discharge). A standard point of concentration decrease for CLP was not established in contrast to CRP and IL-6. Finally, in this study, we did not analyze the influence of additional demographical and clinical factors that may have influenced the final results.

Conclusions

1. Serial serum CLP measurements during the early postoperative period revealed a close to linear increase of concentration up to postoperative day 5 without the evident point of decrease in non-complicated cases.

2. A significant difference in median values and the course of the curve patterns between the non-complicated and SSI groups was not observed. There is a need to verify our findings and the potential value of CLP in the diagnosis of PJI/SSI on a larger group of patients to determine when the peak, the start of concentration decrease and its normalization occurs after elective TJAs.

Data availability

The datasets generated and/or analyzed during the current study are available from the corresponding author on reasonable request.

Consent for publication

Not applicable.

ORCID iDs

Dariusz Grzelecki  <https://orcid.org/0000-0003-1812-7061>

Dariusz Marczak  <https://orcid.org/0000-0002-4652-9837>

Jacek Kowalczewski  <https://orcid.org/0000-0002-4977-3923>

References

- Ashraf I, Mohib Y, Hasan O, Malik A, Ahmad K, Noordin S. Surgical site infection surveillance following total knee arthroplasty: Tertiary care hospital experience. *Ann Med Surg.* 2018;31:14–16. doi:10.1016/j.amsu.2018.04.006
- Yokoe DS, Avery TR, Platt R, Huang SS. Reporting surgical site infections following total hip and knee arthroplasty: Impact of limiting surveillance to the operative hospital. *Clin Infect Dis.* 2013;57(9):1282–1288. doi:10.1093/cid/cit516
- Tandon T, Tadros BJ, Akehurst H, Avasthi A, Hill R, Rao M. Risk of surgical site infection in elective hip and knee replacements after confirmed eradication of MRSA in chronic carriers. *J Arthroplasty.* 2017; 32(12):3711–3717. doi:10.1016/j.arth.2017.06.036
- Henriksen NA, Meyhoff CS, Wetterslev J, Wille-Jørgensen P, Rasmussen LS, Jørgensen LN. Clinical relevance of surgical site infection as defined by the criteria of the Centers for Disease Control and Prevention. *J Hosp Infect.* 2010;75(3):173–177. doi:10.1016/j.jhin.2009.12.022
- Stevens DL, Bisno AL, Chambers HF, et al. Executive summary: Practice Guidelines for the Diagnosis and Management of Skin and Soft Tissue Infections: 2014 Update by the Infectious Diseases Society of America. *Clin Infect Dis.* 2014;59(2):147–159. doi:10.1093/cid/ciu444
- Parvizi J, Fassihi SC, Enayatollahi MA. Diagnosis of periprosthetic joint infection following hip and knee arthroplasty. *Orthop Clin North Am.* 2016;47(3):505–515. doi:10.1016/j.oacl.2016.03.001
- Wasko MK, Bobecka-Wesołowska K, Tomasiuk R, Kowalczewski J. Measurement of the inflammatory response in the early postoperative period after hip and knee arthroplasty. *Clin Chem Lab Med.* 2015;53(11):1785–1792. doi:10.1515/cclm-2014-1055
- Ware JH, Zhou Z, Guan J, Kennedy AR, Kopelovich L. Establishment of human cancer cell clones with different characteristics: A model for screening chemopreventive agents. *Anticancer Res.* 2007;27(1A):1–16. PMID:17352209.

9. Fernández-Sampedro M, Fariñas-Alvarez C, Garcés-Zarzalejo C, et al. Accuracy of different diagnostic tests for early, delayed and late prosthetic joint infection. *BMC Infect Dis.* 2017;17(1):592. doi:10.1186/s12879-017-2693-1
10. Sherwood R, Walsham N. Fecal calprotectin in inflammatory bowel disease. *Clin Exp Gastroenterol.* 2016;9:21–29. doi:10.2147/CEG.S51902
11. Turvill J, Aghahoseini A, Sivarajasingham N, et al. Faecal calprotectin in patients with suspected colorectal cancer: A diagnostic accuracy study. *Br J Gen Pract.* 2016;66(648):e499–e506. doi:10.3399/bjgp16X685645
12. Wouthuyzen-Bakker M, Ploegmakers JJW, Ottink K, et al. Synovial calprotectin: An inexpensive biomarker to exclude a chronic prosthetic joint infection. *J Arthroplasty.* 2018;33(4):1149–1153. doi:10.1016/j.arth.2017.11.006
13. Grzelecki D, Walczak P, Szostek M, Grajek A, Rak S, Kowalczewski J. Blood and synovial fluid calprotectin as biomarkers to diagnose chronic hip and knee periprosthetic joint infections. *Bone Joint J.* 2021;103-B(1):46–55. doi:10.1302/0301-620X.103B1.BJJ-2020-0953.R1
14. Salari P, Grassi M, Cinti B, Onori N, Gigante A. Synovial fluid calprotectin for the preoperative diagnosis of chronic periprosthetic joint infection. *J Arthroplasty.* 2020;35(2):534–537. doi:10.1016/j.arth.2019.08.052
15. Grassi M, Salari P, Farinelli L, D'Anzeo M, Onori N, Gigante A. Synovial biomarkers to detect chronic periprosthetic joint infection: A pilot study to compare calprotectin rapid test, calprotectin ELISA immunoassay and leukocyte esterase test. *J Arthroplasty.* 2022;37(4):781–786. doi:10.1016/j.arth.2021.12.040
16. Niskanen RO, Korkala O, Pammo H. Serum C-reactive protein levels after total hip and knee arthroplasty. *J Bone Joint Surg Br.* 1996;78(3):431–433. PMID:8636181.
17. Domecky P, Rejman Patkova A, Mala-Ladova K, Maly J. Inflammatory blood parameters as prognostic factors for implant-associated infection after primary total hip or knee arthroplasty: A systematic review. *BMC Musculoskelet Disord.* 2023;24(1):383. doi:10.1186/s12891-023-06500-z
18. Kim TW, Kim DH, Oh WS, Sim JA, Lee YS, Lee BK. Analysis of the causes of elevated C-reactive protein level in the early postoperative period after primary total knee arthroplasty. *J Arthroplasty.* 2016;31(9):1990–1996. doi:10.1016/j.arth.2016.02.037
19. Rohe S, Böhle S, Matziolis G, Jacob B, Wassilew G, Brodt S. C-reactive protein during the first 6 postoperative days after total hip arthroplasty cannot predict early periprosthetic infection. *Arch Orthop Trauma Surg.* 2022;143(6):3495–3503. doi:10.1007/s00402-022-04565-4
20. Windisch C, Brodt S, Roehner E, Matziolis G. C-reactive protein course during the first 5 days after total knee arthroplasty cannot predict early prosthetic joint infection. *Arch Orthop Trauma Surg.* 2017;137(8):1115–1119. doi:10.1007/s00402-017-2709-8
21. Maniar RN, Navaneethan G, Ranvir S, Maniar AR, Dhiman A, Agrawal A. What is the normal trajectory of interleukin-6 and C-reactive protein in the hours and days immediately after TKA? *Clin Orthop Relat Res.* 2019;477(1):41–46. doi:10.1097/CORR.0000000000000332
22. Aichmair A, Frank B, Simon S, et al. Postoperative IL-6 levels cannot predict early onset periprosthetic hip/knee infections: An analysis of 7,661 patients at a single institution. *Eur Cell Mater.* 2022;43:293–298. doi:10.22203/eCM.v043a20